technische universität dortmund

Chair of Energy Conversion

Design and Evaluation of a New Type of Harmonic-Excited Synchronous Machine for Variable-Speed Applications

A thesis approved for the academic degree of

Doktor der Ingenieurwissenschaften
— Dr.-Ing. —

at the
Chair of Energy Conversion
Faculty of Electrical Engineering and Information Technology
TU Dortmund University

by
Jan Pötter, M.Sc.
Dortmund, 2023

Supervisor: Prof. Dr.-Ing. Martin Pfost, TU Dortmund University
Co-Advisor: Prof. Dr.-Ing. Gernot Schullerus, Reutlingen University

Date of Oral Examination: 04.12.2024

PhD thesis at the Faculty of Electrical Engineering and Information Technology
TU Dortmund University
Dortmund

Date of disputation: 04.12.2024
Author: Jan Pötter

Examination committee:
Prof. Dr.-Ing. Martin Pfost
Prof. Dr.-Ing. Gernot Schullerus
Prof. Dr.-Ing. Stephan Frei
Prof. Dr. Stefan Palzer

Abstract

In this work a new type of brushless-excited wound-rotor synchronous machine for variable-speed applications is proposed and analyzed. The excitation of the field winding is achieved using inductive power transmission which normally requires an additional transmission coil on the stator and receiver coil on the rotor. However, the proposed machine does not need any additional windings or ferromagnetic material on either stator or rotor. This is achieved by applying pole phase modulation to the existing coil groups of a conventional wound-rotor synchronous machine with the help of a modified stator power electronic converter and rotor rectifier. Thus, two distinct airgap fields can be produced with independent current components — one for controlling the torque production and one for inductively exciting the field winding. A prototype of the machine concept is designed, constructed and investigated experimentally on a machine test bench.

The theoretical analysis of the proposed machine is performed based on the one-dimensional approximation of the airgap flux density. An analytical full-order machine model is derived and simplifications for steady-state are discussed. A field-oriented control algorithm is conceived which can track both the torque-producing currents and the excitation currents. The machine model, its drive electronics and the control algorithm are then investigated and verified using dynamic simulations.

A machine test bench is built and used to identify the designed machine and verify the capability of the machine concept to produce a load torque and excite the field winding inductively. The no-load experiment is used to isolate the effects of the excitation system and find those excitation system settings that grant the best efficiency. The influence of iron losses are identified as a major contributor to the losses. This is why a computationally quick and simple iron loss model is implemented, applied to the machine concept and compared with measurements. The iron losses are attributed to the additional speed-dependent forward and backward rotating fields superimposed on the conventional fields of a wound-rotor synchronous machine.

As a significant amount of DC link voltage is required to inductively excite the field winding, the torque-speed region of the machine concept is investigated analytically, numerically and experimentally. Simple formulas for the reduced maximum torque-speed curve are given and the loss of efficiency and speed range is calculated. An experimental comparison for a reduced DC link voltage is performed to verify the reduction of speed range. Lastly, an extension to the proposed concept which can address both the iron losses and the DC link voltage demand is discussed.

Acknowledgment

I would like to express my sincere gratitude to my supervisor, Prof. Dr.-Ing. Martin Pfost, for his valuable guidance and trust throughout this research, especially because this research work was detached from the other topics at the chair of energy conversion both in topic and in location. The opportunity and freedom to investigate freely the HESM concept from an idea to a working prototype would not have been possible without his support. His encouragement was vital in finishing this dissertation when I questioned whether such a fringe topic was even worthy of a PhD. I would also like to thank my co-supervisor, Prof. Dr.-Ing. Gernot Schullerus, who also supported this work from the very beginning in both encouragement and technical insight.

I also wish to thank my former colleagues at the chair of energy conversion: Hannes Schmidt for the countless hours of help - from aligning shafts to ordering PCBs; Christian Unger, Lukas Schmitz, Lukas Knappstein, Patrick Lenzen and Tim Krigar for their help in all things power electronics and semiconductors; Sebastian Lange for the good memories and wonderful work atmosphere; Simone Müller for her tireless help in all bureaucratic matters; and also all the other colleagues who I don't want to mention by name for fear of missing one. Thank you for the wonderful work environment.

I would also like to thank my wonderful parents whose support in over ten years of university was invaluable - and whose gentle encouragement to bring this work to a close proved essential.

Most importantly, I would like to thank God. Some time at the end of 2019 right around when the HESM concept was born, through a long personal struggle I found the meaning of life.

„*Since, then, you have been raised with Christ, set your hearts on things above, where Christ is, seated at the right hand of God. Set your minds on things above, not on earthly things. For you died, and your life is now hidden with Christ in God. When Christ, who is your life, appears, then you also will appear with him in glory.*“- Colossians 3,1-3

May the careful reader forgive any errors that doubtlessly remain in this work.

Contents

Chapter 1

Introduction

The conception of vector control for AC machines in the 1970s, the commercialization of microprocessors in the 1980s and the growing maturity of IGBT power semiconductors since the late 1980s are the three major technological milestones that have paved the way for variable-speed drives. Contrary to grid-connected AC machines where the fixed grid voltage and frequency limit the operating region to a fixed speed (or a narrow speed interval), variable-speed drives allow adjusting both the voltage and frequency of an electrical machine. Therefore, the machine can be operated in a wide speed interval and follow trajectories with high precision and requirements on the dynamic behavior. These advances have been crucial for the growing transportation and servo industry. Even in fan and pump applications driven by grid-connected induction motors, retrofitting a variable-speed drive has significant energy savings potential compared to using throttle valves to limit the flow rate. Furthermore, while a grid-connected machine traditionally only runs optimally in a single operating point, the ability to adjust the voltage and frequency gives additional degrees of freedom for optimizing the machine efficiency in the entire operating region.

With the growing awareness of climate change, efforts are being undertaken to increase the efficiency of electrical machines and to minimize the environmental impact of the materials used in the manufacturing process. While a wide range of electrical machine types are available for variable-speed drives, the preferred option for transportation and servo applications are permanent-magnet synchronous machines (PMSMs), because they have the highest power-to-weight and power-to-volume ratio of any machine type. However, their disadvantages are threefold: From an **economic** standpoint, the utilization of the rare-earth magnets used in PMSMs is the highest cost factor compared to the copper, steel and insulation material required in magnet-free machine topologies. Furthermore, in view of the strained geopolitical relations with China and Russia, the monopoly of the rare-earth market by China is problematic which is only changing slowly [1]. Additionally, the mining of rare earths is **ecologically** harmful as toxic chemicals are needed to separate the metals from the

soil which has led to the contamination of soil and water supplies in China [2]. From the perspective of **performance**, the PMSM is limited by its constant excitation field imposed by the permanent magnets. While the PMSM reaches its optimal efficiency near the rated torque and in the vicinity of the field-weakening region the constant excitation field causes high iron losses at high speeds and partial loads. Furthermore, at high speeds the injection of an additional field-weakening current is required to oppose the high induced voltage caused by the constant excitation field.

All these disadvantages can be addressed with a wound-rotor synchronous machine (WRSM) which has a field winding located on the rotor, instead of permanent magnets. Therefore, rare-earth metals are eliminated from the construction process in favor of copper coils. The field winding also enables a variable excitation field by adjusting the field current flowing in the coils [3]. However, as the field winding is located on the **moving** rotor and is supplied by a **stationary** DC source a connection of the rotating leads of the field winding with the leads of the power supply is needed. One way to achieve this is with stationary carbon brushes which slide on the slip rings mounted on the shaft. They create a conductive interface between the stationary DC source and the rotating field winding. However, the continuous sliding motion leads to brush wear, and the resulting abrasion releases conductive particles that contaminate the slip ring compartment. This not only increases the need for maintenance, but also introduces additional frictional losses and power losses due to the contact resistance between brush and slip ring. Nevertheless, WRSMs have been used successfully as traction motors in electric vehicles (EVs) e.g. in the Renault Zoe and the BMW iX3. In order to address the increased need for maintenance, current projects in industry and academia are investigating the elimination of the brushes and slip rings in WRSMs. This objective is referred to as **brushless excitation** and is the focus of this dissertation.

Chapter 2

State of the Art

The two main methods for transferring power wirelessly between a stationary and a rotating object are inductive and capacitive power transmission. In the field of wireless (brushless) excitation for WRSMs most proposed concepts are based on magnetic induction. The commonality of these inductive power transmission systems is that there is a stationary (transmitter) winding and a rotating winding (receiver) which are each wound around a ferromagnetic core and separated by an airgap. The leads of the receiver winding connect to the field winding of the WRSM through a diode rectifier. Brushless excitation is achieved by a rate of change of the magnetic field caused by shaft rotation or by an alternating current in the stationary winding. The resultant induced voltage into the receiver winding is then rectified to produce the DC field current.
Historically, the brushless excitation of WRSMs is a rich area of research motivated by the need to supply the variable field current of large synchronous generators free of maintenance. The most widely used brushless excitation system for turbo generators is shown in Fig. 2.1. It consists of an additional external-pole synchronous generator — called main exciter — mounted on the same shaft as the turbo generator [4].

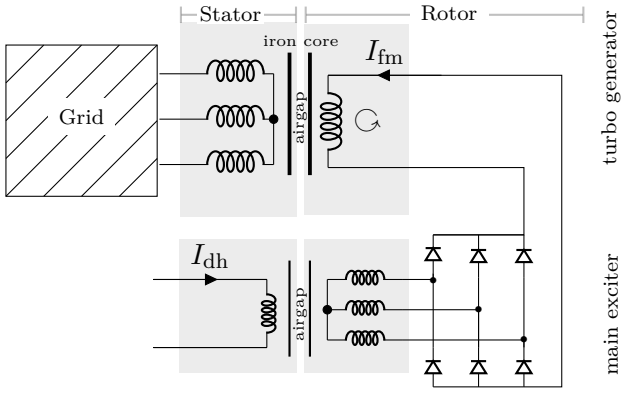

Figure 2.1: Brushless excitation of grid-connected, single-speed synchronous generators.

The main exciter has its field winding (transmitter) placed in the stator and its three-phase winding (receiver) in the rotor which connects to the turbo generator field winding through a rotating diode bridge. While the field winding of the turbo generator cannot be accessed during rotation, the stationary field winding of the main exciter can be supplied by the DC field current I_{dh} so that a voltage is induced into the three-phase winding of the main exciter when the shaft rotates. This voltage is rectified by the diode bridge to produce the turbo generator field current I_{fm}. Thus, the turbo generator field winding is inductively excited by substitutionally controlling the field current I_{dh} of the main exciter.

A great number of brushless excitation concepts for generators of different sizes and applications have been proposed [4]–[6] based on various types of exciter machines. However, most of these brushless excitation concepts have been conceived for **grid connection**. This means that the WRSM only operates under load at a single speed imposed by the constant grid frequency. Hence, before the WRSM is synchronized with the grid, it has to be accelerated close to synchronous speed while operating as an induction motor. To enable this, the rotor is typically equipped with features that support asynchronous starting such as special damper windings. As a consequence, the brushless excitation system only has to provide excitation close to its synchronous speed. Furthermore, in an industrial plant where these machines are used **space requirements** are not a critical space requirement. as opposed to high power density being a major requirement.

In contrast, this dissertation focuses only on motors driven by a frequency inverter and on those brushless excitation systems which guarantee arbitrary excitation control independent of the shaft speed and at a small excitation system size. If the literature on brushless single-speed, grid-connected synchronous generators is excluded, the following three categories of brushless excitation applicable to variable-speed drives remain.

2.1 Current-Excited Flux Modulation Machines

The first category stands out from all other brushless excitation systems because here no power needs to be transferred to the rotor. Instead, current-excited Flux Modulation Machines (FMMs) are inherently brushless because they have **both** the three-phase **and** field winding located on the stator so that no slip rings or brushes are needed. Nevertheless, FMMs can be categorized as synchronous machines because they produce a synchronous torque due to the interaction of the stator and excitation field. Thus, they have the same advantages in the high-speed and partial load region as conventional WRSMs, which is why they cannot be omitted in the discussion of brushless-excited synchronous machines.
As the name suggests, current-excited FMMs function on the basis of flux modulation and deviate significantly from conventional WRSMs in both geometry and winding layout: They possess a salient stator and/or rotor, but produce no reluctance torque. Instead, the stator and field winding are wound to produce different pole-pair numbers p_{s} and p_{f} which only

interact with each other because the fields of unequal pole-pair numbers are modulated by the saliency so that a synchronous torque is produced. FMMs have received some attention recently due to their magnetic gearing effect, which enables a high torque density [7]. Even though most FMMs have been conceptualized with permanent magnets, current-excited FMMs with a field winding instead of permanent magnets exist.
One of these machines is the DC-excited flux-switching machine [8]. This machine has both a single-phase p_f pole-pair field winding and a three-phase p_s pole-pair winding located in the stator and therefore no windings on the rotor. Both the stator and rotor have saliency with Z_s stator and Z_f rotor poles. If the relationship

$$|p_\mathrm{s} \pm Z_\mathrm{s}| = |p_\mathrm{f} \pm Z_\mathrm{f}| \tag{2.1}$$

is fulfilled and the rotor rotates with a frequency of f_m, the p_f pole-pair field of the field winding is modulated by the stator and rotor reluctance so that a voltage of frequency

$$f_\mathrm{el} = Z_\mathrm{f} f_\mathrm{m} \tag{2.2}$$

is induced into the p_s pole-pair stator winding. Thus, a synchronous torque is produced if an appropriately oriented three-phase system of electrical frequency f_el is fed into the AC winding. This equation highlights that the electrical frequency of flux-modulation machines is usually very large for realistic rotor saliencies Z_f.
Another type of FMM without permanent magnets — the brushless doubly-fed machine (BDFM) — is obtained from (2.1) if the stator saliency is neglected and, hence, the rotor saliency fulfills the condition $Z_\mathrm{f} = |p_\mathrm{s} \pm p_\mathrm{f}|$. The BDFM can also be built without rotor saliency, but with a special nested rotor cage with $n = |p_\mathrm{s} \pm p_\mathrm{f}|$ isolated cages. BDFMs with two distinct three-phase winding sets located in the stator have attracted some interest as a brushless alternative to the doubly-fed induction motor in wind power or heavy-duty traction applications [9], [10]. However, as [11] points out, the torque density is lower than for inherently brushless and magnet-free reluctance machines which is why they are not feasible for most variable-speed applications.
Even though a host of different (current-excited) flux modulation machines exist, recurring drawbacks mentioned in the literature are the high distortion of the airgap flux and the large electrical frequencies. This causes large iron losses, a large harmonic leakage inductance (low power factor) and restricts the usage of FMMs mostly to high-torque applications. Furthermore, the design and calculation of FMMs is a relatively novel field in comparison with the more mature WRSM technology which is well-established in the industry and well-researched in academia. This is why a brushless synchronous machine which does not deviate from the established WRSM topology is more attractive than using flux modulation.

2.2 Rotary Exciters

The second category of brushless excitation viable for variable-speed drives are rotary exciters. These are external inductive power transfer devices that are mounted on the shaft of a conventional WRSM [12]. There are some schematical similarities to the main exciter machine in Fig. 2.1 mounted on the shaft of brushless-excited turbo generators, but — unlike the main exciter — rotating exciters are **not** electrical motors. While they also transfer the excitation power inductively or capacitively, their main attribute is that their magnetic (electric) field is independent of the rotational speed. This is exemplified in the rotary transformer structure in Fig. 2.2b, where the blue flux lines are independent of the rotational speed, so that the induced voltage only depends on the frequency of the current in the primary coil. Thus, rotary transformers can supply the WRSM field current regardless of the operating conditions (speed and load) of the WRSM. The schematic of a conventional inverter-driven WRSM whose field winding is fed by a rotating transformer through a bridge rectifier is depicted exemplarily in Fig. 2.2a. The stationary side of the rotating transformer is fed by a fast-switching power source indicated as an H-Bridge.
The operating frequencies of rotating exciters are from tens of kHz to multiple MHz [12], [13] and are thus significantly larger than the frequencies which occur in electrical machines. The large operating frequencies take advantage of the fact that a smaller inductor (capacitor) can be used to reach a given impedance (admittance). Inductive exciters are preferred to capacitive exciters due to the need for small, mechanically challenging airgaps and large surfaces needed to obtain a sufficiently large coupling capacitance, although progress has been made by using MHz frequencies [13]. Efficiencies upwards of 90 % are consistently being reported in rotary exciters [12] with sizes not much larger than needed for the slip rings and brushes [14], which makes them the preferred option for brushless WRSMs.

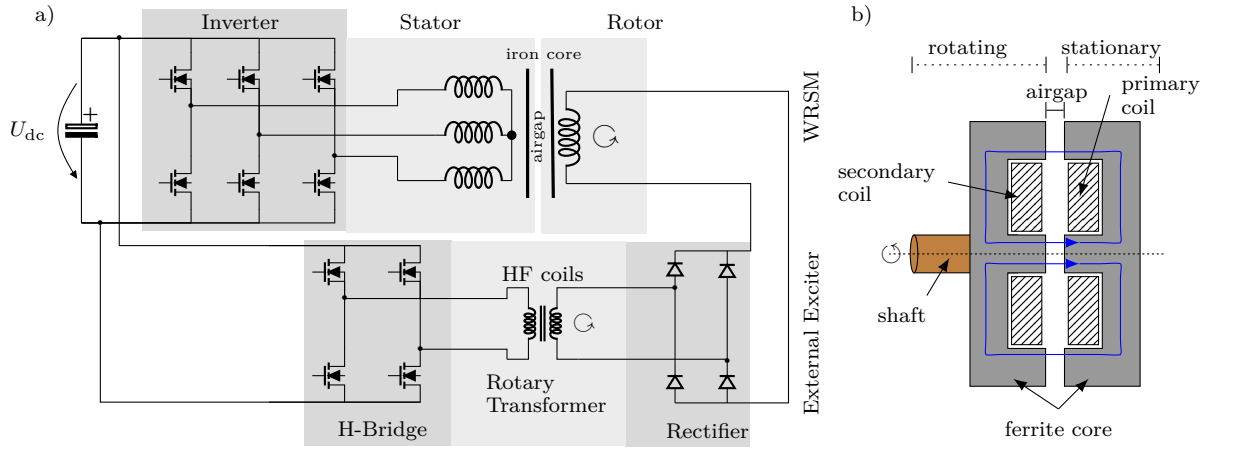

Figure 2.2: a) Schematic of WRSM with independent rotating transformer and b) axial rotary transformer.

However, just like the main exciter in Fig. 2.1, the rotary transformer in Fig. 2.2 also introduces an additional magnetic core and another set of windings into the drive system. It should be remarked that an equivalent already exists in any WRSM in the form of the iron stack and the machine windings. This motivates another area of brushless excitation which attempts to jointly utilize the already existing machine core and windings of the WRSM for the inductive power transfer to the field winding. This third category of brushless excitation is called *harmonic excitation*.

2.3 Harmonic Excitation

The principle of harmonic excitation is similar to the brushless excitation of turbo generators in that an electrical machine (main exciter) feeds the field winding of the WRSM through a rectifier. The distinguishing feature here is that the main exciter is not an external electrical machine with its own frame, windings and iron core. Instead, the main exciter is **integrated into** the existing machine and shares the same iron core and — if possible — the windings of the WRSM. This is achieved by using the existing or additional airgap space harmonics. Thus, instead of constructing an additional device, the existing copper and iron material of the WRSM are jointly utilized by the brushless excitation system. This has the potential of reducing material costs and machine space.
However, in order to integrate a harmonic excitation system into a WRSM only a limited number of options is available. In fact, most of the degrees of freedom like the machine dimensions, winding locations and iron material are already pre-determined by the WRSM design. This is contrary to the main exciter in Fig. 2.1 or to rotary transformers like Fig. 2.2 which are external devices that can be designed independently from the WRSM. Furthermore, the joint usage of the iron core inevitably leads to an interaction between normal WRSM operation and harmonic excitation, because the additional magnetic fields produced by the excitation system share the same flux paths as the WRSM. The additional losses generated in the iron core and conductors are also dissipated over the same thermal paths.
The literature on harmonic excitation focuses mainly on single-speed generator applications. Some inverter-driven concepts and even variable-speed motors have been presented, but often the investigations do not far exceed the proposal so that little follow-up publications or detailed analysis is given. Hence, in the following sections the main methods to integrate harmonic excitation into a WRSM are categorized and their limitations are briefly pointed out without claiming completeness.

2.3.1 Utilizing the Space Harmonics of the Stator Winding

Any m-phase winding supplied by an m-phase current system produces space harmonics at multiples v of order

$$v = 1 + 2 \cdot m \cdot a \text{ with } a \in \{0, \pm 1, \pm 2, ..., \pm\infty\} \tag{2.3}$$

if the corresponding winding factor ${}^{v}k_{\mathrm{w}}$ is non-zero. In integer-slot windings the fundamental ($v = 1$st) space harmonic is the operating harmonic[1] and higher order harmonics of order $v = -5, 7, -11, 13$ constitute leakage flux which inevitably arises in the airgap flux whenever a load current flows in the machine windings. While these space harmonics are usually undesired and increase the leakage inductance, torque ripple, noise and iron losses, one of these space harmonics can be used for harmonic excitation. In order to achieve this, an additional auxiliary rotor winding is placed on the rotor to pick up one of the higher order space harmonics generated by the stator load current. As a consequence, a voltage is induced into the auxiliary winding that is proportional to the machine speed and amplitude of the load current. Fig. 2.3 depicts the conceptual overview of a harmonic excitation system using an auxiliary rotor winding to pick up a spatial harmonic of pole pair p_{h}. It can be seen that the additional auxiliary winding behaves as an additional p_{h} pole-pair induction generator which shares the same iron stack as the conventional p_{m} pole-pair WRSM.

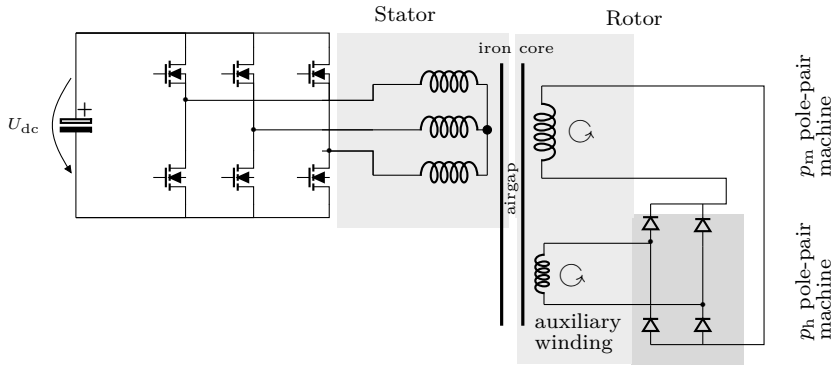

Figure 2.3: HESM with auxiliary rotor winding of pole pair p_{h} which picks up a spatial harmonic generated by the load current.

In [15] the $v = -5$th space harmonic of an integer slot winding is used for the harmonic excitation of a grid-connected generator. Alternatively, [16] proposes special stator winding schemes in which the magneto-motive forces (MMFs) of two consecutive pole pairs are unequal. This produces both a working harmonic and an additional subharmonic which is picked up by a corresponding auxiliary winding. The main drawback of this approach is that

[1] This is not the case in fractional slot windings where e.g. the $v = 5$-th space harmonic is the operating harmonic.

the supplied field current is uniquely defined by the speed and load current of the machine. It cannot be changed in a given operating point and vanishes at a speed of zero. Therefore, the concept is infeasible for variable-speed applications. This is why the authors of [16] use additional magnets to improve the startup.

2.3.2 Utilization of Auxiliary Stator Windings

The main drawback of the previously presented concept is that the space harmonic used for harmonic excitation cannot be generated independently because it is a byproduct of the load current in the stator winding. However, if a winding of pole-pair number p_h is placed in the stator **and** rotor slots of the conventional WRSM two independent machines — one p_m pole-pair machine for torque production and a p_h pole-pair machine for brushless excitation — are obtained. Fig. 2.4 illustrates the general overview of a harmonic excitation system that is applicable even for variable-speed applications. It can be seen that the additional p_h pole-pair auxiliary windings form an independent induction generator sharing the iron stack of the p_m pole-pair machine which operates as a conventional inverter-fed WRSM. As the auxiliary windings are independent winding sets, an arbitrary pole-pair number p_h can be chosen for them. Such a concept has been realized e.g. in [17], where $p_\mathrm{h} = 6$ pole-pair stator and rotor windings are integrated into a WRSM of pole-pair number $p_\mathrm{m} = 2$. The application in [17] is a grid-connected, single-speed generator, but the concept can be extended to variable-speed applications if the two stator windings are both fed from independent inverters as in Fig. 2.4.

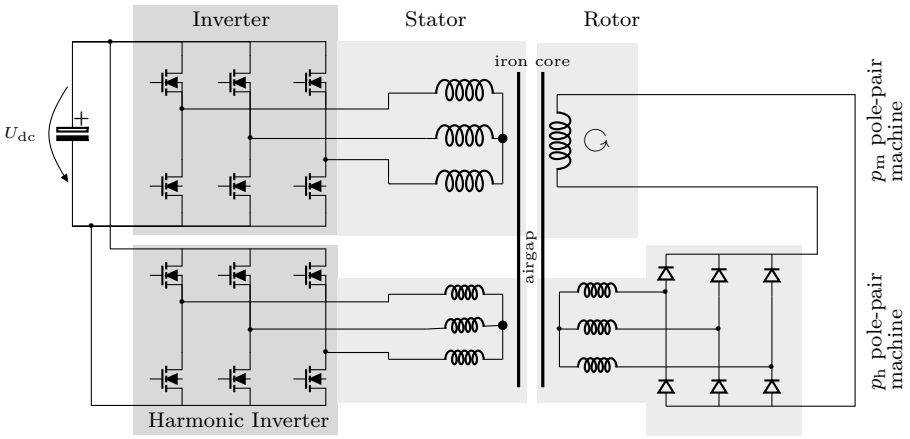

Figure 2.4: A HESM viable for variable-speed applications with two winding sets in stator and rotor according to [17].

The harmonic inverter can adjust the frequency and voltage amplitude of the p_h pole-pair stator winding to inductively excite the p_m pole-pair machine field winding even at standstill. As long as the p_m and p_h pole-pair fields have no common space harmonics, they do not

interact with each other so that arbitrary control of the field current is possible independently of the speed and load of the p_m pole-pair machine. The main disadvantage of this concept is that the auxiliary windings in both stator and rotor increase the size of the machine and thus decrease its power density. Furthermore, additional power electronics are needed.

2.3.3 Harmonic Injection into the Existing Stator Winding

While the drawback of Section 2.3.1 is the speed and load dependence of the field current and its advantage is the lack of additional windings, Section 2.3.2 eliminates the disadvantage at the cost of additional stator windings and an inverter. This brings up the question if the generation of an additional p_h pole-pair field is even necessary. A HESM concept feasible for variable-speed applications which achieves harmonic excitation without generating an additional p_h pole-pair field is shown in Fig. 2.5a [18]. It consists of a conventional three-phase drive inverter and a conventional WRSM with the only modification that the field winding is short-circuited by a diode.

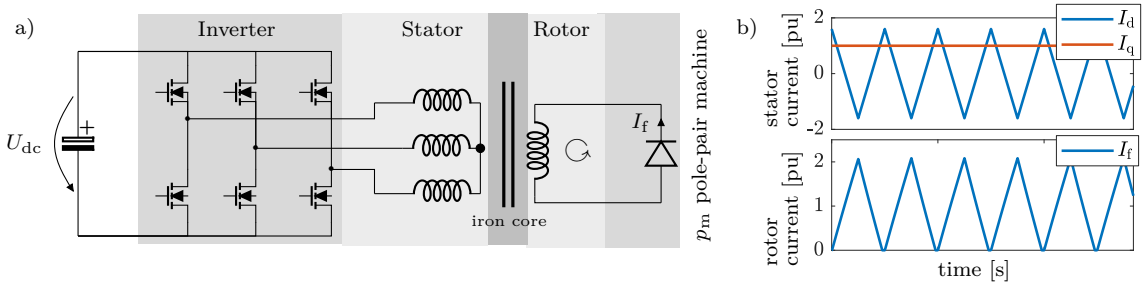

Figure 2.5: a) WRSM topology with field winding short-circuited by a diode providing one-wave rectification and b) current injection strategy in dq reference frame.

Fig. 2.5b shows the operating currents in the rotor-oriented coordinate system qualitatively. The general idea is to use the d-axis to excite the field winding and the q-axis for torque production. In the d-axis a sawtooth (or sinusoidal) current is injected which produces an asynchronously rotating field with respect to the field winding. As a consequence, an AC voltage is induced which is rectified by the diode. The q-axis current is then used just as in a conventional WRSM to produce the torque. As the field winding is short-circuited by the diode, the d-axis behaves like a machine under short-circuit condition. This is why large AC currents in the d-axis and field winding occur to transfer the desired field current. These current components almost have the same rms value as the rated currents and therefore almost double the total losses. Furthermore, a large torque ripple occurs for realistic WRSM designs, because the AC component of the field current produces an oscillating torque when q-axis load current is present. While smoother field currents can be obtained with more

rotor phases and diodes [19], these inherent drawbacks cannot be eliminated and show the advantage of using a decoupled pole-pair number p_h for harmonic excitation.

2.3.4 Generation of Independent Pole Pairs from a Single Winding

In the previous sections it has been indicated that the integration of an independent p_h pole-pair machine into the machine frame is desirable for harmonic excitation, but can only be realized by using auxiliary windings. Therefore, attempts have been made to produce independent pole pairs p_h from the existing, conventional p_m pole-pair windings.
In [20] the third time harmonic is injected into a three-phase winding using a modified inverter that allows star point currents so that a standing wave at spatial harmonic $p_\mathrm{h} = 3p_\mathrm{m}$ is generated. As the standing wave does not induce a voltage for arbitrary rotor positions, no standstill torque is possible. Another possibility is to split the existing p_m pole-pair stator winding into two independent three-phase consequent-pole windings as in [21]. The degree of current asymmetry in the two consequent-pole stator windings is used to control the magnitude of the p_h pole-pair field. However, the induced voltage is also speed-dependent and vanishes at standstill so that no standstill torque is produced.
In [22] a tooth-wound 11-phase stator winding with each phase being supplied by its own H-bridge is used to realize a $p_\mathrm{m} = 4$ pole-pair MMF in conjunction with a $p_\mathrm{h} = 2$ pole-pair MMF. Through the use of pole phase modulation (PPM) both components can be excited independently, which is why a machine based on this concept is capable of variable-speed operation. However, the machine design differs significantly from a conventional WRSM design, has large harmonic winding factors and requires a large amount of power switches.
A related concept extends third harmonic injection using a dual three-phase winding with two 30 degrees spatially shifted three-phase groups [23], [24]. These two zero-systems create a two-phase $p_\mathrm{h} = 3 \cdot p_\mathrm{m}$ pole-pair machine which can be supplied with 90 degrees phase-shifted currents in order to produce a rotary field. While [23] has not been investigated for variable-speed applications by the authors, the concept is very much viable. However, as will be shown in Section 4.3.2 of this work, a high pole-pair number p_h is not desirable. Furthermore, a commonality of all harmonic excitation concepts mentioned in this section is that they only go as far as eliminating the auxiliary stator winding. They all still require auxiliary windings in the rotor and sometimes even modifications of the rotor geometry to place additional slots in the machine, e.g. [21], [23].

2.4 Goals and Structure of this Work

It must be stated that all presented harmonic excitation concepts for WRSMs have inherent shortcomings, have not been conceptualized for variable-speed applications or have found little successful use beyond their initial proposal. Overall, harmonic-excited synchronous

machines (HESMs) are not considered serious contenders for brushless-excited WRSMs so far as the scarce literature indicates. From the few concepts viable for variable-speed applications, a critical omission is that the excitation system losses and its effect on the speed-region have not been analyzed in detail. This dissertation attempts to revisit and extend the idea of harmonic excitation and identify its shortcomings. The fundamental goal of the research investigated in this work is to synthesize a HESM without any auxiliary windings (contrary to Fig. 2.4) and with no additional torque ripple (contrary to Fig. 2.5) that is also viable for variable-speed applications. Rather than simply proposing and validating the concept, the inherent problems and limitations of harmonic excitation such as the influence on the torque-speed region and the additional iron losses are analyzed in detail using both simulation and experiments on a prototype.

To this end, in Chapter 3 the general analytical framework for the analysis of electrical machines based on the first armature reaction is presented. This theory is then used to derive the working principle of HESMs. Chapter 4 gives an overview and generalization of the methods and limitations for producing the two distinct pole pairs p_m and p_h from a single winding. Based on these methods, a novel HESM concept investigated in this dissertation is synthesized and criteria for a favorable HESM design are discussed.

In Chapter 5 the mathematical model of the proposed HESM concept is derived. Special consideration is given to the different coordinate transformations. Furthermore, the control system of the HESM is derived based on the obtained model. Chapter 6 describes the design of a machine prototype of the HESM concept based on analytical scaling laws and Finite-Element Analysis (FEA). The FE model is then used to analyze the cross saturation behavior due to the shared flux paths of the p_m and p_h pole-pair machine in the iron laminations. The control system of the designed machine is parametrized, implemented and verified with the help of dynamic simulations. In Chapter 7 the constructed machine prototype is investigated experimentally. Firstly, the test bench and its limitations are presented and afterwards experiments for the identification of the HESM parameters are performed. The HESM concept is then verified near rated torque and at different operating parameters of the excitation system. Furthermore, a close look at the additional losses measured due to the inclusion of the p_h pole-pair machine is taken.

Chapter 8 takes a deep dive into the HESM iron losses and explains the complex flux density waveforms under harmonics excitation. A simplified iron loss model is then presented which can be used to predict and isolate the additional speed-dependent iron losses. Chapter 9 investigates the effect of the excitation system on the torque-speed region and highlights the main disadvantage of the proposed concept. A simplified approach to modelling the voltage demand and efficiency of the HESM in steady-state is presented and used in the analysis. The derating of the maximum torque-speed curve is quantified and confirmed with experiments. Lastly, some ideas for improving the proposed concept are discussed. Chapter 10 concludes this dissertation.

Chapter 3

Theory of Harmonic Excited Synchronous Machines

An electrical machine is a complex multi-physical system which can be investigated electromagnetically, structurally, thermally and acoustically. While each of these physical domains is an essential part of machine prototyping, in the scope of this work the focus is on the **electromagnetic** design and modelling of synchronous machines. As the magnetic fields inside of a HESM only differ from those of a conventional WRSM by the additional space or time harmonics to achieve inductive power transmission, HESMs can be modelled using the same well-established methods as for regular WRSMs. Analysis of the electromagnetic domain requires accurately describing the three-dimensional magnetic fields inside of an electrical machine. For radial flux machines the following approaches are available:

- **Numerical** 3D magnetic field calculation using Finite-Element-Analysis (FEA) or 2D analysis under neglect of the endwinding region.
- **Analytical** one-dimensional [25] (or two-dimensional [26]) approximation of the airgap flux density.

As an HESM consists of additional winding sets, multi-phase windings or modifications to the conventional WRSM windings, a modelling approach that can take into account these effects is needed. The one-dimensional approximation of the airgap flux density is a computationally fast and general framework and is therefore used extensively in all chapters of this work. In this section, a general formulation of the magnetic fields inside of a WRSM will be performed. Afterwards the results are applied to derive the functioning principle of HESMs.

3.1 Harmonic Field Theory

The spatial location of phase k $\in \{1, 2, 3\}$ of an $m = 3$-phase, p pole-pair stator winding with N_s turns can be expressed by a winding function [25]

$$W_\mathrm{k}(\varphi) = \frac{2}{\pi} N_\mathrm{s} \sum_{\mathrm{v}=1}^{\infty} \frac{{}^{v}k_\mathrm{ws}}{vp} \sin\left(v\left(p\varphi - (\mathrm{k}-1)\frac{2\pi}{m}\right)\right) \tag{3.1}$$

where ${}^{v}k_\mathrm{ws}$ is the winding factor of the vth spatial harmonic and the variable φ denotes the position along the airgap. An MMF that varies in space (φ) and time (t) is produced if phase k is supplied by a current

$$I_\mathrm{s,k} = \hat{I}_\mathrm{s} \cdot \cos\left(\omega t + \mathrm{sign} \cdot (\mathrm{k}-1)\frac{2\pi}{3} + \theta_\mathrm{s}\right) \tag{3.2}$$

where $\hat{I}_\mathrm{s}$ is the current amplitude, ω an arbitrary frequency to be determined later and θ_s the initial phase shift. The parameter 'sign' expresses the direction of rotation of the three-phase system and can only take on the values 1 or -1. Multiplication of the winding function (3.1) with the winding current (3.2) yields the MMF

$$\Theta_\mathrm{s,k} = \frac{2}{\pi} N_\mathrm{s} \hat{I}_\mathrm{s} \sum_{v=1}^{\infty} \frac{{}^{v}k_\mathrm{ws}}{vp} \cos\left(\omega t + \mathrm{sign} \cdot (\mathrm{k}-1)\frac{2\pi}{3} + \theta_\mathrm{s}\right) \sin\left(v\left(p\varphi - (\mathrm{k}-1)\frac{2\pi}{3}\right)\right). \tag{3.3}$$

Since the total MMF consists of the contribution of all phases, the resultant three-phase MMF can be calculated as the sum of all three phases. Applying the relationship $\cos x = \mathrm{Re}\left\{e^{\mathrm{j}x}\right\}$ to the first cosine and Euler's formula $\sin x = \frac{1}{2\mathrm{j}}\left(\mathrm{e}^{\mathrm{j}x} - \mathrm{e}^{-\mathrm{j}x}\right)$ to the sine, the following representation can be obtained

$$\Theta_\mathrm{s} = \sum_{\mathrm{k}=1}^{3} \Theta_\mathrm{s,k} = \frac{1}{\pi} N_\mathrm{s} \hat{I}_\mathrm{s} \mathrm{Re}\left\{\frac{1}{\mathrm{j}} \mathrm{e}^{\mathrm{j}(\omega t + \theta_\mathrm{s})} \sum_{v=-\infty}^{\infty} \frac{{}^{v}k_\mathrm{ws}}{vp} \mathrm{e}^{\mathrm{j}(vp\varphi)} \underbrace{\sum_{\mathrm{k}=1}^{3} \mathrm{e}^{\mathrm{j}\frac{2\pi}{3}(\mathrm{k}-1)(\mathrm{sign}-v)}}_{=3 \text{ for } v \text{ in (3.5)}}\right\}. \tag{3.4}$$

The underbraced term is only $\neq 0$, more precisely $= 3$ (and thus becomes real-valued), if $\frac{2\pi}{3}(\mathrm{sign} - v) \stackrel{!}{=} b \cdot 2\pi$, with $b = 0, \pm 1 \pm 2, \ldots$. This is only the case if the indices v take on the values

$$v = (\mathrm{sign} + 3b) = \begin{cases} 1, -2, 4, -5, 7, \ldots & \text{for sign} = 1 \\ -1, 2, -4, 5, -7, \ldots & \text{for sign} = -1 \end{cases}. \tag{3.5}$$

As the winding factor ${}^{v}k_{\mathrm{w}}$ of integer-slot windings is zero for all even-numbered v they can be omitted [27]

$$v = (\mathrm{sign} + 6b) = \begin{cases} 1,\ -5,\ 7,\ -11,\ 13,\ \ldots & \text{for sign} = 1 \\ -1,\ 5,\ -7,\ 11,\ -13,\ \ldots & \text{for sign} = -1 \end{cases} . \tag{3.6}$$

The parameter 'sign' determines whether a forward rotating field (fundamental $v = 1$) or a backward rotating field (fundamental $v = -1$) is generated. Now the total real-valued MMF can be specified as

$$\Theta_{\mathrm{s}} = \frac{3}{\pi} N_{\mathrm{s}} \hat{I}_{\mathrm{s}} \mathrm{Re}\left\{ \frac{1}{\mathrm{j}} \sum_{v} \frac{{}^{v}k_{\mathrm{ws}}}{vp} \mathrm{e}^{\mathrm{j}(\omega t + vp\varphi + \theta_{\mathrm{s}})} \right\} \text{ with } v = \mathrm{sign} + 6b. \tag{3.7}$$

3.1.1 Generalized Rotor MMF

The rotor winding can be modelled analogously to the stator winding with a winding function and a current excitation. In order to maintain generality, the single-phase rotor winding is supplied by an arbitrary current

$$I_{\mathrm{f}}(t) = \hat{I}_{\mathrm{f}} \cos(\omega_{\mathrm{r}} t) \tag{3.8}$$

of amplitude $\hat{I}_{\mathrm{f}}$ and frequency ω_{r}. In the special case of $\omega_{\mathrm{r}} = 0$ the winding is DC-excited. The MMF produced by the field winding is calculated analogously to (3.3) by multiplying the field current (3.8) with the corresponding winding function which yields an MMF

$$\Theta_{\mathrm{f}} = \frac{2}{\pi} N_{\mathrm{f}} \hat{I}_{\mathrm{f}} \sum_{\mu=1}^{\infty} \frac{{}^{\mu}k_{\mathrm{wf}}}{\mu p} \sin(\mu p \varphi_{\mathrm{f}}) \cos(\omega_{\mathrm{r}} t) . \tag{3.9}$$

The parameter N_{f} is the number of rotor series turns and ${}^{\mu}k_{\mathrm{wf}}$ is the rotor winding factor of the μ-th spatial harmonic. As the field winding is rotating, the variable φ_{f} is introduced which denotes the angular position in the moving rotor coordinate system. Using trigonometric identities leads to

$$\begin{aligned} \text{AC excited} \quad & \Theta_{\mathrm{f}} = \frac{1}{\pi} N_{\mathrm{f}} \hat{I}_{\mathrm{f}} \mathrm{Re}\left\{ \frac{1}{\mathrm{j}} \sum_{\mu=-\infty}^{\infty} \frac{{}^{\mu}k_{\mathrm{wf}}}{\mu p} \mathrm{e}^{\mathrm{j}(\mu p \varphi_{\mathrm{f}} + \omega_{\mathrm{r}} t)} \right\} \\ \text{DC excited} \quad & \Theta_{\mathrm{f}} = \frac{1}{\pi} N_{\mathrm{f}} I_{\mathrm{f}} \mathrm{Re}\left\{ \frac{1}{\mathrm{j}} \sum_{\mu=-\infty}^{\infty} \frac{{}^{\mu}k_{\mathrm{wf}}}{\mu p} \mathrm{e}^{\mathrm{j}\mu p \varphi_{\mathrm{f}}} \right\} \end{aligned} \tag{3.10}$$

where the current amplitude $\hat{I}_{\mathrm{f}}$ is replaced with I_{f} in the case of DC excitation. An important result of (3.9) is that any single-phase MMF can be separated into rotary fields rotating in forward direction (indices $\mu = 1, 3, 5, \ldots$) **and** backward direction (indices $\mu = -1, -3, -5, \ldots$).

3.1.2 Stator and Rotor Slotting

From the MMFs the airgap flux density can be determined as [25]

$$B_\delta = \frac{\mu_0}{h_\delta} \Lambda_\mathrm{s} \Lambda_\mathrm{f} \Theta. \tag{3.11}$$

The permeance waves Λ_s and Λ_f are functions of the angular position and increase the airgap length h_δ locally to take into account the drop of the airgap flux density above a slot opening. Thus, the adjustment of the airgap length by the permeance waves does not depend on the geometrical distances, but on the solution of the magnetic field. They can be evaluated analytically with the Schwarz-Christoffel transformation or numerically with FEA [28] and can be modelled according to [25] as

$$\begin{aligned} \Lambda_\mathrm{s} &= \frac{1}{2} \sum_{n_\mathrm{s}=-\infty}^{\infty} {}^{n_\mathrm{s}}\Lambda_\mathrm{s} \mathrm{e}^{j n_\mathrm{s} Z_\mathrm{s} \varphi} \\ \Lambda_\mathrm{f} &= \frac{1}{2} \sum_{n_\mathrm{f}=-\infty}^{\infty} {}^{n_\mathrm{f}}\Lambda_\mathrm{f} \mathrm{e}^{j n_\mathrm{f} Z_\mathrm{f} \varphi_\mathrm{f}}. \end{aligned} \tag{3.12}$$

The actual determination of the Fourier coefficients ${}^{n_\mathrm{s}}\Lambda_\mathrm{s}$ (${}^{n_\mathrm{f}}\Lambda_\mathrm{f}$) is performed in Section 8.1 for a HESM prototype machine. If harmonic effects are neglected, the permeance waves become $\Lambda_\mathrm{s} \cdot \Lambda_\mathrm{f} = {}^{0}\Lambda_\mathrm{s} \cdot {}^{0}\Lambda_\mathrm{f} = 4/k_\mathrm{c}$ where k_c is the well-known (double-sided) Carter factor that enlarges the effective airgap length. If higher order slotting effects are considered, the airgap length has a periodic angular dependence at multiples $n_\mathrm{s} Z_\mathrm{s}$ ($n_\mathrm{f} Z_\mathrm{f}$) of the Z_s stator slots ($Z_\mathrm{f} = 2p$ rotor poles).
It should be noted that the rotor coordinate system (variable φ_f) is rotating with the angular frequency ω_m relative to the stator coordinate system (variable φ). In order to calculate the airgap flux density in stator (rotor) reference frame, the MMFs and permeance waves in (3.11) must all be transformed into the same stator or rotor reference frame by applying the substitution.

$$\varphi_\mathrm{f} = \varphi + \omega_\mathrm{m} t + \beta \qquad \text{or inversely} \qquad \varphi = \varphi_\mathrm{f} - \omega_\mathrm{m} t - \beta \tag{3.13}$$

where β denotes the rotor position. Applying (3.13) to (3.7), (3.10), and (3.12), a summary of the stator and rotor MMFs and permeance waves in their respective stator and rotor reference frames can be given in Tab. 3.1. The impact of the different reference frames is highlighted in blue.

Table 3.1: Summary of MMFs and permeance waves in their respective reference frame

	Stator Reference Frame	Rotor Reference Frame
Stator MMF $v = \text{sign} + 6b$	$\Theta_\mathrm{s} = \frac{3}{\pi} N_\mathrm{s} \hat{I}_\mathrm{s} \mathrm{Re}\left\{ \frac{1}{\mathrm{j}} \sum_v \frac{{}^v k_\mathrm{ws}}{vp} \mathrm{e}^{\mathrm{j}vp\varphi} \mathrm{e}^{\mathrm{j}(\omega t + \theta_\mathrm{s})} \right\}$	$\Theta_\mathrm{S} = \frac{3}{\pi} N_\mathrm{s} \hat{I}_\mathrm{s} \mathrm{Re}\left\{ \frac{1}{\mathrm{j}} \sum_v \frac{{}^v k_\mathrm{ws}}{vp} \cdot \mathrm{e}^{\mathrm{j}(vp\varphi_\mathrm{f} + (\omega - vp\omega_\mathrm{m})t)} \mathrm{e}^{\mathrm{j}(\theta_\mathrm{s} - v\beta)} \right\}$
Rotor MMF $\mu = \pm 1, \pm 3, \ldots$	$\Theta_\mathrm{f} = \frac{1}{\pi} N_\mathrm{f} \hat{I}_\mathrm{f} \mathrm{Re}\left\{ \frac{1}{\mathrm{j}} \sum_\mu \mathrm{e}^{\mathrm{j}(\mu p\varphi + (\omega_\mathrm{r} + \mu p\omega_\mathrm{m})t)} \mathrm{e}^{\mathrm{j}\mu p\beta} \right\}$	$\Theta_\mathrm{f} = \frac{1}{\pi} N_\mathrm{f} \hat{I}_\mathrm{f} \mathrm{Re}\left\{ \frac{1}{\mathrm{j}} \sum_\mu \mathrm{e}^{\mathrm{j}(\mu p\varphi_\mathrm{f} + \omega_\mathrm{r} t)} \right\}$
Stator Permeance	$\Lambda_\mathrm{s} = \frac{1}{2} \sum_{n_\mathrm{s}=-\infty}^{\infty} {}^{n_\mathrm{s}}\Lambda_\mathrm{s} \mathrm{e}^{jn_\mathrm{s} Z_\mathrm{s} \varphi}$	$\Lambda_\mathrm{s} = \frac{1}{2} \sum_{n_\mathrm{s}=-\infty}^{\infty} {}^{n_\mathrm{s}}\Lambda_\mathrm{s} \mathrm{e}^{jn_\mathrm{s} Z_\mathrm{s} (\varphi_\mathrm{f} - \omega_\mathrm{m} t)} \mathrm{e}^{-jn_\mathrm{s} Z_\mathrm{s} \beta}$
Rotor Permeance	$\Lambda_\mathrm{f} = \frac{1}{2} \sum_{n_\mathrm{f}=-\infty}^{\infty} {}^{n_\mathrm{f}}\Lambda_\mathrm{f} \mathrm{e}^{jn_\mathrm{f} Z_\mathrm{f} (\varphi + \omega_\mathrm{m} t)} \mathrm{e}^{jn_\mathrm{f} Z_\mathrm{f} \beta}$	$\Lambda_\mathrm{f} = \frac{1}{2} \sum_{n_\mathrm{f}=-\infty}^{\infty} {}^{n_\mathrm{f}}\Lambda_\mathrm{f} \mathrm{e}^{jn_\mathrm{f} Z_\mathrm{f} \varphi_\mathrm{f}}$

3.1.3 First Armature Reaction

The first armature reaction expresses the first reaction of a winding due to the magnetic field produced by a current flowing in another (or the same) winding. It is obtained by first calculating the airgap flux density of a winding and then evaluating the flux that couples with another winding.

Total stator flux coupling to a single stator phase k: With the results in Tab. 3.1, the total airgap flux density caused by the stator MMF (subscript s) and given in stator reference frame (superscript s) is obtained from (3.11) as

$$ {}^{(s)}B_{\delta\mathrm{s}} = \frac{\mu_0}{h_\delta} \frac{3}{\pi} N_\mathrm{s} \hat{I}_\mathrm{s} \frac{1}{4} \cdot \mathrm{Re}\left\{ \frac{1}{\mathrm{j}} \sum_{n_\mathrm{s}} \sum_{n_\mathrm{f}} \sum_v {}^{n_\mathrm{s}}\Lambda_\mathrm{s} \, {}^{n_\mathrm{f}}\Lambda_\mathrm{f} \frac{{}^v k_\mathrm{ws}}{vp} \mathrm{e}^{\mathrm{j}\left((vp + n_\mathrm{s} Z_\mathrm{s} + n_\mathrm{f} Z_\mathrm{f})\varphi + n_\mathrm{f} Z_\mathrm{f} \beta\right)} \cdot \mathrm{e}^{\mathrm{j}\left((\omega + n_\mathrm{f} Z_\mathrm{f} \omega_\mathrm{m})t + \theta_\mathrm{s}\right)} \right\}. \tag{3.14} $$

The flux coupling into one phase k of the stator winding (self-inductance) is obtained by integrating the airgap flux density over the winding coils. This is identical with evaluating the surface integral of ${}^{(s)}B_{\delta\mathrm{s}}$ times the winding function W_k of phase k

$$ \Psi_{\mathrm{k,s}} = r l_\mathrm{Fe} \int_0^{2\pi} {}^{(s)}B_{\delta\mathrm{s}} \cdot W_\mathrm{k} \mathrm{d}\varphi = r l_\mathrm{Fe} \frac{3}{\pi^2} N_\mathrm{s}^2 \frac{\mu_0}{h_\delta} \frac{\hat{I}_\mathrm{s}}{4} \cdot \mathrm{Re}\left\{ \frac{1}{\mathrm{j}} \sum_{n_\mathrm{s}} \sum_{n_\mathrm{f}} \sum_v {}^{n_\mathrm{s}}\Lambda_\mathrm{s} \, {}^{n_\mathrm{f}}\Lambda_\mathrm{f} \frac{{}^v k_\mathrm{ws}}{vp} \cdot \sum_{a=-\infty}^{\infty} \frac{{}^a k_\mathrm{ws}}{ap} \underbrace{\int_0^{2\pi} \mathrm{e}^{\mathrm{j}(vp + n_\mathrm{s} Z_\mathrm{s} + n_\mathrm{f} Z_\mathrm{f} + ap)\varphi} \mathrm{d}\varphi}_{\neq 0} \cdot \mathrm{e}^{\mathrm{j}\left((\omega + n_\mathrm{f} Z_\mathrm{f} \omega_\mathrm{m})t + \theta_\mathrm{s}\right)} \cdot \mathrm{e}^{\mathrm{j}(n_\mathrm{f} Z_\mathrm{f} \beta - a(\mathrm{k}-1)\frac{2\pi}{3})} \right\}. \tag{3.15} $$

where r is the airgap radius and l_{Fe} is the length of the iron stack. The integration of the underbraced expression is only $\neq 0$, more precisely $= 2\pi$ if the indices $ap \stackrel{!}{=} -vp - n_{\mathrm{s}}Z_{\mathrm{s}} - n_{\mathrm{f}}Z_{\mathrm{f}}$. Therefore, the summation over a can be replaced with a multiplication of 2π if a is replaced by

$$a = -v - n_{\mathrm{s}}\frac{Z_{\mathrm{s}}}{p} - n_{\mathrm{f}}\frac{Z_{\mathrm{f}}}{p}.$$

For all other values of a the integration is zero, so that the flux yields

$$\Psi_{\mathrm{k,s}} = rl_{\mathrm{Fe}}\frac{6}{\pi}N_{\mathrm{s}}^2\frac{\mu_0}{h_\delta}\frac{\hat{I}_{\mathrm{s}}}{4}\cdot \mathrm{Re}\Bigg\{\frac{1}{\mathrm{j}}\sum_{n_{\mathrm{s}}}\sum_{n_{\mathrm{f}}}\sum_{v} {}^{n_{\mathrm{s}}}\Lambda_{\mathrm{s}}\,{}^{n_{\mathrm{f}}}\Lambda_{\mathrm{f}}\,{}^{v}k_{\mathrm{ws}}\frac{{}^{-v-n_{\mathrm{s}}\frac{Z_{\mathrm{s}}}{p}-n_{\mathrm{f}}\frac{Z_{\mathrm{f}}}{p}}k_{\mathrm{ws}}}{vp}\cdot \frac{1}{-vp-n_{\mathrm{s}}Z_{\mathrm{s}}-n_{\mathrm{f}}Z_{\mathrm{f}}}\cdot \mathrm{e}^{\mathrm{j}\left((\omega+n_{\mathrm{f}}Z_{\mathrm{f}}\omega_{\mathrm{m}})t+\theta_{\mathrm{s}}\right)}\cdot \mathrm{e}^{\mathrm{j}(n_{\mathrm{f}}Z_{\mathrm{f}}\beta-(-vp-n_{\mathrm{s}}Z_{\mathrm{s}}-n_{\mathrm{f}}Z_{\mathrm{f}})(\mathrm{k}-1)\frac{2\pi}{3p})}\Bigg\}. \tag{3.16}$$

The induced voltage can be calculated from the time-derivative of the flux linkage, but another long expression is avoided here. Instead, it can be already seen from the flux that the rate of change of the stator flux induces a voltage of frequency $(\omega + n_{\mathrm{f}}Z_{\mathrm{f}}\omega_{\mathrm{m}})$ back into the stator phase k for all combinations of n_{s} and v for which the corresponding winding factors ${}^{v}k_{\mathrm{w}}$, ${}^{-v-n_{\mathrm{s}}\frac{Z_{\mathrm{s}}}{p}-n_{\mathrm{f}}\frac{Z_{\mathrm{f}}}{p}}k_{\mathrm{w}}$ and permeance coefficients ${}^{n_{\mathrm{s}}}\Lambda_{\mathrm{s}}$, ${}^{n_{\mathrm{f}}}\Lambda_{\mathrm{f}}$ are $\neq 0$. Strictly speaking, the stator current excitation in (3.2) has to be extended to take into account currents induced by these additional frequencies. This is known as second armature reaction, but it is assumed that the frequency component induced due to rotor slotting is negligibly small and eliminated to zero by the controller. Using the calculated flux linkage the stator self-inductance follows directly from $L = \Psi/I$ as

$$L_{\mathrm{s}} = rl_{\mathrm{Fe}}\frac{6}{\pi}N_{\mathrm{s}}^2\frac{\mu_0}{h_\delta}\frac{1}{4}\cdot \mathrm{Re}\Bigg\{\frac{1}{\mathrm{j}}\sum_{n_{\mathrm{s}}}\sum_{n_{\mathrm{f}}}\sum_{v} {}^{n_{\mathrm{s}}}\Lambda_{\mathrm{s}}\,{}^{n_{\mathrm{f}}}\Lambda_{\mathrm{f}}\,{}^{v}k_{\mathrm{ws}}\frac{{}^{-v-n_{\mathrm{s}}\frac{Z_{\mathrm{s}}}{p}-n_{\mathrm{f}}\frac{Z_{\mathrm{f}}}{p}}k_{\mathrm{ws}}}{vp}\cdot \frac{1}{-vp-n_{\mathrm{s}}Z_{\mathrm{s}}-n_{\mathrm{f}}Z_{\mathrm{f}}}\cdot \mathrm{e}^{\mathrm{j}(n_{\mathrm{f}}Z_{\mathrm{f}}\beta-(-vp-n_{\mathrm{s}}Z_{\mathrm{s}}-n_{\mathrm{f}}Z_{\mathrm{f}})(\mathrm{k}-1)\frac{2\pi}{3p})}\Bigg\}. \tag{3.17}$$

Total stator flux coupling to rotor: The stator field also interacts with the rotor winding. In order to determine the stator flux coupling with the rotor winding, the stator airgap flux density (subscript s) has to be calculated in rotor reference frame (superscript f)

$${}^{(f)}B_{\delta\mathrm{s}} = \frac{\mu_0}{h_\delta}\frac{3}{\pi}N_{\mathrm{s}}\hat{I}_{\mathrm{s}}\frac{1}{4}\mathrm{Re}\Bigg\{\frac{1}{\mathrm{j}}\sum_{n_{\mathrm{s}}}\sum_{n_{\mathrm{f}}}\sum_{v} {}^{n_{\mathrm{S}}}\Lambda_{\mathrm{s}}\,{}^{n_{\mathrm{f}}}\Lambda_{\mathrm{f}}\frac{{}^{v}k_{\mathrm{wf}}}{vp}\cdot \mathrm{e}^{\mathrm{j}(vp+n_{\mathrm{s}}Z_{\mathrm{s}}+n_{\mathrm{f}}Z_{\mathrm{f}})\varphi_{\mathrm{f}}}\cdot \mathrm{e}^{\mathrm{j}\left((\omega-vp\omega_{\mathrm{m}}-n_{\mathrm{s}}Z_{\mathrm{s}}\omega_{\mathrm{m}})t+\theta_{\mathrm{s}}\right)}\cdot \mathrm{e}^{-\mathrm{j}(vp+n_{\mathrm{s}}Z_{\mathrm{s}})\beta}\Bigg\} \tag{3.18}$$

and the flux coupling with the rotor winding follows analogously as

$$\Psi_{\mathrm{f,s}} = rl_{\mathrm{Fe}}\frac{6}{\pi}N_{\mathrm{f}}N_{\mathrm{s}}\frac{\mu_0}{h_\delta}\frac{\hat{I}_{\mathrm{s}}}{4}\cdot\mathrm{Re}\Bigg\{\frac{1}{\mathrm{j}}\sum_{n_{\mathrm{s}}}\sum_{n_{\mathrm{f}}}\sum_{v}{}^{n_{\mathrm{s}}}\Lambda_{\mathrm{s}}{}^{n_{\mathrm{f}}}\Lambda_{\mathrm{f}}\frac{{}^{v}k_{\mathrm{ws}}}{vp}\frac{-v-n_{\mathrm{s}}\frac{Z_{\mathrm{s}}}{p}-n_{\mathrm{f}}\frac{Z_{\mathrm{f}}}{p}k_{\mathrm{ws}}}{-vp-n_{\mathrm{s}}Z_{\mathrm{s}}-n_{\mathrm{f}}Z_{\mathrm{f}}}\cdot \mathrm{e}^{\mathrm{j}\left((\omega-vp\omega_{\mathrm{m}}-n_{\mathrm{s}}Z_{\mathrm{s}}\omega_{\mathrm{m}})t+\theta_{\mathrm{s}}\right)}\mathrm{e}^{-\mathrm{j}(vp+n_{\mathrm{s}}Z_{\mathrm{s}})\beta}\Bigg\}. \tag{3.19}$$

It can be seen that frequencies $(\omega - vp\omega_{\mathrm{m}} - n_{\mathrm{s}}Z_{\mathrm{s}}\omega_{\mathrm{m}})$ are induced into the rotor winding. It can be seen that additional frequencies due to stator slotting arise which have to considered in the second armature reaction, but their influence is insignificant in the scope of this work so they are neglected.The mutual inductance from stator to rotor follows directly from the flux as

$$L_{\mathrm{f,s}} = rl_{\mathrm{Fe}}\frac{6}{\pi}N_{\mathrm{f}}N_{\mathrm{s}}\frac{\mu_0}{h_\delta}\frac{1}{4}\mathrm{Re}\left\{\frac{1}{\mathrm{j}}\cdot\sum_{n_{\mathrm{s}}}\sum_{n_{\mathrm{f}}}\sum_{v}{}^{n_{\mathrm{s}}}\Lambda_{\mathrm{s}}{}^{n_{\mathrm{f}}}\Lambda_{\mathrm{f}}\frac{{}^{v}k_{\mathrm{ws}}}{vp}\frac{-v-n_{\mathrm{s}}\frac{Z_{\mathrm{s}}}{p}-n_{\mathrm{f}}\frac{Z_{\mathrm{f}}}{p}k_{\mathrm{wf}}}{-vp-n_{\mathrm{s}}Z_{\mathrm{s}}-n_{\mathrm{f}}Z_{\mathrm{f}}}\cdot\mathrm{e}^{-\mathrm{j}(vp+n_{\mathrm{s}}Z_{\mathrm{s}})\beta}\right\}. \tag{3.20}$$

Flux coupling from rotor to rotor: Now the rotor airgap flux density (subscript f) in rotor reference frame (superscript f) is the starting point

$${}^{(f)}B_{\delta\mathrm{f}} = \frac{\mu_0}{h_\delta}\frac{1}{\pi}N_{\mathrm{fm}}\hat{I}_{\mathrm{f}}\frac{1}{4}\cdot\mathrm{Re}\left\{\frac{1}{\mathrm{j}}\sum_{n_{\mathrm{s}}}\sum_{n_{\mathrm{f}}}\sum_{\mu}{}^{n_{\mathrm{S}}}\Lambda_{\mathrm{s}}{}^{n_{\mathrm{f}}}\Lambda_{\mathrm{f}}\frac{{}^{\mu}k_{\mathrm{wf}}}{\mu p}\mathrm{e}^{\mathrm{j}(\mu+n_{\mathrm{s}}Z_{\mathrm{s}}+n_{\mathrm{f}}Z_{\mathrm{f}})\varphi_{\mathrm{f}}}\mathrm{e}^{\mathrm{j}(\omega_{\mathrm{r}}-n_{\mathrm{s}}Z_{\mathrm{s}}\omega_{\mathrm{m}})t}\cdot\mathrm{e}^{-\mathrm{j}n_{\mathrm{s}}Z_{\mathrm{s}}\beta}\right\}. \tag{3.21}$$

The flux follows after integration as

$$\Psi_{\mathrm{f,f}} = rl_{\mathrm{Fe}}\frac{2}{\pi}N_{\mathrm{f}}^2\frac{\mu_0}{h_\delta}\frac{\hat{I}_{\mathrm{f}}}{4}\mathrm{Re}\Bigg\{\frac{1}{\mathrm{j}}\cdot\sum_{n_{\mathrm{s}}}\sum_{n_{\mathrm{f}}}\sum_{\mu}{}^{n_{\mathrm{s}}}\Lambda_{\mathrm{s}}{}^{n_{\mathrm{f}}}\Lambda_{\mathrm{f}}\frac{{}^{\mu}k_{\mathrm{wf}}}{\mu p}\frac{-\mu-n_{\mathrm{s}}\frac{Z_{\mathrm{s}}}{p}-n_{\mathrm{f}}\frac{Z_{\mathrm{f}}}{p}k_{\mathrm{wf}}}{-\mu p-n_{\mathrm{s}}Z_{\mathrm{s}}-n_{\mathrm{f}}Z_{\mathrm{f}}}\cdot \mathrm{e}^{\mathrm{j}(\omega_{\mathrm{r}}-n_{\mathrm{s}}Z_{\mathrm{s}}\omega_{\mathrm{m}})t}\cdot\mathrm{e}^{-\mathrm{j}n_{\mathrm{s}}Z_{\mathrm{s}}\beta}\Bigg\}. \tag{3.22}$$

It can be observed again that the rotor field induces additional frequencies $(\omega_{\mathrm{r}} - n_{\mathrm{s}}Z_{\mathrm{s}}\omega_{\mathrm{m}})$ related to the stator slot number Z_{s} into the rotor winding. However, the additional frequencies are insignificant and thus neglected. The self-inductance is directly obtained as

$$L_{\mathrm{f}} = rl_{\mathrm{Fe}}\frac{2}{\pi}N_{\mathrm{f}}^2\frac{\mu_0}{h_\delta}\frac{1}{4}\cdot\mathrm{Re}\left\{\frac{1}{\mathrm{j}}\sum_{n_{\mathrm{s}}}\sum_{n_{\mathrm{f}}}\sum_{\mu}{}^{n_{\mathrm{s}}}\Lambda_{\mathrm{s}}{}^{n_{\mathrm{f}}}\Lambda_{\mathrm{f}}\frac{{}^{\mu}k_{\mathrm{wf}}}{\mu p}\frac{-\mu-n_{\mathrm{s}}\frac{Z_{\mathrm{s}}}{p}-n_{\mathrm{f}}\frac{Z_{\mathrm{f}}}{p}k_{\mathrm{wf}}}{-\mu p-n_{\mathrm{s}}Z_{\mathrm{s}}-n_{\mathrm{f}}Z_{\mathrm{f}}}\cdot\mathrm{e}^{-\mathrm{j}n_{\mathrm{s}}Z_{\mathrm{s}}\beta}\right\}. \tag{3.23}$$

Flux coupling from rotor to a single stator phase k With the rotor airgap flux density (subscript f) transformed into the stator reference frame (superscript s)

$$
{}^{(s)}B_{\delta\mathrm{f}} = \frac{\mu_0}{h_\delta}\frac{1}{\pi}N_\mathrm{f}\hat{I}_\mathrm{f}\frac{1}{4}\cdot\mathrm{Re}\left\{\frac{1}{\mathrm{j}}\sum_{n_\mathrm{s}}\sum_{n_\mathrm{f}}\sum_{\mu}{}^{n_\mathrm{S}}\Lambda_\mathrm{s}\,{}^{n_\mathrm{f}}\Lambda_\mathrm{f}\frac{{}^{\mu}k_\mathrm{wf}}{\mu p}\mathrm{e}^{\mathrm{j}(\mu+n_\mathrm{s}Z_\mathrm{s}+n_\mathrm{f}Z_\mathrm{f})\varphi}\cdot\right.
\left.\mathrm{e}^{\mathrm{j}(\,\omega_\mathrm{r}+\mu p\omega_\mathrm{m}+n_\mathrm{f}Z_\mathrm{f}\omega_\mathrm{m})t}\mathrm{e}^{\mathrm{j}(\mu p\beta+n_\mathrm{f}Z_\mathrm{f}\beta)}\right\},
\tag{3.24}
$$

the flux coupling with a single phase k of the stator winding follows after integration as

$$
\Psi_{\mathrm{k,f}} = rl_\mathrm{Fe}\frac{2}{\pi}N_\mathrm{s}N_\mathrm{f}\frac{\mu_0}{h_\delta}\frac{\hat{I}_\mathrm{f}}{4}\mathrm{Re}\left\{\frac{1}{\mathrm{j}}\cdot\sum_{n_\mathrm{s}}\sum_{n_\mathrm{f}}\sum_{\mu}{}^{n_\mathrm{s}}\Lambda_\mathrm{s}\,{}^{n_\mathrm{f}}\Lambda_\mathrm{f}\frac{{}^{\mu}k_\mathrm{wf}}{\mu p}\frac{-\mu-n_\mathrm{s}\frac{Z_\mathrm{s}}{p}-n_\mathrm{f}\frac{Z_\mathrm{f}}{p}}{-\mu p-n_\mathrm{s}Z_\mathrm{s}-n_\mathrm{f}Z_\mathrm{f}}k_\mathrm{ws}\cdot\right.
\left.\mathrm{e}^{\mathrm{j}(\,\omega_\mathrm{r}+\mu p\omega_\mathrm{m}+n_\mathrm{f}Z_\mathrm{f}\omega_\mathrm{m})t}\mathrm{e}^{\mathrm{j}(\mu p\beta+n_\mathrm{f}Z_\mathrm{f}\beta+(\mu p+n_\mathrm{s}Z_\mathrm{s}+n_\mathrm{f}Z_\mathrm{f})(\mathrm{k}-1)\frac{2\pi}{3p})}\right\}.
\tag{3.25}
$$

It can be seen that frequencies ($\omega_\mathrm{r}+\mu p\omega_\mathrm{m}+n_\mathrm{f}Z_\mathrm{f}\omega_\mathrm{m}$) are induced into the stator winding by the rotor winding. The mutual inductance from the rotor winding to a stator phase follows as

$$
L_{\mathrm{k,f}} = rl_\mathrm{Fe}\frac{2}{\pi}N_\mathrm{s}N_\mathrm{f}\frac{\mu_0}{h_\delta}\frac{1}{4}\cdot\mathrm{Re}\left\{\frac{1}{\mathrm{j}}\sum_{n_\mathrm{s}}\sum_{n_\mathrm{f}}\sum_{\mu}{}^{n_\mathrm{s}}\Lambda_\mathrm{s}\,{}^{n_\mathrm{f}}\Lambda_\mathrm{f}\frac{{}^{\mu}k_\mathrm{wf}}{\mu p}\frac{-\mu-n_\mathrm{s}\frac{Z_\mathrm{s}}{p}-n_\mathrm{f}\frac{Z_\mathrm{f}}{p}}{-\mu p-n_\mathrm{s}Z_\mathrm{s}-n_\mathrm{f}Z_\mathrm{f}}k_\mathrm{ws}\cdot\right.
\left.\mathrm{e}^{\mathrm{j}(\mu p\beta+n_\mathrm{f}Z_\mathrm{f}\beta+(\mu p+n_\mathrm{s}Z_\mathrm{s}+n_\mathrm{f}Z_\mathrm{f})(\mathrm{k}-1)\frac{2\pi}{3p})}\right\}.
\tag{3.26}
$$

Table 3.2 summarizes the (blue) frequencies of the induced voltages as a result of first armature reaction if the stator is excited by a three-phase system of frequency ω and the rotor by an AC current of frequency ω_r.

Table 3.2: Frequencies induced into the stator and rotor

	From Stator ($v = \mathrm{sign}+6b$)	From Rotor ($\mu = \pm1, \pm3, \pm5, ...$)
To Stator	$\omega + n_\mathrm{f}Z_\mathrm{f}\omega_\mathrm{m}$	$\omega_\mathrm{r} + \mu p\omega_\mathrm{m} + n_\mathrm{f}Z_\mathrm{f}\omega_\mathrm{m}$
To Rotor	$\omega - vp\omega_\mathrm{m} - n_\mathrm{s}Z_\mathrm{s}$	$\omega_\mathrm{r} - n_\mathrm{s}Z_\mathrm{s}\omega_\mathrm{m}$

3.1.4 Fundamental Approximation

Higher order winding and slotting harmonics do not contribute to the functionality of conventional synchronous machines and are mostly responsible for cogging torques, higher leakage inductance and undesired induction distorting the terminal voltages. While these parasitic

effects are important design aspects, they can be neglected when qualitative results are sufficient. In this section, the goal is to simplify the exhaustive expressions in the previous section and obtain the fundamental approximation for the inductances, induced voltages and the machine torque. The simplest approximation is obtained by eliminating the effects of permeance harmonics ($\rightarrow n_\mathrm{s} = n_\mathrm{f} = 0,\ {}^0\Lambda_\mathrm{s} \cdot {}^0\Lambda_\mathrm{f} = 4/k_\mathrm{c}$) and winding harmonics ($\rightarrow \nu = 1,\ \mu = \pm 1$). Thus, the self and mutual **inductances** follow directly from (3.17), (3.20), (3.23) and (3.26) as

stator self inductance
$$L_\mathrm{d} = L_{\sigma\mathrm{s}} + r l_\mathrm{Fe} \frac{6}{\pi} \frac{\mu_0}{k_\mathrm{c} h_\delta} \left(\frac{N_\mathrm{s}\, {}^1k_\mathrm{ws}}{p} \right)^2 \tag{3.27}$$

mutual inductance (rotor to single stator winding)
$$L_\mathrm{df} = r l_\mathrm{Fe} \frac{4}{\pi} \frac{\mu_0}{k_\mathrm{c} h_\delta} N_\mathrm{s} N_\mathrm{f} \frac{{}^1k_\mathrm{ws}\, {}^1k_\mathrm{wf}}{p^2} \tag{3.28}$$

mutual inductance (all stator windings to rotor)
$$L_\mathrm{fd} = \frac{3}{2} L_\mathrm{df} \tag{3.29}$$

rotor self inductance
$$L_\mathrm{f} = L_{\sigma\mathrm{f}} + r l_\mathrm{Fe} \frac{4}{\pi} \frac{\mu_0}{k_\mathrm{c} h_\delta} \left(\frac{N_\mathrm{f}\, {}^1k_\mathrm{wf}}{p} \right)^2 \tag{3.30}$$

with the stator (rotor) leakage inductances $L_{\sigma\mathrm{s}}$ ($L_{\sigma\mathrm{f}}$) not further defined here, because apart from harmonic leakage additional leakage components like slot, end-winding and overhang leakage flux which are exhaustive to analytically quantify have to be included. The **induced voltage** (back EMF) into a single phase of the stator winding due to rotation and excitation of the rotor follows from (3.25) as

rotor AC excited:
$$\begin{aligned} U_\mathrm{k,f} = {} & (\,\omega_\mathrm{r} + p\omega_\mathrm{m})\, L_\mathrm{df} \frac{\hat{I}_\mathrm{f}}{2} \sin\left((\,\omega_\mathrm{r} + p\omega_\mathrm{m})\, t + p\beta + (k-1)\frac{2\pi}{3} \right) \\ & + (\,\omega_\mathrm{r} - p\omega_\mathrm{m})\, L_\mathrm{df} \frac{\hat{I}_\mathrm{f}}{2} \sin\left((\,\omega_\mathrm{r} - p\omega_\mathrm{m})\, t - p\beta - (k-1)\frac{2\pi}{3} \right) \end{aligned} \tag{3.31}$$

rotor DC excited:
$$U_\mathrm{k,f} = p\omega_\mathrm{m} L_\mathrm{df} I_\mathrm{f} \sin\left(p\omega_\mathrm{m} t + p\beta + (k-1)\frac{2\pi}{3} \right)$$

where the inductance mutual inductance L_df from (3.28) has been substituted. Here, again, it can be observed that the induced voltage into the stator inevitably consists of two components with distinct frequencies — one related to the forward rotating field and one to the backward rotating field. Only for DC excitation $\omega_\mathrm{r} = 0$ do the two fields align with each other.

Analogously, the **induced voltage** from the stator winding into the rotor winding follows from (3.19) as

$$\begin{aligned} &\text{forward rotating ('sign' = 1)} && U_{\mathrm{f,s}} = (\omega - p\omega_{\mathrm{m}})\,\frac{3}{2} L_{\mathrm{df}} \hat{I}_{\mathrm{s}} \sin((\omega - p\omega_{\mathrm{m}})\,t - p\beta + \theta_{\mathrm{s}}) \\ &\text{backward rotating ('sign' = } -1) && U_{\mathrm{f,s}} = (\omega + p\omega_{\mathrm{m}})\,\frac{3}{2} L_{\mathrm{df}} \hat{I}_{\mathrm{s}} \sin((\omega + p\omega_{\mathrm{m}})\,t + p\beta + \theta_{\mathrm{s}}). \end{aligned} \tag{3.32}$$

This highlights that depending on the direction of the rotary stator field, there are two options (sign = ± 1) to induce a voltage of the same frequency into the rotor winding exist. This is the basis of harmonic excitation.

An approximation for the average **torque** can be calculated by the method of virtual work: When the rotor moves by an infinitesimally small angle $\delta\beta$ in the time δt, the magnetic energy $E = \frac{1}{2}\sum_{\mathrm{i}} \Psi_{\mathrm{i}} I_{\mathrm{i}}$ which consists of the contribution of all i windings changes

$$\delta E = \sum_{\mathrm{i}} \frac{1}{2} \left(\delta\Psi_{\mathrm{i}} I_{\mathrm{i}} + \Psi_{\mathrm{i}} \delta I_{\mathrm{i}}\right). \tag{3.33}$$

The energy balance of the system after the angular displacement must be zero so that the work $M_{\mathrm{el}}\delta\beta$ performed by the torque **plus** the change of energy δE of the magnetic field **must be equal** to the electrical energy input

$$\sum_{\mathrm{i}} U_{\mathrm{i}} I_{\mathrm{i}} \delta t = \delta E + M_{\mathrm{el}} \delta\beta \tag{3.34}$$

where i loops through all stator phases and the rotor winding. The induced voltage follows from the rate of change of the flux as $U_{\mathrm{i}} = \frac{\delta\Psi_{\mathrm{i}}}{\delta t}$. If only the synchronous torque is considered, the derivation of the stator flux $\Psi_{\mathrm{k,s}}$ (3.16) and rotor flux $\Psi_{\mathrm{f,f}}$ (3.22) which are responsible for the reluctance and cogging torque components are neglected. By rearranging the energy balance (3.34) an expression for the (synchronous) torque is obtained

$$M_{\mathrm{el}} = \frac{1}{2} \sum_{\mathrm{i}} \left(\frac{\delta\Psi_{\mathrm{i}}}{\delta\beta} I_{\mathrm{i}} - \Psi_{\mathrm{i}} \frac{\delta I_{\mathrm{i}}}{\delta\beta} \right) = \frac{1}{2} \left(\frac{\mathrm{d}\Psi_{\mathrm{f,s}}}{\mathrm{d}\beta} \hat{I}_{\mathrm{f}} + \sum_{\mathrm{k}=1}^{3} \frac{\mathrm{d}\Psi_{\mathrm{k,f}}}{\mathrm{d}\beta} I_{\mathrm{s,k}} \right). \tag{3.35}$$

Inserting the flux linkages (3.19), (3.25) and currents (3.2), (3.8) yields

$$M_{\mathrm{el}} = r l_{\mathrm{Fe}} \frac{3}{\pi} N_{\mathrm{f}} N_{\mathrm{s}} \frac{\mu_0}{k_{\mathrm{c}} h_\delta} \hat{I}_{\mathrm{s}} \hat{I}_{\mathrm{f}} \frac{{}^1k_{\mathrm{ws}}\, {}^1k_{\mathrm{wf}}}{p} \cdot \begin{cases} -\sin\left((\omega + \omega_{\mathrm{r}} - p\omega_{\mathrm{m}})t - p\beta + \theta_{\mathrm{s}}\right) & \text{for 'sign'} = 1 \\ \sin\left((\omega + \omega_{\mathrm{r}} + p\omega_{\mathrm{m}})t + p\beta + \theta_{\mathrm{s}}\right) & \text{for 'sign'} = -1 \end{cases} \tag{3.36}$$

where $\hat{I}_{\mathrm{f}}$ is replaced by I_{f} and $\omega_{\mathrm{r}} = 0$ in case of DC excitation.

3.2 HESM operation

The induced voltages given by (3.31) and (3.32), and the torque equations in (3.36) are applicable to a generic stator frequency ω and rotor frequency ω_r. These equations can be used to derive the working principle of harmonic excitation. In this work, all types of investigated HESMs can be modeled as — or transformed into — two sets of independent stator and rotor windings as portrayed in Fig. 2.4, each with distinct pole-pair numbers p_m and p_h – one for producing torque and the other for harmonic excitation. The generic parameters, such as pole-pair number p, number of winding turns N_s, N_f, and winding currents $\hat{I}_\mathrm{s}$ and $\hat{I}_\mathrm{f}$, which were used in the previous sections, are now modified with the subscript 'm' or 'h' to indicate their affiliation with the p_m or p_h pole-pair machine.

3.2.1 Torque-Production

The primary objective of a rotating electrical machine is to generate the shaft torque. This is accomplished through the use of the p_m pole-pair machine. In order to produce a net average torque greater than zero, the time-dependent terms inside of the torque equation (3.36) must cancel out. This is achieved with a forward rotating stator field ('sign' = 1) which rotates synchronously with respect to the rotor ($\omega = p_\mathrm{m}\omega_\mathrm{m}$) and the rotor is excited by a DC current. In this case, the torque produced by the main machine (3.36) expressed in terms of the mutual inductance L_dfm yields the synchronous torque

$$M_\mathrm{el} = r l_\mathrm{Fe} \frac{3}{\pi} N_\mathrm{fm} N_\mathrm{sm} \frac{\mu_0}{k_\mathrm{c} h_\delta} \hat{I}_\mathrm{sm} I_\mathrm{fm} \frac{{}^1k_\mathrm{wsm}\, {}^1k_\mathrm{wfm}}{p_\mathrm{m}} = \frac{3}{2} p_\mathrm{m} L_\mathrm{dfm} I_\mathrm{fm} \hat{I}_\mathrm{sm} \sin(p_\mathrm{m}\beta + \theta_\mathrm{s}) \tag{3.37}$$

where L_dfm is obtained by substituting the main machine pole-pair number, winding factors and series turns into (3.28). This is the conventional synchronous torque equation for WRSMs. The induced voltage from the rotor to a single stator phase k of the p_m pole-pair machine follows from (3.31) as the back EMF equation

$$U_\mathrm{kf} = p_\mathrm{m}\omega_\mathrm{m} L_\mathrm{dfm} I_\mathrm{fm} \sin\left(p_\mathrm{m}\omega_\mathrm{m} t + p_\mathrm{m}\beta + (k-1)\frac{2\pi}{3}\right). \tag{3.38}$$

Naturally, the induced voltage (due to the fundamental) from the stator to the rotor winding is zero in a WRSM according to (3.32) which coincides with the fact that a fundamental field rotating synchronously with respect to the rotor does not induce any voltage into the rotor winding.

3.2.2 Harmonic Excitation

In order to supply the field current to the p_m pole-pair machine, a voltage $U_\mathrm{fh,ind}$ must be induced into the rotor winding of the p_h pole-pair machine which is then rectified into the

DC field voltage and feeds the p_m pole-pair field winding. The equivalent circuit of the p_m and p_h pole-pair rotor windings which couple through a bridge rectifier is given in Fig. 3.1.

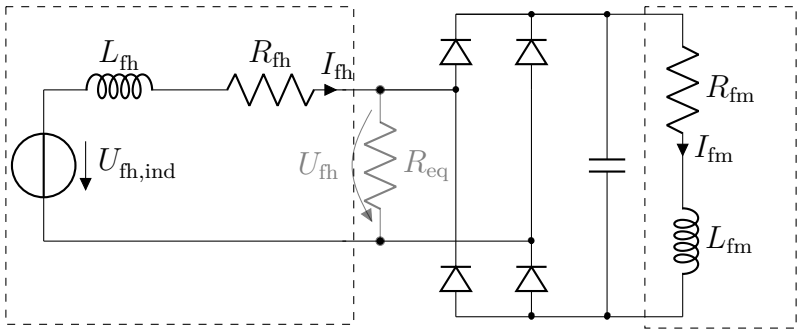

Figure 3.1: Equivalent Circuit of the p_h- and p_m pole-pair rotor winding.

In order for the induced rotor voltage (3.32) to take on a frequency ω_exc, the stator frequency ω can take on the two values

$$\omega_+ = \omega_\mathrm{exc} + p\omega_\mathrm{m} \text{ for 'sign'} = 1 \quad \text{and} \quad \omega_- = \omega_\mathrm{exc} - p\omega_\mathrm{m} \text{ for 'sign'} = -1. \tag{3.39}$$

If the stator field is rotating in forward direction ($v = 1$) a frequency ω_+ must be used, while in backward direction ($v = -1$) a frequency of ω_- induces a voltage of frequency ω_exc into the rotor winding. In both cases, the induced voltage $U_\mathrm{fh,ind}$ due to a current $\hat{I}_\mathrm{s}$ is

$$U_\mathrm{fh,ind} = \omega_\mathrm{exc}\frac{3}{2}L_\mathrm{dfh}\hat{I}_\mathrm{sh}\sin(\omega_\mathrm{exc}t + \theta_\mathrm{I}) \tag{3.40}$$

where L_dfh is obtained by substituting the appropriate pole-pair number, winding factors and series turns of the p_h pole-pair machine into (3.28). Instead of using **either** the forward **or** backward rotating field, **both** frequency components can be used simultaneously to induce the rotor voltage $U_\mathrm{fh,ind}$. If the current phase shift θ_s of the forward (backward) rotating field takes on the value $\theta_{\mathrm{s}+} = \theta_\mathrm{I} - p_\mathrm{h}\beta$ ($\theta_{\mathrm{s}-} = \theta_\mathrm{I} + p_\mathrm{h}\beta$), each component of (3.32) is responsible for half of the induced voltage and the produced torque (3.36) vanishes. The advantage of using both stator frequencies ω_+ and ω_- simultaneously in order to reach a desired $U_\mathrm{fh,ind}$ compared to using only one component is the reduction of the stator copper losses by half as seen in (3.41).

$$\begin{aligned}
&\text{Either } \omega_- \text{ or } \omega_+\text{:} \quad P_\mathrm{vs,cu} &&= \frac{3}{2}R_\mathrm{sh}\hat{I}_\mathrm{s}^2 \\
&\text{Both } \omega_- \text{ and } \omega_+\text{:} \quad P_\mathrm{vs,cu} = \frac{3}{2}R_\mathrm{sh}\left(\underbrace{\left(\frac{\hat{I}_\mathrm{s}}{2}\right)^2}_{\text{for } \omega_+} + \underbrace{\left(\frac{\hat{I}_\mathrm{s}}{2}\right)^2}_{\text{for } \omega_-}\right) &&= \frac{3}{4}R_\mathrm{sh}\hat{I}_\mathrm{s}^2
\end{aligned} \tag{3.41}$$

As a consequence of the induced voltage $U_{\mathrm{fh,ind}}$ an AC current I_{fh} of the same frequency ($\omega_{\mathrm{r}} = \omega_{\mathrm{exc}}$) flows in the rotor winding. The relationship between input and output values of the diode rectifier coupling the p_{h} pole-pair winding to the p_{m} pole-pair winding is not trivial because diodes are nonlinear components which only conduct when their threshold voltage is exceeded. In order to obtain a closed-form expression for the equivalent circuit in Fig. 3.1, the first harmonic approximation (3.42) for the equivalent impedance R_{eq} of the diode rectifier is used. It is only valid under the simplifying assumption of a threshold voltage of zero, a sinusoidal input current with peak value $\hat{I}_{\mathrm{fh}}$, a rectangular voltage at the rectifier terminals with a peak value of $\hat{U}_{\mathrm{fh}}$ (first harmonic) and no phase-shift between I_{fh} and U_{fh}.

$$\hat{I}_{\mathrm{fh}} = \frac{\pi}{2} I_{\mathrm{fm}} \qquad \hat{U}_{\mathrm{fh}} = \frac{4}{\pi} U_{\mathrm{fm}} \qquad R_{\mathrm{eq}} = \frac{8}{\pi^2} R_{\mathrm{fm}} \tag{3.42}$$

Thus, the power transferred from the stator to the rotor via harmonic excitation can be calculated from (3.8) and (3.40) with the help of complex AC calculation in terms of the current or the induced voltage as

$$P_{\mathrm{fh}} = \begin{cases} \omega_{\mathrm{exc}} \dfrac{3}{4} L_{\mathrm{dfh}} \hat{I}_{\mathrm{sh}} \hat{I}_{\mathrm{fh}} \sin(\theta_{\mathrm{I}}) & \text{Current Representation} \\ \dfrac{1}{2} \hat{U}^2_{\mathrm{fh,ind}} \dfrac{R_{\mathrm{fh}} + R_{\mathrm{eq}}}{(R_{\mathrm{fh}} + R_{\mathrm{eq}})^2 + (\omega_{\mathrm{exc}} L_{\mathrm{fh}})^2} & \text{Voltage Representation.} \end{cases} \tag{3.43}$$

The voltage representation of (3.43) highlights that the transferred power to the rotor P_{fh} depends significantly on the voltage drop over the self-inductance L_{fh}. In the current representation this is indicated by the current phase shift θ_{I} which maximizes the power transmission for $\theta_{\mathrm{I}} = 90°$, but is significantly smaller due to the reactive power. The rotor winding efficiency is obtained by dividing the output power by the input power to the rotor winding

$$\eta_{\mathrm{r}} = \frac{\frac{1}{2} R_{\mathrm{eq}} \hat{I}^2_{\mathrm{fh}}}{\frac{1}{2}(R_{\mathrm{fh}} + R_{\mathrm{eq}}) \hat{I}^2_{\mathrm{fh}}} = \frac{1}{1 + \frac{R_{\mathrm{fh}}}{R_{\mathrm{eq}}}} = \frac{1}{1 + \frac{\pi^2}{8} \frac{R_{\mathrm{fh}}}{R_{\mathrm{fm}}}}. \tag{3.44}$$

It can be seen that the rotor efficiency is inversely proportional to the ratio of the p_{h} pole-pair field winding resistance R_{fh} to the (equivalent) load resistor R_{eq}. The equations derived in this section describe the general functionality of harmonic excitation and are extensively applied and extended in the following chapters.

3.2.3 Frequency Spectrum

In the previous sections, the electrical frequencies present in a HESM have been determined: The p_{m} pole-pair machine functions as a conventional WRSM with DC excitation in the rotor and a rotating stator field $p_{\mathrm{m}}\omega_{\mathrm{m}}$ rotating synchronously with respect to the rotor. On

the contrary, in the p_h pole-pair machine an AC current of frequency ω_exc flows in the rotor winding and **two different** three-phase current components of frequencies ω_+ and ω_- are injected into the stator winding. These operating currents realize the basic functionality of torque production (pole pair p_m) and harmonic excitation (pole pair p_h).
A summary of the induced voltages inside of a HESM due to first armature reaction is given in Tab. 3.3 by substituting the generic frequencies ω and ω_r in Tab. 3.2 with the above frequencies. The ordinal numbers are distinguished by their affiliation to the pole pair p_m or p_h so that $\nu_\mathrm{m} = 1 + 6b$ and $\mu_\mathrm{m} = \pm1, \pm3, \pm5, ...$ denote the ordinal numbers of the p_m pole-pair machine. Analogously, ordinal numbers related to the p_h pole-pair machine are $\nu_{\mathrm{h}+} = 1 + 6b$ and $\nu_{\mathrm{h}-} = -1 + 6b$ for the forward and backward rotating stator field and $\mu_\mathrm{h} = \pm1, \pm3, \pm5, ...$ for the rotor field. The actual occurrence of a particular frequency in the stator or rotor voltage depends on whether the winding factors and permeance waves of the respective ordinal numbers are non-zero. This indicates the importance of low harmonic winding factors especially for the p_h pole-pair machine. The term highlighted in blue of Tab. 3.3 showcases an important result: Even if e.g. the backward rotating field ω_- is excited by the p_h pole-pair stator winding, a voltage related to the forward rotating field (frequency ω_+) is induced back into the stator because the single-phase rotor winding supplied with a current of frequency ω_exc and rotating at a speed of ω_m always excites fields related to both ordinal numbers $\mu_\mathrm{h} = \pm1$.

Table 3.3: Frequencies of the induced voltage in stator and rotor as a consequence of first armature reaction.

		From Stator	From Rotor
To Stator	p_m	$p_\mathrm{m}\omega_\mathrm{m} + n_\mathrm{f}Z_\mathrm{f}\omega_\mathrm{m}$	$\mu_\mathrm{m}p_\mathrm{m}\omega_\mathrm{m} + n_\mathrm{f}Z_\mathrm{f}\omega_\mathrm{m}$
	p_h	'sign' $= \quad 1:\ \omega_\mathrm{exc} + p_\mathrm{h}\omega_\mathrm{m} + n_\mathrm{f}Z_\mathrm{f}\omega_\mathrm{m}$ 'sign' $= -1:\ \omega_\mathrm{exc} - p_\mathrm{h}\omega_\mathrm{m} + n_\mathrm{f}Z_\mathrm{f}\omega_\mathrm{m}$	$\omega_\mathrm{exc} + \mu_\mathrm{h}p_\mathrm{h}\omega_\mathrm{m} + n_\mathrm{f}Z_\mathrm{f}\omega_\mathrm{m}$
To Rotor	p_m	$(1-\nu_\mathrm{m})p_\mathrm{m}\omega_\mathrm{m} - n_\mathrm{s}Z_\mathrm{s}\omega_\mathrm{m}$	$n_\mathrm{s}Z_\mathrm{s}\omega_\mathrm{m}$
	p_h	'sign' $= \quad 1:\ \ (1-\nu_{\mathrm{h}+})p_\mathrm{h}\omega_\mathrm{m} + \omega_\mathrm{exc} - n_\mathrm{s}Z_\mathrm{s}\omega_\mathrm{m}$ 'sign' $= -1:\ -(1-\nu_{\mathrm{h}-})p_\mathrm{h}\omega_\mathrm{m} + \omega_\mathrm{exc} - n_\mathrm{s}Z_\mathrm{s}\omega_\mathrm{m}$	$n_\mathrm{s}Z_\mathrm{s}\omega_\mathrm{m} - \omega_\mathrm{exc}$

Chapter 4

Novel Harmonic-Excited Synchronous Machine

In Section 3.2 the two operation modes of a HESM have been presented: Torque production and harmonic excitation each of which are designated an independent pole-pair number p_m and p_h. As the primary goal of a rotating machine is to generate a torque, the design of the torque-producing p_m pole-pair machine is the first priority. The subsequent integration of the p_h pole-pair machine into the HESM presents a unique challenge because the geometry which is usually determined during the machine design is already fixed by the p_m pole-pair machine. In this work, this challenge is further constrained by the fact that a HESM without any auxiliary windings is targeted. This means that even the coil locations in the slots are predetermined by the p_m pole-pair winding layout. As the successful design of a HESM concept hinges upon the ability to realize both the p_m and p_h pole-pair machines optimally, in the upcoming sections the theoretical basis of the various methods for producing multiple pole pairs from a single winding will be presented. These methods will then be applied to synthesize a novel HESM concept.

4.1 Methods of Producing Multiple Pole-Pair Numbers

The challenge of eliminating auxiliary windings from HESMs is to find a winding layout that allows the integration of an additional harmonic pole pair p_h within the conventional p_m pole-pair WRSM. This winding layout must fulfill the following requirements:

- The performance of the p_m pole-pair machine should not degrade due to the integration of the p_h pole-pair machine.
- The pole pairs p_m and p_h can be produced **simultaneously** and ...
- ... **independently** from each other via distinct current components.

- The p_{m} pole-pair machine does not induce any voltages into the p_{h} pole-pair machine and vice versa.

Generally, there are the three following ways to create multiple pole-pairs from a single winding.

4.1.1 Pole Amplitude Modulation

Pole Amplitude Modulation (PAM) is used in grid-connected pole-changing squirrel-cage induction motors to switch between two pole-pair numbers p_{m} and p_{h}, thus altering the synchronous speed. The general idea of pole-changing motors is to rearrange the coil groups of the stator winding with the help of relays to cleverly reverse the current direction in specific coil groups. The most simple and well-known PAM concept is the Dahlander circuit, which produces the pole-pair ratio 1:2. A large number of pole-pair combinations are possible albeit often only with complicated winding diagrams and even spatial winding asymmetries [29], [30].
In Fig. 4.1a, a conventional Dahlander connection diagram with three three-phase relays is shown.

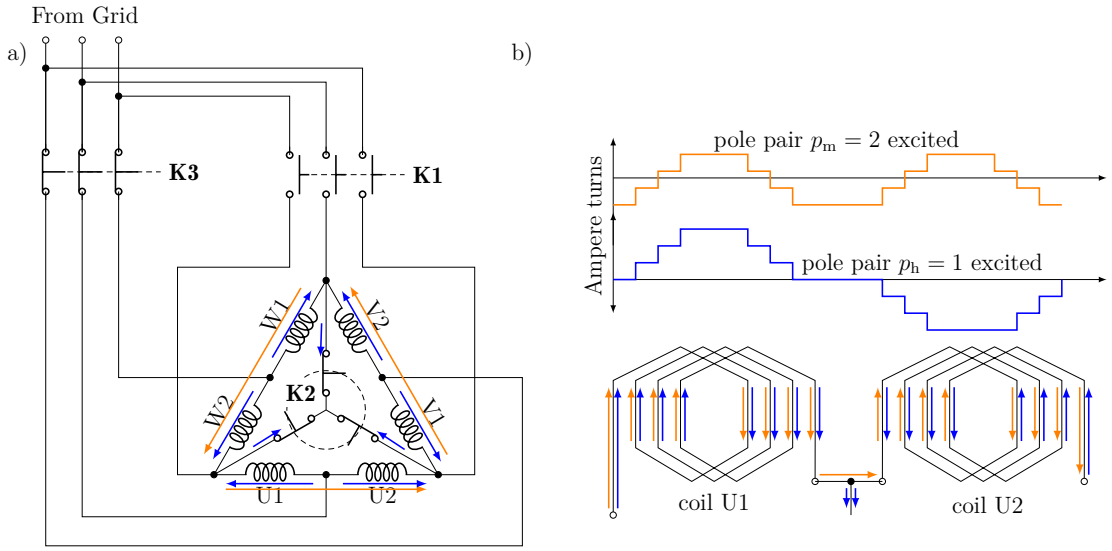

Figure 4.1: Dahlander method: a) Dahlander circuit with three relays K1, K2 and K3; b) Corresponding MMFs for U1-U2.

If relays K2 and K3 are closed and K1 is open, two corresponding coil groups U1-U2, V1-V2 and W1-W2 are paralleled and a star connection is obtained. In this case, the direction of the currents in the windings is highlighted by the orange arrows. Pole-changing is achieved by closing K1 and opening relays K2 and K3. Now, the coil groups U1-U2, V1-V2 and W1-W2 are connected in series into a delta configuration. The blue arrows highlight that the

direction of the current flow in one coil group of each phase changes direction. Depending on the direction of the currents in two related coils, the MMF switches between two pole pairs p_m and p_h. An example for this is given in Fig. 4.1b: The blue MMF (due to blue currents) corresponds to a conventional $p_\mathrm{m} = 2$ pole-pair, $q = 2$ slot-per-pole-per-phase two-layer winding short-pitched by two slots. To obtain the orange MMF (due to orange currents) the MMF produced by the coil group U2 is reversed so that a $p_\mathrm{h} = 1$ pole-pair MMF with a substantially higher harmonic content is produced.
It is obvious that only one relay position — and hence one pole pair — can be adopted at a given time with the relays hard-switching between the two coil arrangements during operation. Hence, PAM cannot be applied to produce both pole pairs simultaneously.

4.1.2 Pole Phase Modulation

Pole Phase Modulation (PPM) takes advantage of the fact that the phase shift of the currents in a multi-phase system has an effect on the harmonics produced by the machine windings. The mathematical basis for PPM was already indicated in (3.4) for the special case of a three-phase machine. It is generalized here by assuming that phase k of an m-phase winding is supplied by a current

$$I_\mathrm{s,k} = \hat{I}_\mathrm{s} \cdot \cos\left(\omega t + n(\mathrm{k}-1)\frac{2\pi}{m}\right) \tag{4.1}$$

where now the current phase shift can take on different values denoted by a parameter $n = 1, ..., \mathrm{floor}\left(\frac{m}{2}\right)$. Multiplication with the winding function (3.1) and summing over all m phases (see (3.4)) yields

$$\Theta_\mathrm{s} = \frac{N_\mathrm{s}}{\pi}\hat{I}_\mathrm{s}\mathrm{Re}\left\{\frac{1}{\mathrm{j}}\mathrm{e}^{\mathrm{j}\omega t}\sum_{v=-\infty}^{\infty}\frac{{}^{v}k_\mathrm{ws}}{vp}\mathrm{e}^{\mathrm{j}(vp\varphi)}\underbrace{\sum_{\mathrm{k}=1}^{m}\mathrm{e}^{-\mathrm{j}\frac{2\pi}{m}(\mathrm{k}-1)(n-v)}}_{=m \text{ for } (4.3)}\right\}. \tag{4.2}$$

The underbraced condition is only $\neq 0$, more precisely $= m$, if $\frac{2\pi}{m}(n-v) \stackrel{!}{=} b \cdot 2\pi$ where $b = 0, \pm 1 \pm 2, ...$ Hence, an m-phase winding (where m is odd) for a given current phase shift n produces the following harmonics

$$v = n + bm \qquad \text{for } b = 0, \pm 1, \pm 2, \pm 3, ... \tag{4.3}$$

This result is the generalization of the $m = 3$-phase winding case in (3.6) with phase-shift $n = 1$ and now includes even harmonics. The harmonics v that are created by an m-phase winding phase-shifted with n are highlighted exemplarily in Tab. 4.1 for several m and n. Harmonics in bold type denote odd harmonics which normally occur in machine windings. Unbolded harmonics denote even harmonics which do not usually occur in conventional ma-

Table 4.1: Possible fundamental fields v that can be created in relation to a base pole-pair number p.

n \ m	3	5	7	9	...
1	**1**,-2,4,**-5,7**,...	**1**,-4,6,**-9,11**,...	**1**,-6,8,**-13,15**,...	**1**,-8,10,**-17,19**,...	
2	2,**-1**,**5**,-4,8,...	2,**-3**,**7**,-8,12	2,**-5**,**9**,-12,16,...	2,**-7**,**11**,-16,20,...	
3	3,0,6,...	**3**,-2,8,**-7,13**,...	**3**,-4,10,**-11,17**,...	**3**,-6,12,**-15,21**,...	
4		4,**-1**,**9**,-6,14,...	4,**-3,11**,-10,18,...	4,**-5,13**,-14,22,...	
5		5,0,10,...	**5**,-2,12,**-9,19**,...	**5**,-4,14,**-13,23**,...	

chine windings. Blue cells show that the harmonic combinations simply repeat for higher n. It can be seen that an m phase winding can theoretically produce up to 'floor $\left(\frac{m}{2}\right)$' fundamental fields distinct from each other. For $n = 0$ and $n = m$ (highlighted in red) the standing-wave zero system is created. It should be noted that normal windings are designed to maximize the magnetic field of a single pole-pair number and suppress all other harmonics. However, for the synthesis of a HESM, two fundamentals $v_\mathrm{m} = p_\mathrm{m}/p$ and $v_\mathrm{h} = p_\mathrm{h}/p$ (relating to a base pole-pair number p) from two different columns of Tab. 4.1 can be chosen. The challenge is to find a corresponding winding layout with high winding factors ${}^{v_\mathrm{m}}k_\mathrm{w}$ **and** ${}^{v_\mathrm{h}}k_\mathrm{w}$ for which the two pole pairs can then be generated using the two corresponding phase shifts n. It should be noted that even though even phase numbers are not included in Tab. 4.1, PPM can very much be used for them, albeit with different current phase shifts and coil positions. Therefore, the options presented in Tab.4.1 are not a complete list of all PPM possibilities, but rather provide results for symmetrically spaced m-phase windings which are described by the winding function (3.1).
As PPM requires the injection of appropriately phase-shifted currents, it is mostly used in conjunction with power electronic inverters. It was used e.g. in [31] for the creation of pole pairs two ($n = 2$) and six ($n = 3$) with a $m = 9$-phase induction machine to improve the speed-range by going to a lower pole-pair number at higher speeds. [32] realizes as much as five base pole pairs from an 18-phase machine. All PPM concepts work on the basis of multi-phase machines. Hence, it is apparent that PPM cannot be used for single-phase windings.

4.1.3 Dual-Purpose-No-Voltage Windings

Another approach related to PAM and PPM is the use of *Dual-Purpose-No-Voltage* (DPNV) windings which emerged out of the field of bearingless machines [33]. In bearingless machines — just as in HESMs — two decoupled pole-pair numbers are present simultaneously — one responsible for producing suspension forces which balance the rotor in the middle of the airgap, and the other for conventional torque production. DPNV windings are the attempt to integrate the suspension winding into the existing torque winding. In order to realize this, certain end-winding connections of the existing torque winding function as terminals

of the suspension winding. Thus, DPNV windings have two independent three-phase stator terminals which produce a current flow in the **same** conductors, but in varying directions. Similar to the HESM design goal, special attention has been paid to the decoupling of the suspension terminals and torque terminals, i.e. there is no voltage (hence the name *No-Voltage*) induced in the suspension terminals when the torque winding is excited and vice versa. However, the problem of using the DPNV approach is that while the design rules are helpful to identify and synthesize certain pole-pair numbers for the suspension winding, the injection of the currents into the DPNV windings is only possible with the help of additional isolated DC links. It should also be mentioned that the application of bearingless machines has different requirements for the pole pairs p_h and p_m than a HESM as a pole-pair ratio of $p_\mathrm{h} = p_\mathrm{m} \pm 1$ is targeted for bearingless radial flux motors [33].

4.2 Winding Synthesis

The similarity of all three previously discussed PAM, PPM and DPNV windings is that by some method the current phase-shift is altered in specific coil groups when pole pair p_h is generated. In PAM the current direction is reversed (i.e. phase-shifted by 180°) by **mechanically commutating** and rearranging the coil group connections. In PPM an inverter **electrically commutates** the coil groups by changing the current phase-shift of the m-phase system fed into the windings. Analogously, DPNV windings bring out specific coil group connections as **independent terminals** by which the current flow in certain coil groups is reversed.
Thus, all concepts start with the coil groups which in the case of HESM synthesis are simply the coil groups of the conventional WRSM. Secondly, appropriate phase-shifts for the currents in each coil group must be identified so that certain pole-pair numbers can be generated. Thirdly, a strategy to realize the p_h and p_m phase shifts simultaneously must be found. This approach is now used starting with the single-phase field winding.

4.2.1 Rotor Winding

A single rotor coil r wound around one of the salient poles of a p_m pole-pair WRSM has a winding factor

$$ {}^{\mu}k_\mathrm{wf} = \sin\left(\mu\frac{\pi}{2p_\mathrm{m}}\right) \tag{4.4} $$

This is represented exemplarily in Fig. 4.2 for a single rotor coil of a $p_\mathrm{m} = 4$ pole-pair salient pole WRSM. It can be seen that non-zero winding factors for odd multiples μ of the base pole-pair numbers $p_0 = 1, p_1 = 2$ and $p_\mathrm{m} = p_2 = 4$ occur. An important observation is that a **single coil** r of the $p_\mathrm{m} = 4$ pole-pair rotor winding also inevitably generates the base pole

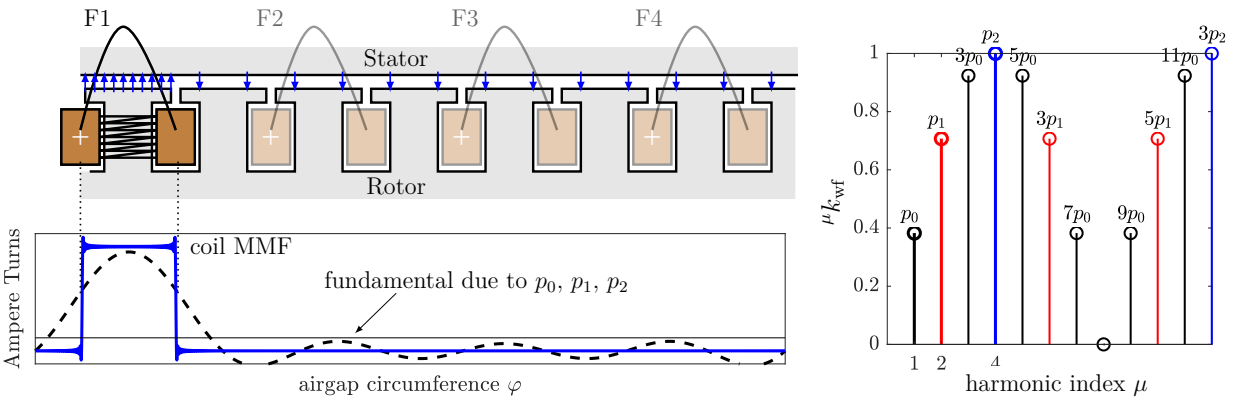

Figure 4.2: Coil groups, winding factor and MMF of a single rotor coil of the field winding.

$^{\mu}\alpha_{el}$ Slot	1	2	3	4	5	6	7	8
$^{p_0}\alpha_{el}$	0	45	90	135	180	225	270	315
$^{p_1}\alpha_{el}$	0	90	180	270	0	90	180	270
$^{p_m}\alpha_{el}$	0	180	0	180	0	180	0	180
W_{F1}	1	-1	0	0	0	0	0	0
W_{F2}	0	0	1	-1	0	0	0	0
W_{F3}	0	0	0	0	1	-1	0	0
W_{F4}	0	0	0	0	0	0	1	-1

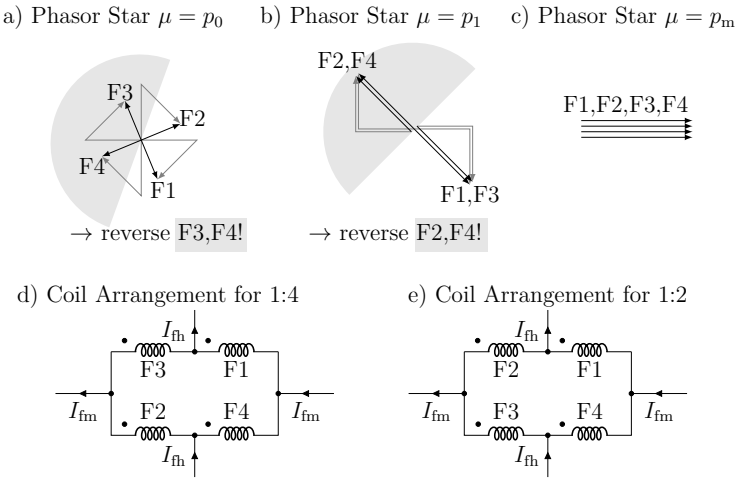

Figure 4.3: Application of the phasor star to each of the rotor coils generated from the left table, where $^{\mu}\alpha_{el} = \mu\frac{2\pi}{2p_m}$ is the electrical angle denoting the slot position and W_F denotes the ampere turns per slot (in per unit).

pairs $p_0 = 1$ and $p_1 = 2$. However, these pole-pair numbers do not occur when the resultant MMF due to **all coils** is considered because the phasors of the four rotor coils cancel each other out. This is shown in the phasor star of Fig. 4.3a and b. In contrast, the phasors of pole pair p_m in Fig. 4.3c reinforce each other so that the rotor coils can be connected in series or parallel to realize the p_m pole-pair field winding. However, if specific coils F2,F4 (F3,F4) are reversed the four phasors of pole pair $p_1 = 2$ ($p_0 = 1$) also add up constructively so that the base pole pair $p_h = 2$ ($p_h = 1$) can be generated all the same. This can be achieved by arranging the four rotor coils in the bridge configuration Fig. 4.3d or e.
For both coil arrangements, the current I_{fm} produces the phasor star from Fig. 4.3c. The additional terminals in the bridge arrangement allow feeding a current I_{fh} into the new terminals which effectively reverses the current in two of those coils and thus produces pole pair $p_h = 2$ ($p_h = 1$). The arrangement resembles the approach reported in [34] and also

of [33]. It should be noted that the arrangement of the four coils uniquely defines which pole pair $p_\mathrm{h} = 1$ or $p_\mathrm{h} = 2$ is generated. Both cannot be generated simultaneously. The fundamental winding factors can be extracted from the phasor star as

$$ {}^{4}k_\mathrm{wf} = 1 \qquad {}^{2}k_\mathrm{wf} = \frac{1}{\sqrt{2}} \qquad {}^{1}k_\mathrm{wf} = 0.382 \tag{4.5} $$

While these results are for the specific pole-pair number $p_\mathrm{m} = 4$, the approach is analogous for other pole-pair numbers p_m and p_h which can be arranged into the four-coil bridge configuration. The winding factor of a rotor coil (Fig. 4.2) and the phasor star (Fig. 4.3) present a generic method to synthesize specific pole pairs p_h from the existing coil groups of a conventional p_m salient-pole field winding. For the HESM concept investigated in this work, the arrangement of Fig. 4.3e is adopted so that pole-pair numbers $p_\mathrm{h} = 2$ and $p_\mathrm{m} = 4$ are realized. A more detailed explanation at the choice of pole-pair ratio is given in Section 4.3.1.

Thus, the winding function of each rotor coil $r = 1, ..., p_\mathrm{m}$ can be expressed mathematically using the winding factor of a single rotor coil (4.4)

$$ W_\mathrm{Fr} = \frac{N_\mathrm{cf}}{\pi} \mathrm{Re}\left\{ \frac{1}{\mathrm{j}} \sum_{\mu=-\infty}^{\infty} \frac{{}^{\mu}k_\mathrm{wf}}{\mu} \mathrm{e}^{\mathrm{j}\mu\left(\varphi_\mathrm{f} - (r-1)\frac{2\pi}{p_\mathrm{m}}\right)} \right\} \text{ with } r = 1, ..., 4 \tag{4.6} $$

where N_cf is the number of series turns of the rotor coil. The reversal of the currents in the arrangement of Fig. 4.3e can be expressed mathematically with the coil r currents

$$ I_\mathrm{Fr} = I_\mathrm{fm} + \mathrm{Re}\left\{ I_\mathrm{fh} \mathrm{e}^{jr\pi} \right\} \tag{4.7} $$

Now the total rotor MMF can be calculated by multiplying the coil winding function (4.6) with the coil current (4.7) and then summing the contribution of all r coils.

$$ \Theta_\mathrm{f} = \sum_\mathrm{r} W_\mathrm{Fr} I_\mathrm{Fr} = \frac{N_\mathrm{cf}}{\pi} I_\mathrm{fm} \mathrm{Re}\left\{ \frac{1}{\mathrm{j}} \sum_{\mu=(1+2\mathrm{b})\mathrm{p_m}} \frac{{}^{\mu}k_\mathrm{wf}}{\mu} \mathrm{e}^{\mathrm{j}\mu\varphi_\mathrm{f}} \right\} + \frac{N_\mathrm{cf}}{\pi} I_\mathrm{fh} \mathrm{Re}\left\{ \frac{1}{\mathrm{j}} \sum_{\mu=(1+2\mathrm{b})\mathrm{p_h}} \frac{{}^{\mu}k_\mathrm{wf}}{\mu} \mathrm{e}^{\mathrm{j}\mu\varphi_\mathrm{f}} \right\} \tag{4.8} $$

This procedure is simply a mathematical evaluation of the phasor star for each harmonic μ so that after multiplication only odd multiples $1 + 2b$, $b = 0, \pm1, \pm2, ...$ of the base pole pairs p_m and p_h occur in the MMF spectrum. It can be seen that the MMF can be decoupled into a contribution with a fundamental pole-pair number p_m excited by a current I_fm and a fundamental pole-pair number p_h excited by a current I_fh. This is highlighted in Fig. 4.4.

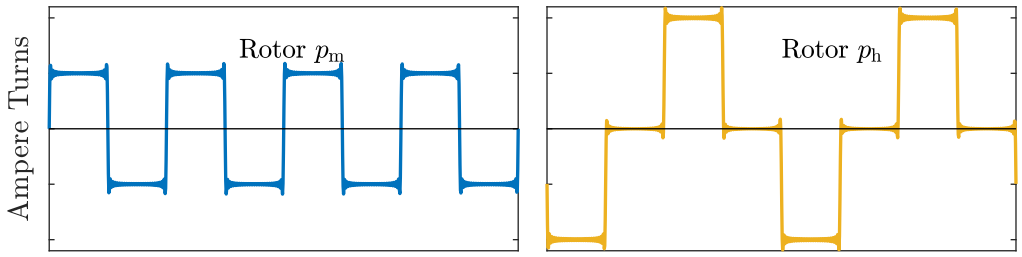

Figure 4.4: Rotor MMFs when the coils are DC-excited only by I_fm (left) or I_fh (right). The coil currents are identical with the current arrows depicted in Fig. 4.8.

4.2.2 Stator Winding

Now a stator winding which can also generate the pole-pair ratio $p_\mathrm{h} : p_\mathrm{m} = 1 : 2$ must be found. In [35] the author investigated the use of PPM in a five-phase HESM that can produce the pole pair $p_\mathrm{m} = 4$ and $p_\mathrm{h} = 2$ simultaneously. A corresponding five-phase inverter was then used to feed both current components into the stator winding. However, a significant drawback of this approach is that conventionally designed WRSM windings do not produce even harmonics. Hence, in [35] the coil pitch was increased by 20% to generate both odd and even harmonics. This decreases the p_m pole-pair machine performance, because of a higher end-winding length (and thus more copper), higher harmonic leakage and decreased fundamental winding factor. This contradicts the design goals which demand no deterioration of the p_m pole-pair machine. Hence, the PPM method is not ideal for this pole-pair ratio and thus abandoned here. Instead, the methodology used for the synthesis of the rotor winding is applied again.
First, each phase of a conventional three-phase WRSM stator winding is split up into its p_m coil groups. This is done exemplarily for a $q = 2$ slot-per-pole-per-phase, $p_\mathrm{m} = 4$ pole-pair winding as shown in Fig. 4.5a. As the coil pitch is the same as for the rotor coil shown in Fig. 4.2, the MMF of a single stator coil and its harmonic content are similar with the only difference being that the winding factor (4.4) has to be extended by the distribution factor

$$ {}^{v}k_\mathrm{ws} = \sin\left(v\frac{\pi}{2p_\mathrm{m}}\right)\frac{\sin\left(vq\frac{\pi}{Z_\mathrm{s}}\right)}{q\sin\left(v\frac{\pi}{Z_\mathrm{s}}\right)}. \tag{4.9} $$

After the coils of the three-phase stator winding have been identified and labeled according to Fig. 4.5a, the phasor star for the desired pole-pair numbers p_h and p_m phase and coil can be constructed (Fig. 4.5b). Firstly, the phasor star reveals that the coils can be summarized into groups of two which produce the same phasor, e.g. $\mathrm{U_{c2}}$-$\mathrm{U_{c4}}$ and $\mathrm{U_{c1}}$-$\mathrm{U_{c3}}$. Secondly, it can be seen that the phasors for $v = p_\mathrm{m} = 4$ produce a three-phase system when the current direction in all coils of a phase are connected in parallel or in series. This is no surprise as the coil groups have been obtained from a p_m pole-pair three-phase winding. However, in

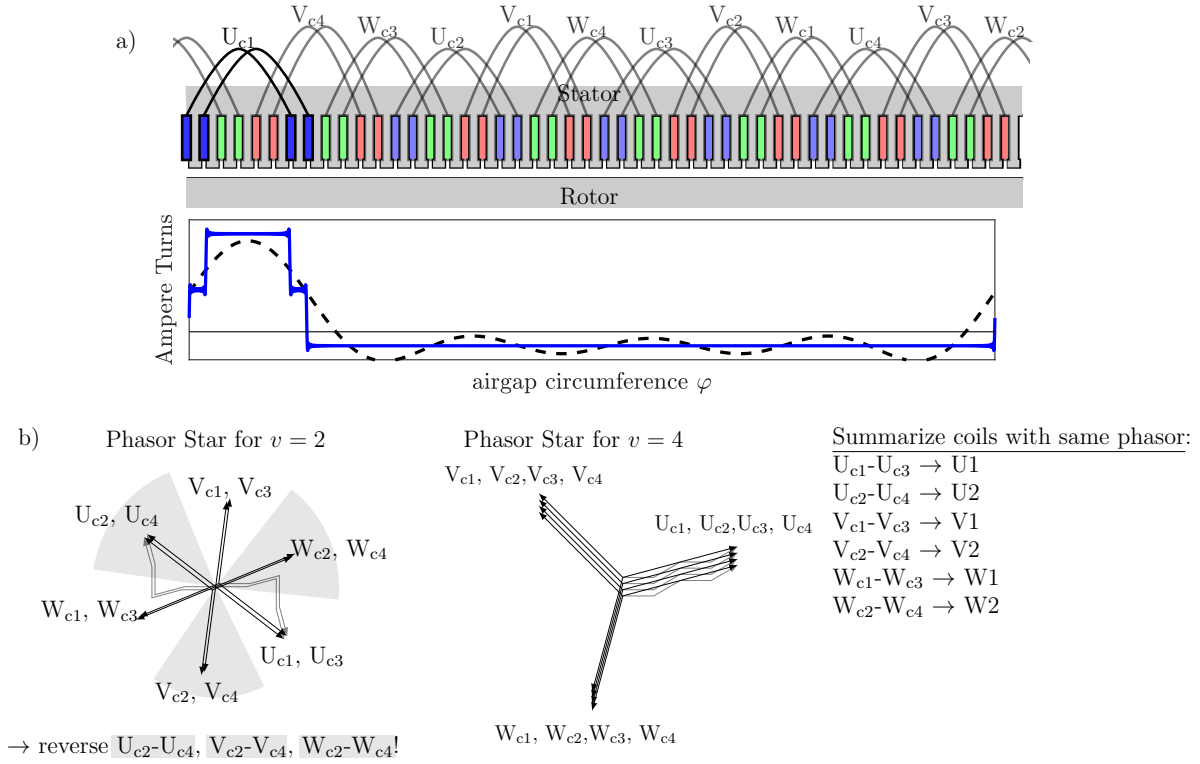

Figure 4.5: Coil notation, exemplary coil MMF of U_{c1} and phasor Star for all coil groups of the three phases of the stator winding for the two fundamental harmonics.

order to produce a three-phase system of pole pair $p_h = 2$ the current direction in the shaded coil group pairs of Fig. 4.5b needs to be reversed. Now the key idea is to regard each coil group U1,U2,V1,V2,W1,W2 as a separate phase and supply each phase with appropriate phase-shifts. In order to achieve this, each coil group is connected to its own inverter leg as in Fig. 4.6b. The novel concept is portrayed in unison with a conventional Dahlander pole-changing circuit to highlight the similarity. If the power switches S1 and S3 are closed (and S2 and S4 are open), the coils U1-U2 are connected in parallel. The (blue) current return path is over V1-V2 and W1-W2. If S1 and S4 are closed (and S2 and S3 closed), U1-U2 are connected in series and the (orange) current flows. In exactly the same way V1-V2 and W1-W2 can be connected in series and in parallel. It can be seen that this has the same effect as the Dahlander relay circuit Fig. 4.6a, but with an important distinction: As the current has a return path in the free-wheeling diodes (not depicted in Fig. 4.6b) of the inverter, switching between the coil arrangements can be done without arcing. Hence, the inverter half legs can be controlled via Pulse-Width-Modulation (PWM) and thus a combination of series and parallel connections can be adopted in a given PWM cycle to produce an averaged field that contains the pole pairs p_m and p_h. The schematic Fig. 4.6b can be simplified even further by rearranging the six coil groups into two three-phase systems U1, V1, W1 and U2, V2, W2. This has the added advantage that all zero system currents are eliminated. An interesting

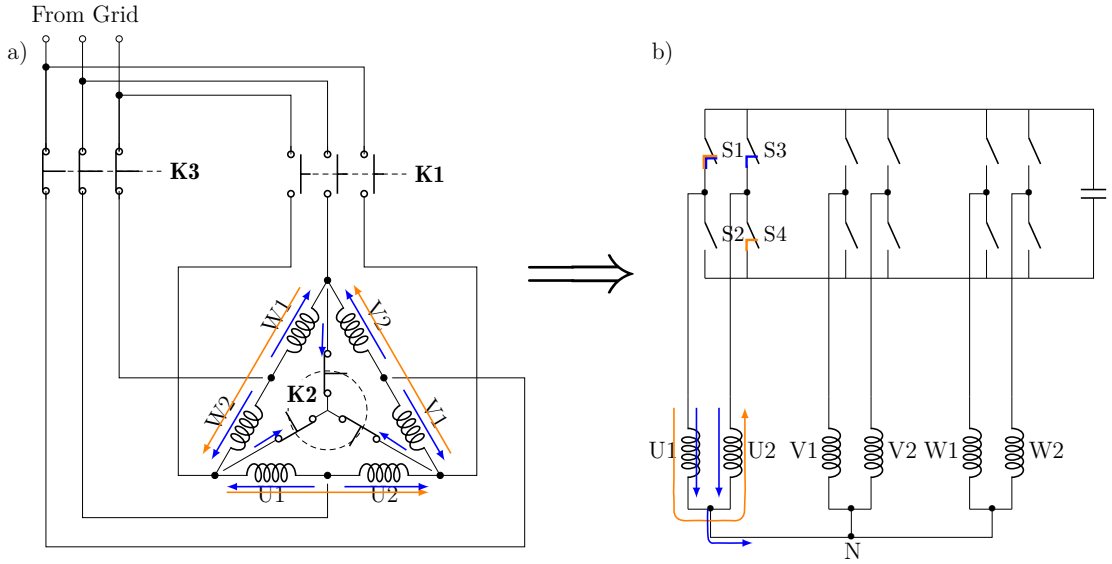

Figure 4.6: Similarity between Dahlander concept of Fig. 4.1 and novel HESM concept.

result of this approach is that this concept allows transferring any PAM concept to HESMs. This was demonstrated in [35] for a pole-pair ratio 2:3. The winding function of coil c=1,2 and phase k=1,2,3 (U,V,W) of the stator winding can be expressed in mathematical terms by a single expression

$$W_{\mathrm{kc}} = \frac{N_{\mathrm{c}}}{\pi}\mathrm{Re}\left\{\frac{1}{\mathrm{j}}\sum_{v=-\infty}^{\infty}\frac{{}^{v}k_{\mathrm{ws}}}{v}\cdot \mathrm{e}^{\mathrm{j}v\left(\varphi-(k-1)\frac{2\pi}{3p_{\mathrm{h}}}-(c-1)\frac{2\pi}{p_{\mathrm{m}}}\right)}\right\} \text{ with k} = 1,\ 2,\ 3 \tag{4.10}$$

with the respective number of stator coil series turns N_{c}. Each coil c of phase k is connected to its own inverter leg so that the following distinct currents can be injected

$$I_{\mathrm{kc}} = \mathrm{Re}\left\{\hat{I}_{\mathrm{cm}}\mathrm{e}^{\mathrm{j}(\omega+(k-1)\frac{2\pi}{3})} + \hat{I}_{\mathrm{ch}}\mathrm{e}^{\mathrm{j}(\omega+(k-1)\frac{2\pi}{3})+(c-1)\pi}\right\} \tag{4.11}$$

where $\hat{I}_{\mathrm{cm}}$ ($\hat{I}_{\mathrm{ch}}$) is the coil current related to pole-pair number p_{m} (p_{h}) and ω is a generic frequency. The resultant MMF is obtained after multiplication of (4.11) with (4.10) and then summing over all k phases and c coils

$$\Theta_{\mathrm{s}} = \frac{3}{\pi}N_{\mathrm{c}}\hat{I}_{\mathrm{cm}}\mathrm{Re}\left\{\frac{1}{\mathrm{j}}\sum_{v=(1+6b)p_{\mathrm{m}}}\frac{{}^{v}k_{\mathrm{ws}}}{v}\mathrm{e}^{\mathrm{j}(\omega t-v\varphi)}\right\} + \frac{3}{\pi}N_{\mathrm{c}}\hat{I}_{\mathrm{ch}}\mathrm{Re}\left\{\frac{1}{\mathrm{j}}\sum_{v=(1+6b)p_{\mathrm{h}}}\frac{{}^{v}k_{\mathrm{ws}}}{v}\mathrm{e}^{\mathrm{j}(\omega t-v\varphi)}\right\}. \tag{4.12}$$

Exemplary MMFs are shown in Fig. 4.7 for a single three-phase current distribution when either $\hat{I}_{\mathrm{cm}}$ or $\hat{I}_{\mathrm{ch}}$ are excited. It can be seen that the fundamental pole pair p_{m} and its related higher harmonics are produced solely by the current $\hat{I}_{\mathrm{cm}}$ and the pole pair p_{h} and its higher order fields only due to the current $\hat{I}_{\mathrm{ch}}$.

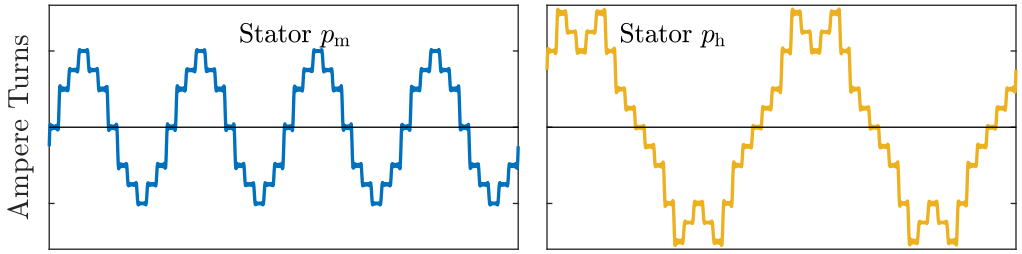

Figure 4.7: MMFs of stator for coil current $\hat{I}_{\mathrm{sm}}$ (left) and $\hat{I}_{\mathrm{sh}}$ (right) for one time instance. The coil currents are identical with the current arrows depicted in Fig. 4.8.

4.2.3 Decoupling

The most important result of the rotor MMF (4.8) and stator MMF (4.12) is that the total MMF can be split up into independent p_{m} and p_{h} pole-pair components with no common ordinal numbers υ or μ. If parasitical effects are neglected, this result allows treating the HESM just like two independent p_{m} and p_{h} pole-pair machines. Thus, the formulas and the operation modes derived in Section 3.2 for arbitrary p_{m} and p_{h} pole-pair machines are fully applicable to a HESM which uses the winding layouts presented above. This is why in the following section references to the results and relationships derived in Section 3.2 are made.

4.3 Novel Concept

Summarizing the results from Sections 4.2.1 and 4.2.2, the total HESM concept which is investigated in this dissertation can be portrayed schematically in Fig. 4.8. It can be seen that the conventional three-phase stator winding is separated into six independently-fed coil groups which form two independent three-phase systems. In order to supply the stator winding, the conventional three-phase inverter must be replaced with two three-phase inverters rated for half the current. Analogously, the field winding is divided into the four-coil two-port network in Fig. 4.3e. It can be observed that the p_{h} pole-pair terminals of the field winding do not couple directly to the p_{m} pole-pair terminals through the diode bridge rectifier. Instead, a DCDC converter is connected after the rectifier.
This DCDC converter is a conventional synchronous buck converter with a symmetrical output portrayed in Fig. 4.9. The converter is necessary to adjust the load resistance of the diode rectifier. To understand this, it was shown in (3.44) that the efficiency of the rotor winding depends on the ratio of the p_{h} to the p_{m} pole-pair terminal resistance. For the

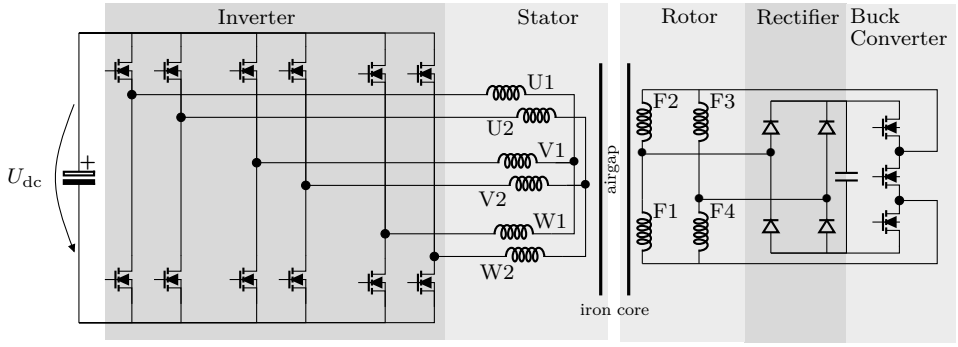

Figure 4.8: Novel HESM concept with drive electronics and exemplary current directions of the p_m (p_h) pole-pair machine denoted by blue (orange) arrows. Corresponding MMFs for the current arrows are plotted in Figs. 4.4 and 4.7.

proposed HESM concept these resistances are the same ($R_{fh} = R_{fm}$) because from the perspective of both terminals two (identical) rotor coils are in series and two in parallel. Thus, without any load resistance adjustment, the rotor winding efficiency would be $\eta_r \approx 50\%$ and no benefit would be obtained out of the combined winding utilization. The introduction of the buck converter operating with a duty cycle D can adjust the effective load resistance to R_{fm}/D^2 such that the efficiency after rectifier and buck converter yields (compare (3.44))

$$\eta_r = \frac{1}{1 + \frac{\pi^2}{8}\frac{R_{fh}}{R_{fm}}D^2} = \frac{1}{1 + \frac{\pi^2}{8}D^2}. \tag{4.13}$$

An important result is that with a sufficiently low duty cycle D, the efficiency of the rotor winding becomes very high, i.e. $\eta_r \approx 99\,\%$ for $D = 10\%$ which is close to the optimal value adopted in this work. The adjustment of the load resistance via D only has to be done once à priori so that no communication with the rotor winding during operation is required. The explanation of the **differential** output of the buck converter topology in Fig. 4.8 is explained in detail in Section 5.1. While it should be remarked that the existence of active switches

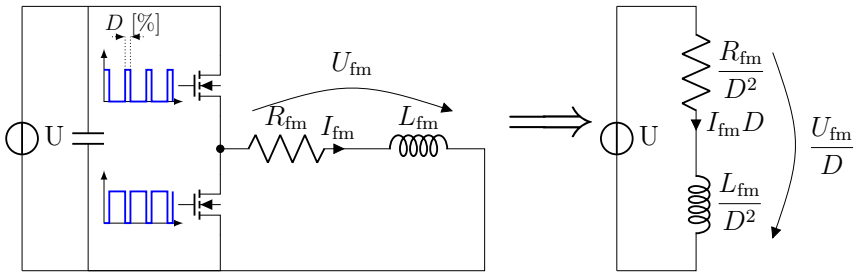

Figure 4.9: Equivalent Circuit of synchronous buck converter with p_m pole-pair field winding as output inductor referred to primary side [36].

in the synchronous buck converter is problematic from a reliability and thermal perspective, an adjustment of the load impedance via a buck converter has also been reported [13] in the literature on external rotating exciters.

4.3.1 Analysis of the Pole-Pair Numbers

When the winding configurations in Section 4.2.1 and 4.2.2 are adopted, a HESM behaving as two independently controllable p_m and p_h pole-pair machines is obtained. In order to assess the quality of the HESM design, in Tab. 4.2 the performance of the p_h pole-pair machine with respect to the p_m pole-pair machine is analyzed. In the first part of Tab. 4.2, the machine parameters are specified by taking into account the respective parallel and series coil connections when pole pair p_m or p_h is excited. It should be noted that the stator coil groups are not actually physically connected in series or parallel, but the current directions set by the inverter **behave** just as a parallel or series connected winding. In the second part of Tab. 4.2, the parameters are used to evaluate the inductances, torque capability and flux density levels of the p_h pole-pair machine if it were operated as a WRSM (torque-production). All geometric dimensions are identical for both machines so that they differ mainly in their winding factors, coil currents and number of series turns. The main benefit of the combined winding usage is that the coil currents in p_h pole-pair connection can be as high as in p_m pole-pair machine connection because they share the entire copper. This is why the p_h pole-pair machine has the same torque capability and voltage demand as the main p_m pole-pair machine if the same current densities (= coil currents) in the stator and field winding are used (and reluctance is neglected). This is a very good result considering that the p_h pole-pair machine is designed as a compromise around the constraints of the p_m pole-pair machine.
However, the flux densities in the p_h pole-pair machine reveal an important limitation: At rated torque a 41 % higher airgap flux and a 180 % larger yoke flux occur. This is due to the fact that in radial flux synchronous machines the inner stator diameter and the airgap between stator and rotor generally increase with higher pole-pair numbers [27]. This means that an optimally designed p_h pole-pair synchronous machine would in theory have a smaller inner stator diameter and a larger airgap than a p_m pole-pair machine. However, in the HESM the p_h pole-pair machine geometry is determined à priori by the p_m pole-pair machine design which explains the larger airgap flux density. Furthermore, the lower pole-pair number $p_\mathrm{h} = p_\mathrm{m}/2$ directly affects the flux per pole. A machine designed for a higher pole-pair number p_m always has a lower flux (per pole) in the stator and rotor yoke (at the same airgap flux density) which allows reducing the yoke height. As the yoke heights in the HESM are designed for the larger p_m pole-pair number, excessive yoke saturation occurs when the lower p_h pole-pair number is excited. While the higher core saturation is problematic, the p_h pole-pair machine currents required for harmonic excitation are far below the rated coil current which somewhat counteracts this problem.

Table 4.2: Comparison between p_m and p_h pole-pair machine if both are operated as a WRSM at the same current density

Parameter		Main machine (p_m)	Harmonic machine (p_h)
Stator Connection		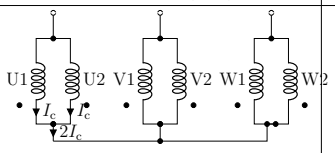	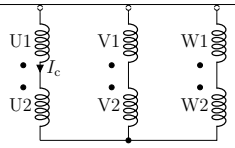
Stator series turns	N_sx	N_c (2 coils parallel)	$2 \cdot N_\mathrm{c}$ (2 coils in series)
cont. stator current	I_sx	$2 \cdot I_\mathrm{c}$	I_c
Rotor Connection		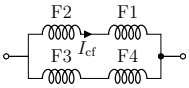	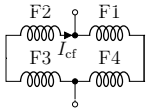
Rotor series turns	N_fx	N_cf (2 parallel, 2 series)	N_cf (2 parallel, 2 series)
cont. rotor current	I_fx	$2 \cdot I_\mathrm{cf}$	$2 \cdot I_\mathrm{cf}$
winding factor	${}^1k_\mathrm{wsx}$, ${}^1k_\mathrm{wfx}$	≈ 1	≈ 0.7071
Geometry parameters	r, l_Fe, h_δ, A_cu	identical	
Operational Parameters			
Self Inductance	$L_\mathrm{dx} \sim \frac{N_\mathrm{Sx}^2 k_\mathrm{ws,x}^2}{p_\mathrm{x}^2}$	L_dm	$8 \cdot L_\mathrm{dm}$
Mutual Inductance	$L_\mathrm{dfx} \sim \frac{N_\mathrm{Sx} N_\mathrm{fx} k_\mathrm{ws,x} k_\mathrm{wf,x}}{p_\mathrm{x}^2}$	L_dfm	$4 \cdot L_\mathrm{dfm}$
Torque	$M_\mathrm{el,x} \sim p_\mathrm{x} L_\mathrm{dfx} I_\mathrm{Sx} I_\mathrm{fx}$	$M_\mathrm{el,m}$	$1 \cdot M_\mathrm{el,m}$
Airgap flux density	$\hat{B}_{\delta,\mathrm{x}} \sim \frac{N_\mathrm{Sx} I_\mathrm{Sx} k_\mathrm{ws,x}}{p_\mathrm{x}}$	$\hat{B}_{\delta,\mathrm{m}}$	$\sqrt{2} \cdot \hat{B}_{\delta,\mathrm{m}}$
Desired tooth Width	$b_\mathrm{tooth,x} \sim \hat{B}_{\delta,\mathrm{x}}$	$b_\mathrm{tooth,m}$	$\sqrt{2} \cdot b_\mathrm{tooth,m}$
Desired yoke Height	$h_\mathrm{yoke,x} \sim \frac{B_{\delta,\mathrm{x}}}{p_\mathrm{x}}$	$h_\mathrm{yoke,m}$	$2\sqrt{2} \cdot h_\mathrm{yoke,m}$

4.3.2 Criteria for HESM Design

An interesting observation from (3.37) and (3.43) is that the mechanical power equation (4.14) looks almost identical to the transferred power during harmonic excitation (4.15).

$$P_\mathrm{mech,h} = \omega_\mathrm{m} M_\mathrm{el,h} = p_\mathrm{h}\omega_\mathrm{m} \frac{3}{2} L_\mathrm{dfh} \underbrace{I_\mathrm{fh}}_{\mathrm{DC}} \hat{I}_\mathrm{sh} \sin(\theta_\mathrm{B}) \tag{4.14}$$

$$P_\mathrm{exc} = \frac{1}{2} \omega_\mathrm{exc} \frac{3}{2} L_\mathrm{dfh} \sqrt{2} \underbrace{\hat{I}_\mathrm{fh}}_{\mathrm{ac}} \sqrt{2} \underbrace{\hat{I}_\mathrm{sh}}_{=\hat{I}_\mathrm{dh}} \sin(\theta_\mathrm{I}) \tag{4.15}$$

The terms highlighted in blue denote the induced voltage from the rotor to the stator (back EMF) in the case of (4.14) and from the stator to the rotor due to harmonic excitation in case of (4.15). The factors $\sqrt{2}$ in (4.15) consider that for harmonic excitation only AC currents flow in the rotor winding and both forward and rotating stator fields are used (which halves the stator copper losses) so that the peak current amplitude can be increased at the same current density. θ_B is the torque angle between stator and rotor field and θ_I is the

current angle between the stator current I_{dh} and rotor current I_{fh}. The results show that the maximum transferrable power is proportional to the maximum torque capability ($\theta_{\mathrm{B}} = 90°$) of the p_{h} pole-pair machine if it were operated as a conventional WRSM

$$P_{\mathrm{exc}} = \frac{\omega_{\mathrm{exc}}}{p_{\mathrm{h}}} M_{\mathrm{el,h,max}} \sin\theta_{\mathrm{I}} \tag{4.16}$$

This means that the excitation power that can be transferred via the excitation system at a certain current loading is affected by the following parameters:

1. Effective excitation frequency: $\frac{\omega_{\mathrm{exc}}}{p_{\mathrm{h}}}$
2. Machine design: Better torque capability $M_{\mathrm{el,h,max}}$
3. Rotor winding: Decrease of reactive current (ideally $\theta_{\mathrm{I}} = 90°$)
4. Iron Saturation
5. Voltage Demand

The **first** dependency reveals that the choice of a small pole-pair number p_{h} is beneficial to achieving a smaller excitation frequency ω_{exc}. As derived in (3.39), the excitation frequency relates to the actual stator frequencies as a function of speed by

$$\omega_{+} = \omega_{\mathrm{exc}} + p_{\mathrm{h}}\omega_{\mathrm{m}} \qquad \omega_{-} = \omega_{\mathrm{exc}} - p_{\mathrm{h}}\omega_{\mathrm{m}} \quad . \tag{4.17}$$

A conventional drive inverter operating at e.g. 10 kHz as in electric vehicles can only realize fundamental frequencies up to ~ 1 kHz. This means that the maximum excitation frequency f_{exc} is limited by the highest fundamental frequency of the HESM. The dominant frequency component in the relevant speed region is the forward rotating field of frequency f_{+} related to the p_{h} pole-pair machine. Furthermore, large excitation frequencies are infeasible because they cause larger iron losses. Note that in the previous sections the radial frequencies have been used. The frequency values used here can be obtained from the radial frequencies using the well-known expression $\omega = 2\pi f$.

The improvement of the **second** dependency is the main motivation for the combined winding usage performed in Sections 4.2.1 and 4.2.2: The high torque capability of the p_{h} pole-pair machine is **only** possible, because the p_{h} pole-pair machine shares its current paths with the copper conductors designed for the far higher ampere turns of the p_{m} pole-pair machine. The higher copper volume coincides with significantly lower copper losses in the p_{h} pole-pair machine.
The **third** dependency relates to the reactive power demand of the rotor winding. Before the induced voltage appears at the rectifier terminals a voltage drop over the self-inductance L_{fh} occurs (see Fig. 3.1), which is the main reason for a high reactive current (= low θ_{I}). The self-inductance can only be reduced by decreasing the leakage component or increasing the pole-pair number p_{h}, which contradicts the preceding two demands for a small p_{h}. The

fourth and **fifth** dependencies are limitations that constrain the previous three dependencies. A HESM with a low p_h, a high torque capability $M_\mathrm{el,h,max}$ and a high $\theta_\mathrm{I} \to 90°$, but with excessive core saturation and voltage demand, is not feasible.
From these design criteria, the following preliminary evaluation of the proposed HESM concept can be made: The choice of pole-pair number $p_\mathrm{h} = \frac{p_\mathrm{m}}{2}$ and the high torque capability $M_\mathrm{el,h,max}$ are favorable. A minimization of the rotor leakage inductance can only be achieved by rotor geometry optimization. A major problem that can be predicted from Tab. 4.2 is the high additional flux density due to p_h pole-pair currents in the machine iron. This is why Chapter 8 is devoted to the iron losses. Furthermore, in Chapter 9 special attention to the voltage demand is paid by investigating the torque-speed curve.

Chapter 5

HESM Machine Model

In this chapter, an analytical model for the transient analysis of the HESM concept presented in the previous chapter is derived. The deduction of a machine model starts from the actual machine windings which are connected to the power electronics, i.e. the three stator phases U, V, W (denoted in the same order as $k = 1, 2, 3$) split into two coils ($c = 1, 2$) each and the four rotor coils F1, F2, F3, F4 (referred to in the same order as $r = 1, 2, 3, 4$). Each coil is modelled as a resistor in series with an inductor

$$U = RI + \frac{\mathrm{d}\Psi}{\mathrm{d}t}. \tag{5.1}$$

If more than one coil is present, the voltages and currents in (5.1) become vectors and the resistance and inductor become matrices. Vectors and matrices are henceforth denoted in bold. Thus, in phase representation (denoted with superscript ph), the full-order model of the HESM is modelled with the voltage equation

$$\underbrace{\left[\begin{array}{c}\mathbf{U_{S,ph}}\\\hline\mathbf{U_{F,ph}}\end{array}\right]}_{\mathbf{U_{ph}}} = \underbrace{\left[\begin{array}{c|c}{}^{(\mathbf{ph})}\mathbf{R_s} & \mathbf{0}\\\hline\mathbf{0} & {}^{(\mathbf{ph})}\mathbf{R_f}\end{array}\right]}_{\mathbf{R_{ph}}}\underbrace{\left[\begin{array}{c}\mathbf{I_{S,ph}}\\\hline\mathbf{I_{F,ph}}\end{array}\right]}_{\mathbf{I_{ph}}} + \frac{\mathrm{d}}{\mathrm{d}t}\left(\underbrace{\left[\begin{array}{c|c}{}^{(\mathbf{ph})}\mathbf{L_{s,s}} & {}^{(\mathbf{ph})}\mathbf{L_{s,f}}\\\hline{}^{(\mathbf{ph})}\mathbf{L_{f,s}} & {}^{(\mathbf{ph})}\mathbf{L_{f,f}}\end{array}\right]}_{\mathbf{L_{ph}}}\left[\begin{array}{c}\mathbf{I_{S,ph}}\\\hline\mathbf{I_{F,ph}}\end{array}\right]\right) \tag{5.2}$$

where values in bold denote matrices. The voltage and current vectors as well as resistance matrices are

$$\mathbf{I_{S,ph}} = \begin{bmatrix} I_{\mathrm{U1}} \\ I_{\mathrm{U2}} \\ I_{\mathrm{V1}} \\ I_{\mathrm{V2}} \\ I_{\mathrm{W1}} \\ I_{\mathrm{W2}} \end{bmatrix} \quad \mathbf{U_{S,ph}} = \begin{bmatrix} U_{\mathrm{U1}} \\ U_{\mathrm{U2}} \\ U_{\mathrm{V1}} \\ U_{\mathrm{V2}} \\ U_{\mathrm{W1}} \\ U_{\mathrm{W2}} \end{bmatrix} \quad \mathbf{I_{F,ph}} = \begin{bmatrix} I_{\mathrm{F1}} \\ I_{\mathrm{F2}} \\ I_{\mathrm{F3}} \\ I_{\mathrm{F4}} \end{bmatrix} \quad \mathbf{U_{F,ph}} = \begin{bmatrix} U_{\mathrm{F1}} \\ U_{\mathrm{F2}} \\ U_{\mathrm{F3}} \\ U_{\mathrm{F4}} \end{bmatrix} \quad \begin{aligned} {}^{(\mathbf{ph})}\mathbf{R_s} &= \mathrm{diag}(R_{\mathrm{c}}) \\ {}^{(\mathbf{ph})}\mathbf{R_f} &= \mathrm{diag}(R_{\mathrm{cf}}) \end{aligned}$$

where R_c (R_cf) are the coil resistances of the stator (rotor) winding. Likewise, the inductance matrices consist of the mutual inductances between two coils

$$ {}^{(\mathbf{ph})}\mathbf{L}_{\mathbf{f,f}} = \begin{bmatrix} L_{\mathrm{F1,F1}} & L_{\mathrm{F1,F2}} & L_{\mathrm{F1,F3}} & L_{\mathrm{F1,F4}} \\ L_{\mathrm{F2,F1}} & L_{\mathrm{F2,F2}} & L_{\mathrm{F2,F3}} & L_{\mathrm{F2,F4}} \\ L_{\mathrm{F3,F1}} & L_{\mathrm{F3,F2}} & L_{\mathrm{F3,F3}} & L_{\mathrm{F3,F4}} \\ L_{\mathrm{F4,F1}} & L_{\mathrm{F4,F2}} & L_{\mathrm{F4,F3}} & L_{\mathrm{F4,F4}} \end{bmatrix} \qquad {}^{(\mathbf{ph})}\mathbf{L}_{\mathbf{s,f}} = \begin{bmatrix} L_{\mathrm{U1,F1}} & L_{\mathrm{U1,F2}} & L_{\mathrm{U1,F3}} & L_{\mathrm{U1,F4}} \\ L_{\mathrm{U2,F1}} & L_{\mathrm{U2,F2}} & L_{\mathrm{U2,F3}} & L_{\mathrm{U2,F4}} \\ L_{\mathrm{V1,F1}} & L_{\mathrm{V1,F2}} & L_{\mathrm{V1,F3}} & L_{\mathrm{V1,F4}} \\ L_{\mathrm{V2,F1}} & L_{\mathrm{V2,F2}} & L_{\mathrm{V2,F3}} & L_{\mathrm{V2,F4}} \\ L_{\mathrm{W1,F1}} & L_{\mathrm{W1,F2}} & L_{\mathrm{W1,F3}} & L_{\mathrm{W1,F4}} \\ L_{\mathrm{W2,F1}} & L_{\mathrm{W2,F2}} & L_{\mathrm{W2,F3}} & L_{\mathrm{W2,F4}} \end{bmatrix} $$

$$ {}^{(\mathbf{ph})}\mathbf{L}_{\mathbf{s,s}} = \begin{bmatrix} L_{\mathrm{U1,U1}} & L_{\mathrm{U1,U2}} & L_{\mathrm{U1,V1}} & L_{\mathrm{U1,V2}} & L_{\mathrm{U1,W1}} & L_{\mathrm{U1,W2}} \\ L_{\mathrm{U2,U1}} & L_{\mathrm{U2,U2}} & L_{\mathrm{U2,V1}} & L_{\mathrm{U2,V2}} & L_{\mathrm{U2,W1}} & L_{\mathrm{U2,W2}} \\ L_{\mathrm{V1,U1}} & L_{\mathrm{V1,U2}} & L_{\mathrm{V1,V1}} & L_{\mathrm{V1,V2}} & L_{\mathrm{V1,W1}} & L_{\mathrm{V1,W2}} \\ L_{\mathrm{V2,U1}} & L_{\mathrm{V2,U2}} & L_{\mathrm{V2,V1}} & L_{\mathrm{V2,V2}} & L_{\mathrm{V2,W1}} & L_{\mathrm{V2,W2}} \\ L_{\mathrm{W1,U1}} & L_{\mathrm{W1,U2}} & L_{\mathrm{W1,V1}} & L_{\mathrm{W1,V2}} & L_{\mathrm{W1,W1}} & L_{\mathrm{W1,W2}} \\ L_{\mathrm{W2,U1}} & L_{\mathrm{W2,U2}} & L_{\mathrm{W2,V1}} & L_{\mathrm{W2,V2}} & L_{\mathrm{W2,W1}} & L_{\mathrm{W2,W2}} \end{bmatrix} \qquad {}^{(\mathbf{ph})}\mathbf{L}_{\mathbf{f,s}} = {}^{(\mathbf{ph})}\mathbf{L}_{\mathbf{s,s}}^{\mathrm{T}} $$

Now all elements in the matrices are parametrized based on the first armature reaction starting from the permeance waves (3.12) and winding functions (4.6) and (4.10). A complete derivation is omitted here, because the approach has already been applied extensively in Chapter 3. Only the fundamentals of the p_h and p_m pole-pair machine and the first reluctance harmonic ($n_\mathrm{f} = 0, \pm 1$) are taken into account. It should be noted that for the mutual inductances reciprocity is given so that $L_{\mathrm{x,y}} = L_{\mathrm{y,x}}$.
The elements of ${}^{(\mathbf{ph})}\mathbf{L}_{\mathbf{s,s}}$ are filled with the mutual inductance between coil $c = 1, 2$ of phase $k = 1, 2, 3$ (U, V, W) and coil $d = 1, 2$ of phase $j = 1, 2, 3$ (U, V, W)

$$ \begin{aligned} L_{\mathrm{kc,jd}} = L_{\mu\mathrm{m}} \cos\left((j-k)\frac{4\pi}{3}\right) + L_{\mu\mathrm{h}} \cos\left((j-k)\frac{2\pi}{3} + (d-c)\pi\right) \\ + L_{\sim\mathrm{m}} \cos\left(2(p_\mathrm{m}\beta - (j+k-2)\frac{2\pi}{3}\right) \end{aligned} \tag{5.3} $$

$$ \text{with } L_{\mu\mathrm{m}} = r l_{\mathrm{Fe}} \frac{\mu_0}{k_\mathrm{c} h_\delta} \frac{4}{\pi} N_\mathrm{c}^2 \frac{k_{\mathrm{wsm}}^2}{p_\mathrm{m}^2} \qquad L_{\mu\mathrm{h}} = r l_{\mathrm{Fe}} \frac{\mu_0}{k_\mathrm{c} h_\delta} \frac{4}{\pi} N_\mathrm{c}^2 \frac{k_{\mathrm{wsh}}^2}{p_\mathrm{h}^2} $$

$$ L_{\sim\mathrm{m}} = r l_{\mathrm{Fe}} \frac{\mu_0}{k_{\mathrm{cs}} h_\delta} \frac{2}{\pi} N_\mathrm{c}^2 \, {}^1\Lambda_\mathrm{f} \frac{k_{\mathrm{wsm}}^2}{p_\mathrm{m}^2} $$

where $k_{\mathrm{cs}} = \frac{2}{{}^0\Lambda_\mathrm{s}}$ is the carter factor from the stator side and $k_\mathrm{c} = \frac{4}{{}^0\Lambda_\mathrm{s} \, {}^0\Lambda_\mathrm{f}}$ is the double-sided carter factor. (5.3) reveals that the inductances depend on a contribution from the p_m and p_h pole-pair machine. The blue term denotes the influence of reluctance which only occurs for the p_m pole-pair machine and is dependent on the rotor position (see also Section 7.2.4). Analogously, the inductance matrix ${}^{(\mathbf{ph})}\mathbf{L}_{\mathbf{f,f}}$ is filled with the mutual inductances between

coil $r = 1, 2, 3, 4$ (F1, F2, F3, F4) and coil $t = 1, 2, 3, 4$ (F1, F2, F3, F4) of the field winding

$$L_{\mathrm{r,t}} = L'_{\mu 0} \cos\left((t-r)\frac{\pi}{2}\right) + L'_{\mu \mathrm{m}} + L'_{\mu \mathrm{h}} \cos\left((t-r)\pi\right) \tag{5.4}$$

$$\text{with } L'_{\mu 0} = r l_{\mathrm{Fe}} \frac{\mu_0}{k_{\mathrm{c}} h_\delta} \frac{4}{\pi} N_{\mathrm{cf}}^2 \frac{{}^{p_0}k_{\mathrm{wf}}^2}{p_0^2} \qquad L'_{\mu \mathrm{m}} = r l_{\mathrm{Fe}} \frac{\mu_0}{h_\delta} \frac{4}{\pi} N_{\mathrm{cf}}^2 \frac{k_{\mathrm{wfm}}^2}{p_{\mathrm{m}}^2} \left(\frac{1}{k_{\mathrm{c}}} + \frac{{}^1\Lambda_{\mathrm{f}}}{2k_{\mathrm{cs}}}\right)$$
$$L'_{\mu \mathrm{h}} = r l_{\mathrm{Fe}} \frac{\mu_0}{k_{\mathrm{c}} h_\delta} \frac{4}{\pi} N_{\mathrm{cf}}^2 \frac{k_{\mathrm{wfh}}^2}{p_{\mathrm{h}}^2}$$

It can be observed that the inductances are constant and depend on the contribution due to the p_{m} and p_{h} machine as well as pole pair $p_0 = 1$. Analogously, the inductance matrices ${}^{(\mathbf{ph})}\mathbf{L}_{\mathbf{s,f}}$ and ${}^{(\mathbf{ph})}\mathbf{L}_{\mathbf{f,s}}$ contain the mutual inductances between coil $c = 1, 2$ of stator phase $k = 1, 2, 3$ (U, V, W) and rotor coil $r = 1, 2, 3, 4$ (F1, F2, F3, F4)

$$L_{\mathrm{r,kc}} = L''_{\mu \mathrm{m}} \cos\left(p_{\mathrm{m}}\beta + (k-1)\frac{4\pi}{3}\right) + L''_{\mu \mathrm{h}} \cos\left(p_{\mathrm{h}}\beta + (k-1)\frac{2\pi}{3} + (c-r)\pi\right) \tag{5.5}$$

$$\text{with } L''_{\mu \mathrm{m}} = r l_{\mathrm{Fe}} \frac{\mu_0}{h_\delta} \frac{4}{\pi} N_{\mathrm{c}} N_{\mathrm{cf}} \frac{k_{\mathrm{wsm}}\, k_{\mathrm{wfm}}}{p_{\mathrm{m}}^2} \left(\frac{1}{k_{\mathrm{c}}} + \frac{{}^1\Lambda_{\mathrm{f}}}{2k_{\mathrm{cs}}}\right) \qquad L''_{\mu \mathrm{h}} = r l_{\mathrm{Fe}} \frac{\mu_0}{k_{\mathrm{c}} h_\delta} \frac{4}{\pi} N_{\mathrm{c}} N_{\mathrm{cf}} \frac{k_{\mathrm{wsh}}\, k_{\mathrm{wfh}}}{p_{\mathrm{h}}^2}$$

which is dependent on the rotor position and also consists of a p_{m} and p_{h} pole-pair component. Reviewing the results from (5.3) to (5.5), it can be observed that handling the phase equations is cumbersome because the information about the two pole-pairs p_{m} and p_{h} is hidden in the asymmetry of the inductances. Conventional dq modelling strategies for synchronous machines cannot be applied to the HESM in phase representation unless a transformation is applied which decouples the p_{m} and p_{h} components.

5.1 Pole-Pair Coordinate System

For this reason, the *pole-pair coordinate system* (superscript pp) is introduced which transforms the phase values into two decoupled p_{m} and p_{h} pole-pair synchronous machines. From the single-phase equivalent circuit Fig. 5.1 of two corresponding coil groups, the stator transformation matrices (5.6) can immediately be derived which can be applied to each of the 2 coils of the three phases U, V, W.

$$\begin{bmatrix} U_{1\mathrm{x}} \\ U_{2\mathrm{x}} \end{bmatrix} = \begin{bmatrix} 1 & 0.5 \\ 1 & -0.5 \end{bmatrix} \begin{bmatrix} U_{\mathrm{xm}} \\ U_{\mathrm{xh}} \end{bmatrix} \quad \begin{bmatrix} I_{\mathrm{x1}} \\ I_{\mathrm{x2}} \end{bmatrix} = \begin{bmatrix} 0.5 & 1 \\ 0.5 & -1 \end{bmatrix} \begin{bmatrix} I_{\mathrm{xm}} \\ I_{\mathrm{xh}} \end{bmatrix} \quad \text{with } x \in \{\mathrm{U,V,W}\} \tag{5.6}$$

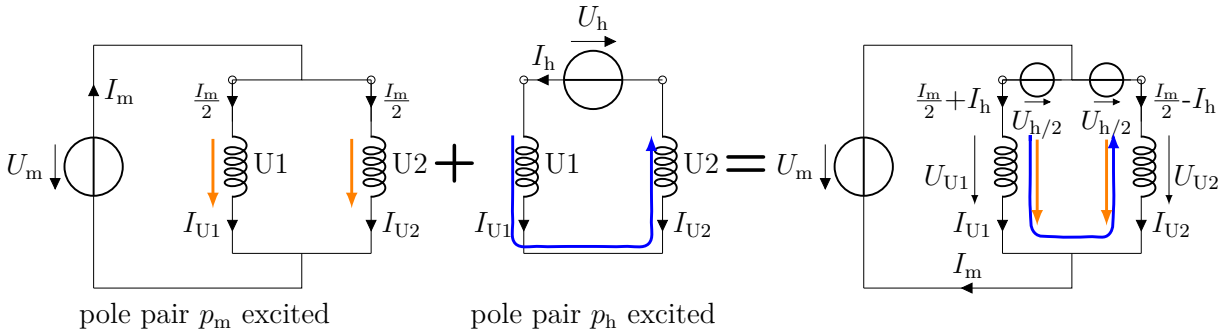

Figure 5.1: Derivation of stator transformation from single-phase equivalent circuit.

Thus, all phase currents (voltages) can be transformed into pole-pair coordinates with the transformation $\mathbf{T_{sI}}$ ($\mathbf{T_{sU}}$) by applying the phase transformations (5.6) to each phase U,V,W.

$$\underbrace{\left[\begin{array}{c} U_{\mathrm{Um}} \\ U_{\mathrm{Vm}} \\ U_{\mathrm{Wm}} \\ \hline U_{\mathrm{Uh}} \\ U_{\mathrm{Vh}} \\ U_{\mathrm{Wh}} \end{array}\right]}_{\mathbf{U_{S,pp}}} = \underbrace{\left[\begin{array}{cccccc} 0.5 & 0.5 & 0 & 0 & 0 & 0 \\ 0 & 0 & 0.5 & 0.5 & 0 & 0 \\ 0 & 0 & 0 & 0 & 0.5 & 0.5 \\ 1 & -1 & 0 & 0 & 0 & 0 \\ 0 & 0 & 1 & -1 & 0 & 0 \\ 0 & 0 & 0 & 0 & 1 & -1 \end{array}\right]}_{\mathbf{T_{sU}}} \left[\begin{array}{c} U_{\mathrm{U1}} \\ U_{\mathrm{U2}} \\ U_{\mathrm{V1}} \\ U_{\mathrm{V2}} \\ U_{\mathrm{W1}} \\ U_{\mathrm{W2}} \end{array}\right] \tag{5.7}$$

$$\underbrace{\left[\begin{array}{c} I_{\mathrm{Um}} \\ I_{\mathrm{Vm}} \\ I_{\mathrm{Wm}} \\ \hline I_{\mathrm{Uh}} \\ I_{\mathrm{Vh}} \\ I_{\mathrm{Wh}} \end{array}\right]}_{\mathbf{I_{S,pp}}} = \underbrace{\left[\begin{array}{cccccc} 1 & 1 & 0 & 0 & 0 & 0 \\ 0 & 0 & 1 & 1 & 0 & 0 \\ 0 & 0 & 0 & 0 & 1 & 1 \\ 0.5 & -0.5 & 0 & 0 & 0 & 0 \\ 0 & 0 & 0.5 & -0.5 & 0 & 0 \\ 0 & 0 & 0 & 0 & 0.5 & -0.5 \end{array}\right]}_{\mathbf{T_{sI}}} \left[\begin{array}{c} I_{\mathrm{U1}} \\ I_{\mathrm{U2}} \\ I_{\mathrm{V1}} \\ I_{\mathrm{V2}} \\ I_{\mathrm{W1}} \\ I_{\mathrm{W2}} \end{array}\right] \tag{5.8}$$

The subscripts Um, Vm and Wm denote the three-phase equivalent windings of the p_m pole-pair machine after transformation into pole-pair coordinates. Analogously, Uh, Vh and Wh describe the equivalent windings of the p_h pole-pair machine.
For the rotor inductance the p_m and p_h pole-pair information must be decoupled analogously, but here, a transformation matrix is more complicated since the four coil bridge configuration has four degrees of freedom and can excite the $p_0 = 1$st subharmonic if asymmetric currents flow. The search for an appropriate transformation matrix is identical with the

diagonalization of the inductance matrix ${}^{(\mathbf{ph})}\mathbf{L}_{\mathbf{f},\mathbf{f}}$ which, when evaluating (5.4), looks like

$$
{}^{(\mathbf{ph})}\mathbf{L}_{\mathbf{f},\mathbf{f}} = \begin{bmatrix} L_{\mathrm{ff}} & M_{\mathrm{f1}} & M_{\mathrm{f2}} & M_{\mathrm{f1}} \\ M_{\mathrm{f1}} & L_{\mathrm{ff}} & M_{\mathrm{f1}} & M_{\mathrm{f2}} \\ M_{\mathrm{f2}} & M_{\mathrm{f1}} & L_{\mathrm{ff}} & M_{\mathrm{f1}} \\ M_{\mathrm{f1}} & M_{\mathrm{f2}} & M_{\mathrm{f1}} & L_{\mathrm{ff}} \end{bmatrix} \quad \text{with} \quad \begin{aligned} L_{\mathrm{ff}} &= L'_{\mu 0} + L'_{\mu \mathrm{m}} + L'_{\mu \mathrm{h}} \\ M_{\mathrm{f1}} &= L'_{\mu \mathrm{m}} - L'_{\mu \mathrm{h}} \\ M_{\mathrm{f2}} &= -L'_{\mu 0} + L'_{\mu \mathrm{m}} + L'_{\mu \mathrm{h}} \end{aligned} \tag{5.9}
$$

A matrix $\mathbf{T_f}$ that diagonalizes ${}^{(\mathbf{ph})}\mathbf{L}_{\mathbf{f},\mathbf{f}}$ so that $\mathbf{T_f} \cdot {}^{(\mathbf{ph})}\mathbf{L}_{\mathbf{f},\mathbf{f}} \cdot \mathbf{T_f^{-1}} = \mathbf{I_{4x4}}$ (identity matrix) consists of the eigenvectors of ${}^{(\mathbf{ph})}\mathbf{L}_{\mathbf{f},\mathbf{f}}$. One suitable matrix $\mathbf{T_f}$ that transforms voltages **and** currents from phase coordinates into pole-pair coordinates is

$$
\mathbf{T_f} = \begin{bmatrix} 0.5 & 0.5 & 0.5 & 0.5 \\ -0.5 & 0.5 & -0.5 & 0.5 \\ -1 & 0 & 1 & 0 \\ 0 & -1 & 0 & 1 \end{bmatrix} \text{ so that } \underbrace{\begin{bmatrix} U_{\mathrm{fm}} \\ U_{\mathrm{fh}} \\ U_{\mathrm{xf1}} \\ U_{\mathrm{xf2}} \end{bmatrix}}_{\mathbf{U_{f,pp}}} = \mathbf{T_f} \begin{bmatrix} U_{\mathrm{F1}} \\ U_{\mathrm{F2}} \\ U_{\mathrm{F3}} \\ U_{\mathrm{F4}} \end{bmatrix}, \quad \underbrace{\begin{bmatrix} I_{\mathrm{fm}} \\ I_{\mathrm{fh}} \\ I_{\mathrm{xf1}} \\ I_{\mathrm{xf2}} \end{bmatrix}}_{\mathbf{U_{f,pp}}} = \mathbf{T_f} \begin{bmatrix} I_{\mathrm{F1}} \\ I_{\mathrm{F2}} \\ I_{\mathrm{F3}} \\ I_{\mathrm{F4}} \end{bmatrix}. \tag{5.10}
$$

The currents I_{fm} and I_{fh} are the field currents of pole pair p_{h} and p_{m}, respectively. The two additional degrees of freedom I_{xf1} and I_{xf2} describe unintended rotor currents as a consequence of asymmetric loading of the diode bridge. The corresponding voltages U_{xf1} und U_{xf2} drive these parasitic currents and must be suppressed. From (5.10) it can be observed that they become zero only if $U_{\mathrm{F1}} = U_{\mathrm{F3}}$ and $U_{\mathrm{F2}} = U_{\mathrm{F4}}$. This is highlighted by Fig. 5.2: For $U_{\mathrm{F2}} = U_{\mathrm{F4}}$ (and hence $U_{\mathrm{xf1}} = 0$) to be satisfied, the two red and blue branch voltages (5.11) must be equal. Thus, the diode voltage drop U_{D2} and U_{D4} must also be equal which is the case as they are either both blocking or both conducting. However, the buck converter voltage drop U_{top} – which is either conducting or blocking — must also have a counterpart U_{bot} in the lower path, otherwise a current I_{xf1} would be driven. This can only be realized by inserting a bottom switch. The voltage U_{xf2} is also suppressed if this configuration is adopted. With the differential output stage, the transformed windings xf1 and xf2 can be neglected and the rotor winding can be considered as two separate field windings of pole pair p_{m} and p_{h}. As a result, the HESM voltage equations in pp coordinates can be given

$$
\underbrace{\left[\begin{array}{c} \mathbf{U_{S,pp}} \\ \hline \mathbf{U_{f,pp}} \end{array}\right]}_{\mathbf{U}_{\mathrm{pp}}} = \left[\begin{array}{c|c} {}^{(\mathbf{pp})}\mathbf{R_s} & \mathbf{0} \\ \hline \mathbf{0} & {}^{(\mathbf{pp})}\mathbf{R_f} \end{array}\right] \underbrace{\left[\begin{array}{c} \mathbf{I_{S,pp}} \\ \hline \mathbf{I_{f,pp}} \end{array}\right]}_{\mathbf{I}_{\mathrm{pp}}} + \frac{\mathrm{d}}{\mathrm{d}t} \left(\underbrace{\left[\begin{array}{c|c} {}^{(\mathbf{pp})}\mathbf{L_{s,s}} & {}^{(\mathbf{pp})}\mathbf{L_{s,f}} \\ \hline {}^{(\mathbf{pp})}\mathbf{L_{f,s}} & {}^{(\mathbf{pp})}\mathbf{L_{f,f}} \end{array}\right]}_{\mathbf{L_{pp}}} \left[\begin{array}{c} \mathbf{I_{S,pp}} \\ \hline \mathbf{I_{f,pp}} \end{array}\right] \right) \tag{5.12}
$$

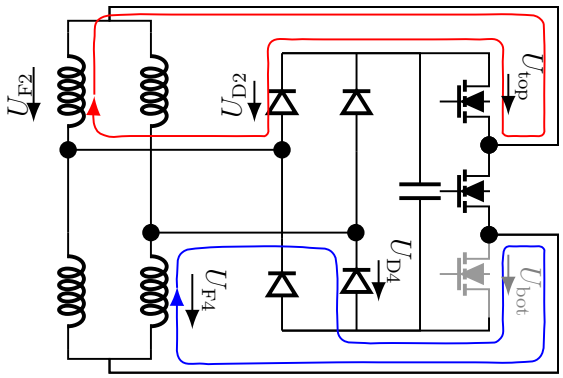

$$U_{F2} = -U_{top} + U_{D2}$$
$$U_{F4} = -U_{bot} + U_{D4} \tag{5.11}$$

Figure 5.2: Explanation for Differential buck converter.

with the matrices

$$\begin{aligned}
&{}^{(pp)}\mathbf{L}_{f,f} = \mathbf{T_f} \cdot {}^{(ph)}\mathbf{L}_{f,f} \cdot \mathbf{T_f^{-1}}, \quad {}^{(pp)}\mathbf{L}_{s,s} = \mathbf{T_{sU}} \cdot {}^{(ph)}\mathbf{L}_{s,s} \cdot \mathbf{T_{sI}^{-1}}, \quad {}^{(pp)}\mathbf{L}_{s,f} = \mathbf{T_{sU}} \cdot {}^{(ph)}\mathbf{L}_{s,f} \cdot \mathbf{T_f^{-1}} \\
&{}^{(pp)}\mathbf{L}_{f,s} = \mathbf{T_f} \cdot {}^{(ph)}\mathbf{L}_{f,s} \cdot \mathbf{T_{sI}^{-1}}, \quad {}^{(pp)}\mathbf{R}_{s} = \mathbf{T_{sU}} \cdot {}^{(ph)}\mathbf{R}_{s} \cdot \mathbf{T_{sI}^{-1}}, \quad {}^{(pp)}\mathbf{R}_{f} = \mathbf{T_f} \cdot {}^{(ph)}\mathbf{R}_{f} \cdot \mathbf{T_f^{-1}}
\end{aligned} \tag{5.13}$$

The matrix ${}^{(pp)}\mathbf{L}_{s,s}$ is arranged in 4 submatrices which contain the stator inductance matrix ${}^{(pp)}\mathbf{L}_{s,s}^{m,m}$ (${}^{(pp)}\mathbf{L}_{s,s}^{h,h}$) of the p_m (p_h) pole-pair machine and two parasitical inductance matrices ${}^{(pp)}\mathbf{L}_{s,s}^{h,m}$ and ${}^{(pp)}\mathbf{L}_{s,s}^{m,h}$ which denote coupling between the pole-pair numbers p_m and p_h:

$${}^{(pp)}\mathbf{L}_{s,s} = \left[\begin{array}{c|c} {}^{(pp)}\mathbf{L}_{s,s}^{m,m} & {}^{(pp)}\mathbf{L}_{s,s}^{m,h} \\ \hline {}^{(pp)}\mathbf{L}_{s,s}^{h,m} & {}^{(pp)}\mathbf{L}_{s,s}^{h,h} \end{array}\right] = \left[\begin{array}{ccc|ccc} L_{Um,Um} & L_{Um,Vm} & L_{Um,Wm} & L_{Um,Uh} & L_{Um,Vh} & L_{Um,Wh} \\ L_{Vm,Um} & L_{Vm,Vm} & L_{Vm,Wm} & L_{Vm,Uh} & L_{Vm,Vh} & L_{Vm,Wh} \\ L_{Wm,Um} & L_{Wm,Vm} & L_{Wm,Wm} & L_{Wm,Uh} & L_{Wm,Vh} & L_{Wm,Wh} \\ \hline L_{Uh,Um} & L_{Uh,Vm} & L_{Uh,Wm} & L_{Uh,Uh} & L_{Uh,Vh} & L_{Uh,Wh} \\ L_{Vh,Um} & L_{Vh,Vm} & L_{Vh,Wm} & L_{Vh,Uh} & L_{Vh,Vh} & L_{Vh,Wh} \\ L_{Wh,Um} & L_{Wh,Vm} & L_{Wh,Wm} & L_{Wh,Uh} & L_{Wh,Vh} & L_{Wh,Wh} \end{array}\right] \tag{5.14}$$

Coupling between two phases $k = 1,2,3$ (U,V,W) and $j = 1,2,3$ (U,V,W) of the same pole-pair number (index m for pole pair p_m and index h for pole pair p_h) is expressed by

$$L_{km,jm} = L_{\mu m} \cos\left((k-j)\frac{4\pi}{3}\right) + L_{m\sim} \cos\left(2(p_m\beta - (k+j-2)\frac{2\pi}{3})\right), \quad L_{kh,jh} = 4L_{\mu h} \cos\left((k-j)\frac{2\pi}{3}\right) \quad . \tag{5.15}$$

The elements highlighted in red denote coupling between pole-pairs p_m and p_h and are zero if the machine is ideal. Analogously, after performing the pp transformation the matrix ${}^{(pp)}\mathbf{L}_{f,s}$ is also arranged into the mutual inductance submatrices ${}^{(pp)}\mathbf{L}_{f,s}^{m,m}$ (${}^{(pp)}\mathbf{L}_{f,s}^{h,h}$) of the p_m (p_h) pole-pair machine as well as two parasitical matrices ${}^{(pp)}\mathbf{L}_{f,s}^{h,m}$, ${}^{(pp)}\mathbf{L}_{f,s}^{m,h}$ for coupling between pole pair p_m and p_h (5.16). Furthermore, coupling matrices from the p_m and p_h pole-pair stator winding to the virtual xf1 and xf2 rotor windings occur, but they are zero if the machine is unsaturated.

$$ {}^{(\mathbf{pp})}\mathbf{L}_{\mathbf{f,s}} = \left[\begin{array}{c|c} {}^{(\mathbf{pp})}\mathbf{L}_{\mathbf{f,s}}^{\mathrm{m,m}} & {}^{(\mathbf{pp})}\mathbf{L}_{\mathbf{f,s}}^{\mathrm{m,h}} \\ \hline {}^{(\mathbf{pp})}\mathbf{L}_{\mathbf{f,s}}^{\mathrm{h,m}} & {}^{(\mathbf{pp})}\mathbf{L}_{\mathbf{f,s}}^{\mathrm{h,h}} \\ \hline \mathbf{L}_{\mathbf{xf,f}}^{1,\mathrm{m}} & \mathbf{L}_{\mathbf{xf,f}}^{1,\mathrm{h}} \\ \mathbf{L}_{\mathbf{xf,f}}^{2,\mathrm{m}} & \mathbf{L}_{\mathbf{xf,f}}^{2,\mathrm{h}} \end{array}\right] = \left[\begin{array}{ccc|ccc} L_{\mathrm{Fm,Um}} & L_{\mathrm{Fm,Vm}} & L_{\mathrm{Fm,Wm}} & L_{\mathrm{Fm,Uh}} & L_{\mathrm{Fm,Vh}} & L_{\mathrm{Fm,Wh}} \\ \hline L_{\mathrm{Fh,Um}} & L_{\mathrm{Fh,Vm}} & L_{\mathrm{Fh,Wm}} & L_{\mathrm{Fh,Uh}} & L_{\mathrm{Fh,Vh}} & L_{\mathrm{Fh,Wh}} \\ \hline L_{\mathrm{xf1,Um}} & L_{\mathrm{xf1,Vm}} & L_{\mathrm{xf1,Wm}} & L_{\mathrm{xf1,Uh}} & L_{\mathrm{xf1,Vh}} & L_{\mathrm{xf1,Wh}} \\ L_{\mathrm{xf2,Um}} & L_{\mathrm{xf2,Vm}} & L_{\mathrm{xf2,Wm}} & L_{\mathrm{xf2,Uh}} & L_{\mathrm{xf2,Vh}} & L_{\mathrm{xf2,Wh}} \end{array}\right] \tag{5.16} $$

The non-zero elements of the matrix ${}^{(\mathbf{pp})}\mathbf{L}_{\mathbf{f,s}}$ contain the mutual inductances between phase $k = 1, 2, 3$ (U,V,W) and the rotor winding (f) where each stator and rotor winding either has a p_{m} **or** p_{h} pole-pair component

$$ L_{\mathrm{fm,km}} = 2L''_{\mu\mathrm{m}} \cos(p_{\mathrm{m}}\beta + (k-1)\frac{4\pi}{3}), \quad L_{\mathrm{fh,kh}} = 4L''_{\mu\mathrm{h}} \cos(p_{\mathrm{h}}\beta + (k-1)\frac{2\pi}{3}). \tag{5.17} $$

${}^{(\mathbf{pp})}\mathbf{L}_{\mathbf{f,f}}$, ${}^{(\mathbf{pp})}\mathbf{R}_{\mathbf{s}}$ and ${}^{(\mathbf{pp})}\mathbf{R}_{\mathbf{f}}$ are also diagonalized as a consequence of the transformation

$$ {}^{(\mathbf{pp})}\mathbf{L}_{\mathbf{f,f}} = \begin{bmatrix} 4L'_{\mu\mathrm{m}} & 0 & 0 & 0 \\ 0 & 4L'_{\mu\mathrm{h}} & 0 & 0 \\ 0 & 0 & L'_{\mu 0} & 0 \\ 0 & 0 & 0 & L'_{\mu 0} \end{bmatrix} \quad ,{}^{(\mathbf{pp})}\mathbf{R}_{\mathbf{f}} = {}^{(\mathbf{ph})}\mathbf{R}_{\mathbf{f}} \quad ,{}^{(\mathbf{pp})}\mathbf{R}_{\mathbf{s}} = \left[\begin{array}{c|c} \frac{R_{\mathrm{c}}}{2} \cdot \mathbf{I_{3x3}} & \mathbf{0_{3x3}} \\ \hline \mathbf{0_{3x3}} & 2R_{\mathrm{c}} \cdot \mathbf{I_{3x3}} \end{array}\right] \tag{5.18} $$

It can be seen that in pp coordinates the stator resistance $R_{\mathrm{sm}} = \frac{R_{\mathrm{c}}}{2}$ for the p_{m} pole-pair machine is not equal to the resistance $R_{\mathrm{sh}} = 2R_{\mathrm{c}}$ of the p_{h} pole-pair machine. After the transformations have been applied there is no more cross-coupling between the p_{m} pole-pair and p_{h} pole-pair machine. The equations are now identical with two independent WRSM which allows treatment with the dq transformation.

5.2 DQ Coordinate System

The voltage equations (5.12) are still difficult to deal with because the mutual inductance matrices ${}^{(\mathbf{ph})}\mathbf{L}_{\mathbf{s,f}}$, ${}^{(\mathbf{ph})}\mathbf{L}_{\mathbf{f,s}}$ (and ${}^{(\mathbf{ph})}\mathbf{L}_{\mathbf{s,s}}$ in case of reluctance) are angle-dependent. The well-known Two-Reaction Theory for synchronous machines [37] deals with this issue and transforms the pp coordinates into the dq coordinate system via the well-known dq transformation

$$ \mathbf{T}(\beta) = \frac{2}{3} \begin{bmatrix} \cos(\beta) & \cos(\beta - \frac{2\pi}{3}) & \cos(\beta + \frac{2\pi}{3}) \\ -\sin(\beta) & -\sin(\beta - \frac{2\pi}{3}) & -\sin(\beta + \frac{2\pi}{3}) \\ 0.5 & 0.5 & 0.5 \end{bmatrix} \quad . \tag{5.19} $$

However, (5.19) cannot be applied directly as the HESM voltage equations contain two different pole-pair numbers p_{m} and p_{h}. Instead, the dq transformation matrix $\mathbf{T_{dq}}$ for the

HESM must incorporate both ...

- a transformation $\mathbf{T_{dq,m}} = \mathbf{T}(p_\mathrm{m}\omega_\mathrm{m}t + \beta_{0\mathrm{m}})$ rotating at an angular frequency $p_\mathrm{m}\omega_\mathrm{m}$ and aligned with the d-axis of the p_m pole-pair d-axis through a phase shift $\beta_{0\mathrm{m}}$ and
- a transformation $\mathbf{T_{dq,h}} = \mathbf{T}(p_\mathrm{h}\omega_\mathrm{m}t + \beta_{0\mathrm{h}})$ rotating at an angular frequency $p_\mathrm{h}\omega_\mathrm{m}$ and aligned with the d-axis of the p_h pole-pair d-axis through a phase shift $\beta_{0\mathrm{h}}$.

Thus, the complete dq transformation matrix for both pole pairs yields

$$\underbrace{\left[\begin{array}{c} U_\mathrm{dm} \\ U_\mathrm{qm} \\ U_\mathrm{0m} \\ \hline U_\mathrm{dh} \\ U_\mathrm{qh} \\ U_\mathrm{0h} \end{array}\right]}_{\mathbf{U_{S,dq}}} = \mathbf{T_{dq}} \left[\begin{array}{c} U_\mathrm{Um} \\ U_\mathrm{Vm} \\ U_\mathrm{Wm} \\ U_\mathrm{Uh} \\ U_\mathrm{Vh} \\ U_\mathrm{Wh} \end{array}\right], \quad \underbrace{\left[\begin{array}{c} I_\mathrm{dm} \\ I_\mathrm{qm} \\ I_\mathrm{0m} \\ \hline I_\mathrm{dh} \\ I_\mathrm{qh} \\ I_\mathrm{0h} \end{array}\right]}_{\mathbf{I_{S,dq}}} = \mathbf{T_{dq}} \left[\begin{array}{c} I_\mathrm{Um} \\ I_\mathrm{Vm} \\ I_\mathrm{Wm} \\ I_\mathrm{Uh} \\ I_\mathrm{Vh} \\ I_\mathrm{Wh} \end{array}\right], \quad \mathbf{T_{dq}} = \left[\begin{array}{c|c} \mathbf{T_{dq,m}} & \mathbf{0_{3x3}} \\ \hline \mathbf{0_{3x3}} & \mathbf{T_{dq,h}} \end{array}\right] \tag{5.20}$$

where subscripts dm, qm, 0m (dh, qh, 0h) denote the d-axis, q-axis and zero-system voltages and currents of the p_m (p_h) pole-pair machine. Now the transformation $\mathbf{T_{dq}}$ is applied to the voltage equations in (5.12)

$$\begin{aligned} \mathbf{U_{S,dq}} = \;& \mathbf{T_{dq}} \cdot {}^{(\mathbf{pp})}\mathbf{R_s} \cdot \mathbf{T_{dq}^{-1}} \cdot \mathbf{I_{S,dq}} \;+\; \mathbf{T_{dq}} \cdot \frac{\mathrm{d}}{\mathrm{d}t}\left({}^{(\mathbf{pp})}\mathbf{L_{s,s}} \cdot \mathbf{I_{S,pp}}\right) \;+\; \mathbf{T_{dq}} \cdot \frac{\mathrm{d}}{\mathrm{d}t}\left({}^{(\mathbf{pp})}\mathbf{L_{s,f}} \cdot \mathbf{I_{f,pp}}\right) \\ \mathbf{U_{f,pp}} = \;& {}^{(\mathbf{pp})}\mathbf{R_f} \cdot \mathbf{I_{f,pp}} \;+\; {}^{(\mathbf{pp})}\mathbf{L_{f,f}} \cdot \frac{\mathrm{d}}{\mathrm{d}t}\mathbf{I_{f,pp}} \;+\; \frac{\mathrm{d}}{\mathrm{d}t}\left({}^{(\mathbf{pp})}\mathbf{L_{f,s}} \cdot \mathbf{I_{S,pp}}\right). \end{aligned} \tag{5.21}$$

Here, the time-dependence of the dq transformation $\mathbf{T_{dq}}(\beta(t))$ needs to be taken into account

$$\begin{aligned} \mathbf{T_{dq}} \cdot {}^{(\mathbf{pp})}\mathbf{R_s} \cdot \mathbf{T_{dq}^{-1}} &= {}^{(\mathbf{pp})}\mathbf{R_s} \quad . \\ \mathbf{T_{dq}} \cdot \frac{\mathrm{d}}{\mathrm{d}t}\left({}^{(\mathbf{pp})}\mathbf{L_{s,s}} \cdot \mathbf{I_{S,pp}}\right) &= \omega_\mathrm{m} \cdot \mathbf{J} \cdot {}^{(\mathbf{dq})}\mathbf{L_{s,s}} \cdot \mathbf{I_{S,dq}} \;+\; {}^{(\mathbf{dq})}\mathbf{L_{s,s}} \cdot \frac{\mathrm{d}}{\mathrm{d}t}\mathbf{I_{S,dq}} \\ \mathbf{T_{dq}} \cdot \frac{\mathrm{d}}{\mathrm{d}t}\left({}^{(\mathbf{pp})}\mathbf{L_{s,f}} \cdot \mathbf{I_{f,pp}}\right) &= \omega_\mathrm{m} \cdot \mathbf{J} \cdot {}^{(\mathbf{dq})}\mathbf{L_{s,f}} \cdot \mathbf{I_{S,dq}} \;+\; {}^{(\mathbf{dq})}\mathbf{L_{s,f}} \cdot \frac{\mathrm{d}}{\mathrm{d}t}\mathbf{I_{f,pp}} \\ \frac{\mathrm{d}}{\mathrm{d}t}\left({}^{(\mathbf{pp})}\mathbf{L_{f,s}} \cdot \mathbf{I_{S,pp}}\right) &= {}^{(\mathbf{dq})}\mathbf{L_{f,s}}\frac{\mathrm{d}}{\mathrm{d}t}\mathbf{I_{S,dq}} \end{aligned} \tag{5.22}$$

where $\dot{\beta} = \omega_\mathrm{m}$ is the rotational speed and

$$\mathbf{J} = \mathbf{T_{dq}} \left(\frac{\mathrm{d}}{\mathrm{d}t} \mathbf{T_{dq}^{-1}} \right) = \left[\begin{array}{ccc|ccc} 0 & -p_\mathrm{m} & 0 & 0 & 0 & 0 \\ p_\mathrm{m} & 0 & 0 & 0 & 0 & 0 \\ 0 & 0 & 0 & 0 & 0 & 0 \\ \hline 0 & 0 & 0 & 0 & -p_\mathrm{h} & 0 \\ 0 & 0 & 0 & p_\mathrm{h} & 0 & 0 \\ 0 & 0 & 0 & 0 & 0 & 0 \end{array}\right].$$

Inserting (5.22) into (5.21) and rearranging into hypermatrix form the Park equations for the HESM are obtained

$$\begin{aligned} \underbrace{\left[\begin{array}{c|c} \mathbf{U_{S,dq}} \\ \hline \mathbf{U_{f,pp}} \end{array}\right]}_{\mathbf{U}_\mathrm{dq}} &= \left[\begin{array}{c|c} {}^{(\mathbf{pp})}\mathbf{R_s} & \mathbf{0_{3x3}} \\ \hline \mathbf{0_{3x3}} & {}^{(\mathbf{pp})}\mathbf{R_f} \end{array}\right] \underbrace{\left[\begin{array}{c|c} \mathbf{I_{S,dq}} \\ \hline \mathbf{I_{f,pp}} \end{array}\right]}_{\mathbf{I}_\mathrm{dq}} + \underbrace{\omega_\mathrm{m} \left[\begin{array}{c|c} \mathbf{J}^{(\mathbf{dq})}\mathbf{L_{s,s}} & \mathbf{J}^{(\mathbf{dq})}\mathbf{L_{s,f}} \\ \hline \mathbf{0_{4x6}} & \mathbf{0_{4x4}} \end{array}\right] \left[\begin{array}{c|c} \mathbf{I_{S,dq}} \\ \hline \mathbf{I_{f,pp}} \end{array}\right]}_{\text{induced voltage due to rotation}} \\ &+ \underbrace{\left[\begin{array}{c|c} {}^{(\mathbf{dq})}\mathbf{dL_{s,s}} & {}^{(\mathbf{dq})}\mathbf{dL_{s,f}} \\ \hline {}^{(\mathbf{dq})}\mathbf{dL_{f,s}} & {}^{(\mathbf{pp})}\mathbf{dL_{f,f}} \end{array}\right] \frac{\mathrm{d}}{\mathrm{d}t} \left[\begin{array}{c|c} \mathbf{I_{S,dq}} \\ \hline \mathbf{I_{f,pp}} \end{array}\right]}_{\text{induced voltage due to change in current}} \end{aligned} \tag{5.23}$$

with the inductance matrices in dq coordinates

$${}^{(\mathbf{dq})}\mathbf{L_{s,s}} = \mathbf{T_{dq}} \cdot {}^{(\mathbf{pp})}\mathbf{L_{s,s}} \cdot \mathbf{T_{dq}^{-1}} = \left[\begin{array}{c|c} {}^{(\mathbf{dq})}\mathbf{L}_{\mathbf{s,s}}^{\mathrm{m,m}} & {}^{(\mathbf{dq})}\mathbf{L}_{\mathbf{s,s}}^{\mathrm{m,h}} \\ \hline {}^{(\mathbf{dq})}\mathbf{L}_{\mathbf{s,s}}^{\mathrm{h,m}} & {}^{(\mathbf{dq})}\mathbf{L}_{\mathbf{s,s}}^{\mathrm{h,h}} \end{array}\right]$$

$$= \left[\begin{array}{ccc|ccc} L_\mathrm{dm} & L_\mathrm{dm,qm} & L_\mathrm{dm,0m} & L_\mathrm{dm,dh} & L_\mathrm{dm,qh} & L_\mathrm{dm,0h} \\ L_\mathrm{qm,dm} & L_\mathrm{qm} & L_\mathrm{qm,0m} & L_\mathrm{qm,dh} & L_\mathrm{qm,qh} & L_\mathrm{qm,0h} \\ L_\mathrm{0m,dm} & L_\mathrm{0m,qm} & L_\mathrm{0m} & L_\mathrm{0m,dh} & L_\mathrm{0m,qh} & L_\mathrm{0m,0h} \\ \hline L_\mathrm{dh,dm} & L_\mathrm{dh,qm} & L_\mathrm{dh,0m} & L_\mathrm{dh} & L_\mathrm{dh,qh} & L_\mathrm{dh,0h} \\ L_\mathrm{qh,dm} & L_\mathrm{qh,qm} & L_\mathrm{qh,0m} & L_\mathrm{qh,dh} & L_\mathrm{qh} & L_\mathrm{qh,0h} \\ L_\mathrm{0h,dm} & L_\mathrm{0h,qm} & L_\mathrm{0h,0m} & L_\mathrm{0h,dh} & L_\mathrm{0h,qh} & L_\mathrm{0h} \end{array}\right]$$

$${}^{(\mathbf{dq})}\mathbf{L_{s,f}} = \mathbf{T_{dq}} \cdot {}^{(\mathbf{pp})}\mathbf{L_{s,f}} = \left[\begin{array}{c|c} {}^{(\mathbf{dq})}\mathbf{L}_{\mathbf{f,s}}^{\mathrm{m,m}} & {}^{(\mathbf{dq})}\mathbf{L}_{\mathbf{f,s}}^{\mathrm{m,h}} \\ \hline {}^{(\mathbf{dq})}\mathbf{L}_{\mathbf{f,s}}^{\mathrm{h,m}} & {}^{(\mathbf{dq})}\mathbf{L}_{\mathbf{f,s}}^{\mathrm{h,h}} \\ \hline \mathbf{L}_{\mathbf{xf,f}}^{\mathrm{1,m}} & \mathbf{L}_{\mathbf{xf,f}}^{\mathrm{1,h}} \\ \mathbf{L}_{\mathbf{xf,f}}^{\mathrm{2,m}} & \mathbf{L}_{\mathbf{xf,f}}^{\mathrm{2,h}} \end{array}\right] = {}^{(\mathbf{dq})}\mathbf{L}_{\mathbf{f,s}}^{\mathrm{T}}$$

$$= \left[\begin{array}{ccc|ccc} L_\mathrm{dfm} & L_\mathrm{fm,qm} & L_\mathrm{fm,0m} & L_\mathrm{fm,dh} & L_\mathrm{fm,qh} & L_\mathrm{fm,0h} \\ \hline L_\mathrm{fh,dm} & L_\mathrm{fh,qm} & L_\mathrm{fh,0m} & L_\mathrm{dfh} & L_\mathrm{fh,qh} & L_\mathrm{fh,0h} \\ \hline L_\mathrm{xf1,dm} & L_\mathrm{xf1,qm} & L_\mathrm{xf1,0m} & L_\mathrm{xf1,dh} & L_\mathrm{xf1,qh} & L_\mathrm{xf1,0h} \\ L_\mathrm{xf2,dm} & L_\mathrm{xf2,qm} & L_\mathrm{xf2,0m} & L_\mathrm{xf2,dh} & L_\mathrm{xf2,qh} & L_\mathrm{xf2,0h} \end{array}\right]. \tag{5.24}$$

Note that the rotor values are not influenced by the Park transformation, this is why voltage $\mathbf{U_{f,pp}}$ and current $\mathbf{I_{f,pp}}$ remain in pole-pair coordinates.

All mutual inductances between different pole-pair numbers, between the d- and q-axes and to the virtual xf1 and xf2 rotor windings (highlighted in red) can be set to zero if the machine is not deeply saturated. The red terms are still listed because they can be calculated from FEA parameters in order to check if unintended coupling in an HESM prototype occurs (see Section 6.2). The matrices denoted as **dL** in (5.23) indicate the differential inductance matrix which incorporate the saturation phenomenon (see Section 5.2.1).
The torque can be obtained by calculating the mechanical power from the induced voltage due to rotation in (5.23)

$$M_{\mathrm{el}} = \frac{P_{\mathrm{mech}}}{\omega_{\mathrm{m}}} = \begin{bmatrix} \mathbf{I_{S,dq}} & \mathbf{I_{f,dq}} \end{bmatrix}^{\mathrm{T}} \left[\begin{array}{c|c} \mathbf{J^{(dq)}L_{s,s}} & \mathbf{J^{(dq)}L_{s,f}} \\ \hline \mathbf{0_{4x6}} & \mathbf{0_{4x4}} \end{array}\right] \left[\begin{array}{c} \mathbf{I_{S,dq}} \\ \hline \mathbf{I_{f,pp}} \end{array}\right] \tag{5.25}$$

which after neglecting the red parasitical inductances and introducing the d- and q-axes fluxes of p_{m} and p_{h} pole-pair machine

$$\begin{aligned} \Psi_{\mathrm{dm}} &= L_{\mathrm{dm}} I_{\mathrm{dm}} + L_{\mathrm{dfm}} I_{\mathrm{fm}} & \Psi_{\mathrm{qm}} &= L_{\mathrm{qm}} I_{\mathrm{qm}} \\ \Psi_{\mathrm{dh}} &= L_{\mathrm{dh}} I_{\mathrm{dh}} + L_{\mathrm{dfh}} I_{\mathrm{fh}} & \Psi_{\mathrm{qh}} &= L_{\mathrm{qh}} I_{\mathrm{qh}} \end{aligned} \tag{5.26}$$

yields the well-known torque equation that consists of each a contribution from the p_{m} and p_{h} quantities

$$M_{\mathrm{el}} = \underbrace{\frac{3}{2} p_{\mathrm{m}} \left(\Psi_{\mathrm{dm}} I_{\mathrm{qm}} - \Psi_{\mathrm{qm}} I_{\mathrm{dm}} \right)}_{\text{pole pair } p_{\mathrm{m}}} + \underbrace{\frac{3}{2} p_{\mathrm{h}} \left(\Psi_{\mathrm{dh}} I_{\mathrm{qh}} - \Psi_{\mathrm{qh}} I_{\mathrm{dh}} \right)}_{\text{pole pair } p_{\mathrm{h}}} \tag{5.27}$$

An important result is that the Park equations referring to pole-pair p_{m} and p_{h} (5.23) can be completely separated from each other, so that the HESM behaves as two completely independent synchronous machines.

5.2.1 Saturation

The inductances of an electric machine are not constant, but depend on the distribution of the relative permeability μ_{r} in the iron core. The relative permeability is a function of the magnetic field strength H in the iron core which is related to the position and magnitude of the airgap MMF. As the MMF is created by the winding currents, all inductances in an electric machine are functions of the currents which contribute to the magnetic field in the iron core — called *magnetizing currents*. The effect this has on the machine model is shown qualitatively in Fig. 5.3 for an iron core that saturates depending on a single magnetizing current I_{mag}. It can be seen that up to a certain current I_0 the inductance remains constant

and the flux rises linearly. Once the iron begins to saturate, the inductances split into the *absolute* inductance L and the *differential* inductance dL. Absolute inductances describe the effective inductance when the magnetization state in the machine remains constant so that the derivative of the flux linkage yields

$$L = \frac{\mathrm{d}\Psi}{\mathrm{d}I_{\mathrm{mag}}} = \frac{\Psi}{I_{\mathrm{mag}}} \tag{5.28}$$

This is valid e.g. under a constant rotating field where the iron flux density at two distinct time instances has simply rotated further in space but is otherwise identical. Thus, absolute inductances model steady-state operation. However, for changes in the magnetization state, e.g. for a small-signal oscillation of the core flux the derivative of the flux linkage yields a different inductance value

$$dL = \frac{\mathrm{d}\Psi}{\mathrm{d}I_{\mathrm{mag}}} = \frac{\mathrm{d}L(I_{\mathrm{mag}})I_{\mathrm{mag}}}{\mathrm{d}I_{\mathrm{mag}}} = \underbrace{\left(L + \frac{\mathrm{d}L}{\mathrm{d}I_{\mathrm{mag}}}I_{\mathrm{mag}}\right)}_{\mathrm{dL}} \tag{5.29}$$

The differential inductance dL is always smaller than the absolute inductance L, because it is defined by the slope of the flux linkage curve. A more detailed treatise on differential

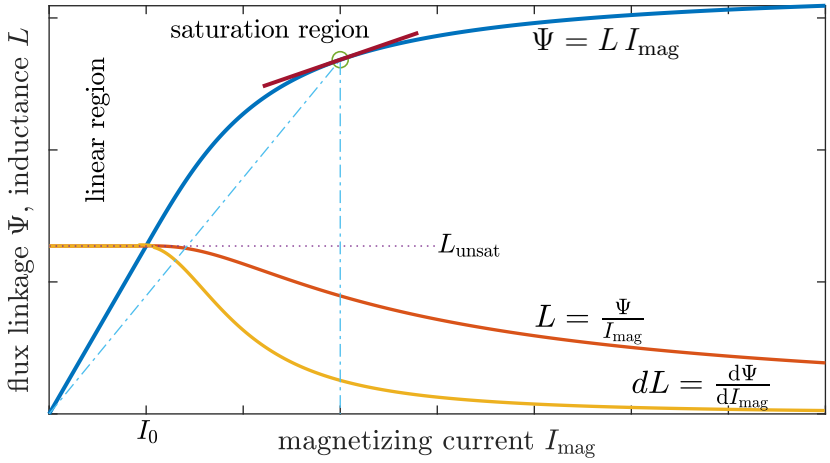

Figure 5.3: Explanation of differential and absolute inductances.

inductances in synchronous machines can be found in [38]. In a WRSM, two magnetizing currents describe the magnetization state of the machine — one for the d-axis and one for the q-axis. These magnetizing currents depend on all current components that contribute to the flux of that axis. Expanding this to HESM operation, two sets of magnetizing currents occur — one for d- and q-axis of p_{m} and p_{h} pole-pair machine respectively

$$I_{\mathrm{di,mag}} = I_{\mathrm{di}} + u_{\mathrm{i}} I_{\mathrm{fi}} \qquad I_{\mathrm{qi,mag}} = I_{\mathrm{qi}} \qquad i \in \{\mathrm{m}, \mathrm{h}\} \qquad . \tag{5.30}$$

The parameter u_i refers the rotor current to an equivalent stator current and is given later in (5.33). If the iron saturates, the matrices denoted as ${}^{(\mathbf{dq})}\mathbf{dL_{s,s}}$, ${}^{(\mathbf{dq})}\mathbf{dL_{s,f}}$, ${}^{(\mathbf{dq})}\mathbf{dL_{f,s}}$ and ${}^{(\mathbf{pp})}\mathbf{dL_{f,f}}$ in (5.23) contain the differential inductances and ${}^{(\mathbf{dq})}\mathbf{L_{s,s}}$ and ${}^{(\mathbf{dq})}\mathbf{L_{s,f}}$ the absolute inductances which are functions of all four magnetizing currents. An important observation in (5.23) is that the differential inductances determine the induced voltage due to a change in current. As the excitation system currents I_dh and I_fh are not constant, but vary in time, the p_h pole-pair machine behavior is described by differential inductances even in steady state. This saturation behavior is investigated in Sections 6.2 and 6.4.1 in more detail.

5.2.2 Dynamic Voltage-Behind-Reactance Model

A disadvantage of the model equations (5.23) in dq coordinates is that they cannot be implemented directly in a circuit simulator, because the dq equivalent windings are purely mathematical abstractions that cannot be connected to the actual power electronics of stator and rotor. This means that the HESM equations must be modelled physically with a voltage-behind-reactance (VBR) model [39]. While the HESM model in phase coordinates is completely parametrized by the phase inductances (5.3), (5.4) and (5.5), the parameters are given as a function of the winding and design parameters which are rarely known precisely and, even if they are, require sophisticated methods to determine permeance, slot- and end-winding leakage and saturation phenomena. A more general approach is the parametrization from the constant dq parameters easily obtainable from measurements. In order to obtain a phase model dependent on dq parameters, the dq equations (5.23) are transformed back into their phase representation

$$\begin{aligned}\mathbf{U_{ph}} = \mathbf{R_{ph}}\mathbf{I_{ph}} + \underbrace{\mathbf{T_{ppU}^{-1}}\mathbf{T_{dqf}^{-1}}\mathbf{dL_{dq}}\mathbf{T_{dqf}}\mathbf{T_{ppI}}}_{\mathbf{dL_{ph}}}\frac{\mathrm{d}\mathbf{I_{ph}}}{\mathrm{d}t} + \\ \underbrace{\omega_\mathrm{m}\mathbf{T_{ppU}^{-1}}\mathbf{T_{dqf}^{-1}}\left(\mathbf{J_2}\mathbf{L_{dq}}\mathbf{I_{dq}} + \mathbf{dL_{dq}}\frac{\mathrm{d}\mathbf{T_{dqf}}}{\mathrm{d}\beta}\mathbf{T_{ppI}}\mathbf{I_{ph}}\right)}_{\mathbf{U_i}}\end{aligned} \tag{5.31}$$

with the previous transformation matrices (5.6), (5.10) and (5.19) padded to 10x10 matrices

$$\mathbf{J_2} = \left[\begin{array}{c|c} \mathbf{J} & \mathbf{0_{6x4}} \\ \hline \mathbf{0_{4x6}} & \mathbf{0_{4x4}} \end{array}\right], \quad \mathbf{T_{dqf}} = \left[\begin{array}{c|c} \mathbf{T_{dq}} & \mathbf{0_{6x4}} \\ \hline \mathbf{0_{4x6}} & \mathbf{I_{4x4}} \end{array}\right], \quad \mathbf{T_{ppI}} = \left[\begin{array}{c|c} \mathbf{T_{sI}} & \mathbf{0_{6x4}} \\ \hline \mathbf{0_{4x6}} & \mathbf{T_f} \end{array}\right], \quad \mathbf{T_{ppU}} = \left[\begin{array}{c|c} \mathbf{T_{sU}} & \mathbf{0_{6x4}} \\ \hline \mathbf{0_{4x6}} & \mathbf{T_f} \end{array}\right]. \tag{5.32}$$

Each term in (5.31) can then be assigned a (10x10 matrix) circuit element as shown in Fig. 5.4. The (differential) self-inductance matrix $\mathbf{dL_{ph}}$ and the induced voltage due to rotation $\mathbf{U_i}$ need to be recalculated for each time step. This model is implemented in Plecs Standalone for transient analysis and control prototyping in Section 6.4.

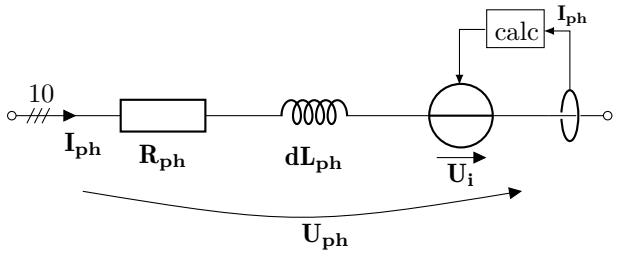

Figure 5.4: Coupled inductor VBR model of the HESM which implements (5.31).

5.2.3 Park Equivalent Circuit

In this section, the Park equivalent circuit of the HESM will be derived based on the dq model equations (5.23). A simplified steady-state model of the HESM will then be obtained which can be used to analytically describe the voltage and current demand of the excitation system. To this end, all parasitical terms in between pole pairs p_m and p_h and the equivalent xf1 and xf2 rotor windings are neglected. In order to obtain a galvanically coupled equivalent circuit, the rotor windings (subscript fm and fh) need to be referred to the respective p_m (p_h) stator [40]. The referral factor u_x indicates how much field current I_fx is needed to produce the same airgap flux as one ampere of stator current I_dx

$$L_\mathrm{hd,x} I_\mathrm{dx} = L_\mathrm{dfx} I_\mathrm{fx} \qquad \rightarrow \qquad u_\mathrm{x} = \frac{I_\mathrm{dx}}{I_\mathrm{fx}} = \frac{2}{3} \frac{k_\mathrm{px} N_\mathrm{fx}\, k_\mathrm{wfx}}{N_\mathrm{sx}\, k_\mathrm{wsx}} \qquad x \in \{\mathrm{m}, \mathrm{h}\} \tag{5.33}$$

where the stator magnetizing inductance $L_\mathrm{hd,x}$ is obtained by excluding the leakage term from the d-axis self inductance (3.27) and the mutual inductance L_dfx follows from (3.28) by inserting the respective p_m (p_h) pole-pair winding factors and number of series turns. The parameter k_px in (5.33) indicates that the rotor MMF is not only shaped by the winding factor, but also by the pole shape of the salient pole. Now the rotor currents, voltages and impedance can be referred to stator values using

$$I'_\mathrm{fx} = u_\mathrm{x} I_\mathrm{fx} \qquad U'_\mathrm{fx} = \frac{2}{3} \frac{1}{u_\mathrm{x}} U_\mathrm{fx} \qquad Z'_\mathrm{x} = \frac{2}{3} \frac{1}{u_\mathrm{x}^2} Z_\mathrm{x} \qquad \text{with } x \in \{\mathrm{m}, \mathrm{h}\} \qquad . \tag{5.34}$$

The magnetizing inductances $L_\mathrm{hd,x}$ are the most important parameters, because they determine the coupling in-between stator and rotor of the respective pole pair. They can be calculated by referring the mutual inductance $L_\mathrm{df,x}$ to the stator. The leakage components can then be obtained by subtracting the magnetizing inductances $L_\mathrm{hd,x}$ from the self-inductances of stator L_dx and rotor L'_fx (referred to stator). Thus the remaining parameters of the Park

model can be given as

$$\begin{aligned} L_{\mathrm{hd,x}} &= \frac{1}{u_{\mathrm{x}}} L_{\mathrm{dfx}} & L'_{\mathrm{fx}} &= \frac{2}{3}\frac{1}{u_{\mathrm{x}}^2} L_{\mathrm{fx}} \\ L_{\sigma\mathrm{s,x}} &= L_{\mathrm{dx}} - L_{\mathrm{hd,x}} & L_{\sigma\mathrm{f,x}} &= L'_{\mathrm{fx}} - L_{\mathrm{hd,x}} \\ R'_{\mathrm{fx}} &= \frac{2}{3}\frac{1}{u_{\mathrm{x}}^2} R_{\mathrm{fx}} & x &\in \{m, h\} \end{aligned} \quad . \tag{5.35}$$

Now the HESM Park equivalent circuit in Fig. 5.5 is fully defined. It consists of the p_{m} and p_{h} pole-pair Park equivalent circuit coupling back-to-back with the diode rectifier and differential buck converter.

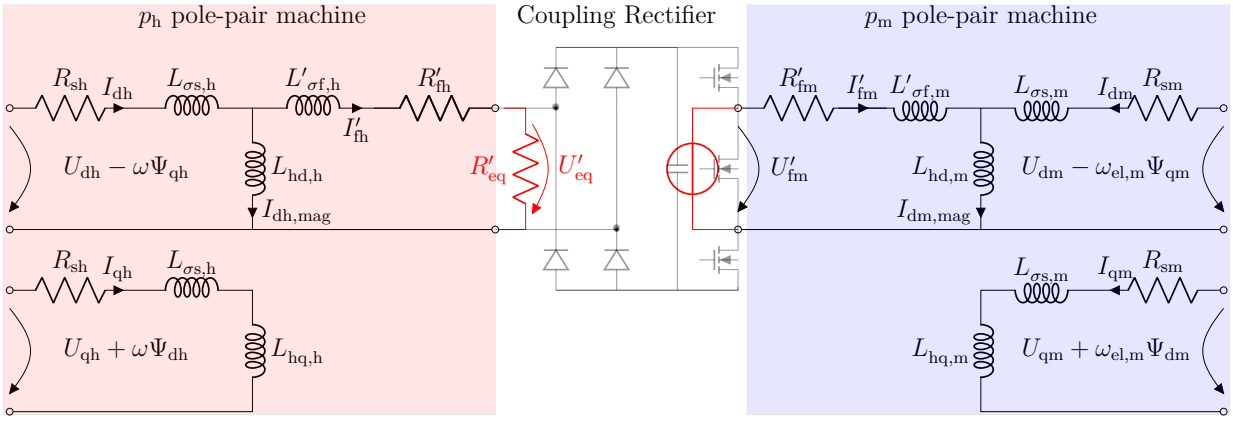

Figure 5.5: Full Park equivalent circuit of HESM.

Steady-State Model

In steady-state all p_{m} pole-pair machine currents I_{dm}, I_{qm} and I_{fm} are constant so that all inductances indexed with m can be replaced with short-circuits. In this case, the p_{m} pole-pair field behaves as if it is fed by a constant DC source. Analogously, the p_{h} pole-pair machine behaves as if it is loaded in the rotor by an equivalent resistance R'_{eq}. These simplifications highlighted in red in Fig. 5.5 allow a decoupled investigation of the p_{m} and p_{h} machines. The load resistance R'_{eq} can be obtained from the first harmonic approximation of the diode rectifier and buck converter and satisfies

$$R'_{\mathrm{eq}} = \frac{2}{3}\frac{1}{u_{\mathrm{h}}^2}\frac{R_{\mathrm{fm}}}{D^2}\frac{8}{\pi^2} \tag{5.36}$$

where the diode and MOSFET ON resistances are neglected for simplicity. For the p_{h} pole-pair machine the voltages and currents in steady-state are not constant. In order to induce a voltage into the field winding of the p_{h} pole-pair machine it can be seen in Fig. 5.5 that a time-varying d-axis current I_{dh} must be used. The q-axis current I_{qh} does not contribute in any way to harmonic excitation and only produces copper losses. That is why it can be set

to zero. This is simply another way of describing the reduction of copper losses in (3.41). In fact, applying the inverse dq transformation to a sinusoidal current reference

$$\left.\begin{aligned} I_{\mathrm{dh}} &= \hat{I}_{\mathrm{dh}}\cos(\omega_{\mathrm{exc}}t) \\ I_{\mathrm{qh}} &= 0 \end{aligned}\right\} \xrightarrow{\mathbf{T}^{-1}_{\mathbf{dq,h}}} \begin{cases} I_{\mathrm{uh}} = \dfrac{\hat{I}_{\mathrm{dh}}}{2}\cos(\,\omega_{+}t + ...) + \dfrac{\hat{I}_{\mathrm{dh}}}{2}\cos(\,\omega_{-}t + ...) \\ I_{\mathrm{vh}} = \dfrac{\hat{I}_{\mathrm{dh}}}{2}\cos(\,\omega_{+}t + \dfrac{2\pi}{3}...) + \dfrac{\hat{I}_{\mathrm{dh}}}{2}\cos(\,\omega_{-}t - \dfrac{2\pi}{3} + ...) \\ I_{\mathrm{wh}} = \dfrac{\hat{I}_{\mathrm{dh}}}{2}\cos(\,\omega_{+}t + \dfrac{4\pi}{3}...) + \dfrac{\hat{I}_{\mathrm{dh}}}{2}\cos(\,\omega_{-}t - \dfrac{4\pi}{3}...) \end{cases} \tag{5.37}$$

coincides with a **both** forward ω_+ **and** backward rotating field ω_- in pole-pair coordinates. On the other hand, if an additional I_{qh} current reference phase-shifted by 90° occurs

$$\left.\begin{aligned} I_{\mathrm{dh}} &= \hat{I}_{\mathrm{sh}}\cos(\omega_{\mathrm{exc}}t) \\ I_{\mathrm{qh}} &= \hat{I}_{\mathrm{sh}}\cos(\omega_{\mathrm{exc}}t \pm \frac{\pi}{2}) \end{aligned}\right\} \xrightarrow{\mathbf{T}^{-1}_{\mathbf{dq,h}}} \begin{cases} I_{\mathrm{uh}} = \hat{I}_{\mathrm{sh}}\cos(\,\omega_{\pm}t + ...) \\ I_{\mathrm{vh}} = \hat{I}_{\mathrm{sh}}\cos(\,\omega_{\pm}t + \dfrac{2\pi}{3}...) \\ I_{\mathrm{wh}} = \hat{I}_{\mathrm{sh}}\cos(\,\omega_{\pm}t + \dfrac{4\pi}{3}...) \end{cases} \tag{5.38}$$

the corresponding currents in pole-pair coordinates constitute an excitation of a **single** frequency **either** rotating in forward direction ω_+ **or** in backward direction ω_- depending on the sign of the phase shift. For all simulations and experiments in the scope of this work the dual frequency injection with only a current reference in I_{dh} and $I_{\mathrm{qh}} = 0$ is used to reduce stator copper losses.

Steady-State Behavior

Applying Euler's formula $\mathrm{Re}\left\{\mathrm{e}^{j\omega t}\right\} = \cos(\omega t)$ to the sinusoidal voltages and currents in the p_{h} pole-pair machine, the equivalent circuit can be analyzed using the complex AC calculation approach. In this case the Park equivalent circuit becomes Fig. 5.6. Complex values are underlined. The total input power to the p_{h} pole-pair machine consists of a contribution from the stator to the rotor via induction **and** a mechanical power contribution from the shaft due to rotation.

$$P_{\mathrm{in}} = \underbrace{\frac{3}{2}\left(\underline{U}_{\mathrm{dh}}\underline{I}^{*}_{\mathrm{dh}} + \underline{U}_{\mathrm{qh}}\underline{I}^{*}_{\mathrm{qh}}\right)}_{\text{Electrical Power}} + \underbrace{\frac{3}{2}p_{\mathrm{h}}\omega_{\mathrm{m}}\left(\underline{\Psi}_{\mathrm{qh}}\underline{I}^{*}_{\mathrm{dh}} - \underline{\Psi}_{\mathrm{dh}}\underline{I}^{*}_{\mathrm{qh}}\right)}_{\text{Shaft Power}} \tag{5.39}$$

It can be seen that if the qh-axis is not excited ($\underline{I}_{\mathrm{qh}} = 0, \underline{\Psi}_{\mathrm{qh}} = 0$) the shaft torque (power) becomes zero (see also Section 3.2.2). This shows that no torque is generated by the harmonic excitation system and the entire field excitation power is sourced from the stator DC link. The voltage demand is difficult to analyze with complex AC calculation as the voltages $\underline{U}_{\mathrm{dh}}$

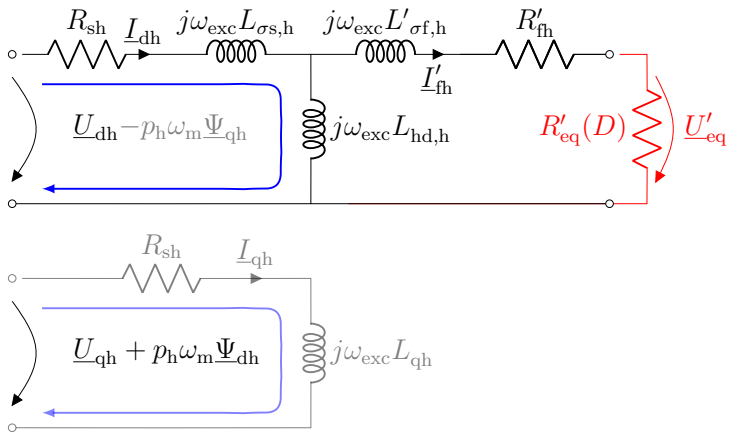

Figure 5.6: Equivalent circuit for the complex AC analysis of the p_{h} pole-pair machine. The greyed out parts can be neglected under certain circumstances as discussed in this section.

and $\underline{U}_{\mathrm{qh}}$ are now both displaced 90° in space (phase shift between d- and q-axes) **and** are oscillating in time with an arbitrary phase angle as highlighted by the complex notation. This means that the voltage phasor traverses a three-dimensional plane. This is why the voltage is calculated in time-domain here. The voltage equations from the blue branches in Fig. 5.6 are

$$\begin{aligned} U_{\mathrm{dh}} &= R_{\mathrm{sh}}I_{\mathrm{dh}} + L_{\sigma\mathrm{s,h}}\frac{\mathrm{d}}{\mathrm{d}t}I_{\mathrm{dh}} + L_{\mathrm{hd,h}}\frac{\mathrm{d}}{\mathrm{d}t}\left(I_{\mathrm{dh}} + I'_{\mathrm{fh}}\right) - p_{\mathrm{h}}\omega_{\mathrm{m}}L_{\mathrm{qh}}I_{\mathrm{qh}} \\ U_{\mathrm{qh}} &= R_{\mathrm{sh}}I_{\mathrm{qh}} + L_{\mathrm{qh}}\frac{\mathrm{d}}{\mathrm{d}t}I_{\mathrm{qh}} + p_{\mathrm{h}}\omega_{\mathrm{m}}L_{\sigma\mathrm{s,h}}I_{\mathrm{dh}} + p_{\mathrm{h}}\omega_{\mathrm{m}}L_{\mathrm{hd,h}}\left(I_{\mathrm{dh}} + I'_{\mathrm{fh}}\right) \end{aligned} \tag{5.40}$$

Controlling I_{qh} to zero and neglecting the ohmic voltage drop R_{sh} and the leakage inductance $L_{\sigma\mathrm{s,h}}$, the voltage can be given only in terms of the d-axis magnetizing current $\hat{I}_{\mathrm{dh,mag}}$

$$I_{\mathrm{dh}} + I'_{\mathrm{fh}} = \hat{I}_{\mathrm{dh,mag}}\cos(\omega_{\mathrm{exc}}t) \tag{5.41}$$

so that the voltage equations (5.40) become

$$U_{\mathrm{dh}} = -\omega_{\mathrm{exc}}L_{\mathrm{hd,h}}\hat{I}_{\mathrm{dh,mag}}\sin(\omega_{\mathrm{exc}}t) \qquad U_{\mathrm{qh}} = p_{\mathrm{h}}\omega_{\mathrm{m}}L_{\mathrm{hd,h}}\hat{I}_{\mathrm{dh,mag}}\cos(\omega_{\mathrm{exc}}t) \tag{5.42}$$

Now the time-dependent voltage demand $\hat{U}_{\mathrm{h}}$ of the p_{h} pole-pair machine can be calculated

$$\begin{aligned} U_{\mathrm{h}}(t) &= \sqrt{U_{\mathrm{dh}}^2 + U_{\mathrm{qh}}^2} = L_{\mathrm{hd,h}}\hat{I}_{\mathrm{dh,mag}}\sqrt{(\omega_{\mathrm{exc}}\sin(\omega_{\mathrm{exc}}t))^2 + (p_{\mathrm{h}}\omega_{\mathrm{m}}\cos(\omega_{\mathrm{exc}}t))^2} \\ \text{Peak value: } \hat{U}_{\mathrm{h}} &= \begin{cases} L_{\mathrm{hd,h}}\hat{I}_{\mathrm{dh,mag}}\omega_{\mathrm{exc}} & = \text{const} \quad \text{for } \omega_{\mathrm{m}} \le \frac{\omega_{\mathrm{exc}}}{p_{\mathrm{h}}} \\ L_{\mathrm{hd,h}}\hat{I}_{\mathrm{dh,mag}}p_{\mathrm{h}}\omega_{\mathrm{m}} & \quad\quad\;\; \text{for } \omega_{\mathrm{m}} > \frac{\omega_{\mathrm{exc}}}{p_{\mathrm{h}}} \end{cases}. \end{aligned} \tag{5.43}$$

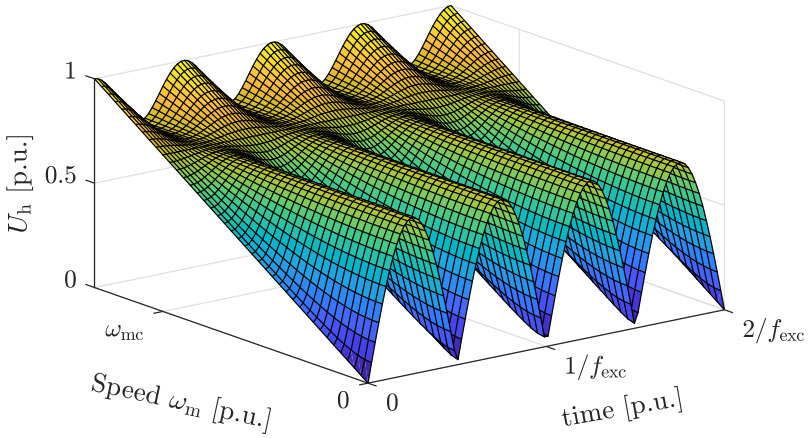

Figure 5.7: Qualitative time-dependent voltage demand $\hat{U}_\mathrm{h}$ as a function of speed and time when the operating currents I_dh ($\rightarrow I_\mathrm{fh}$, I_fm) and excitation system parameters D, f_exc stay the same.

A qualitative graphical representation of (5.43) in Fig. 5.7 reveals that the **peak** voltage demand is constant until a corner speed $\omega_\mathrm{mc} = \frac{\omega_\mathrm{exc}}{p_\mathrm{h}}$ is reached so that the (blue) voltage due to self-induction determines the peak voltage in the interval $\omega_\mathrm{m} < \omega_\mathrm{mc}$. The (red) induced voltage due to rotation only increases the rms value, but not the peak voltage. Only until the speed of ω_mc is exceeded the peak voltage demand rises.

This is why the contribution from the q-axis can be neglected if the machine speed is smaller than the corner speed. In this case Fig. 5.6 resembles the equivalent circuit of a single-phase induction motor where the variable duty cycle of the buck converter D takes on the meaning of the slip. Thus, the d-axis equivalent circuit can be used to analytically predict the excitation system behavior as a function of the excitation system parameters f_exc and D. Neglecting the winding resistances, assuming $I_\mathrm{qh} = 0$ and a machine speed $\omega_\mathrm{m} < \omega_\mathrm{m}/p_\mathrm{h}$. two important performance criteria can immediately be calculated: The parameter k_Idh (5.44) describes how much current $\hat{I}_\mathrm{dh}$ per 1 A of field current I_fm is needed. The parameter k_Uh (5.45) determines the DC link voltage that is required to supply 1 A of field current I_fm.

$$k_\mathrm{Idh}(f_\mathrm{exc}, D) = \frac{I_\mathrm{fm}}{\hat{I}_\mathrm{dh}} = \frac{\omega_\mathrm{exc} L_\mathrm{hd,h}}{\sqrt{(\omega_\mathrm{exc} L'_\mathrm{fh})^2 + (R'_\mathrm{eq})^2}} \frac{1}{D} \frac{2}{\pi} \frac{1}{u_\mathrm{h}} \tag{5.44}$$

$$k_\mathrm{Uh}(f_\mathrm{exc}, D) = \frac{U_\mathrm{dc}}{I_\mathrm{fm}} = \frac{1}{2k_\mathrm{mod}} \frac{\hat{U}_\mathrm{h}}{I_\mathrm{fm}} = \frac{2}{k_\mathrm{mod}} \frac{\sqrt{(L_\mathrm{dh} R'_\mathrm{eq})^2 + \omega_\mathrm{exc}^2 (L_\mathrm{hd,h}^2 - L_\mathrm{dh} L'_\mathrm{fh})^2}}{L_\mathrm{hd,h}} \frac{\pi}{2} D u_\mathrm{h} \tag{5.45}$$

The terms highlighted in red occur due to the referral to Park parameters, terms in green denote the first harmonic approximation of the diode bridge rectifier according to (3.42) and the blue term considers the voltage conversion of the DCDC converter. Parameter k_mod denotes the maximum modulation index of the PWM strategy. The analytically obtained quantities k_Idh and k_Uh are verified experimentally in Section 7.3.1.

5.3 Control System

The proposed HESM concept differs from conventional variable-speed drive systems in that two current components of different amplitude, phase and frequency are superimposed in each conductor — one attributed to the p_m pole-pair machine and the other to the p_h pole-pair machine. Furthermore, instead of a three-phase drive, the conventional stator winding is split up into six phases which are arranged into two three-phase systems. These distinctions necessitate an extension of the conventional WRSM control systems. To this end, firstly the control of conventional WRSMs is discussed and afterwards an extension to include the p_h pole-pair machine is presented.

5.3.1 Field-Oriented Control of WRSMs

The goal of a machine controller is to set the terminal voltages of the machine such that a desired torque (speed) is reached. As the torque is proportional to the current, this is equivalent with controlling the machine currents. The fundamental difficulty of controlling AC machines is that there is no easy single-input-single-output (SISO) relationship between the three-phase currents and the torque or flux of the machine. In order to tackle this issue, the field-oriented control (FOC) method has been conceived. The general idea of FOC is to transform the phase quantities into a coordinate system where SISO behavior exists, i.e. the torque is proportional to a so-called q-axis current I_q and the flux is proportional to a d-axis current I_d. The coordinate system which achieves this is the dq system already used in Section 5.2. The idea of FOC can be derived directly from the steady-state torque and voltage (flux) equations in the dq reference frame of a conventional WRSM [27]

$$M_\mathrm{el} = \frac{3}{2}p(\Psi_\mathrm{q} I_\mathrm{d} - \Psi_\mathrm{d} I_\mathrm{q}) = \frac{3}{2}pL_\mathrm{df} I_\mathrm{f} I_\mathrm{q} + \frac{3}{2}p\left(L_\mathrm{d} - L_\mathrm{q}\right) I_\mathrm{d} I_\mathrm{q} \tag{5.46}$$

$$U_\mathrm{s} = \sqrt{U_\mathrm{d}^2 + U_\mathrm{q}^2} = p\omega_\mathrm{m}\sqrt{(L_\mathrm{d} I_\mathrm{d} + L_\mathrm{df} I_\mathrm{f})^2 + \left(L_\mathrm{q} I_\mathrm{q}\right)^2}. \tag{5.47}$$

If a constant excitation current I_f is applied, the torque (5.46) is a function of the drive currents I_d, I_q and — if the (gray) reluctance term is neglected for the sake of simplicity — depends mainly on I_q. However, while I_d does not contribute significantly to torque production, it very much affects the (blue) expression of the phase voltage (5.47). It can be seen that a negative I_d reduces the (blue) d-axis flux Ψ_d and thus reduces the voltage U_s which is commonly referred to as field-weakening operation. Field-weakening is needed when the voltage demand of the machine exceeds the maximum voltage imposed by the limited DC link voltage. A typical schematic of the FOC algorithm for a WRSM is depicted in Fig. 5.8. The FOC algorithm is implemented by first transforming the measured three-phase currents into the dq coordinate system using the dq transformation $\mathbf{T}$ given in (5.19). In order to achieve the correct alignment with the d-axis the momentary rotor position β

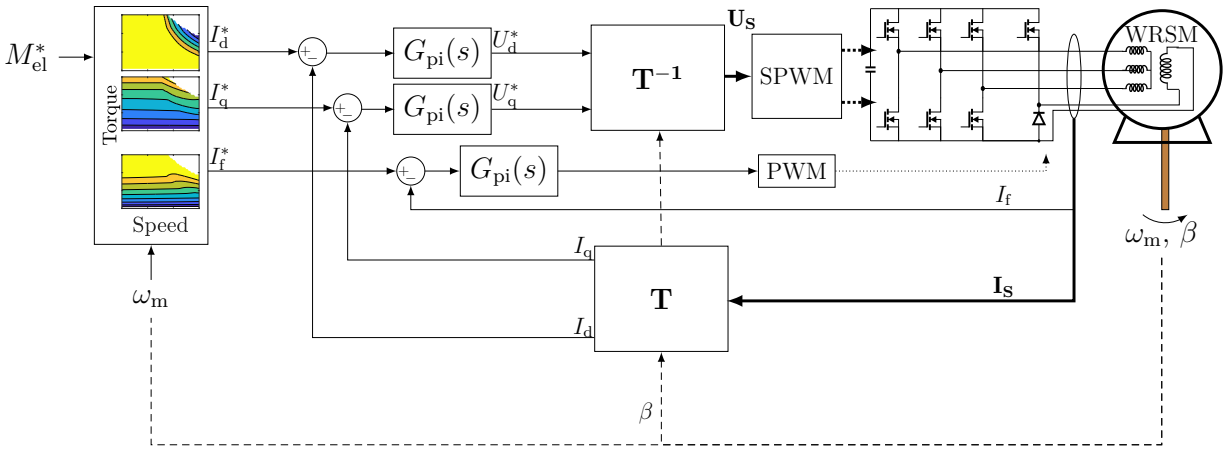

Figure 5.8: Field-oriented control of WRSMs.

must be measured or estimated. In dq reference frame two PI current controllers — one for the d-axis and one for the q axis — are used to track the desired currents I^*_d, I^*_q. The commands I^*_d and I^*_q are obtained from look-up-tables (LUT) which take into account field-weakening, reluctance torque and the saturation-dependence of the torque. The output of the PI controllers are the voltage commands U^*_d and U^*_q which are transformed back into phase coordinates via the inverse dq transformation $\mathbf{T^{-1}}$ and then used to generate the inverter gate signals by a modulation strategy. In the scope of this work sinusoidal pulse-width modulation (SPWM) with a maximum modulation index of $k_{mod} = 0.5$ is used [41]. Fig. 5.8 also includes a field current control loop which allows adjusting the field current I_f in the partial load and field-weakening region. The field current is set by a buck converter connected to the inverter DC link through the slip rings and brushes.

For the design of the PI controllers the plant transfer function must be identified. The block diagram of the WRSM in dq coordinates is shown in Fig. 5.9 according to the voltage equations from (5.23). Due to the coupling between the d- and q-axes denoted in red the plant is a multiple-input-multiple-output (MIMO) system and not a SISO system. However, for the controller design the coupling terms from the other axis can be considered as disturbances which are eliminated by the controller so that the plant for each axis can be modelled by the first order transfer functions

$$G_{s,d}(s) = \frac{1}{L_d s + R_s} \qquad G_{s,q}(s) = \frac{1}{L_q s + R_s} \tag{5.48}$$

It should be noted that the coupling terms depend on both stator currents I_d, I_q and the field current I_f. As all disturbances and signals I_d, I_q are constant during steady-state, a PI controller for each axis is sufficient in eliminating the steady-state control error for the

constant d- and q-current commands. The transfer function of a PI controller is given by

$$G_{\mathrm{pi}}(s) = K_{\mathrm{p}} + \frac{K_{\mathrm{i}}}{s} \tag{5.49}$$

with K_{p} and K_{i} as the proportional and integral gain. With all disturbances neglected, all

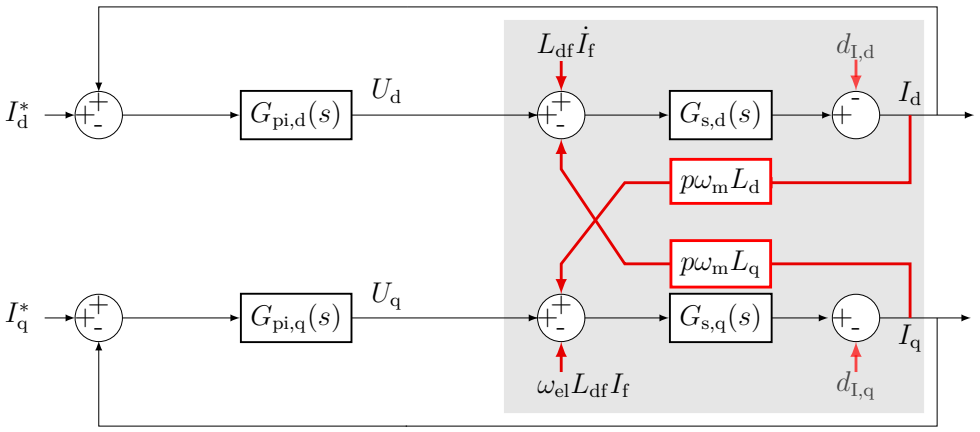

Figure 5.9: Block diagram of the closed-loop current control system. The current disturbances $d_{\mathrm{I,d}}$ and $d_{\mathrm{I,q}}$ used for plotting the disturbance bode plots of Fig. 6.7 are substitutes for the actual voltage disturbances denoted in red.

PI controllers in the scope of this work are designed according to the optimum criteria by eliminating the dominant time constant [41] from the open loop transfer function of each axis

$$G_0(s) = G_{\mathrm{pi}}(s)G_{\mathrm{s}} = \frac{K_{\mathrm{i}}}{sR_{\mathrm{s}}} \frac{\frac{K_{\mathrm{p}}}{K_{\mathrm{i}}}s + 1}{\frac{L}{R_{\mathrm{s}}}s + 1} \qquad \rightarrow \qquad K_{\mathrm{p}} = \frac{L}{R_{\mathrm{s}}}K_{\mathrm{i}} \tag{5.50}$$

From the closed loop transfer function and the desired bandwidth the parameters K_{p} and K_{i} for the closed loop current controller can then be identified.

$$G_{\mathrm{w}}(s) = \frac{G_0(s)}{1 + G_0(s)} = \frac{1}{s\frac{R_{\mathrm{s}}}{K_{\mathrm{i}}} + 1} \quad \rightarrow \text{ Choose controller bandwidth } \omega_{\infty} \quad \rightarrow \quad K_{\mathrm{i}} = \frac{R_{\mathrm{s}}}{\omega_{\infty}} \tag{5.51}$$

5.3.2 Extension for HESM

In Section 5.2 it has been shown that the HESM can be transformed into two respective dq systems — one for pole pair p_{m} and one for pole pair p_{h} — which (ideally) are decoupled. After these transformations have been applied, the p_{m} and p_{h} pole-pair machine can be treated independently so that the control algorithm can be decoupled into a decoupled torque-producing controller and a harmonic-excitation controller. Thus, the HESM control

system consists of two distinct FOC algorithms — one for each pole pair as shown schematically in Fig. 5.10.
The production of the load torque assigned to the p_m pole-pair machine behaves exactly like a conventional WRSM as has been discussed in the previous section (see Fig. 5.8). However, in order to supply the field current I_fm brushlessly via the p_h pole-pair machine it has been shown in Section 5.2.3 that an oscillating current I_dh of excitation frequency ω_exc is needed to induce a voltage into the rotor winding (see (5.37)). Thus, the FOC algorithm for the p_h pole-pair machine differs from conventional FOC in that a sinusoidal reference signal in the d-axis needs to be tracked.

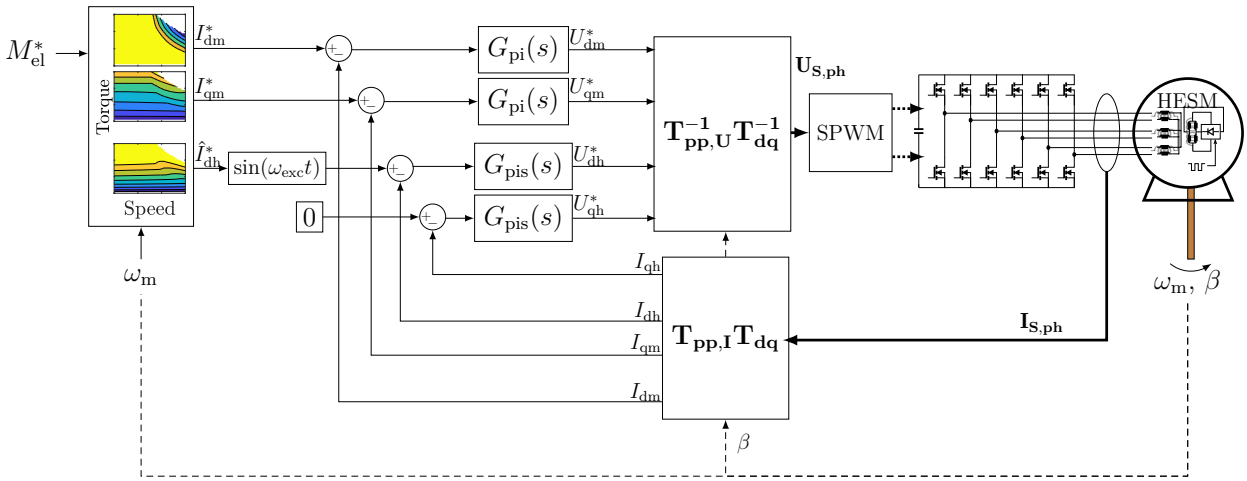

Figure 5.10: Entire HESM control system with two decoupled field-oriented control systems for the p_m and p_h pole-pair machine respectively.

The current vector $\mathbf{I_{S,ph}}$ consists of the six (measured) stator phase currents which are transformed into the p_m and p_h pole-pair dq systems using the 6x6 transformation matrices $\mathbf{T_{sI}}$, $\mathbf{T_{sU}}$ and $\mathbf{T_{dq}}$ defined in (5.7) (5.8) and (5.20). A LUT generates the current commands I^*_dm and I^*_qm of the p_m pole-pair machine just like in conventional FOC. However, as the field current cannot be controlled directly in the HESM, the LUT substitutionally outputs the peak current $\hat{I}^*_\mathrm{dh}$ from which the sinusoidal current reference for the p_h pole-pair machine is generated. The amount of harmonic current $\hat{I}^*_\mathrm{dh}$ needed to produce a certain field current I^*_fm is given in the LUT. The p_m and p_h pole-pair current control loops generate the voltage vector $\mathbf{U_{S,ph}}$ which consists of the six desired terminal voltages. They can be arranged into two independent three-phase systems so that the SPWM strategy can be applied to each of the three-phase voltages in order to generate the gate signals. In the depicted control scheme, the field current is only controlled in open loop with no knowledge or feedback whether the desired field current I^*_fm is reached as no slip rings or brushes are present to measure the rotor currents. Therefore, a small steady-state error occurs due to speed- and temperature-dependent effects. Furthermore, due to the open-loop control of I_fm, the dynamic behavior

is defined mainly by the rotor time constant. A simple back-EMF based observer for the field current I_{fm} could be implemented in the future to realize closed-loop control.

As the structure of the p_{h} pole-pair FOC algorithm is identical with conventional FOC, the block diagram depicted in Fig. 5.9 is also applicable. The appropriate indices are included in the following equations to indicate that the transfer functions pertain to the p_{h} pole-pair FOC algorithm. The plant of the p_{h} pole-pair machine is

$$G_{\mathrm{s,dh}}(s) = G_{\mathrm{s,qh}}(s) = \frac{1}{L_{\mathrm{dh}}s + R_{\mathrm{sh}}} \qquad \text{with } L_{\mathrm{dh}} = L_{\mathrm{qh}} \tag{5.52}$$

It should be noted here that now the coupling terms highlighted in red in Fig. 5.9 are not constant any more as in conventional FOC because the currents I_{dh} and I_{fh} are sinusoidal. Now the controllers have to track a sinusoidal reference signal $I^*_{\mathrm{dh}} = \hat{I}_{\mathrm{dh}} \sin(\omega_{\mathrm{exc}} t)$ and compensate the sinusoidal disturbances due to the back EMF. As the excitation frequency ω_{exc} of the reference signal I_{dh} stays constant, a sinusoidal (S) component is added to the PI controller which enables tracking sinusoidal reference signals within a narrow frequency interval. This strategy is also used successfully in grid-connected converters [42]. PIS controllers have a transfer function of

$$G_{\mathrm{c,dh}}(s) = G_{\mathrm{c,qh}}(s) = K_{\mathrm{p}} + \frac{K_{\mathrm{i}}}{s} + \frac{\omega_{\mathrm{exc}} K_{\mathrm{r}} s}{s^2 + 2\omega_{\mathrm{c}} s + \omega_{\mathrm{exc}}^2} \tag{5.53}$$

The additional S component is described by the center frequency ω_{exc}, the bandwidth ω_{c} around the center frequency, and the S controller gain K_{r}. The parametrization and investigation of the controller for a real HESM prototype will be performed in Chapter 7.

Chapter 6

Design and Simulation of Machine Prototype

The design of modern electrical machines is an intricate process that is based on a combination of empirical values, analytical formulas and numerical analysis until a prototype machine is constructed. With the rise of High-Performance Computing (HPC) software tools like *ANSYS*, *MotorCAD* or *JMAG-Designer* coupled with optimization software allow the numerical evaluation and optimization of hundreds of machine variations per day, not only electromagnetically, but also thermally and mechanically. This allows for a grand-scale cost and performance optimization. In this chapter, a prototype of the HESM concept is designed, but the focus is not on obtaining a highly optimized machine. Instead, the goal is to design a HESM prototype to test and verify the proposed excitation system. This is why the extensive use of optimization software has been omitted in favor of a simple machine scaling approach using a reference WRSM with known parameters.

6.1 Design of HESM

As a prototype a 10 kW, $p_\mathrm{m} = 4$ pole-pair salient-pole WRSM with a rated speed of $n = 3000$ rpm is targeted. The following design approach only takes the p_m pole-pair machine into account which is responsible for torque-production. The p_h pole-pair machine is realized retroactively by connecting the appropriate stator (rotor) coils into coil groups according to Fig. 4.3 (Fig. 4.5) and afterwards connecting them to the power electronics shown in Fig. 4.8. For the rotor of the prototype a salient-pole structure has been adopted because the higher saliency of salient-pole rotors leads to a slightly higher reluctance torque compared to non-salient pole rotors which have additional (ferromagnetic) teeth in the direction of the q-axis (see Fig. 6.1). The saturation in the teeth of the non-salient poles also leads to a slight reduction of the torque compared to salient-pole rotors [43].

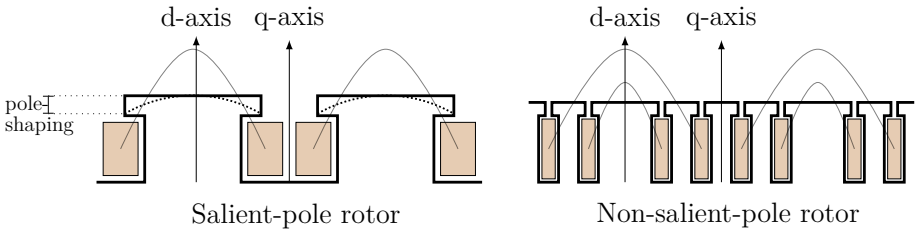

Figure 6.1: Rotor structure for WRSMs.

The choice of the pole-pair number is an important degree of freedom in inverter-fed machines because, on the one hand, larger pole-pair numbers p_m can reduce the iron and copper volume as the yoke heights and end-winding lengths decrease. On the other hand, larger pole-pair numbers necessitate a higher supply frequency which is limited by the switching frequency of the inverter. The higher frequencies of the core flux also cause higher iron losses. In addition to these aspects, in a HESM another criterion for the choice of pole-pair number is the integration of the p_h pole-pair machine. In Section 4.3.2 it has been seen that the HESM performance depends on the factor $f_\mathrm{exc}/p_\mathrm{h}$ which favors a smaller pole-pair number p_h. However, when two airgap fields of pole-pair numbers $|p_\mathrm{m} - p_\mathrm{h}| = 1$ exist simultaneously, unbalanced pulling forces occur which pull the rotor out of the center and decrease bearing life. This is why the pole-pair numbers $p_\mathrm{m} = 2$ and $p_\mathrm{h} = 1$ are not feasible. Instead, the smallest possible pole-pair number for the HESM that can be achieved without unbalanced pulling forces is $p_\mathrm{m} = 4$ (and thus $p_\mathrm{h} = 2$), which is also a widely used pole-pair number for traction motors.

6.1.1 Synchronous Machine Scaling Laws

The idea of scaling an electrical machine based on a reference machine allows adjusting an already tried-and-tested machine design to different geometrical or operational requirements [44]. For machine scaling, analytical formulas which depend on the scalable parameters are needed. Simple scaling laws for WRSMs can be obtained from the fundamental approximation in Section 3.1.4. They are applicable to generic WRSMs, which is why no subscripts m or h are used here.
Neglecting the machine losses and assuming only q-axis stator current, the torque of a synchronous machine can be obtained as a function of the terminal voltage $\hat{U}_\mathrm{s}$ using the power factor

$$\cos\varphi = \frac{P_\mathrm{mech}}{S} = \frac{\omega_\mathrm{m} M_\mathrm{el}}{\frac{3}{2}\hat{U}_\mathrm{s}\hat{I}_\mathrm{s}} \qquad \rightarrow \qquad M_\mathrm{el} = \frac{3}{2}\hat{U}_\mathrm{s}\hat{I}_\mathrm{s}\cos\varphi\frac{1}{\omega_\mathrm{m}} \tag{6.1}$$

Substituting the stator current $\hat{I}_\mathrm{s}$ by the surface loading A_s

$$A_\mathrm{s} = \frac{3}{2}\frac{4}{\pi}\frac{N_\mathrm{s}\hat{I}_\mathrm{s}}{d} \tag{6.2}$$

and the terminal voltage $\hat{U}_\mathrm{s}$ by the total airgap flux density

$$\hat{U}_\mathrm{s} = {}^1k_\mathrm{ws}N_\mathrm{s}\frac{\mathrm{d}\Psi}{\mathrm{d}t} = p\omega_\mathrm{m}\,{}^1k_\mathrm{ws}N_\mathrm{s}\frac{d}{p}l_\mathrm{Fe}\hat{B}_\delta, \tag{6.3}$$

the torque equation can be transformed into the well-known torque equation which is commonly used in the design of induction motors

$$M_\mathrm{el} = \frac{\pi}{4}d^2 l_\mathrm{Fe}\,{}^1k_\mathrm{ws}\hat{B}_\delta A_\mathrm{s} \sim V\cdot\hat{B}_\delta\cdot A_\mathrm{s}\cdot\,{}^1k_\mathrm{ws}\cos\varphi \tag{6.4}$$

where $d = 2r$ is the inner stator diameter. (6.4) shows that the torque capability of an electrical machine is limited by the flux density $\hat{B}_\delta$ due to iron saturation, the surface current A_s due to the cooling system and the winding factor ${}^1k_\mathrm{ws} < 1$. Hence, for a given iron core, winding layout and cooling system, the torque capability of a machine can only be improved by increasing the bore volume $V = \frac{d^2}{4}\pi l_\mathrm{Fe}$. This relationship is expressed by the utilization factor $C \sim M_\mathrm{el}/V$, which is constant for machines with a similar saturation level, current densities and winding designs.
Using the torque equation derived in (3.37), the torque can also be expressed as a function of the stator and rotor currents

$$M_\mathrm{el} = rl_\mathrm{Fe}\frac{3}{\pi}N_\mathrm{f}N_\mathrm{s}\frac{\mu_0}{k_\mathrm{c}h_\delta}\hat{I}_\mathrm{s}I_\mathrm{f}\frac{{}^1k_\mathrm{ws}\,{}^1k_\mathrm{wf}}{p}. \tag{6.5}$$

The stator and rotor currents can be substituted by the isolated stator and rotor airgap flux density

$$\hat{B}_{\delta\mathrm{s}} = \frac{\mu_0}{k_\mathrm{c}h_\delta}\frac{3}{\pi}\frac{N_\mathrm{s}\,{}^1k_\mathrm{ws}}{p}\hat{I}_\mathrm{s} \qquad\qquad \hat{B}_{\delta\mathrm{f}} = \frac{\mu_0}{k_\mathrm{c}h_\delta}\frac{2}{\pi}\frac{N_\mathrm{f}\,{}^1k_\mathrm{wf}}{p}I_\mathrm{f} \tag{6.6}$$

so that the torque equation becomes the **torque scaling law**

$$M_\mathrm{el} = pd\frac{\pi}{2}\frac{k_\mathrm{c}h_\delta}{\mu_0}l_\mathrm{Fe}\hat{B}_{\delta\mathrm{s}}\hat{B}_{\delta\mathrm{f}} \sim p\cdot V\cdot\frac{h_\delta}{d}\cdot\hat{B}_{\delta\mathrm{s}}\cdot\hat{B}_{\delta\mathrm{f}} \tag{6.7}$$

This expression has the advantage that the individual stator and rotor airgap flux which can be set individually in a WRSM and the total airgap flux density which is limited to $\hat{B}_\delta = \sqrt{\hat{B}_{\delta\mathrm{s}}^2 + \hat{B}_{\delta\mathrm{f}}^2} < 1\,\mathrm{T}$ directly occur in the design equation. Rearranging (6.6) and introducing

the number of Ampere turns $AT = N \cdot I$ leads to the **Ampere turn scaling law**

$$AT_\mathrm{s} \sim \frac{k_\mathrm{c} h_\delta \cdot p \cdot \hat{B}_{\delta\mathrm{s}}}{{}^1k_\mathrm{ws}} \qquad AT_\mathrm{f} \sim \frac{k_\mathrm{c} h_\delta \cdot p \cdot \hat{B}_{\delta\mathrm{f}}}{{}^1k_\mathrm{wf}} \tag{6.8}$$

which expresses how much the winding has to be adjusted to account for a variation of airgap length, pole-pair number, airgap flux density or winding factor. An approximation of the tooth width can be calculated from the airgap flux density by taking into account that the maximum slot flux Ψ integrated over one slot pitch τ_n has to pass through the reduced tooth width b_tooth. In the yoke, the flux passes through the yoke and takes its maximum value at half the flux integrated over one pole pitch τ_p. Thus, the following relationships are derived

$$\begin{aligned} B_\mathrm{tooth} &= \frac{\tau_\mathrm{N}}{b_\mathrm{tooth}} \hat{B}_\delta \quad &\rightarrow \quad b_\mathrm{tooth} &\sim \frac{d}{Z_\mathrm{s}} \frac{\hat{B}_\delta}{B_\mathrm{tooth}} \\ B_\mathrm{yoke} &= \frac{d}{2ph_\mathrm{joch}} \hat{B}_\delta \quad &\rightarrow \quad h_\mathrm{yoke} &\sim \frac{d}{p} \frac{\hat{B}_\delta}{B_\mathrm{yoke}} \end{aligned} \tag{6.9}$$

The power factor is an important design criterion, because it influences the inverter size. The theoretical $\cos(\varphi)$ neglecting the stator resistance and assuming only q-axis stator current is calculated using (5.46) and (5.47) as

$$\cos(\varphi) = \frac{P}{S} = \frac{\omega_\mathrm{m} M_\mathrm{el}}{\frac{3}{2} U_\mathrm{s} I_\mathrm{q}} = \frac{L_\mathrm{df} I_\mathrm{f}}{\sqrt{(L_\mathrm{df} I_\mathrm{f})^2 + \left(L_\mathrm{q} I_\mathrm{q}\right)^2}} \tag{6.10}$$

The goal is to express the power factor in terms of a parameter available in the scaling laws. In order to achieve this, the terms $L_\mathrm{df} I_\mathrm{f}$ and $L_\mathrm{q} I_\mathrm{q}$ are substituted using (6.6), (3.27) and (3.28) by the airgap flux densities

$$L_\mathrm{df} I_\mathrm{f} = \frac{4}{p} r l_\mathrm{Fe} N_\mathrm{s}\, k_\mathrm{ws} \hat{B}_{\delta\mathrm{s}} \qquad L_\mathrm{q} I_\mathrm{q} = \frac{4}{p} r l_\mathrm{Fe} N_\mathrm{s}\, k_\mathrm{ws} \hat{B}_{\delta\mathrm{f}} \tag{6.11}$$

All leakage effects are neglected for the sake of simplicity. Inserting (6.11) into (6.10) yields

$$\cos(\varphi) \approx \frac{\hat{B}_{\delta\mathrm{f}}}{\sqrt{\hat{B}_{\delta\mathrm{f}}^2 + \hat{B}_{\delta\mathrm{s}}^2}} = \frac{\hat{B}_{\delta\mathrm{f}}}{\hat{B}_\delta}. \tag{6.12}$$

This expression showcases that for pure q-axis excitation the power factor can only be improved by adjusting the ratio of the rotor airgap field and the stator airgap field. Thus, from (6.10), the **power factor scaling law** follows immediately as

$$\cos(\varphi)\Big|_{\hat{\mathrm{B}}_\delta = \mathrm{const}} \sim \hat{B}_{\delta\mathrm{f}} \tag{6.13}$$

6.1.2 Iterative Machine Scaling

The reference machine for the scaling approach is the traction motor from [45]. The specifications of the reference machine and the final machine design are given in Tab. 6.1. For the **stator core** a catalogue IEC stator pack of frame size IEC132M for eight-pole induction motors ($p_\mathrm{m} = 4$) is used with $q = 2$ slots-per-pole-per-phase. Thus, the slot dimensions, the inner diameter d, the stack length l_Fe and the tooth width b_tooth and yoke height h_yoke of the stator are already fixed beforehand (see Fig. 6.2). The **salient-pole rotor** is custom-lasered. The salient-poles have been shaped à priori to minimize the torque ripple without the need for additional rotor skewing. The iron stack of both stator and rotor is pressed out of M270-35A electrical steel sheets. The remaining degrees of freedom are the airgap length h_δ and the number of series turns per slot for stator and field winding. Furthermore, the rotor geometry has to be completed by determining the tooth width $b_\mathrm{tooth,r}$, yoke height $h_\mathrm{yoke,r}$, shaft diameter d_shaft and rotor pole-shoe height $h_\mathrm{pole,r}$. It should be noted that the

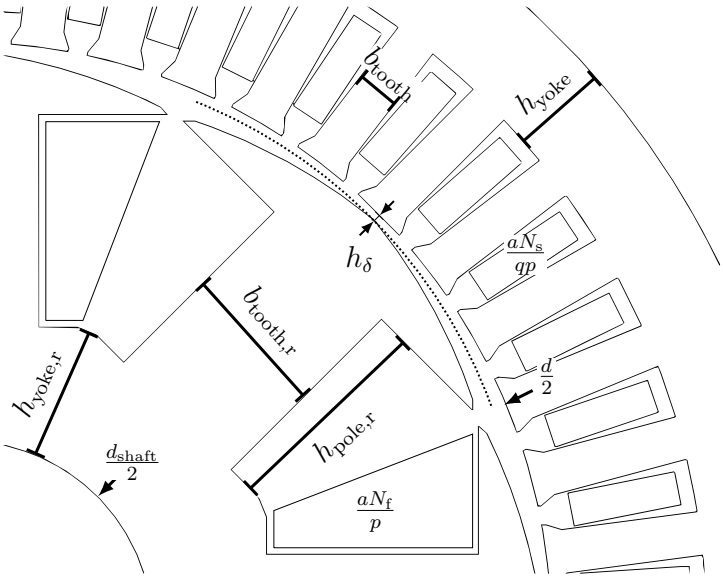

Figure 6.2: Fixed geometry parameters and degrees of freedom used in the machine design; $a = 2$ coils are in parallel with respect to the p_m pole-pair machine (compare Tab. 4.2).

reference machine is water-cooled and the targeted prototype machine is external-fan cooled. The scaling from a water-cooled machine to an external-fan-cooled machine is problematic from a thermal standpoint as the allowed current densities in the conductors are significantly lower. However, the fixed bore volume V of the IEC132M stator pack also imposes a lower utilization factor C by $\sim 30\%$, which accounts for the reduced cooling. As is typical for air cooled machines, a continuous current density of $J_\mathrm{max} = 5\,\frac{\mathrm{A}}{\mathrm{mm}^2}$ and a slot fill factor of $s = 0.4$ have been used [27].

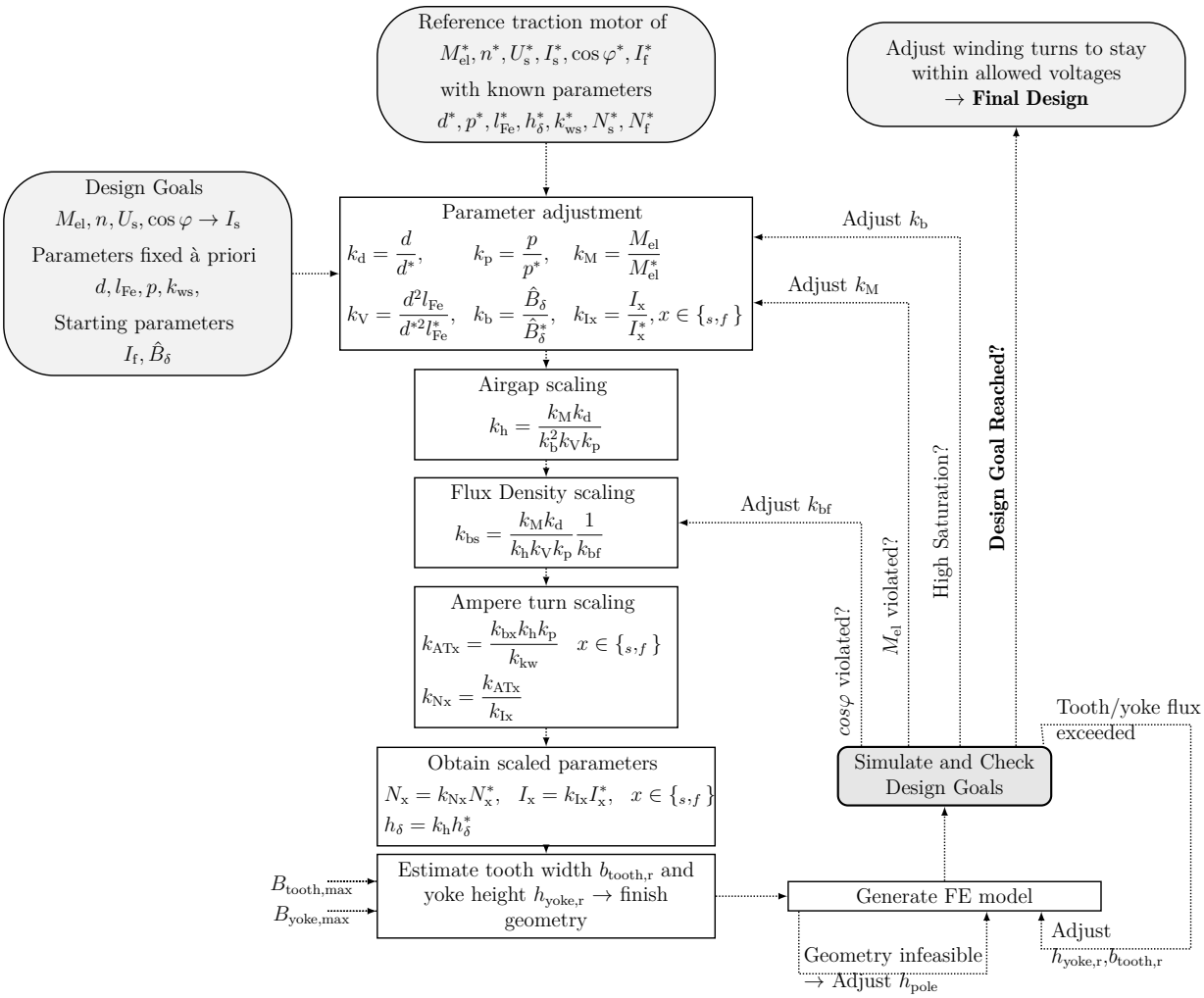

Figure 6.3: Iterative Semi-Analytical Design of the Machine using Scaling Laws in conjunction with FEA.

The iterative algorithm used to design the prototype is presented in Fig. 6.3. It relies on scaling factors and the analytical scaling laws (6.7), (6.8) and (6.13) to generate scaled machines. It should be mentioned that a purely analytical scaling approach is infeasible as the scaled machine and the reference machine have inherent differences, such as a different rotor pole shape, stator geometry, carter factor, saturation level and leakage fluxes. Furthermore, the inherent simplifications of the linear scaling laws which neglect leakage and saturation necessitate checking the design goals of each scaled machine variation using 2D FEA. The scaling laws only provide the information about which parameter to adjust to approach the design goal.

Firstly, the scaling factors of the bore diameter k_{d}, the pole-pair number k_{p}, the bore volume k_{V}, the currents k_{I} and the torque k_{M} are determined based on the input parameters. The initial scaling factor for the total airgap flux density level k_{b} is set to one indicating the

Table 6.1: Specifications of the reference machine and the designed machine. Scaled values are highlighted in red. Constraints or design goals are not highlighted.

parameter		reference machine	→	HESM prototype
pole-pair number p_m		4	→	4
Stator series turns N_sm		20	→	64
Rotor series turns N_fm		800	→	440
bore diameter d	m	0.13	→	0.14
min. airgap length h_δ	mm	1	→	0.9
stack length l_Fe	m	0.225	→	0.135
max. continuous stator current $\hat{I}_\mathrm{sm}$	A	135	→	45.5
max. continuous field current I_fm	A	6	→	10
max. continuous torque M_el	Nm	55	→	34
DC link voltage U_dc	V	300	→	400
Field-weakening speed n_fw	rpm	∼5500	→	3000
rated power factor $\cos\varphi$		0.85	→	0.8
Cooling System		water cooling jacket	→	external fan

scaled machine has the same flux density as the reference machine. The **torque scaling law** (6.7) is then used to estimate by what factor k_h the airgap needs to be adjusted to obtain a machine with the above scaling factors. Afterwards, the **torque scaling law** is used again to scale the rotor flux density k_bf (while keeping the total airgap flux density constant), which affects the $\cos\varphi$ according to (6.13). k_bf is set to one initially. In order to reach the scaled flux densities given the scaled airgap length, the **ampere turn scaling law** must be applied to identify how the number of winding turns has to be adjusted. From these scaling factors the actual number of series turns of stator and rotor and the airgap length are determined from the reference machine. In order to allow for FE calculation, the tooth width and yoke heights on the rotor are estimated using (6.9) and a CAD model of the scaled machine is generated. The rotor geometry parameter $h_\mathrm{pole,r}$ is chosen such that the rotor winding fits into the rotor slot. Once the geometry of the machine is fully defined, a transient analysis for rated operation is performed and the design goals are verified: If the $\cos\varphi$ is too low, the power factor scaling law is used to increase the rotor airgap flux density $\hat{B}_\mathrm{\delta f}$ with a scaling factor $k_\mathrm{bf}\uparrow$. If the torque is too low, the torque scaling factor k_M is increased. Excessive saturation is tackled by iteratively reducing the total machine flux density with a scaling factor k_b which keeps the power factor roughly constant. Lastly, if the tooth and yoke flux density levels are violated, the parameters $b_\mathrm{tooth,r}$ and $h_\mathrm{tooth,r}$ are adjusted, the geometry is regenerated and the FE model is re-analyzed.
It should be noted that the algorithm has not been fully automated. Instead, the adjustments are made manually until a viable machine is obtained. After the design goals are reached, the number of winding turns needs to be reconsidered. For the stator winding, a last adjustment

which takes into account the THD of the terminal voltages is carried out. Furthermore, the number of field winding turns is adjusted to account for the high AC voltages induced during harmonic excitation.

6.2 Analysis of the Saturation Behavior

Up to this point it has always been assumed that the p_m and p_h pole-pair machines are perfectly decoupled in all operating points as if they were independent machines with separate iron cores. It is obvious that this is not the case as the machines share the same iron core and flux paths. This is highlighted for the designed HESM prototype in Fig. 6.4 when the p_m and p_h pole-pair machine fields are excited separately. It can be seen that the fields of both pole pairs saturate the yoke and teeth of stator and rotor. The red and blue arrows indicate the direction of the magnetic fields in the machine iron and highlight that the superposition of the p_m and p_h pole-pair fields reinforces or attenuates the flux density in certain core sections. As the flux in the dh-axis oscillates the core flux pattern is highly irregular in time. Thus, it

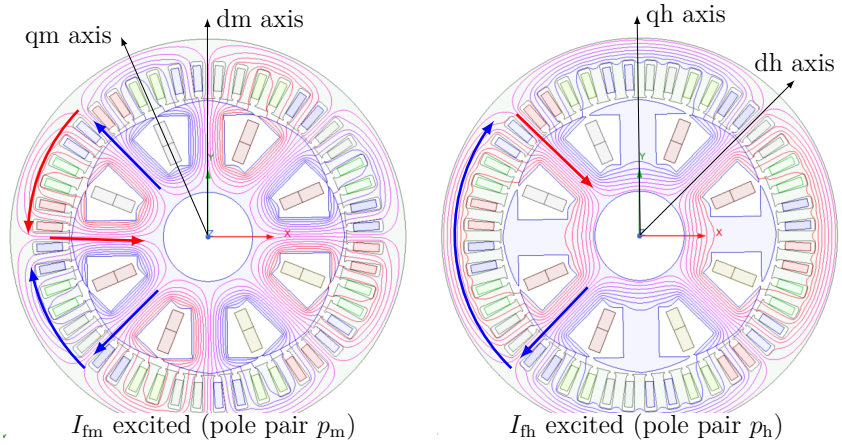

Figure 6.4: Magnetic fields in the HESM at a single time instance.

can be concluded that saturation due to p_m pole-pair machine currents very much affects the p_h pole-pair machine flux paths (and vice versa). In order to investigate this effect, the FEA model is a convenient tool. To this end, all machine inductances are calculated as a function of the saturation state of the machine iron. As explained in Section 5.2.1, four magnetizing currents describe the magnetization state of the HESM which are stated here again

$$\begin{aligned} &p_\mathrm{m}\text{ pole-pair machine} \quad I_\mathrm{dm,mag} = I_\mathrm{dm} + u_\mathrm{m} I_\mathrm{fm} \quad I_\mathrm{qm,mag} = I_\mathrm{qm} \\ &p_\mathrm{h}\text{ pole-pair machine} \quad I_\mathrm{dh,mag} = I_\mathrm{dh} + u_\mathrm{h} I_\mathrm{fh} \quad \cancel{I_\mathrm{qh,mag} = I_\mathrm{qh}} \end{aligned} \tag{6.14}$$

The q-axis magnetizing current of the p_h pole-pair machine can be neglected because the FOC controller keeps I_qh at zero as it does not contribute to the induced voltage in the

field winding. Furthermore, in salient-pole WRSMs the magnetizing current $I_{\mathrm{qm,mag}}$ can be neglected unless the machine is heavily saturated as the qm-axis points into the direction of the large airgap between the pole shapes. Thus, the saturable machine inductances can be simplified as two-dimensional Look-up tables (LUTs) of the d-axis magnetizing currents $I_{\mathrm{dm,mag}}$ and $I_{\mathrm{dh,mag}}$.
A current sweep over the magnetizing currents is performed in the FE model to determine the LUTs. As was explained in Section 5.2.1, the differential inductances determine the induced voltage into the field winding. This is why both the apparent and differential inductances are calculated with FEA using the frozen permeability method [46], [47] in order to parametrize the HESM model. The magnetizing currents are swept until 150% of the expected magnetizing current in the d-axis.
If the p_{m} and p_{h} pole-pair machine were perfectly decoupled, the p_{m} (p_{h}) pole-pair machine inductances would **only** depend on the p_{m} (p_{h}) pole-pair magnetizing current $I_{\mathrm{dm,mag}}$ ($I_{\mathrm{dh,mag}}$) once the iron saturates. In Fig. 6.5 this is investigated for the (absolute and differential) mutual inductances of the p_{m} and p_{h} pole-pair machines.

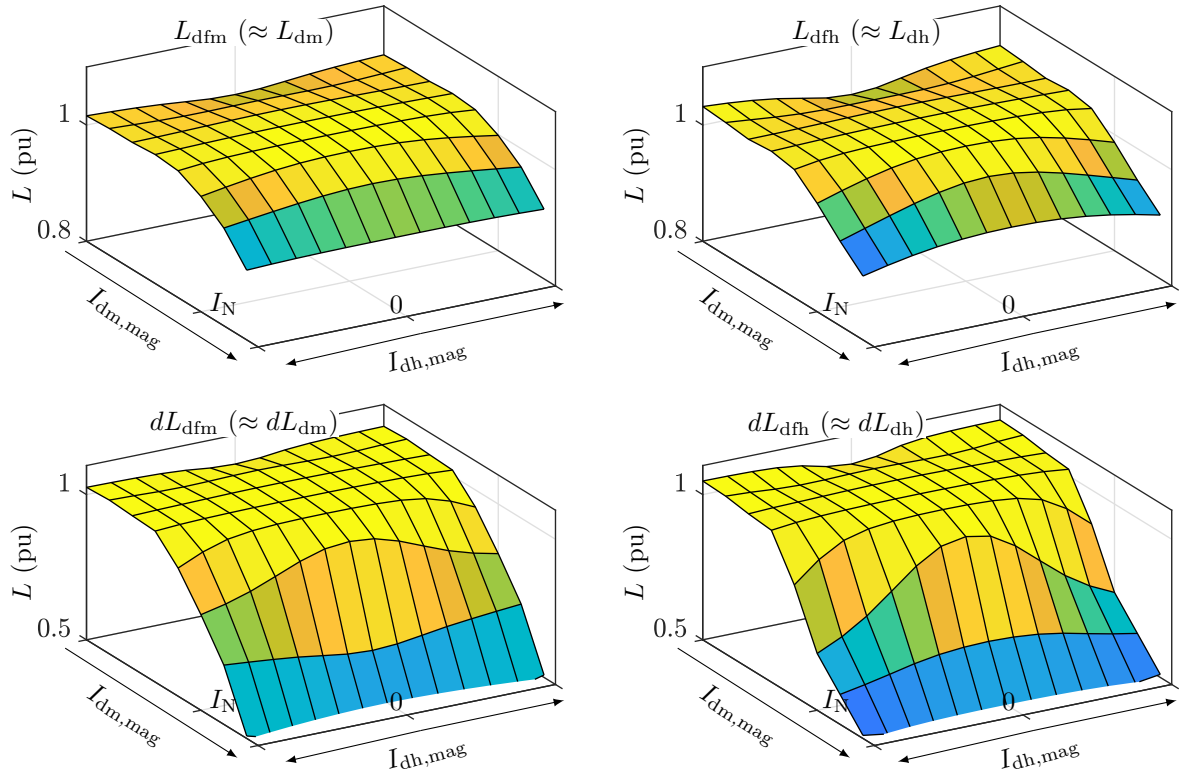

Figure 6.5: Look-up tables for the self- and mutual inductances with respect to their unsaturated values. The parameter sweep is performed until 150 % rated magnetization current. Black (blue,yellow) arrows indicate the influence of the p_{m} (p_{h}) pole-pair machine.

Overall, the effect of saturation is more pronounced in the differential inductances, which coincides with Section 5.2.1. An important observation in **both** mutual inductances L_{dfm} and L_{dfh} is that the saturation behavior is mostly governed by the p_{m} pole-pair magnetizing current $I_{\mathrm{dm,mag}}$. For small magnetizing currents $I_{\mathrm{dm,mag}}$ the inductances remain constant (i.e. they are unsaturated) irregardless of the magnetizing current $I_{\mathrm{dh,mag}}$. For an increasing magnetizing current $I_{\mathrm{dm,mag}}$, both inductances L_{dfm} and L_{dfh} saturate increasingly with only a small effect of $I_{\mathrm{dh,mag}}$. The p_{h} pole-pair magnetizing current $I_{\mathrm{dh,mag}}$ only contributes to saturation if $I_{\mathrm{dm,mag}}$ is also present. It can be concluded that the decoupling of the pole pairs is violated when iron saturation is considered: On the one hand, the p_{m} pole-pair inductances have a slight dependence on the p_{h} pole-pair magnetizing current $I_{\mathrm{dh,mag}}$ when the machine is already saturated by a sufficiently large $I_{\mathrm{dm,mag}}$. This additional saturation due to p_{h} pole-pair machine currents does influence the torque capability to some extent, as there is a slight dependence of the absolute inductances (which determine the torque) on $I_{\mathrm{dh,mag}}$. On the other hand, the p_{h} pole-pair inductances decrease severely due to p_{m} pole-pair magnetizing current $I_{\mathrm{dm,mag}}$ and also have a dependency on the p_{h} pole-pair magnetizing current $I_{\mathrm{dh,mag}}$. It can be predicted that the harmonic excitation system is affected significantly by magnetizing currents of both pole pairs. It should be noted that the smaller effect of the magnetizing current $I_{\mathrm{dh,mag}}$ despite the large tooth and yoke flux densities of the p_{h} pole-pair machine predicted in Tab. 4.2 can be explained by the small magnetizing currents required to achieve harmonic excitation.

The inductance maps in Fig. 6.5 only identify the reduction of the inductances due to the magnetizing currents of both pole pairs. They do not consider the emergence of non-zero coupling inductances **between** pole pairs p_{m} and p_{h} due to saturation. In (5.24) these undesired coupling inductances have been highlighted in red and it has been claimed that they are zero under normal operation. In Fig. 6.6 two mutual inductances between the distinct pole pairs are shown exemplarily. The inductance $L_{\mathrm{dh,dm}}$ ($L_{\mathrm{fh,fm}}$) expresses the mutual inductance between the p_{m} pole-pair d-axis stator (rotor) winding and the p_{h} pole-pair stator (rotor) winding. Other mutual inductances behave analoguously. Only differential inductances are shown here because the effect of parasitical coupling is more easily observed there. The inductances have been referred to per unit using (6.15). This value qualitatively expresses the parasitical reluctance component ${}^{p_0}\Lambda_{\mathrm{f}}$ which only arises when both the p_{m} and p_{h} pole-pair flux paths saturate.

$$L_{\mathrm{dh,dm}}[\mathrm{pu}] = L_{\mathrm{dh,dm}} / \left(\frac{6}{\pi} \frac{\mu_0}{h_\delta} r l_{\mathrm{Fe}} \frac{k_{\mathrm{wsm}} N_{\mathrm{sm}} k_{\mathrm{wsh}} N_{\mathrm{sh}}}{p_{\mathrm{m}} p_{\mathrm{h}}} \right) \quad L_{\mathrm{fh,fm}}[\mathrm{pu}] = L_{\mathrm{fh,fm}} / \left(\frac{4}{\pi} \frac{\mu_0}{h_\delta} r l_{\mathrm{Fe}} \frac{k_{\mathrm{wfh}} N_{\mathrm{fh}} k_{\mathrm{wfm}} N_{\mathrm{fm}}}{p_{\mathrm{h}} p_{\mathrm{m}}} \right) \tag{6.15}$$

In the unsaturated region the coupling is zero for all depicted mutual inductances. Furthermore, if no p_{h} pole-pair magnetizing current $I_{\mathrm{dh,mag}}$ occurs the coupling inductances remain zero even for high p_{m} pole-pair magnetizing currents $I_{\mathrm{dm,mag}}$. However, if **both** magnetizing currents occur, it can be seen that interaction between the different pole pairs arises. This

coupling is most severe between the field windings of the p_m and p_h pole-pair machine as indicated by $dL_\mathrm{fh,fm}$. The yellow arrow shows that in deep saturation the mutual inductances between the pole-pairs decrease again. These mutual inductances lead to undesired induced voltages in steady state from the p_h pole-pair machine into the p_m pole-pair machine due to the oscillating currents I_dh and I_fh. It must be mentioned, however, that the magnitude of the inductances is only up to 0.25 pu in the worst case and the p_h pole-pair currents I_dh and I_fh are relatively small so that they can be neglected as a simplification.

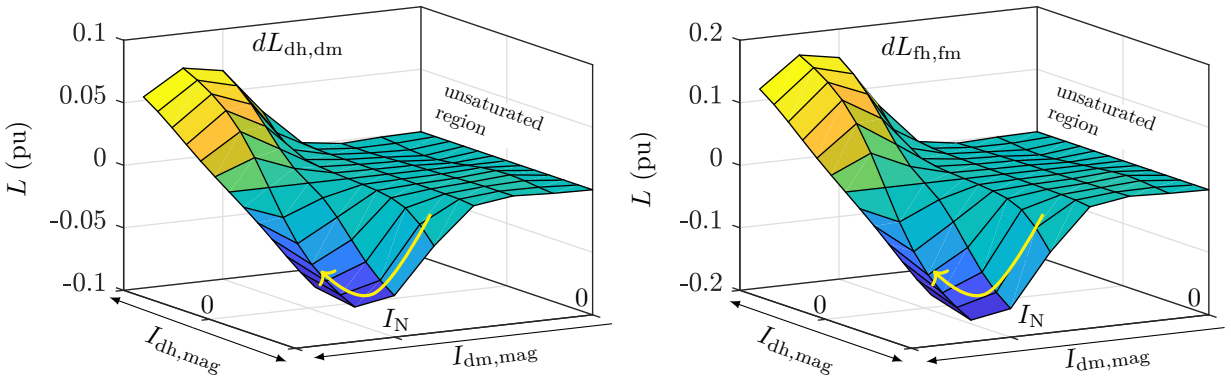

Figure 6.6: Look-up tables for differential mutual inductances between the p_m and p_h pole-pair inductances in per unit. Green and yellow (white) arrows indicate the influence of the p_m (p_h) pole-pair machine.

6.3 PIS Controller Design

In the previous section an investigation of the inductances under saturation has been performed using the FE model. In this section, the linear (unsaturated) values will be used to design the PIS controllers of the control system presented in Section 5.3. While analytical formulas for the determination of the PI controller parameters are given in (5.50) and (5.51), it will be seen that the parametrization of the PIS controller needs to take into account the non-linearity of the diode rectifier. This is why a sensitivity analysis of the closed loop and disturbance bode plots is performed based on the dynamic simulation of the HESM. The closed loop and disturbance rejection transfer functions are (in order)

$$G_\mathrm{w}(s) = \frac{I_\mathrm{d}(s)}{I_\mathrm{d}^*(s)} = \frac{G_\mathrm{c,dh}(s)G_\mathrm{s,dh}(s)}{1 + G_\mathrm{c,dh}(s)G_\mathrm{s,dh}} \tag{6.16}$$

$$G_\mathrm{d}(s) = \frac{d_\mathrm{I,d}(s)}{I_\mathrm{d}^*(s)} = \frac{1}{1 + G_\mathrm{c,dh}(s)G_\mathrm{s,dh}(s)} \tag{6.17}$$

with the notation from the block diagram Fig. 5.9. As the transfer functions for dh and qh axes are identical, only the dh axis is displayed here. For the design of the PIS controller,

the proportional and integral parts are of minor importance. Their function is mainly to compensate low frequency disturbances and not to guarantee the tracking of the excitation frequency f_{exc}. For large bandwidths, the PI component even negatively interferes with the S component, which is why the bandwidth of the PI components has been set to half of the excitation frequency. For the investigation of the S component, the closed-loop bode diagram for variations of the sinusoidal component gain K_{r} and bandwidth ω_{c} are shown in Fig. 6.7. The center frequency is always fixed by the excitation frequency $\omega_{\mathrm{exc}} = 2\pi f_{\mathrm{exc}}$.
Fig. 6.7a shows that the fundamental frequency can be controlled with almost no amplitude error by the S controllers for sufficiently high gains K_{r}. The phase is not displayed here because for harmonic excitation a phase shift of the injected current I_{dh} has no negative effect on the excitation system performance. Only the amplitude of the induced voltage determines the excitation power, so that a phase shift of I_{dh} simply causes I_{fh} to shift in conjunction with it. It can be observed that for $K_{\mathrm{r}} = 300$ a satisfactory control of I_{dh} is obtained, which is why this value has been adopted.

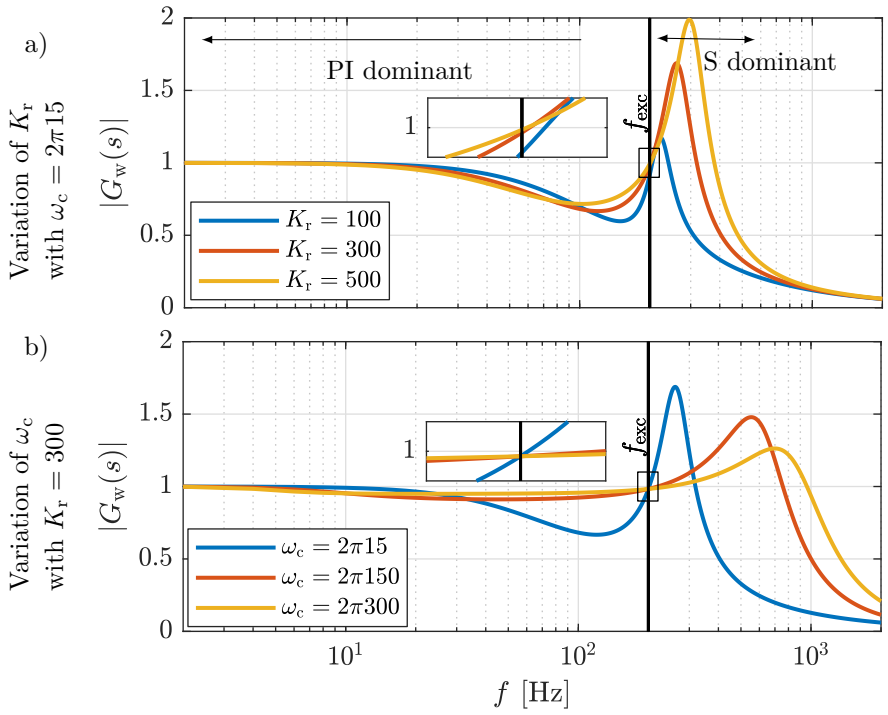

Figure 6.7: Bode plots of the closed loop transfer function for different parameters of K_{r} and ω_{c} and an excitation frequency of $f_{\mathrm{exc}} = 200\,\mathrm{Hz}$.

In Fig. 6.7b the influence of the bandwidth parameter ω_{c} is shown. It has no effect on the gain at the center frequency, but it can be seen that higher ω_{c} lead to a larger plateau in the vicinity of f_{exc} where unity gain is reached. As the excitation frequency f_{exc} is constant, the bandwidth ω_{c} mainly influences the rejection of disturbance in the control system.

To identify disturbances in the control system, Fig. 6.8 compares the simulated waveforms of an ideal controller (proportional control with infinite gain) to real PIS control with a narrow bandwidth $\omega_c = 2\pi 15\frac{1}{s}$. In a diode rectifier it is well known that the rectifier input current (here: I_{fh}) only flows if the rectifier terminal voltage is larger than the DC capacitor voltage.

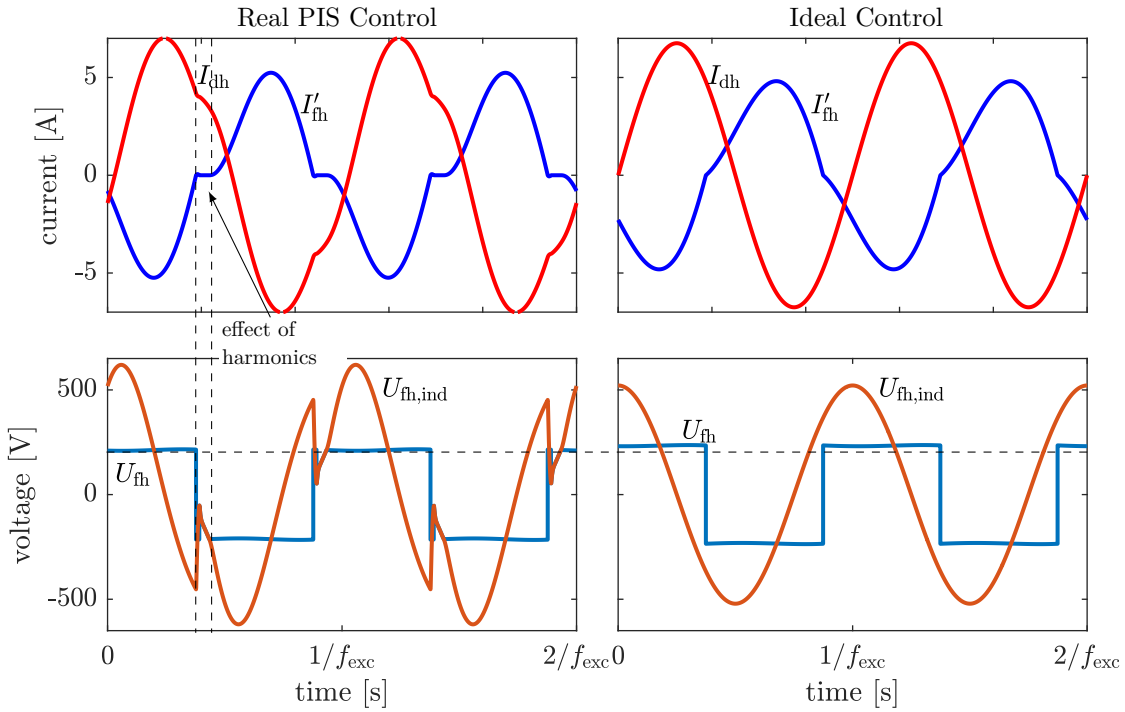

Figure 6.8: Effects of real controller on excitation system performance. The p_h pole-pair machine currents I_{dh}, I_{fh}, the induced rotor voltage $U_{fh,ind}$ and the rectifier terminal voltage U_{fh} are portrayed for real control (left) and an ideal controller (right).

This distortion of the input current I_{fh} imposes additional current harmonics at odd multiples of the excitation frequency hf_{exc} with $h \in \{3, 5, 7, ...\}$. These frequency components also propagate back to the stator as induced voltage disturbances $L_{dfh}\dot{I}_{fh}$ and $\omega_{el,h}L_{dfh}I_{fh}$ (see block diagram Fig. 5.9). This is why, according to Fig. 6.8, both the rotor current I_{fh} **and** the stator current I_{dh} are distorted by odd multiples of the excitation frequency.
In Fig. 6.9 the ability of the PIS controller to compensate these disturbances is investigated using the bode diagram of the disturbance transfer function for different bandwidths ω_c. While the PIS controller is capable of compensating disturbances at the fundamental frequency f_{exc} and in a close vicinity, it can be seen that disturbances at multiples of the excitation frequency cannot be eliminated by the PIS controller for realistic values of ω_c. Higher bandwidths ω_c even exacerbate this problem by amplifying the disturbances, which causes even more distortion of the desired currents and has even been observed to lead to system instability in the real test bench. This is why PIS controllers with a narrow band-

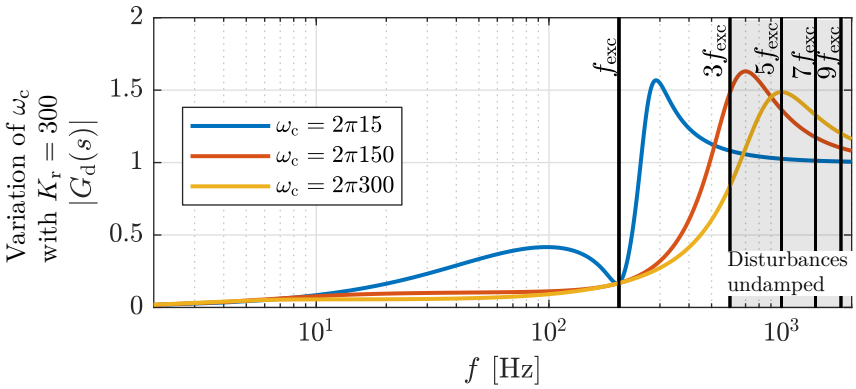

Figure 6.9: Bode plot of the disturbance rejection transfer function for different parameters of K_r and ω_c. While in reality the control system is disturbed by the induced voltage from the first armature reaction d_U, the utilization of the current disturbance d_I clarifies the lack of damping for the harmonics better.

width $\omega_c = 2\pi 15\frac{1}{s}$ are used to avoid amplifying the disturbances. As a consequence, the PIS controllers do not react to the disturbances so that the rectifier harmonics propagate undamped to the stator control system and distort I_{dh}. Better disturbance rejection could be obtained with multiple S controllers for each odd multiple of f_{exc}, with other controllers like hysteresis control or by using an active rectifier which allows sinusoidal rotor currents I_{fh}.

Fig. 6.8 also shows that the undamped disturbances lead to a reduced terminal voltage U_{fh} under real PIS control compared to an ideal controller. This is because the power transfer does not strictly depend on the amplitude of the fundamental frequency f_{exc}, but on the 'charging time' that the rectifier terminal voltage is larger than the DC link voltage. The distortion of I_{dh} and I_{fh} due to rectifier harmonics decreases that 'charging time' and thus causes a loss of performance. In order to consider this effect in an analytical steady-state model, the mutual inductance L_{dfh} must be reduced slightly. The reduction of L_{dfh} depends on the excitation system parameters D and f_{exc} and the machine parameter L_{fh} and is almost 10 % for typical values $f_{exc} = 200\,\text{Hz}$ and $D \approx 10\,\%$. This means that the amplitude of I_{dh} could be reduced by 10 % and hence excitation system stator losses by almost 20 % if a better controller bandwidth which achieves sinusoidal I_{dh}-injection were used.

6.4 Dynamic Simulation

With the saturation-dependent absolute and differential inductances obtained via FEA as look-up tables, the full physical HESM model according to (5.31) was implemented and parametrized in PLECS. The HESM model is completed by connecting the PLECS models of two B6 stator inverters and the rotor circuitry as shown in Fig. 4.8. In order to control

the HESM, the FOC algorithm presented in Fig. 5.10 is also implemented in PLECS. An explanation of the operating voltages and currents during HESM operation is presented in Figs. 6.10, 6.11 and 6.12 by zooming into two fundamental periods of a dynamic simulation after steady state has been reached. All voltages and currents in the HESM are shown in the three HESM coordinate systems discussed in Chapter 5. The exemplary operating conditions are 20 Nm at a speed of 1000 rpm. The excitation system operates at an excitation frequency of $f_{\mathrm{exc}} = 200\,\mathrm{Hz}$ and duty cycle $D = 11.5\,\%$ to supply a field current of 8 A. It can be seen that the stator voltages and currents in phase (ph) coordinate system are rich in harmonics and are mainly composed of the three fundamental frequency components

$$\omega_{\mathrm{el,m}} = p_{\mathrm{m}}\omega_{\mathrm{m}}, \qquad \omega_{+} = \omega_{\mathrm{exc}} + p_{\mathrm{h}}\omega_{\mathrm{m}} \qquad \text{and} \qquad \omega_{-} = \omega_{\mathrm{exc}} - p_{\mathrm{h}}\omega_{\mathrm{m}}$$

related to the p_{m} and p_{h} pole-pair machines. The contribution of the p_{h} pole-pair machine is a large part of the voltage demand so that the fundamental $p_{\mathrm{m}}\omega_{\mathrm{m}}$ frequency is highly distorted by the frequencies ω_{+} and ω_{-}. In the phase currents Fig. 6.11 the (dominant) fundamental frequency $p_{\mathrm{m}}\omega_{\mathrm{m}}$ can more easily be identified as the machine acts as a lowpass filter. Transforming into pole-pair (pp) coordinates splits up the voltages and currents into their virtual p_{m} and p_{h} three-phase components.

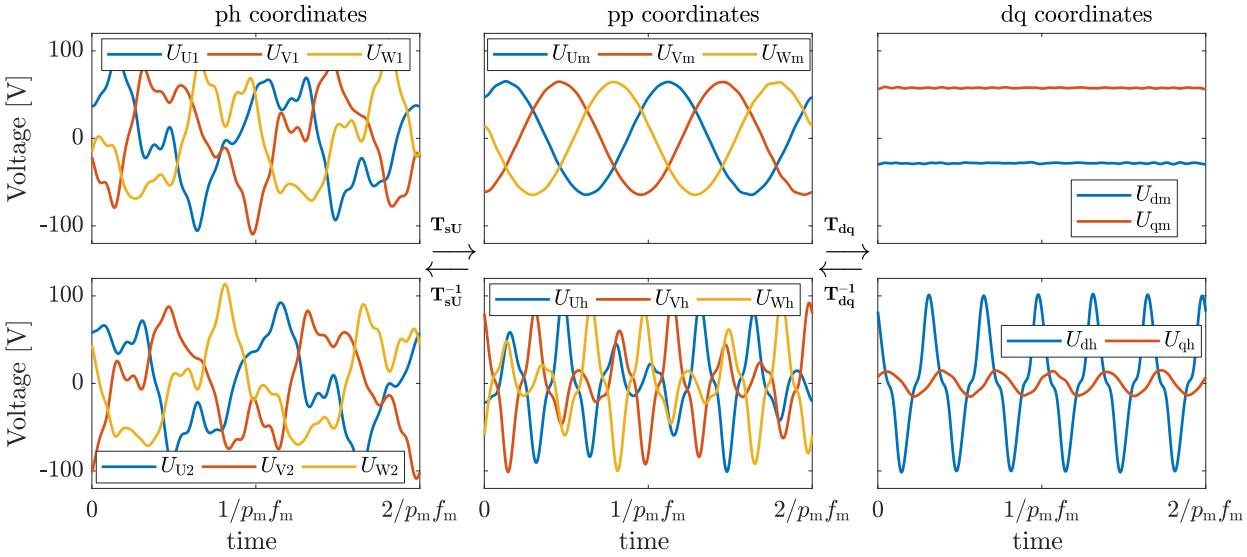

Figure 6.10: Stator voltages in the HESM in their respective coordinate systems. PWM frequencies have been removed.

Now, the p_{m} pole-pair machine voltages and currents are almost perfectly sinusoidal with frequency $p_{\mathrm{m}}\omega_{\mathrm{m}}$. Analogously, in the p_{h} pole-pair machine only the fundamental frequencies ω_{+} and ω_{-} occur. After applying the dq transformation to each respective pole pair, the voltages and currents of the p_{m} pole-pair machine become constant as in a conventional WRSM. Analogously, the dq system of the p_{h} pole-pair machine now mainly includes the

excitation frequency ω_{exc}. The current I_{qh} can successfully be controlled to zero by the PIS controller. In order to achieve this mainly the voltage U_{dh} is used. However, a small voltage U_{qh} is also needed in order to compensate the induced voltages from the field winding and dh axis. This coincides with the theoretical results (5.42).

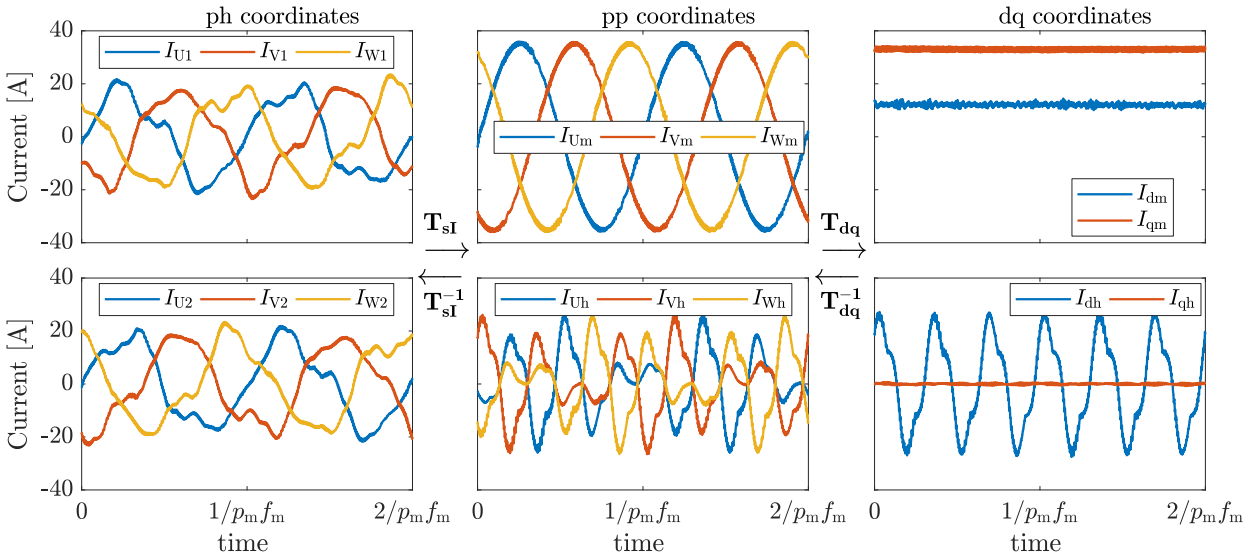

Figure 6.11: Stator currents in the HESM in their respective coordinate systems.

The rectifier harmonics discussed in Section 6.3 can now also clearly be seen by the third harmonic present in the current I_{dh} of Fig. 6.11. An interesting observation is that the PIS controller reacts to the rectifier harmonics to some extent as indicated by the third-harmonic present in the voltage U_{dh}. However, it is unable to eliminate the disturbances caused by the rectifier harmonics.

Fig. 6.12 highlights the voltages and currents in the rotor winding of the HESM. It can be seen that two of the four rotor coil groups (F1=F3 and F2=F4) behave identically. In ph coordinates the (black) voltages contain the rectangular AC shape imposed by the rectifier superimposed by (half of) the switched DC output waveform of the buck converter. The DC component is related to the p_{m} pole-pair machine and the AC component to the p_{h} pole-pair machine. In pp coordinates these two components are decoupled from one another: On the one hand, the rectangular AC voltage U_{fh} is obtained which drives the sinusoidal current I_{fh} of fundamental frequency ω_{exc} with a significant third harmonic. On the other hand, the switched DC voltage U_{fm} are low-pass-filtered by the field winding inductance into the smooth DC field current I_{fm}. The complete dynamic waveforms from which the waveforms in Figs. 6.10, 6.11 and 6.12 have been extracted are given in Fig. 6.13. The simulation uses the current commands from the torque-speed maps calculated in Chapter 9 in advance. It can be seen that the FOC algorithm adjusts the DC currents I_{dm}, I_{qm} and the amplitude of the AC current I_{dh} in order to accelerate to the desired speed and compensate

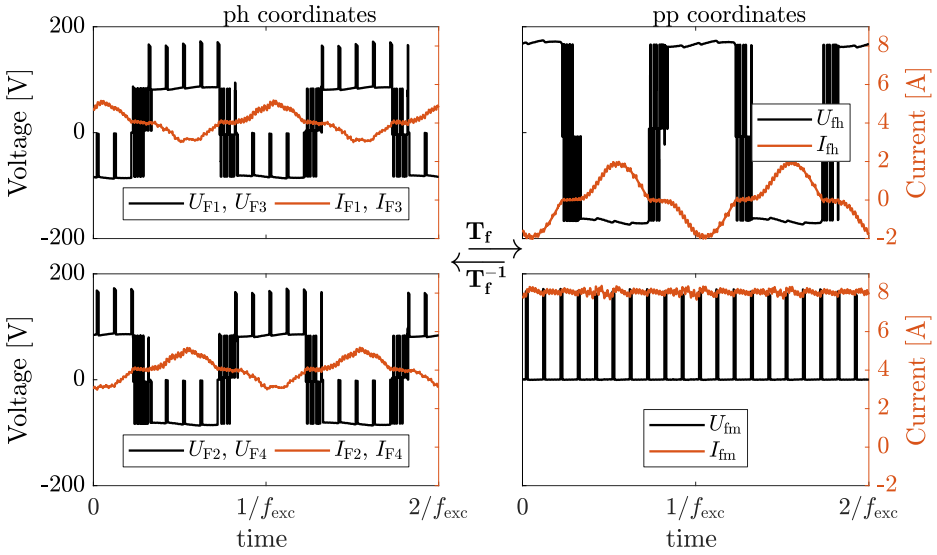

Figure 6.12: Rotor voltages (left axes) and currents (right axes) in the HESM in their respective coordinate systems.

the load step successfully. The p_h pole-pair machine rotor current I_{fh} is the result of I_{dh} and thus has the same envelope. As a result the field current I_{fm} is provided. Thus, the only difference compared to a conventional WRSM is that I_{fm} is the result of a transient event and reacts to changes in $\hat{I}_{dh}$. Here, an intrinsic drawback of all brushless excitation systems becomes apparent: The currents I_{dm}, I_{qm} respond to their respective current commands within milliseconds. However, the field current I_{fm} is only controlled indirectly by adjusting the amplitude $\hat{I}_{dh}$. Thus, the realizable rate of chance of field current $\mathrm{d}I_{fm}/\mathrm{d}t$ is reduced by the slower time constant of the p_h pole-pair machine. This means that the dynamics of the field current of a HESM always lag behind those of a conventional WRSM. It should be noted that the dynamic results presented in this section should not be understood as an optimal control solution with highly optimized dynamic behavior of the HESM, but rather as a functional implementation of the HESM control system.

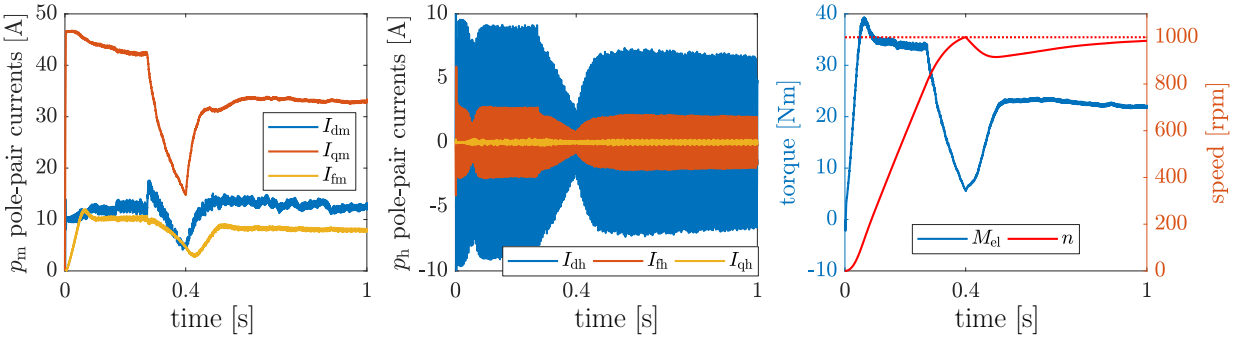

Figure 6.13: Acceleration of HESM from standstill to 1000 rpm with a 20 Nm load step at 0.4 s.

6.4.1 Influence of Saturation

In Fig. 3.1 it has been shown that the transferred excitation power depends mainly on the induced voltage on the rotor $U_{\mathrm{fh,ind}}$, the voltage drop over the self-inductance L_{fh} and an equivalent resistance R_{eq} which models the rectifier, buck converter and p_{m} pole-pair field winding. However, this representation neglects the saturation-dependence of the inductances. If saturation is included, the differential inductances, dL_{dfh} and dL_{fh} which depend on the magnetizing currents $I_{\mathrm{dm,mag}}$ and $I_{\mathrm{dh,mag}}$ must be used in the equivalent circuit. In Section 6.2 it has been shown that there is a significant reduction in the differential inductances dL_{dfh} and dL_{fh} under saturation, which motivates a closer inspection of the saturation behavior of the excitation system. As $I_{\mathrm{dh,mag}}$ — and hence the inductances — are time-dependent, a simple analytical solution for the equivalent circuit cannot be easily found.
In order to investigate the influence of saturation on the excitation system, the dynamic model is used to progressively step up the current amplitude $\hat{I}_{\mathrm{dh}}$ at a constant excitation frequency $f_{\mathrm{exc}} = 200\,\mathrm{Hz}$ and duty cycle $D = 11.5\,\%$. The p_{m} pole-pair machine is in no-load operation so that I_{dm} and I_{qm} are controlled to zero and only the field current I_{fm} is provided. After the field current I_{fm} has reached steady state, the mean value is evaluated and the next $\hat{I}_{\mathrm{dh}}$ step is carried out. The rotor DC link capacitor has a value of $100\,\mu\mathrm{F}$, which leads to a slight transient overshoot of I_{fm}. The results of the dynamic simulation are given in Fig. 6.14.

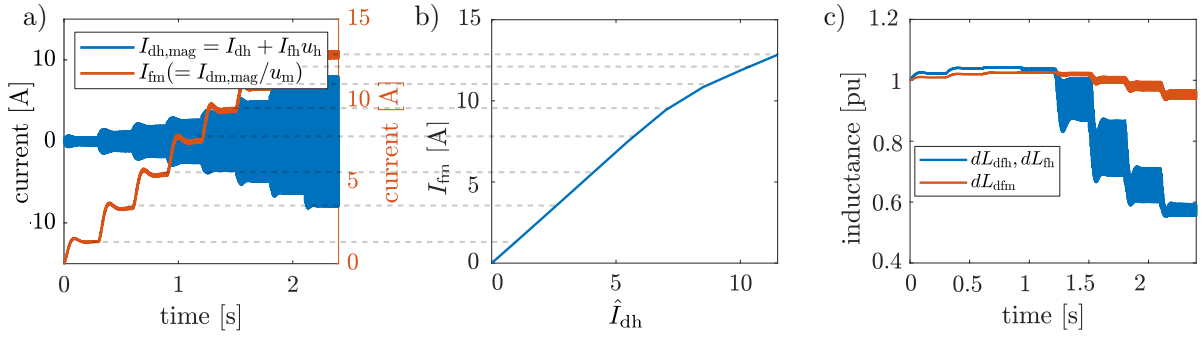

Figure 6.14: Effect of saturation on the excitation system capability to provide the field current I_{fm}: a) magnetizing currents under no load, b) I_{fm} per $\hat{I}_{\mathrm{dh}}$ curve c) time- and load-dependence of the excitation system inductances.

As $\hat{I}_{\mathrm{dh}}$ is increased and thus more field current I_{fm} is provided, both magnetizing currents $I_{\mathrm{dm,mag}} \sim I_{\mathrm{fm}}$ and $I_{\mathrm{dh,mag}} = I_{\mathrm{dh}} + u_{\mathrm{h}} I_{\mathrm{fh}}$ increase. In Fig. 6.14a it can be seen that the p_{m} pole-pair magnetizing current $I_{\mathrm{dm,mag}}$ is DC just like in a conventional WRSM, while the p_{h} pole-pair magnetizing current $I_{\mathrm{dh,mag}}$ oscillates. According to the inductance maps of Fig. 6.5 this leads to both a reduction of the mean value **and** an oscillation of the inductances dL_{dfh} and dL_{fh}, which can be seen in Fig. 6.14c. Once the HESM is strongly saturated, the oscillations almost vanish, which coincides with the inductance LUTs of Fig. 6.5. Overall,

the differential inductances decrease by more than 40 % at a field current of $I_{\mathrm{fm}} = 12.5\,\mathrm{A}$. However, this significant reduction of the mutual inductance L_{dfh} does not lead to a likewise drop of the $I_{\mathrm{fm}} - \hat{I}_{\mathrm{dh}}$ curve. Instead, in Fig. 6.14b only a slight drop of the transferred I_{fm} is observed. This is because the voltage equations (5.31) which govern the power transfer capability depend on both the induced voltage $U_{\mathrm{fh,ind}} \sim L_{\mathrm{dfh}}$ **and** the voltage drop over dL_{fh}. As the magnetizing currents saturate the inductances, the induced voltage $U_{\mathrm{fh,ind}}$ decreases, but the voltage drop over the saturated dL_{fh} also decreases significantly. This is why the $I_{\mathrm{fm}} - \hat{I}_{\mathrm{dh}}$ curve saturates to some extent, but not to the extent that the differential inductance dL_{dfh} implies.

In the following experiments and simulations, the HESM is operated near or below its rated field current $I_{\mathrm{fm}} = 10\,\mathrm{A}$. In this case, the excitation system performance is almost linear. This is why saturation is neglected in the following analysis and constant inductances are assumed for the HESM model. This does not introduce significant errors until rated currents are exceeded.

Chapter 7

Experimental Verification

7.1 Test Bench

In order to test the HESM prototype, a machine test bench has been built. An overview of the complete test bench is given in Fig. 7.1. It consists of the inverter-fed HESM prototype loaded by another inverter-fed load machine. The shafts of both machines as well as the DC links are connected so that the mechanical power circulates back into the DC link and only the losses have to be provided from the grid. The supply of the shared DC link is realized by an adjustable transformer connected to a B6 rectifier. An EMI filter between rectifier and transformer is used to reduce high-frequency leakage currents. Furthermore, blocking capacitors at the positive and negative DC link rails are used to provide a return path for leakage currents. The PWM signals to the HESM and WRSM driver boards are generated by a PLECS RT Box 1 which runs the FOC algorithms of both WRSM and HESM. The WRSM is speed-controlled and imposes the shaft speed on the HESM. Thus, the HESM can be tested with different load currents I_{dm}, I_{qm}, machine speeds and excitation system parameters $\hat{I}_{\mathrm{dh}}$, f_{exc} and D. The test bench is automated and controlled by a Python environment which sends the FOC control commands to the RT Box, triggers the measurement devices and stores the measurement data. A photograph of the test bench is shown in Fig. 7.2. Some important features of the test bench are briefly presented here:

HESM Prototype: The HESM has been constructed according to Chapter 6. For prototyping purposes, the HESM is still equipped with four slip-rings which connect to the external rotor circuitry: The utilization of slip rings has the advantage that mechanical and thermal issues do not have to be considered at the prototyping stage of the HESM. An important benefit of the slip rings is that the HESM can also be operated as a conventional WRSM by simply feeding the field current into the respective slip-ring terminals. Furthermore, the slip rings allow measuring the rotor quantities directly.

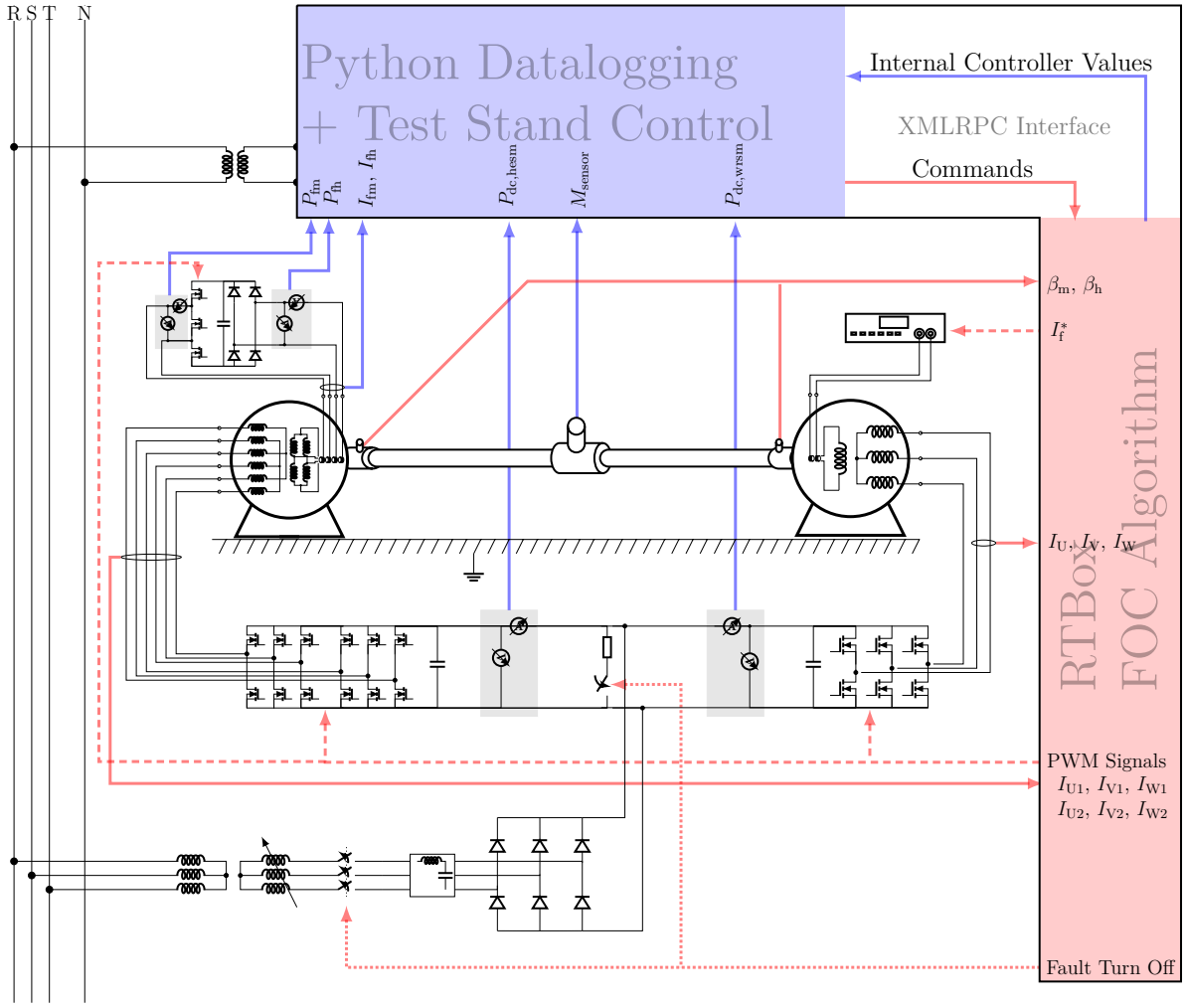

Figure 7.1: Overview of test bench with most important devices and measurement signals. Blue lines denote logged data. Red lines denote measurements that are used for the control algorithm. Dashed lines describe the output values of the control system.

HESM Power Electronics: Two identical custom-made B6 inverters with SiC-MOSFETs IMW120R045M1 have been designed to drive the HESM stator windings. They operate at a switching frequency of 8 kHz. The differential buck converter topology of the rotor circuit has also been designed with the same MOSFETs with a switching frequency of 2 kHz. The PCBs include LEM current transducers to measure the phase currents for the current controllers. The custom inverters have integrated desaturation protection via the half-bridge drivers 2ED020I12-F2, but no overtemperature, overvoltage or overcurrent protection.

HESM Resolver: The HESM requires knowledge of the rotor position with respect to the p_m as well as p_h pole-pair machine d-axes in order for the field-oriented control to work. To

this end the HESM is equipped with a single resolver of pole-pair number p_h. The resolver signal is demodulated using the Evaluation Board *EVAL-AD2S1210*. The raw positional angle β is read via SPI from the Plecs RTBox. The rotor angle β_i used in the respective dq transforms is then calculated as

$$\beta_\mathrm{i} = \beta \frac{p_\mathrm{i}}{p_\mathrm{h}} + \Delta\beta_\mathrm{i0} \qquad \text{with } i \in \{\mathrm{m}, \mathrm{h}\} \tag{7.1}$$

where $\Delta\beta_\mathrm{i0}$ aligns the respective coordinate system with the d-axis of the p_i pole-pair machine.

Load Machine and Inverter: The load WRSM is a prototype machine similar to the traction motor in the first generation of the electrical vehicle Renault Zoe. The machine has an integrated resolver which returns a cos-sin signal. The field winding is fed through brushes and slip-rings from an E&A PSI-5200-10A DC current source. The stator winding of the load motor is driven by a 65 kW, 200 A Semikron IGBT inverter SKS SL 20 GD 50/10 – E4 P1 which receives the digital PWM gate signals and returns the measured phase currents, DC link voltage and temperature as analog signals to the RTBox. Furthermore, the inverter has integrated overcurrent, short-circuit and overtemperature protection.

Rectifier and Break Chopper: A B6 diode bridge is connected through a three-phase contactor with the grid. As the power flows unidirectionally from grid to test bench, energy cannot be fed back into the grid. This is why an inverse power flow e.g. during deceleration of the machines causes the mechanical energy stored in the rotating shaft to be fed back into the DC link which charges the DC link capacitors. To avoid DC link overvoltage, a break chopper is used to dissipate the excess energy. For the break chopper a Semikron *SKM50GB12T4* IGBT module driven by the *SKHI22A* driver is used. The load resistor is a 25 Ω, 1 kW resistor.

Torque Measurement: A *TMS310* torque transducer with a rated torque of 200 Nm and a sensitivity of ±0.1 % is used to log the shaft torque. The torque sensor is highly overdimensioned for the rated HESM machine torque of 34 Nm, which limits the accuracy of the torque readings. This is especially critical for the smaller torques needed for the identification of the iron losses.

Power Measurement: A *ZES Zimmer LMG500* with two Aron circuits was used to directly measure the input to the two three-phase HESM stator windings. Furthermore, an *LMG310* was used to measure the DC link powers to the HESM and load machine. For the rotor, a *Norma Power Analyzer D4355* has been used to measure the mean value of the p_m pole-pair machine rotor current I_fm, voltage U_fm and field power P_fm. For the AC signals flowing in the p_h pole-pair field winding the respective rms values are recorded.

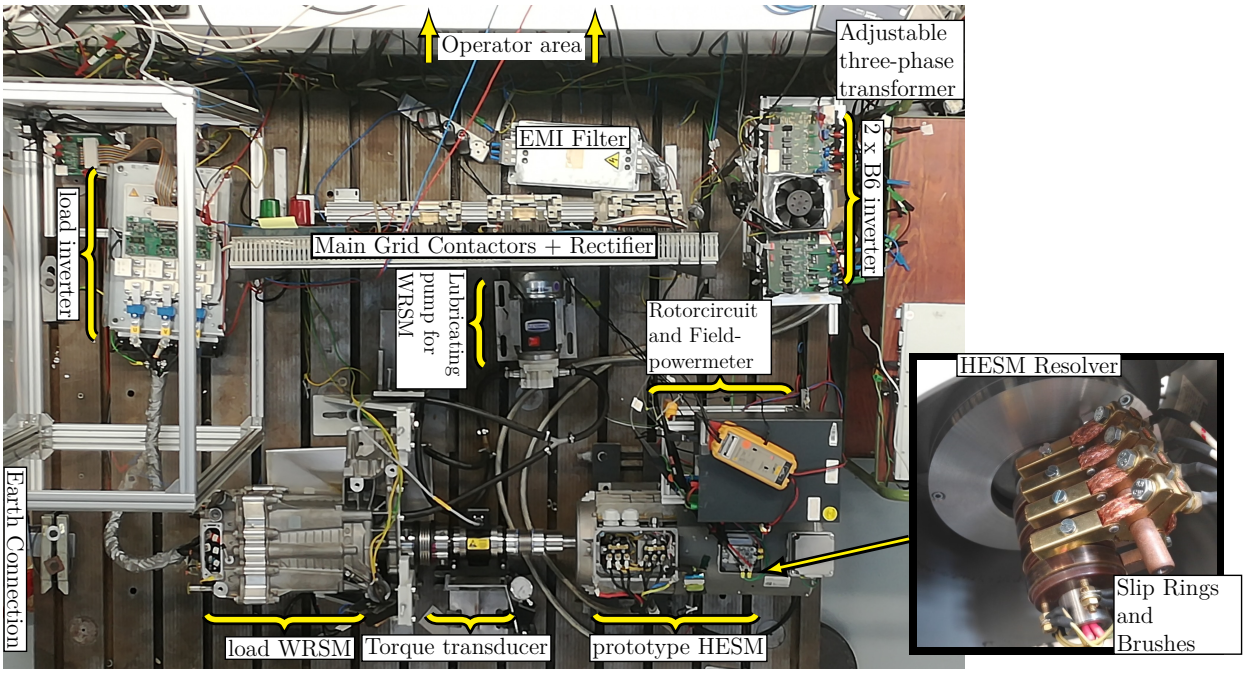

Figure 7.2: Photo of HESM test bench.

Controller: The FOC control algorithm of the HESM, according to Fig. 5.10, and the conventional FOC algorithm of Fig. 5.8 for the WRSM run on a single PLECS RT Box 1. In addition, the RT Box processes a data logging routine which records various internal controller variables and transmits them to the PC. Furthermore, the RT Box monitors the HESM and WRSM currents, the stator and rotor DC link voltages and the machine speed and can disconnect the grid and short-circuit the DC link in case of a fault.

7.1.1 Measurement of Losses

The machine efficiency is one of the most important performance criteria of electrical machines, which necessitates an accurate measurement of the losses. In the test bench the losses are not measured directly, but are determined indirectly from the input power to the stator windings P_{ph} and the mechanical shaft power P_{shaft}. The total power loss that is being dissipated **inside** of the machine is the sum of the **input** powers $P_{\mathrm{ph}} + P_{\mathrm{shaft}}$ minus the power that is being dissipated **outside** of the machine via friction and windage P_{fw}. This relationship is described by the power equilibrium in Fig. 7.3 and satisfies

$$P_{\mathrm{ph}} + P_{\mathrm{shaft}} - P_{\mathrm{fw}} \equiv P_{\mathrm{cu,sm}} + P_{\mathrm{cu,sh}} + P_{\mathrm{cu,fm}} + P_{\mathrm{cu,fh}} + P_{\mathrm{fe,m}} + P_{\mathrm{fe,h}} + P_{\mathrm{rect}}. \tag{7.2}$$

The losses generated inside of the HESM can be ascribed partly to the p_{m} and partly to the p_{h} pole-pair currents, even though such a division is a purely mathematical construct.

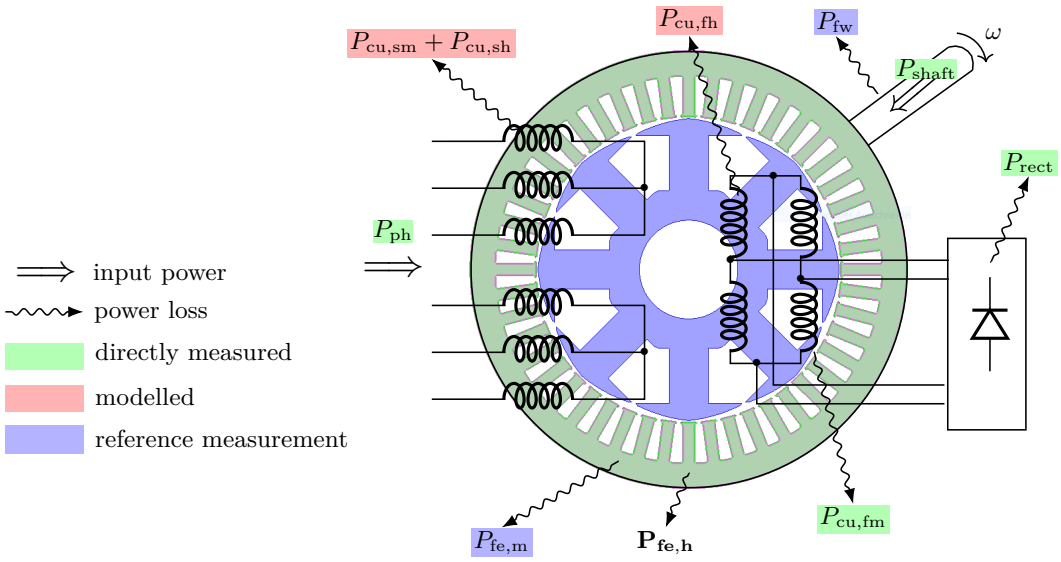

Figure 7.3: Power flow and losses of the HESM.

The loss components in Fig. 7.3 consist of

- the p_{m} pole-pair machine stator copper loss $P_{\mathrm{cu,sm}}$,
- the p_{h} pole-pair machine stator copper loss $P_{\mathrm{cu,sh}}$
- the p_{m} pole-pair machine copper loss $P_{\mathrm{cu,fm}}$, which is the field excitation power P_{fm},
- the p_{h} pole-pair machine rotor copper loss $P_{\mathrm{cu,fh}}$,
- the iron losses $P_{\mathrm{fe,m}}$ only attributable to the p_{m} pole-pair fields,
- the iron losses $P_{\mathrm{fe,h}}$ only attributable to the p_{h} pole-pair fields,
- the conduction and switching losses generated in the rotor power electronics P_{rect}.

Beside these loss components, additional losses occur in WRSMs because stray fields induce eddy currents in near conductive objects, e.g. in the end-winding region due to stray leakage or in the slots due to airgap stray fields penetrating the copper conductors [48]. However, as they can only be isolated with great effort, these losses are simply attributed to the iron losses. It should be noted that the segregation of the iron losses into two distinct components $P_{\mathrm{fe,m}}$ and $P_{\mathrm{fe,h}}$ is physically absurd: The iron losses are the result of a magnetization process which involves the actual magnetic fields in the iron core. This magnetization process cannot be decoupled into independent components. However, $P_{\mathrm{fe,h}}$ should be understood as a quantity which expresses the **iron loss increase under harmonic excitation** compared to the iron losses $P_{\mathrm{fe,m}}$ measured during normal WRSM operation. A thorough investigation of the iron losses $P_{\mathrm{fe,h}}$ is performed in Chapter 8.

In this work, a distinction between two types of efficiency is made. The **drive efficiency** η denotes the standard machine efficiency which is calculated directly from the measured shaft

and electrical power taking into account the directions of the power flow from Fig. 7.3.

$$\begin{array}{lll} & \text{Motor} & \text{Generator} \\ \text{Drive efficiency} & \eta = \dfrac{-P_{\text{shaft}}}{P_{\text{ph}}} & \eta = \dfrac{-P_{\text{ph}}}{P_{\text{shaft}}} \end{array} \tag{7.3}$$

The drive efficiency intrinsically includes all losses from both p_{m} and p_{h} pole-pair machine and is investigated in Chapter 9 of this work. However, as the p_{h} pole-pair machine losses are only a small portion of the total input power, the drive efficiency is not expressive to evaluate the excitation system. This is why an isolated look at only the **excitation system efficiency** η_{exc} is taken which only takes the p_{h} pole-pair machine into account.

$$\text{Excitation system efficiency} \qquad \eta_{\text{exc}} = \frac{P_{\text{fm}}}{P_{\text{ph}} + P_{\text{shaft}} - P_{\text{fe,m}} - P_{\text{fw}} - P_{\text{cu,sm}}} \tag{7.4}$$

For the calculation of η_{exc} the output power is the transferred field power $P_{\text{fm}} = P_{\text{cu,fm}}$. The input power to the excitation system can be obtained from the power balance (7.2) by subtracting all p_{m} pole-pair loss components from the total input power. Each of the terms in (7.4) have to be known: The stator input power P_{ph}, the shaft power P_{shaft}, the field winding input powers P_{fm} are measured directly in the test bench. However, the loss components $P_{\text{fe,m}}$, P_{fw} and $P_{\text{cu,sm}}$ are unknown internal losses. The friction and windage power P_{fw} is obtained by measuring the shaft torque of the current-free HESM at different speeds. The isolated p_{m} pole-par machine iron losses $P_{\text{fe,m}}$ can only be identified for specific operating points by performing a reference measurement at the identical load point with the HESM supplied as a WRSM. The p_{m} pole-pair machine copper losses $P_{\text{cu,sm}}$ can be obtained from the respective stator currents using Joule's law.
An important remark is that the iron losses $P_{\text{fe,h}}$ are sourced partially as electrical energy from the stator and partially as mechanical energy from the rotor: On the one hand, the rotary stator field moves asynchronously over the iron core and thus causes a changing magnetic field (=iron losses) in the stator and rotor iron. On the other hand, the rotating rotor field produces a fluctuating magnetic field which also drives iron losses. This means that both the electrical power as well as the shaft power must be measured in order to determine the excitation system efficiency. A great difficulty of measuring the relatively small excitation system losses experimentally (let alone separating the iron loss component $P_{\text{fe,h}}$) is measurement errors. $P_{\text{fe,h}}$ is only a few tens of percent of the excitation power which itself is only a few percent of the input power under rated operation. If e.g. $P_{\text{fe,h}} = 20\,\text{W}$ and 25 % of $P_{\text{fe,h}}$ were sourced from the shaft, then the large load torque of 30 Nm would be superimposed by a 24 mNm torque due to $P_{\text{fe,h}}$ (at an exemplary speed of $n = 2000\,\text{rpm}$). For the used torque transducer this additional torque is far below the required measurement precision, in fact only 0.012 % of the rated sensor torque. This is why the excitation system efficiency cannot be determined with great precision in this work.

7.2 Experimental Parameter Identification of HESM

In this section the test bench is used to experimentally identify and verify the HESM prototype. Design goals are checked and the influence of manufacturing and end-winding effects are identified.

7.2.1 Winding Resistances

The stator resistances R_{sm} and R_{sh} in pp (dq) coordinates are calculated directly from the coil resistance R_{c} by measuring the resistance between line and neutral and then applying (5.18)

$$R_{\mathrm{c}} = 0.255\,\Omega \qquad \rightarrow \qquad R_{\mathrm{sm}} = \frac{R_{\mathrm{c}}}{2} = 0.128\Omega \qquad R_{\mathrm{sh}} = 2R_{\mathrm{c}} = 0.51\,\Omega \qquad . \tag{7.5}$$

When the field resistance is measured between the slip-ring terminals, the contact resistance between the prototyping slip rings and carbon brushes is included in the measurement. This contact resistance decreases with higher load current and depends on the sliding velocity between the brushes and slip rings and can be roughly modelled with the following equation.

$$R_{\mathrm{fm}}(I_{\mathrm{fm}}, n) = 2.29\,\Omega + \frac{0.25\,\mathrm{V}}{I_{\mathrm{fm}}} + 0.00012\frac{\Omega}{\mathrm{rpm}} \cdot n\,[\mathrm{rpm}]. \tag{7.6}$$

The effect of machine temperature on the winding resistivity has been omitted in this work which is justified when the machine is either operated with relatively low load or loaded for relatively short periods of time.

7.2.2 No-Load and Short-Circuit Experiment

In conventional WRSMs the no-load (short-circuit) experiment is performed with the rotor winding excited and the stator winding left open (short-circuited). The phase voltages (phase currents) are then measured at varying speeds and field currents. The results give an important insight into the machine parameters of the d-axis and its saturation behavior. In a HESM, two no-load and short-circuit curves can be obtained, one for the p_{m} pole-pair machine and one for the p_{h} pole-pair machine by feeding a DC field current I_{fm} or I_{fh} into the appropriate terminals of the field winding. The equations that describe a WRSM in steady-state when the field winding is excited by a DC current can be derived from (5.23) by setting all derivatives to zero

$$\begin{bmatrix} U_{\mathrm{di}} \\ U_{\mathrm{qi}} \end{bmatrix} = \begin{bmatrix} R_{\mathrm{si}} & p_{\mathrm{i}}\omega L_{\mathrm{qi}} \\ -p_{\mathrm{i}}\omega_{\mathrm{m}} L_{\mathrm{di}} & R_{\mathrm{si}} \end{bmatrix} \begin{bmatrix} I_{\mathrm{di}} \\ I_{\mathrm{qi}} \end{bmatrix} + \begin{bmatrix} 0 \\ -p_{\mathrm{i}}\omega_{\mathrm{m}} L_{\mathrm{dfi}} I_{\mathrm{fi}} \end{bmatrix} \qquad i \in \{\mathrm{m}, \mathrm{h}\} \qquad . \tag{7.7}$$

In no-load operation no currents I_{di}, I_{qi} can flow so that only a voltage (back EMF) is induced into the q-axis. The mutual inductance L_{dfi} can directly be calculated from the measured back EMF between line and neutral as

$$U_{\mathrm{qi}} = p_{\mathrm{i}}\omega_{\mathrm{m}} L_{\mathrm{dfi}} I_{\mathrm{fi}} \qquad \rightarrow \qquad L_{\mathrm{dfi}} = \frac{U_{\mathrm{qi}}}{p_{\mathrm{i}}\omega_{\mathrm{m}} I_{\mathrm{fi}}} \quad . \tag{7.8}$$

In short-circuit operation, the voltages U_{di}, U_{qi} in (7.7) become zero. For sufficiently large speeds the stator resistance R_{si} can be neglected so that only a short-circuit current in the q-axis flows

$$I_{\mathrm{di}} = 0 \qquad I_{\mathrm{qi}} = \frac{L_{\mathrm{dfi}}}{L_{\mathrm{di}}} I_{\mathrm{fi}} \qquad \rightarrow \qquad L_{\mathrm{di}} = \frac{I_{\mathrm{qi}}}{I_{\mathrm{fi}}} L_{\mathrm{di}} \tag{7.9}$$

This equation can be used in conjunction with the mutual inductance L_{dfi} from the no-load experiment to determine the self-inductance L_{di}. If the no-load and short-circuit experiment are performed at different field currents I_{fi}, the saturation-dependence of the d-axis inductances can be identified.
This is performed in Fig. 7.4. It can be confirmed that the HESM can be energized as the two independent p_{m} and p_{h} pole-pair machines identified in Tab. 4.2 — each having their own no-load curve and short-circuit curve. The p_{m} pole-pair machine starts to saturate at a

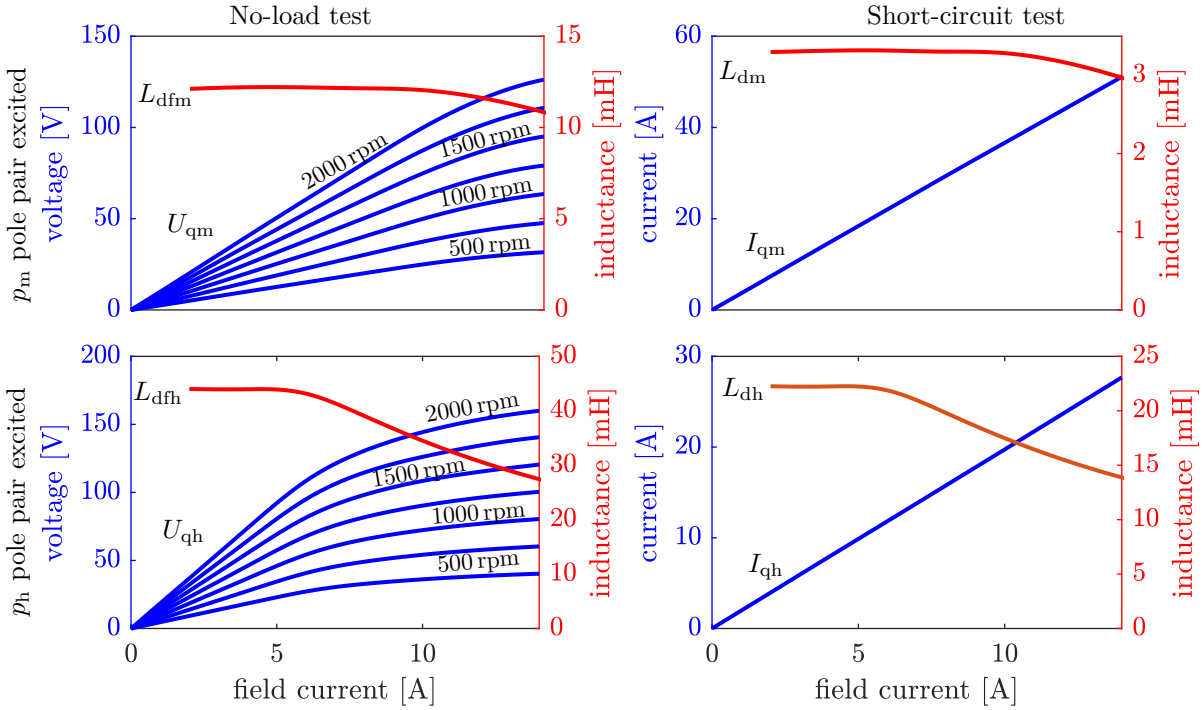

Figure 7.4: No-load and short-circuit curves and saturation-dependent d-axis inductances of the p_{m} and p_{h} pole-pair machine.

field current of $I_{\mathrm{fm}} = 11\,\mathrm{A}$. However, the p_{h} pole-pair machine saturates significantly faster at a field current of $I_{\mathrm{fh}} = 6\,\mathrm{A}$. This is mainly due to the larger yoke and tooth flux density as explained in Tab. 4.2. The non-saturated self- and mutual inductances for the d-axis can be read from Fig. 7.4 as

$$\begin{array}{lll} p_{\mathrm{m}} \text{ pole-pair machine} & L_{\mathrm{dm}} = 3.5\,\mathrm{mH} & L_{\mathrm{dfm}} = 12.2\,\mathrm{mH} \\ p_{\mathrm{h}} \text{ pole-pair machine} & L_{\mathrm{dh}} = 22.5\,\mathrm{mH} & L_{\mathrm{dfh}} = 41\,\mathrm{mH} \end{array} . \tag{7.10}$$

The linearly predicted inductance ratios $\frac{L_{\mathrm{dh}}}{L_{\mathrm{dm}}} = 8$ and $\frac{L_{\mathrm{dfh}}}{L_{\mathrm{dfm}}} = 4$ of Tab. 4.2 are $\sim 15\%$ smaller than those of the measured inductances. This is because saliency has been neglected in the simplified analytical model.

In Fig. 7.5 the no-load voltages and short-circuit current waveforms are depicted: While the p_{m} pole-pair machine waveforms are mostly sinusoidal, the p_{h} pole-pair machine contains large 5th and 7th harmonics due to large corresponding winding factors. Furthermore, it can be observed that the voltages and currents in two paths of a phase e.g. U1 and U2 are in phase for the p_{m} pole-pair machine and 180° out of phase for the p_{h} pole-pair machine. This observation illustrates the phasor star of Fig. 4.5. From the no-load and short-circuit experiment a low estimate of the referral factor u_{m} (u_{h}) used in the magnetizing currents (6.14) can be estimated from (7.9) as

$$u_{\mathrm{m}} > \frac{L_{\mathrm{dfm}}}{L_{\mathrm{dm}}} = 5.5 \qquad\qquad u_{\mathrm{h}} > \frac{L_{\mathrm{dfh}}}{L_{\mathrm{dh}}} = 2.9. \tag{7.11}$$

It should be noted that the real u_{m} (u_{h}) are slightly larger because the actual referral factors are calculated from the magnetizing inductances instead of the self inductances (see Section 5.2.3).

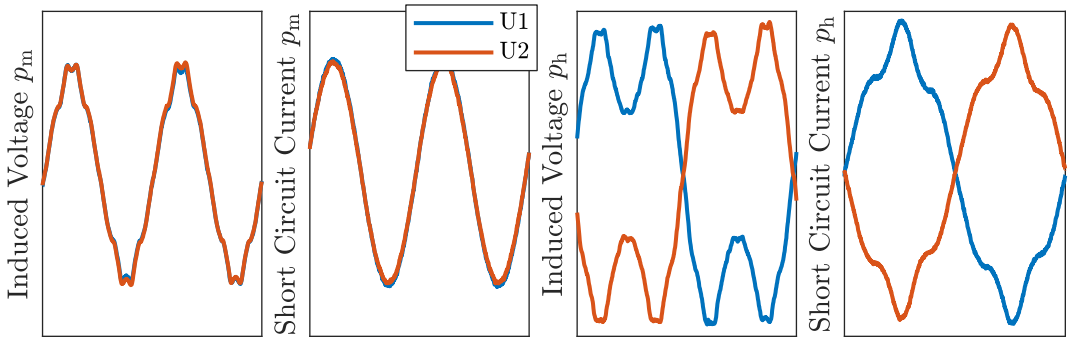

Figure 7.5: Voltage and current shapes for no-load and short-circuit experiment of p_{m} and p_{h} pole-pair machine respectively.

7.2.3 Rotor No-Load and Short-Circuit Experiment

In the previous section the no-load and short-circuit experiments are performed with the stator winding open or short-circuited and the rotor excited. In the HESM, the **inverse** no-load (short-circuit) experiment is an insightful test because it mimics the excitation system behavior. This experiment is only performed for the p_h pole-pair machine and is used to determine the self-inductance L_fh and to determine the correct alignment with the d-axis for the injection of the harmonic current I_dh. In this experiment the stator is excited by an oscillating d-axis current I_dh of amplitude $\hat{I}_\mathrm{dh}$ and excitation frequency f_exc and the rotor windings are open (short-circuited). The equation that governs the rotor no-load and short-circuit experiment is obtained using complex AC analysis as

$$\underline{U}_\mathrm{fh,ind} = \omega_\mathrm{exc}\frac{3}{2}L_\mathrm{dfh}\underline{\hat{I}}_\mathrm{dh} = (R_\mathrm{fh} + j\omega_\mathrm{exc}L_\mathrm{fh})\underline{\hat{I}}_\mathrm{fh} + U_\mathrm{fh} \tag{7.12}$$

according to the equivalent circuit in Fig. 3.1. For the no-load experiment ($\underline{\hat{I}}_\mathrm{fh} = 0$) the peak induced voltage $\hat{U}_\mathrm{ind,fh} = \frac{3}{2}\omega_\mathrm{exc}L_\mathrm{dfh}\hat{I}_\mathrm{dh}$ can be directly measured at the respective slip-ring terminals to determine the mutual inductance L_dfh. The results of the rotor no-load experiment are given in Fig. 7.6a and confirm the $L_\mathrm{dfh} = 41\,\mathrm{mH}$ value determined in the previous section. Saturation in the induced voltage $\hat{U}_\mathrm{ind,fh}$ cannot be observed. This coincides with the inductance map of dL_dfh in Fig. 6.5 which stays in the unsaturated region if no magnetizing current $I_\mathrm{dm,mag}$ is present. For the short-circuit experiment the rotor current $\hat{I}_\mathrm{fh}$ is measured as shown in Fig. 7.6b. For a sufficiently large excitation frequency (rotor resistance neglected), the self-inductance can then be calculated as

$$L_\mathrm{fh} = \frac{3}{2}\frac{\hat{I}_\mathrm{dh}}{\hat{I}_\mathrm{fh}}L_\mathrm{dfh} = 0.203\,\mathrm{H}. \tag{7.13}$$

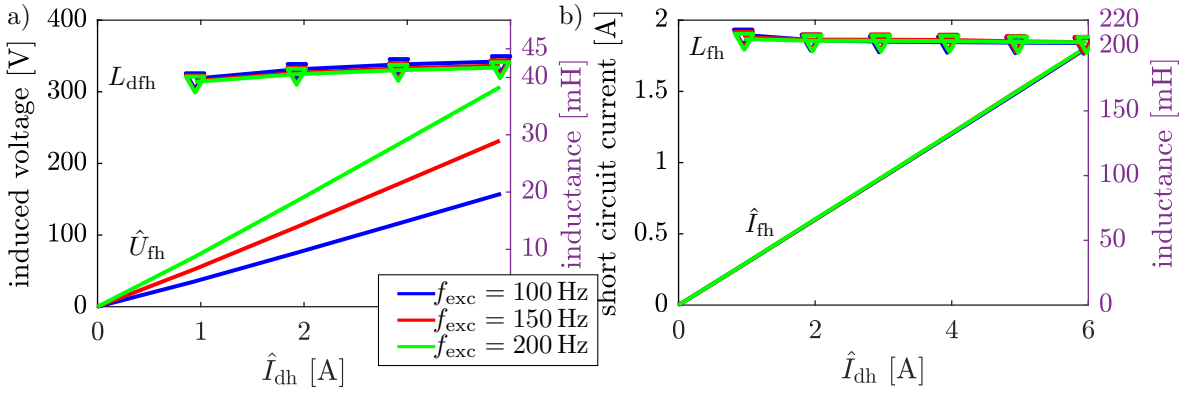

Figure 7.6: a) Rotor no load experiment and b) rotor short circuit experiment for different stator current amplitudes $\hat{I}_\mathrm{dh}$ and excitation frequencies f_exc at a rotor speed of $n = 500\,\mathrm{rpm}$.

7.2.4 Saliency Ratio

The no-load and short-circuit experiments only give insight into the d-axis parameters of the p_m and p_h pole-pair machine. Therefore, in this section a simple harmonic injection method is used to quantify the q-axis inductances L_qm and L_qh. To this end, the stator is fed with a voltage of fixed frequency f_i and amplitude U_i and a small rotor speed $f_\mathrm{m} << f_\mathrm{i}$ is imposed by the load machine so that the produced stator field rotates asynchronously. The field coil remains unfed. Due to the salient rotor, the phase inductance $L_\mathrm{i}(\beta)$ of the stator depends on the rotor position β. As a consequence, the measured stator currents $I_\mathrm{i} = \frac{U_\mathrm{i}}{L(\beta)}$ are modulated as a consequence of the rotor saliency. If the stator field is oriented with the d-axis (in a WRSM the axis of largest inductance) the positional inductance $L_\mathrm{i}(\beta)$ is maximum — referred to as L_di. Analoguously, if the stator field is aligned with the q-axis, $L_\mathrm{qi}(\beta)$ yields its smallest value L_qi. Thus, the saliency ratio can be calculated using

$$L_\mathrm{di} = \max\left(\frac{U_\mathrm{i}}{L(\beta)}\right) \qquad L_\mathrm{qi} = \min\left(\frac{U_\mathrm{i}}{L(\beta)}\right) \quad . \tag{7.14}$$

In Fig. 7.7 this test is performed with a carrier signal of $f_\mathrm{i} = 100\,\mathrm{Hz}$ and a machine speed of $n = 50\,\mathrm{rpm}$. If saliency exists in the machine, the measured current contains a component at the modulated frequency $f_\mathrm{mod} = f_\mathrm{i} - p_\mathrm{i} f_\mathrm{m}$. Fig. 7.7a reveals that this is the case for the p_m pole-pair machine. However, while a positional dependency can be observed for the p_h pole-pair machine in Fig. 7.7b, the frequency does not fit the expected reluctance frequency f_mod. This means that the inductances L_dh and L_qh have a positional dependence, but it cannot be attributed to saliency and is instead caused by higher order (saliency) harmonics. This is an inevitable artifact of the shape of the pole shoes which is fixed by the design of the p_m pole-pair machine. It should be noted that this approach only gives information about the saliency ratio in the unsaturated case. It is well known that in conventional WRSMs

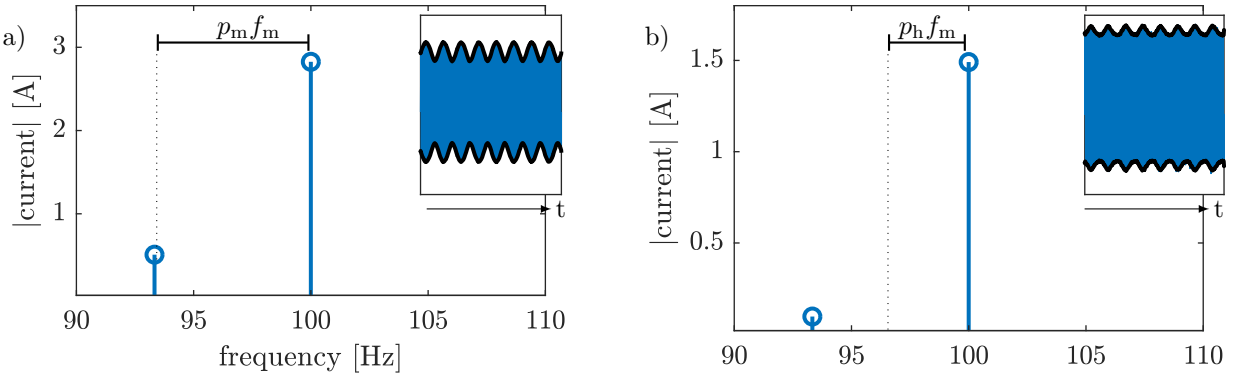

Figure 7.7: Stator currents under harmonic injection a) into the p_m pole-pair machine and b) into the p_h pole-pair machine.

the saliency depends on the saturation state of the machine since the d-axis (axis with more iron in the flux paths) saturates faster than the q-axis (axis of pole gap). The unsaturated saliency ratios of the p_m and p_h pole-pair machine thus yield

$$m_\mathrm{m} = \frac{L_\mathrm{dm}}{L_\mathrm{qm}} = 1.43 \qquad m_\mathrm{h} = \frac{L_\mathrm{dh}}{L_\mathrm{qh}} = 1 \tag{7.15}$$

7.2.5 Rotor Circuitry

The rotor circuitry that couples the p_h and p_m pole-pair slip-ring terminals is a vital part of the HESM functionality, because it performs the rectification and load impedance matching. In this section the losses of the designed rotor circuitry are investigated. They occur mainly due to conduction and switching losses in the diodes and MOSFETs. Conduction losses in MOSFETs arise due to the ohmic voltage drop in the conductive path during the ON state and are therefore proportional to the square of the load current. Switching losses occur when a semiconductor device switches between ON and OFF state because energy is required to charge or discharge the parasitic capacitances during each transition. Switching losses depend on the number of transitions (switching frequency) and the switching energy per transition which is related to the DC link voltage and load current. In order to quantify the losses, the input power P_fh at the rectifier terminals and the output power P_fm of the rotor circuitry are measured during HESM operation. Thus, the rectifier and differential buck converter are treated as an unknown two-port network integrated into the HESM drive system. The results are shown in Fig. 7.8 as a function of the excitation frequency f_exc, duty cycle D and load. The constant load current

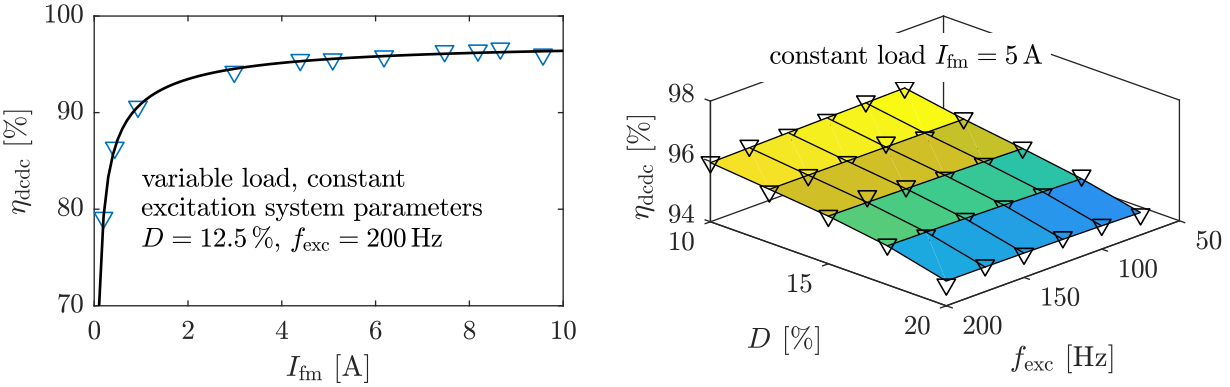

Figure 7.8: Efficiency of the rotor circuitry as part of the excitation system.

The dependence on the load current I_fm for constant excitation system parameters f_exc, D is depicted in Fig. 7.8a. It can be seen that at least 4 % in excitation system efficiency η_exc is lost just in the rotor power electronics, which is due to a non-optimal design. In Fig. 7.8b the influence of the excitation system parameters f_exc and D can be observed for

a constant load. The efficiency depends mainly on the buck converter duty cycle D with no impact of the excitation frequency f_{exc}. This can be explained using the buck converter equivalent circuit shown in Fig. 4.9: The proportional relationship between the input current and the duty cycle $I_{\mathrm{fh}} \sim D$ leads to larger conduction losses in the MOSFETs. While the rotor DC link voltage is antiproportional to the duty cycle $U_{\mathrm{dc,r}} \sim 1/D$ which increases the switching losses, the conduction losses dominate because of the low switching frequency of $f_{\mathrm{dcdc}} = 2\,\mathrm{kHz}$.

7.3 HESM Operation

7.3.1 No-Load Experiment of HESM

In order to investigate and validate the excitation system, the no-load test is performed for HESM operation by sweeping over the excitation system parameters f_{exc} and D at various machine speeds. An important distinction to the conventional no-load test performed for WRSMs is that the stator windings are not in open circuit. Instead, the drive inverters must be connected to the stator winding so that the FOC algorithm can inject the p_{h} pole-pair stator current I_{dh} for brushless excitation of the field current I_{fm}. In order to reach no-load, the p_{m} pole-pair currents $I_{\mathrm{dm}}, I_{\mathrm{qm}}$ are controlled to zero. For each variation of speed, excitation frequency f_{exc} and duty cycle D, the amplitude $\hat{I}_{\mathrm{dh}}$ is adjusted until a desired field current of $I_{\mathrm{fm}} = 5\,\mathrm{A}$ is reached. An I_{fm} value well below the rated field current 10 A is chosen because for low frequencies f_{exc} and high duty cycles D the current amplitude $\hat{I}_{\mathrm{dh}}$ becomes large. In the following figures the surface plot denotes the quantities at the minimum speed 350 rpm for which the experiment has been performed. The speed-dependent evolution of the quantities until a maximum speed of 2400 rpm is highlighted with blue arrows.
In Fig. 7.9 the amplitudes of the p_{h} pole-pair stator current $\hat{I}_{\mathrm{dh}}$, rotor current $\hat{I}_{\mathrm{fh}}$ and magnetizing current $I_{\mathrm{dh,mag}}$ (calculated from (6.14)) are shown. The blue arrows shows that there is only a minor speed-dependence which is likely due to a degradation of the current tracking at higher speeds and a slight speed dependence of the field winding resistance due to the slip rings. This means, that the excitation system can supply the field current I_{fm} regardless of the speed. Only for an excitation frequency of $f_{\mathrm{exc}} = 50\,\mathrm{Hz}$ a noticeable increase of the required stator current $\hat{I}_{\mathrm{dh}}$ can be observed. This is due to the fact that the currents for $f_{\mathrm{exc}} = 50\,\mathrm{Hz}$ are getting increasingly distorted, which relates to a worse power transfer capability as indicated in Section 6.3. The behavior of the excitation system currents $\hat{I}_{\mathrm{dh}}$, $\hat{I}_{\mathrm{fh}}$ and $\hat{I}_{\mathrm{dh,mag}}$ coincides with the linear theory: An increase in excitation frequency f_{exc} goes in line with a reduction of the stator current demand $\hat{I}_{\mathrm{dh}}$. This coincides with (3.43), which reveals a linear relationship of f_{exc} with the transferred power (assuming the rising voltage drop in the field winding inductance is neglected).
An increase of the duty cycle D can either result in an increase or decrease of the current de-

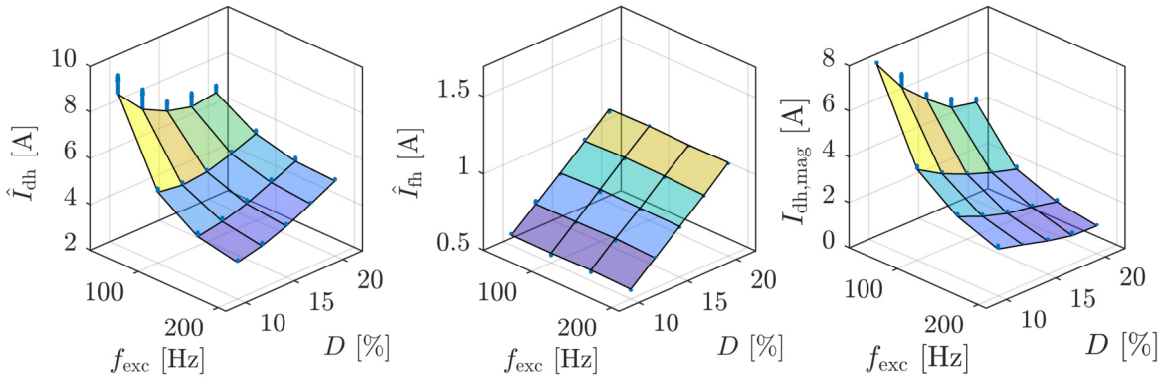

Figure 7.9: Measured p_{h} pole-pair currents as a function of excitation frequency f_{exc} and buck converter duty cycle D and speed.

mand $\hat{I}_{\mathrm{dh}}$ depending on the excitation frequency f_{exc}. The reason for this is that the voltage drop over the inductance $\omega_{\mathrm{exc}} L_{\mathrm{fh}}$ (source impedance) and load resistor R_{eq} is an impedance matching problem. In general, while the inequality $\omega_{\mathrm{exc}} L_{\mathrm{fh}} < \frac{R_{\mathrm{fm}}}{D^2}$ is satisfied, an increase of the duty-cycle D results in lower current demand $\hat{I}_{\mathrm{dh}}$. The field current $\hat{I}_{\mathrm{fh}}$ is dependent only on D, according to the step-down converter transfer function $I_{\mathrm{fh}} \sim I_{\mathrm{fm}}/D$. The peak magnetizing current $\hat{I}_{\mathrm{dh,mag}}$ decreases with increasing f_{exc} as a result of the decreasing stator current amplitude $\hat{I}_{\mathrm{dh}}$. The magnetizing current also decreases with increasing duty cycle D, because at lower load resistances $R'_{\mathrm{eq}} \sim 1/D$ the field winding acts more and more like a short-circuit where the stator and rotor currents approach a 180° phase shift.

In order to evaluate the excitation system efficiency, (7.4) highlights that a reference measurement $P_{\mathrm{fe,m}}$ is necessary. As explained in Section 7.1.1, $P_{\mathrm{fe,m}}$ denotes the iron losses of the machine prototype when it is operated as a WRSM. The no-load experiment has the advantage that the mechanical shaft is only loaded by friction, windage and iron losses. Therefore, $P_{\mathrm{fe,m}}$ can directly be obtained from a WRSM-no-load experiment where only the field current $I_{\mathrm{fm}} = 5\,\mathrm{A}$ is supplied (and the previously measured friction and windage losses are subtracted). However, the question arises whether to leave the stator windings in open circuit (as in WRSM no load), or to connect the inverter to the stator windings (as required in HESM no load). In the first case, iron losses only due to rotation of the electromagnet are supplied from the shaft. In the latter case, the inverter produces an additional, small PWM current ripple in the stator windings which produces noticeable iron losses. On the left side of Fig. 7.10, the efficiency is calculated with stator windings in open circuit, on the right side with the inverter connected. A commonality in both cases is that the efficiency η_{exc} drops significantly for low excitation frequencies f_{exc} and large duty cycles D which coincides with the higher copper losses produced by the currents $\hat{I}_{\mathrm{dh}}$ and $\hat{I}_{\mathrm{fh}}$. The efficiency is less than 80 % in all cases and thus significantly lower than predicted from the copper and power-electronic losses alone. This indicates that iron losses play a major role in the excitation

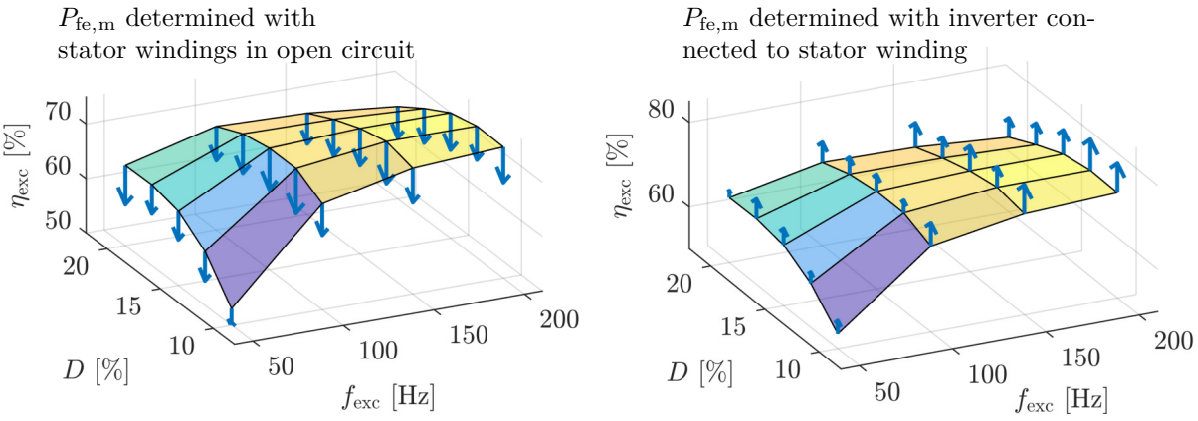

Figure 7.10: Measured excitation system efficiency.

system efficiency. In both cases, the blue arrows highlight a significant speed-dependence of the losses albeit with a different trend: It can be seen that the efficiency **decreases** by 7% as a function of speed if $P_{\mathrm{fe,m}}$ is determined with open stator windings. On the contrary, the efficiency **increases** by 5 % if $P_{\mathrm{fe,m}}$ is determined with the inverter connected. This is because the reference losses $P_{\mathrm{fe,m}}$ (which are subtracted from the HESM-no-load losses) are larger in the latter case as they include the additional PWM-induced iron losses. As the PWM-induced current ripple is also present in the HESM-no-load experiment, the reference measurement $P_{\mathrm{fe,m}}$ with the inverter connected more closely describes the actual excitation system efficiency. Thus, in Fig. 7.10 a peak efficiency of $75 - 80\,\%$ can be observed at duty cycles $10 - 12.5\,\%$ and at an excitation frequency of $f_{\mathrm{exc}} = 200\,\mathrm{Hz}$. A surprising result is that the efficiency increases with rising rotor speed.

Voltage and Current Demand

From the HESM-no-load experiment, two important performance characteristics of the excitation system can be determined: The DC link voltage demand U_{dc} per field current I_{fm} and the field current I_{fm} per harmonic current $\hat{I}_{\mathrm{dh}}$ expressed by the values

$$k_{\mathrm{Uh}} = \frac{U_{\mathrm{dc}}}{I_{\mathrm{fm}}} \qquad \text{and} \qquad k_{\mathrm{Idh}} = \frac{I_{\mathrm{fm}}}{\hat{I}_{\mathrm{dh}}}.$$

Fig. 7.11 compares the measured values of k_{Idh} and k_{Uh} with the values obtained using the analytical steady-state model (5.44) and (5.45). The internal controller voltages U_{dh} and U_{qh} recorded during the experiment are used to calculate the peak voltage demand $\hat{U}_{\mathrm{h}}$ of the p_{h} pole-pair machine. As some speed dependence of the controller voltages occurs due to winding harmonics, noise and irregular voltage spikes, they are removed by performing an FFT and extracting only odd multiples of the excitation frequency f_{exc} so that a smooth voltage demand $\hat{U}_{\mathrm{h}}$ for the calculation of k_{Uh} is obtained. The (lack of) blue arrows confirm

that no significant speed-dependence of the voltage demand k_{Uh} occurs when the relationship $f_{\mathrm{exc}} < f_{\mathrm{m}}/p_{\mathrm{h}}$ is fulfilled which coincides with (5.43). This condition is only violated for an excitation frequency of $f_{\mathrm{exc}} = 50\,\mathrm{Hz}$ once a machine speed of $f_{\mathrm{exc}}/p_{\mathrm{h}} = 1500\,\mathrm{rpm}$ is exceeded so that a significant increase of k_{Uh} is measured. Overall, the analytical model underestimates the voltage demand k_{Uh} and overestimates the current demand k_{Idh}, which is to be expected as the analytical model assumes sinusoidal currents and voltages, which is violated especially for small D and large f_{exc}. The measured values of k_{Uh} and k_{Idh} are used as LUTs in the following work to quickly determine how much stator current $\hat{I}_{\mathrm{dh}} = k_{\mathrm{Idh}} I_{\mathrm{fm}}$ and DC link voltage $U_{\mathrm{dc}} = k_{\mathrm{Uh}} I_{\mathrm{fm}}$ is required by the p_{h} pole-pair machine in order to supply a given field current for any combination of excitation system parameters f_{exc} and D.

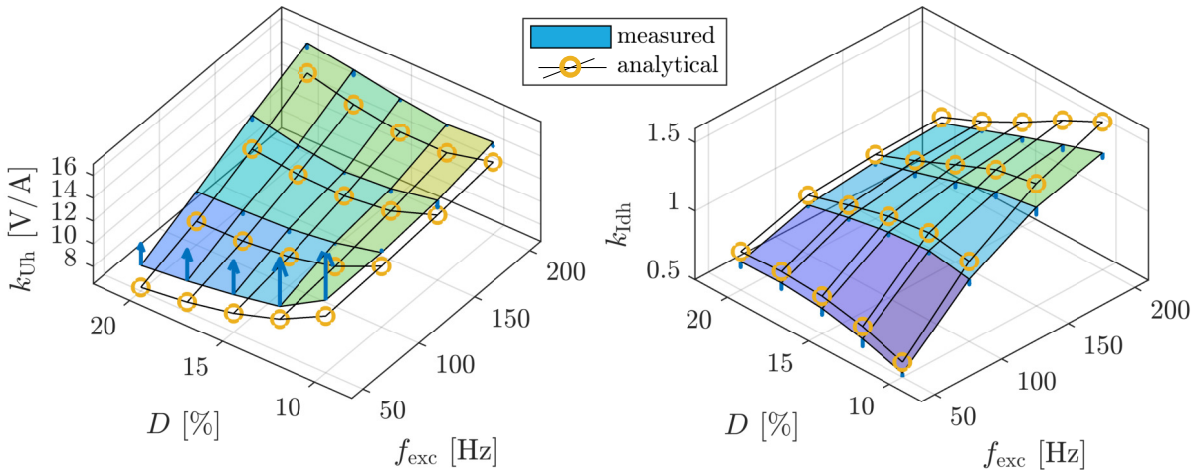

Figure 7.11: Characteristic values k_{Idh} and k_{Uh} of the excitation system.

Excitation System Loss Components

According to the power balance (7.2), the additional losses produced by the excitation system compared to conventional WRSM excitation can be calculated using

$$\Delta P_{\mathrm{v}} = P_{\mathrm{ph}} + P_{\mathrm{shaft}} - P_{\mathrm{fw}} - P_{\mathrm{fm}} - P_{\mathrm{cu,sm}} - P_{\mathrm{fe,m}}. \tag{7.16}$$

However, ΔP_{v} only denotes the total power losses and does not give insight into the distribution of the loss components. In this section, the loss components $P_{\mathrm{cu,sh}}$, $P_{\mathrm{cu,fh}}$, P_{rect} and $P_{\mathrm{fe,h}}$ described in Section. 7.1.1 are identified. The total copper losses $P_{\mathrm{cu,sm}}$ and $P_{\mathrm{cu,fh}}$ dissipated in the stator and rotor can be calculated from the Joule losses as

$$P_{\mathrm{cu,h}} = \sum_{\mathrm{k}} \frac{3}{4} R_{\mathrm{sh}} \left({}^{k}\hat{I}^2_{\mathrm{dh}} + {}^{k}\hat{I}^2_{\mathrm{qh}} \right) + \frac{1}{2} R_{\mathrm{fh}} \, {}^{k}\hat{I}^2_{\mathrm{fh}} \tag{7.17}$$

where ${}^{k}\hat{I}_{\mathrm{dh}}$ (${}^{k}\hat{I}_{\mathrm{fh}}$) denotes the k-th Fourier component of the measured currents I_{dh} (I_{fh}). The Fourier analysis takes into account the harmonic content of the currents I_{dh} and I_{fh}. As the current components due to the fundamental frequency f_{exc} dominates the losses an approximation using only the fundamental component can also be used. The rotor power electronic loss P_{rect} is measured directly. The copper losses and power electronic losses are speed-independent, because the operating currents I_{dh}, I_{fh} (and voltages) do not change (see Fig. 7.9). The difference of the total losses from the known losses yields the iron losses $P_{\mathrm{fe,h}}$ of the excitation system.

$$P_{\mathrm{fe,h}} = \Delta P_{\mathrm{v}} - P_{\mathrm{cu,sh}} - P_{\mathrm{cu,fh}} - P_{\mathrm{rect}}. \tag{7.18}$$

Fig. 7.12 displays the iron losses $P_{\mathrm{fe,h}}$ and their speed-dependence in absolute terms and as a percentage relative to the total excitation system losses. The inverter is connected to the stator winding so that the arrows signify a decreasing trend of $P_{\mathrm{fe,h}}$ with rising speed. Overall, $P_{\mathrm{fe,h}}$ dominates the losses especially for large excitation frequencies f_{exc} and low duty-cycles D: At the operating point $D = 11.5\,\%$ and $f_{\mathrm{exc}} = 200\,\mathrm{Hz}$ where optimal efficiency is reached close to 60 % of the excitation system losses are caused by iron losses. For lower excitation frequencies and high duty cycles the iron losses drop beneath 30 % of the total losses and thus still remain significant. The losses in the rotor circuit P_{rect} only amount to about 5 % (see Section 7.2.5). The rest of the losses is due to stator and rotor copper losses $P_{\mathrm{cu,sh}}$ and $P_{\mathrm{cu,fh}}$. The large proportion of the iron losses motivates a more thorough analysis of the iron losses. This is why a quantitative look at the origin, magnitude and speed-dependence of the iron losses will be taken in Chapter 8.

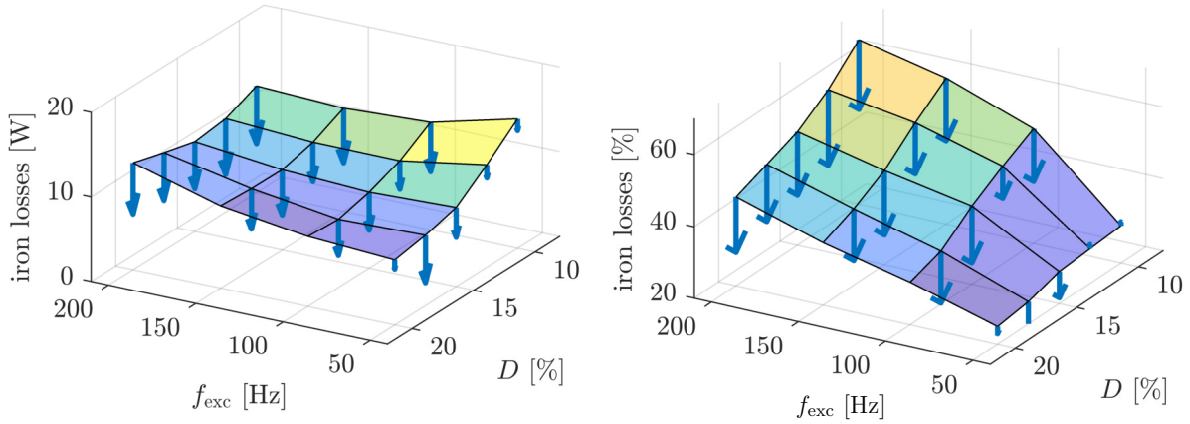

Figure 7.12: Envelope of the speed-dependent iron losses in absolute and relative terms.

7.3.2 Current Tracking and Spectrogram

When operated as a variable-speed drive, the HESM control system needs to track the sinusoidal current I_{dh} even during transient speed changes. In order to demonstrate the capability of the excitation system to provide the excitation current during transient events, a speed ramp from 0 to 2000 rpm is imposed by the load machine while a constant excitation current is supplied. The results are shown in Fig. 7.13. It can be seen that the field current I_{fm} is successfully supplied during the entire transient event. The fundamental f_{exc} frequency components of I_{dh} and I_{fh} obtained via Fourier transformation highlight that the FOC algorithm can track the sinusoidal reference values even during speed changes.

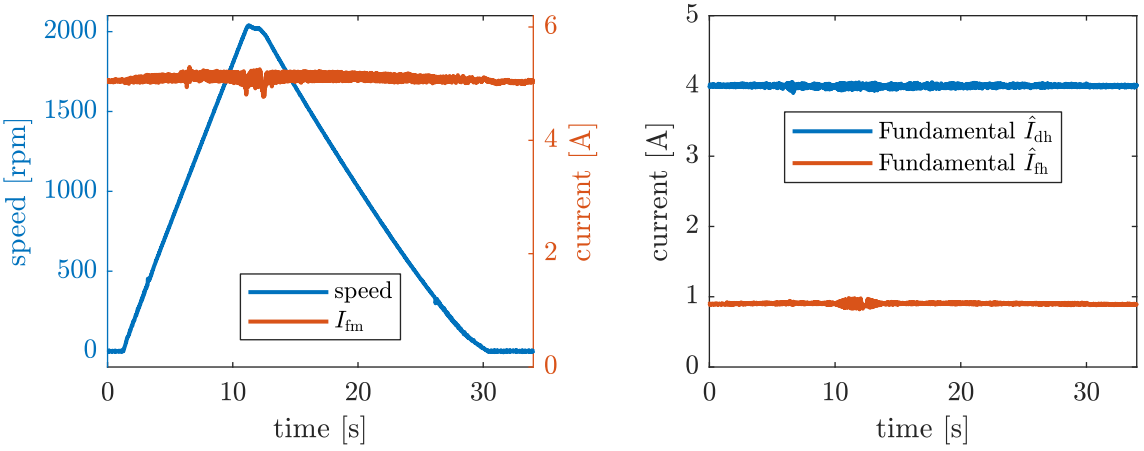

Figure 7.13: Transient behavior of the excitation system during acceleration and deceleration for a constant $I_{\mathrm{fm}} = 4\,\mathrm{A}$ at $f_{\mathrm{exc}} = 200\,\mathrm{Hz}$ and $D = 11.5\%$.

However, the Campbell diagram shown in Fig. 7.14 which extracts the frequency spectrum as a function of speed from a measured stator phase current and rotor current I_{fh} reveals that beside the fundamental frequency, a rich harmonic spectrum occurs. The harmonics correspond to the predicted frequencies from the harmonic field analysis in Tab. 3.3 and are summarized underneath the spectrogram. The dominant fundamental stator frequencies of ordinal numbers $\nu_{\mathrm{h}\pm} = \pm 1$ and $h = 1$ are superimposed by a pronounced third harmonic ($h = 3$) due to the rectifier. Higher order rectifier harmonics $h = 5, 7, \ldots$ occur as well, but are cropped for better visualization here. Furthermore, stator and rotor currents related to the ordinal numbers $\nu_{\mathrm{h}\mp} = \pm 5$ and $\nu_{\mathrm{h}\pm} = \pm 7$ can be identified which occur due to parasitically induced voltages that propagate through the control system undamped. Frequencies related to slotting are almost non-existent. A special case occurs at a speed of $n = 2000\,\mathrm{rpm}$. It can be seen that the frequency of the backward rotating field $f_{-} = f_{\mathrm{exc}} - p_{\mathrm{h}} f_{\mathrm{m}}$ and the p_{m} pole-pair machine electrical frequency $p_{\mathrm{m}} f_{\mathrm{m}}$ coincide. This leads to some interaction between the p_{m} and p_{h} pole-pair FOC controllers.

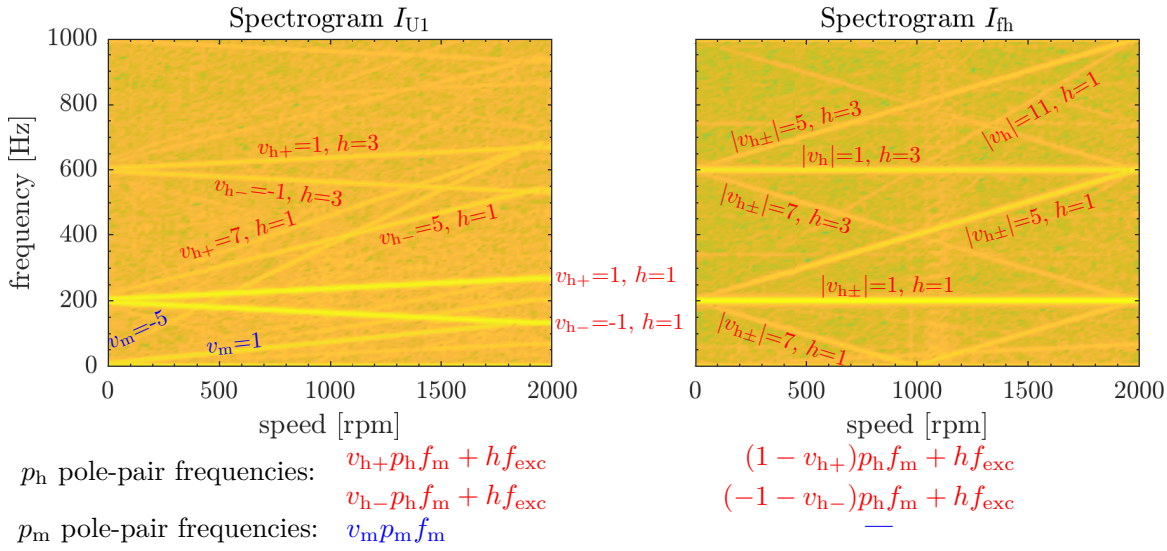

Figure 7.14: Campbell diagram of phase current and field current I_{fh} for HESM-no-load experiment.

7.3.3 Load Step

Up to this point, the HESM has only been operated without load currents I_{dm} and I_{qm}. In this section the response of the HESM to a load step of 30 Nm at a constant speed of $n = 500$ rpm is demonstrated. The desired p_m pole-pair currents are $I^*_{dm} = 0$ A, $I^*_{qm} = 40$ A and rated field current $I^*_{fm} = 10$ A. The excitation system operates at an excitation frequency of $f_{exc} = 200$ Hz and a duty cycle of 11.5 % and requires a current of amplitude $\hat{I}_{dh} = k_{Idh} I_{fm} = 8\,A$ to supply the field current. At this saturation level, a slight reduction of the k_{Idh} value read from Fig. 7.11 must be taken into account which coincides with the results of the dynamic simulation (Section 6.4.1). It should be noted that this operating point has only been chosen to confirm the simultaneous torque generation and harmonic excitation and is not the result of an operating point optimization. For the determination of optimal HESM drive currents and the analysis of the HESM speed region see the dedicated Chapter 9.
The reason for the low speed of $n = 500$ rpm is **firstly** that the maximum DC link voltage $U_{dc} = 400$ V would be exceeded at rated speed and torque due to the voltage demand of the excitation system: According to the k_{Uh} value extracted from Fig. 7.11 the p_h pole-pair machine already takes away about $U_{dc} = k_{Uh} I_{fm} = 150$ V of DC link voltage just to provide the field current of $I_{fm} = 10$ A. Thus, only a stator voltage of $\hat{U}_m = k_{mod}(U_{dc} - k_{Uh} I_{fm}) = 125$ V remains for the phase voltages of the p_m pole-pair machine. This is not sufficient to operate the HESM at rated speed. **Secondly**, due to test bench limitations, operation at lower speeds has been deemed more secure at the prototyping stage.

The results of the load step are shown in Fig. 7.15. While the dynamics of the HESM have not been investigated in the scope of this thesis, it should be noted that the slow build-up of the HESM torque shown in Fig. 7.15c is not due to inherent limitations. In fact, Fig. 7.15a

discloses that the ramp-up of I_{fm} is significantly faster than the ramp-up of the load current I_{qm} which has intentionally been chosen small here. Furthermore, the large response time of the load WRSM to the HESM load step is due to an intentionally slow speed controller. In Fig. 7.15b a close-up of the p_{h} pole-pair excitation system currents is shown. It can be seen that the p_{h} pole-pair machine currents I_{dh} and I_{fh} are largely unaffected by the p_{m} pole-pair load currents. The slight ripple on top of the field current I_{fm} is likely caused by parasitically induced voltages due to coupling from the same pole pair or in-between pole pairs. Fig. 7.15d displays the internal controller voltages U_{dh}, U_{qh}. A sinusoidal shape of the voltages can be observed although harmonics at multiples of the excitation frequency occur because the controller still reacts to harmonics in the measured currents. It can be seen that the d-axis voltage U_{dh} dominates the voltage demand and the q-axis voltage U_{qh} is small, which coincides with the predicted analytical expressions (5.42) for small speeds and large excitation frequencies.

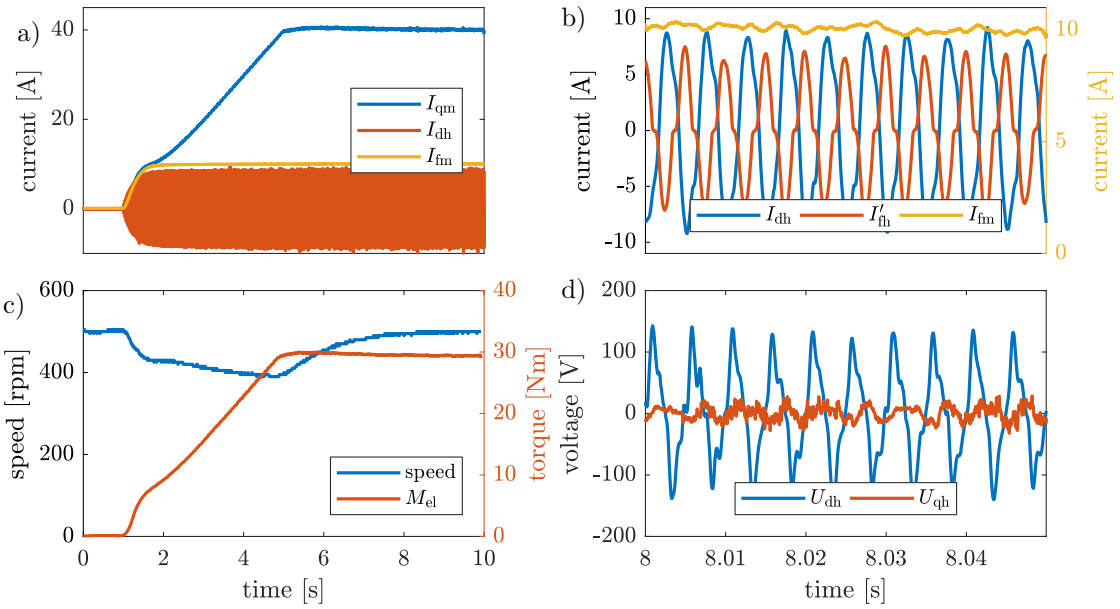

Figure 7.15: Measurement results for load step to 30 Nm at $n = 500$ rpm.

In conclusion, the capability of the HESM to brushlessly supply the field current even during speed changes while simultaneously producing a load torque can be verified in this chapter. However, questions concerning the machine efficiency and the torque speed region arise due to the large amount of iron losses identified in Section 7.3.1 and the large voltage demand expressed by the high k_{Uh} value. These questions are addressed in the following chapters.

Chapter 8

Iron Losses

In the previous chapter the HESM prototype has been put into operation revealing that the excitation system efficiency cannot be explained merely by considering the copper losses produced in stator and rotor. Instead, at the *best* operating conditions $f_{\mathrm{exc}} = 200\,\mathrm{Hz}$, $D = 11.5\,\%$, the iron losses account for more than $50\,\%$ of the total excitation system losses. To highlight the severity of this result, it should be noted that the excitation system efficiency would be larger than $90\,\%$ (instead of $75-80\,\%$) if iron losses were neglected. Thus, in this chapter, the reason for the high iron losses will be analyzed and an attempt at modelling and calculating these losses in advance will be made.

Iron losses constitute the largest loss component in electrical machines apart from copper losses. While copper losses are modelled directly as resistive losses in equivalent circuits, iron losses are not directly included in linear machine theory or even Finite-Element-Analysis: The analytical models derived in Chapter 3 use the relationship $B = \mu_0\mu_{\mathrm{r}}H$ with the assumption of an infinitely permeable iron core ($\mu_{\mathrm{r}} \to \infty$) to model the magnetic fields. Most FE software considers a finite, saturation dependent term $B = \mu_0\mu_{\mathrm{r}}(H)H$ for the relative permeability. However, both formulas omit the actual magnetization process in the steel sheets of electrical machines and imply that the H and B fields are always in phase. Actually, in any ferromagnetic material exposed to a changing magnetic field, the magnetization lags behind the applied field as the magnetic domains rotate and domain walls move in the direction of the field. This phenomenon is commonly referred to as hysteresis and the actual relationship between H and B is thus described by a hysteresis loop. For arbitrary H and B waveforms, the power loss due to magnetization can be calculated by integrating the time-dependent loss density p_{fe} over one electrical (symmetry) period T_{sym} of the H and B waveforms

$$p_{\mathrm{fe}} = \frac{1}{T_{\mathrm{sym}}} \int_0^{T_{\mathrm{sym}}} p_{\mathrm{v}}(t)\mathrm{d}t \qquad \text{with} \qquad p_{\mathrm{v}}(t) = H(t)\frac{\mathrm{d}B(t)}{\mathrm{d}t} \qquad . \tag{8.1}$$

This integral describes that the losses generated in a ferromagnetic material are proportional to the area enclosed by a hysteresis loop. The most common method to quantify these losses in electrical machines is with an empirical approach which categorizes the losses into *classical* hysteresis losses p_{hys}, eddy current losses p_{eddy} and excess losses p_{exc} [49]. Eddy current losses describe the Joule losses generated in the conductive iron laminations due to currents induced by the changing magnetic field. Excess losses denote anomalous eddy losses due to movement of the domain walls under the changing magnetic field. The classical hysteresis loss describes the hysteresis phenomenon under quasi-stationary excitation, i.e. when eddy and excess losses are negligible. If the flux density in a ferromagnetic material is homogenous and sinusoidal, the specific iron losses can be calculated from the frequency f and peak flux density $\hat{B}$ as

$$p_{\mathrm{tot}} = \underbrace{K_{\mathrm{h}}\hat{B}^2 f}_{p_{\mathrm{hys}}} + \underbrace{K_{\mathrm{c}}\hat{B}^2 f^2}_{p_{\mathrm{eddy}}} + \underbrace{K_{\mathrm{e}}\hat{B}^{1.5} f^{1.5}}_{p_{\mathrm{exc}}} \qquad \left[\frac{\mathrm{W}}{\mathrm{m}^3}\right] \tag{8.2}$$

where K_{h}, K_{c}, K_{e} are coefficients that must be fitted to experimental data or determined from material properties. However, in electrical machines, the flux density in the machine iron is neither homogenous nor sinusoidal. A common approach to calculate iron losses for non-homogenous flux density distributions is by discretizing the machine geometry into smaller mesh elements (*finite elements)* where the flux density is assumed homogenous. Applying (8.2) to each partial mesh element and the summing over all elements then yields the total iron losses.
The extension of the eddy and excess losses in (8.2) to non-sinusoidal flux densities waveforms is given according to [50] as

$$\begin{array}{lll} & \text{time domain} & \text{frequency domain} \\ p_{\mathrm{eddy}} = & \frac{1}{T_{\mathrm{sym}}} \int_0^{T_{\mathrm{sym}}} \frac{K_{\mathrm{c}}}{2\pi^2} \left(\frac{\mathrm{d}B(t)}{\mathrm{d}t}\right)^2 \mathrm{d}t & K_{\mathrm{c}} \sum_{\mathrm{k}} \hat{B}_{\mathrm{k}}^2 f_{\mathrm{k}}^2 \\ p_{\mathrm{exc}} = & \frac{1}{T_{\mathrm{sym}}} \int_0^{T_{\mathrm{sym}}} \frac{K_{\mathrm{e}}}{C_{\mathrm{e}}} \left|\frac{\mathrm{d}B(t)}{\mathrm{d}t}\right|^{1.5} \mathrm{d}t & \text{not possible} \end{array} \quad . \tag{8.3}$$

They can be obtained by inserting the time-dependent waveforms of each mesh element into (8.3) and then calculating the mean value over the symmetry period. The eddy current losses can also be expressed in frequency domain by treating each spectral frequency f_{k} and flux density $\hat{B}_{\mathrm{k}}$ independently and adding up the contribution of each frequency. For excess losses a frequency-domain representation is not possible. The classical hysteresis losses p_{hys} in (8.2) can be extended to non-sinusoidal waveforms by using half of the peak-to-peak value of the arbitrary waveforms as $\hat{B}$. This is because the shape of the classical hysteresis loop is only determined by the maximum and minimum value. The assumption is that the hysteresis loop is closed after one period and no subloops occur within the hysteresis loop.

An important remark is that (8.2) and its extension to non-sinusoidal waveforms is a post-processing approach. This means that the iron losses are calculated after an already existing field solution has been obtained using the assumption $B = \mu_0 \mu_\mathrm{r} H$. Therefore, the effects of the iron losses (i.e. the phase shift between flux density and magnetic field) are not included in the field solution. Nevertheless, the approach is extensively used for the iron loss calculation of electrical machines. In the following sections an analysis of the flux density waveforms in the machine iron laminations is performed in order to point out the special case of HESM operation. The eddy, excess and hysteresis losses will then be revisited and quantified in Sections 8.2.1, 8.2.2 and 8.2.3.

8.1 Simplified Core Flux Model

When only the fundamental frequencies are considered, three independent rotating fields are superimposed in the HESM: the rotating p_m pole-pair field for torque production and the two forward and backward rotating fields of the p_h pole-pair machine. The airgap flux density in stator reference frame can therefore qualitatively be expressed by

$$ {}^{(s)}B_\delta = \hat{B}_{\delta,\mathrm{m}} \cos\left(p_\mathrm{m}\omega_\mathrm{m} t + p_\mathrm{m}\varphi\right) + \frac{\hat{B}_{\delta,\mathrm{h}}}{2} \cos(\,\omega_+ t + p_\mathrm{h}\varphi) + \frac{\hat{B}_{\delta,\mathrm{h}}}{2} \cos(\,\omega_- t - p_\mathrm{h}\varphi). \tag{8.4} $$

with the forward rotating field $\omega_+ = \omega_\mathrm{exc} + p_\mathrm{h}\omega_\mathrm{m}$ and a backward rotating field $\omega_- = \omega_\mathrm{exc} - p_\mathrm{h}\omega_\mathrm{m}$. The parameter $\hat{B}_{\delta,\mathrm{m}}$ ($\hat{B}_{\delta,\mathrm{h}}$) denotes the total amplitude of the airgap flux densities created by the p_m (p_h) pole-pair machine as a consequence of stator and rotor currents. In rotor coordinates, the airgap field is obtained analogously as

$$ {}^{(f)}B_\delta = \hat{B}_{\delta,\mathrm{m}} \cos\left(p_\mathrm{m}\varphi_\mathrm{f}\right) + \hat{B}_{\delta,\mathrm{h}} \cos(\omega_\mathrm{exc} t) \sin(p_\mathrm{h}\varphi_\mathrm{f}). \tag{8.5} $$

As (8.4) and (8.5) illustrate, in addition to the electrical frequency of $p_\mathrm{m}\omega_\mathrm{m}$ which also occurs in conventional WRSMs, the airgap flux density also features additional flux density variations at frequencies ω_+ and ω_- in the stator and ω_exc in the rotor iron. On top of the fundamental frequencies, harmonics due stator and rotor slotting, harmonic winding factors and rectifier harmonics occur which motivate a more detailed analysis of the core flux density. FEA is not computationally feasible because **first** of all, the actual steady-state harmonic currents I_dh and I_fh are time-dependent. Their shape and amplitude are the result of a transient event involving nonlinear elements like diodes and active elements like the step-down converter. **Secondly**, the simulation time T_sym is the least common multiple of $\{\omega_+, \omega_-, p_\mathrm{h}\omega_\mathrm{m}, \omega_\mathrm{exc}\}$ which becomes very large for most rotor speeds ω_m.
Hence a simplified core flux model is used. The goal of this model is not to achieve perfect agreement with FEA or measurement data, but to obtain a tool with which flux density waveforms in the HESM can be estimated, the additional iron losses due to the excitation

system can be understood and loss trends can be predicted dependent on parameters like D, f_{exc} and the rotor speed. A quick and easy way to determine the core flux density analytically is via the one-dimensional approximation of the airgap field which has already been used extensively before. Such an approach has already been used in the past, e.g. to size iron loss due to flux pulsation in the teeth of induction machines [51].

8.1.1 Tooth and Yoke Flux Density

First, the winding functions of each phase and coil are evaluated numerically according to (4.6) and (4.10). In order to obtain the MMFs, the winding functions are multiplied with the stator and rotor coil currents I_{kc} and I_{Fr} which are imported from the dynamic simulation (see Section 6.4) after steady-state is reached. These currents include the influence of rectifier harmonics, but do not include current harmonics due to higher order harmonic winding factors. The resultant airgap flux density is calculated from the MMFs and permeance waves in the respective (stator or rotor) reference frame

$$ {}^{(x)}B_{\delta} = {}^{x}\Lambda_{\mathrm{f}}\,{}^{x}\Lambda_{\mathrm{s}} \left(\sum_{\mathrm{k=U,V,W}} \sum_{\mathrm{c=1,2}} {}^{x}W_{\mathrm{kc}} I_{\mathrm{kc}} + \sum_{\mathrm{r=1,2,3,4}} {}^{x}W_{\mathrm{Fr}} I_{\mathrm{Fr}} \right) \text{ with } x \in \{s, f\}. \tag{8.6} $$

To this end, the stator and rotor permeance waves Λ_{s} and Λ_{f} of the machine prototype have to be determined. They have been calculated using the FE approach [52] and are shown in Fig. 8.1. The permeance waves disclose that the local flux density above the stator teeth is identical to a machine with a hypothetical homogenous airgap, but drops significantly in the vicinity of a slot opening. Analogously, the rotor flux density drops to a minimum between poles and is maximum above the pole shoe. It can be observed that the rotor permeance function is lower than one even at the pole tip where the airgap reaches its minimum value which indicates high leakage flux between two consecutive pole shoes.

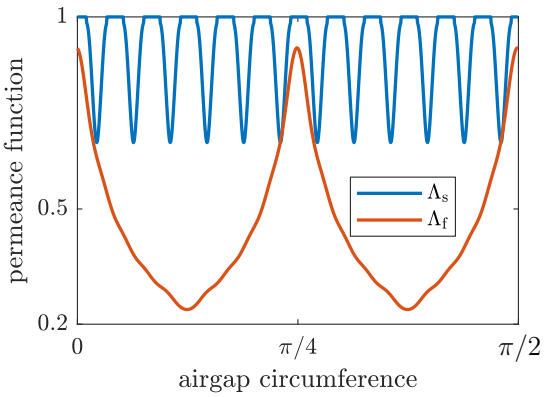

Figure 8.1: Permeance waves of stator and rotor for the machine prototype.

Once the total airgap flux density has been evaluated numerically, the time-dependent stator (rotor) tooth flux density can be obtained by integrating the airgap flux density ${}^{(s)}B_\delta$ in stator coordinates (${}^{(f)}B_\delta$ in rotor coordinates) over one slot (pole) pitch

$$\text{Statortooth i} \quad B_{\text{stooth,i}}(t) = \frac{1}{b_{\text{tooth}}} \int_{\frac{2\pi}{Z_\text{s}}(i-0.5)}^{\frac{2\pi}{Z_\text{s}}(i+0.5)} {}^{(s)}B_\delta(\varphi, t)\mathrm{d}\varphi \qquad i = 1, ..., Z_\text{s} \tag{8.7}$$

$$\text{Rotortooth j} \quad B_{\text{rtooth,j}}(t) = \frac{1}{b_{\text{tooth,r}}} \int_{\frac{\pi}{p_\text{m}}(i-0.5)+\omega_\text{m}t}^{\frac{\pi}{p_\text{m}}(i+0.5)+\omega_\text{m}t} {}^{(f)}B_\delta(\varphi_\text{f}, t)\mathrm{d}\varphi_\text{f} \quad j = 1, ..., 2p_\text{m} \tag{8.8}$$

where b_{tooth} and $b_{\text{tooth,r}}$ are the width of a stator slot and rotor pole according to Fig. 6.2. The averaged, time-dependent stator (rotor) yoke flux density can be obtained by cumulative summation of the tooth flux density

$$\text{Statoryoke i} \qquad B_{\text{syoke,i}}(t) = \frac{1}{h_{\text{yoke}}} \sum_{\text{k}}^{\text{i}} B_{\text{stooth,k}}(t) \qquad i = 1, ..., Z_\text{s} \tag{8.9}$$

$$\text{Rotoryoke j} \qquad B_{\text{ryoke,j}}(t) = \frac{1}{h_{\text{yoke,r}}} \sum_{\text{k}}^{\text{j}} B_{\text{rtooth,k}}(t) \qquad j = 1, ..., 2p_\text{m} \tag{8.10}$$

where h_{yoke} and $h_{\text{yoke,r}}$ are the yoke heights according to Fig. 6.2. Since these flux densities do not include slot leakage, they are then multiplied with stator and rotor leakage coefficients accounting for the flux lines that close through the slots and tooth tips. These coefficients have been obtained heuristically so that a decent agreement with FEA is obtained. The rotor leakage flux is especially significant because of the large embrace of the pole shoes that almost touch each other. Taking into account symmetry, only one half of the motor needs to be modelled, i.e. the flux density in the whole machine is simplified by 24 stator tooth and yoke segments each and 4 rotor tooth and yoke segments each.

8.1.2 Model Limitations and Accuracy

It is obvious that several limitations in the core flux model exist which are briefly pointed out using the FE model as a benchmark. First of all, the flux in the machine iron of electrical machines not only varies in time (i.e. is unidirectional) as is assumed in the core flux model, but varies in space **and** time. Fig. 8.2 depicts the rotationality r of the magnetic field in each mesh element at HESM-no-load operation. The excitation system operates at an excitation frequency of $f_\text{exc} = 200\,\text{Hz}$ and duty cycle of $D = 11.5\,\%$. The rotationality r is defined here as the area enclosed by the ellipse that the radial and tangential flux density form over time normalized to its maximum amplitude.

$$r = \oint B_\text{tang}\mathrm{d}B_\text{rad} \cdot \frac{1}{\max\left(\sqrt{B_\text{rad}^2 + B_\text{tang}^2}\right)} \tag{8.11}$$

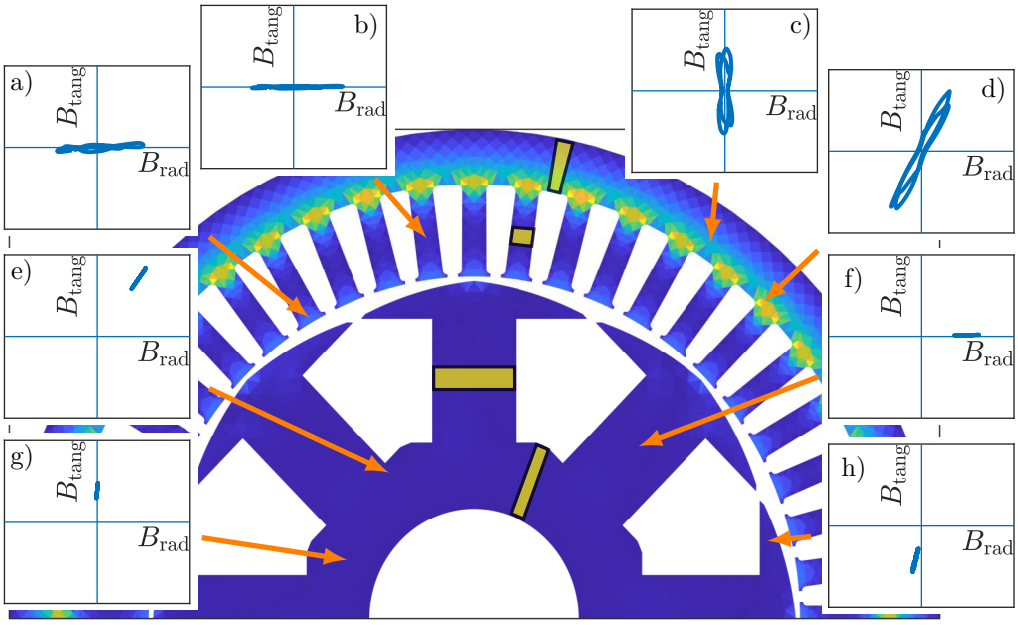

Figure 8.2: Rotationality r of the magnetic field for harmonic excitation. The yellow zones mark the zones where the core flux is mostly unidirectional and thus, where the simplified core flux model is most accurate.

Fig. 8.2 shows that the magnetic field is mostly unidirectional in the middle of the stator teeth b), rotor teeth f) and yoke flux g) and e). However, in the transition between stator tooth and yoke d) the field is highly rotary. Even right in between two stator teeth c), the yoke flux density has a significant rotary component even though the tangential component dominates. The effect of the rotary field in the machine iron is completely omitted in the simplified core flux model. Furthermore, the coarse discretization of the core geometry introduces some errors: As a homogenous flux density is assumed in every tooth and yoke segment, local flux density maxima especially at sharp edges in the machine geometry are completely omitted. In the yoke there is also a radial dependence of the flux density which is disguised in the single-segment yoke representation.
For verification of the model, the flux densities obtained from FEA are compared to the averaged flux densities calculated from the model from (8.7) to (8.10). This is demonstrated exemplarily for a single stator/rotor tooth and yoke segment in Fig. 8.3a-d. Firstly, conventional WRSM-no-load operation is investigated (only field current I_{fm} supplied). As the actual flux densities are not homogenous in a segment, the actual range of flux densities in a given segment are displayed as envelopes. As the flux is not purely unidirectional, the flux in the dominant direction is used with the rotary component neglected. When the FE flux densities are averaged over the light yellow areas in Fig. 8.2, a mean flux density is obtained from FEA which can be compared to the core flux model. This averaged FEA waveform is denoted as *FEA average* in Fig. 8.3.

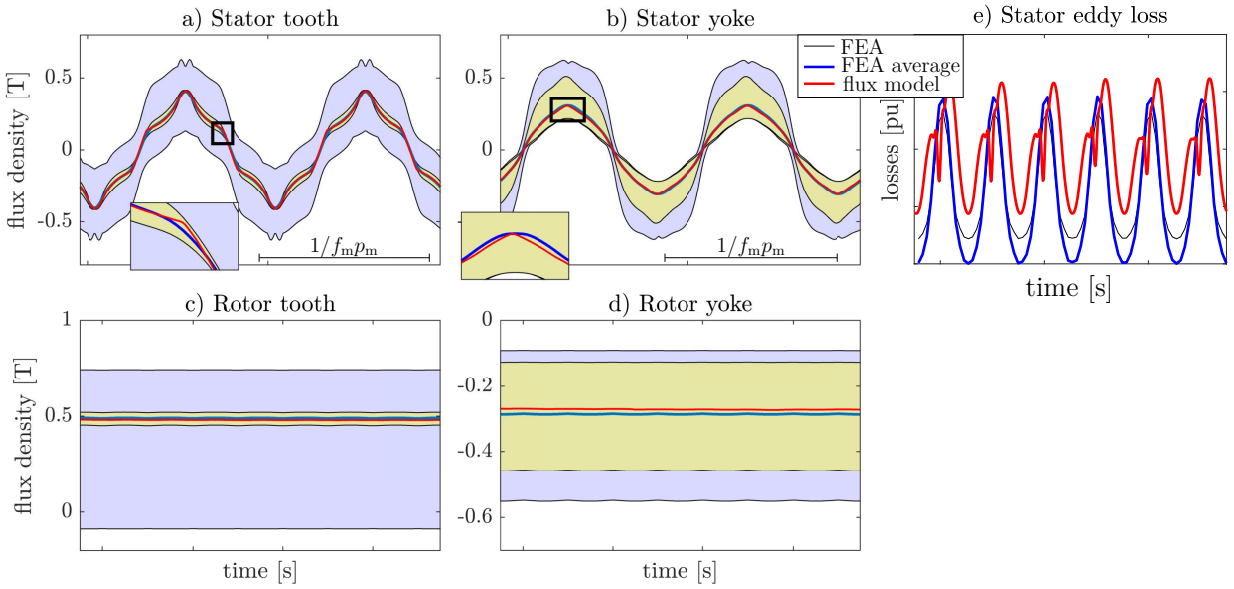

Figure 8.3: Exemplary comparison of the flux densities and eddy losses for WRSM-no-load operation at a speed of $n = 500\,\text{rpm}$ and field current of $I_{\text{fm}} = 4\,\text{A}$. The rotor losses are negligible due to the constant flux density and thus not portrayed.

It can be seen that the (light blue) FE flux envelope of each segment spans a large area and deviates significantly from the averaged fields. This is to be expected because of local flux density maxima and minima at the edges of the iron core and the radial dependency of the flux in the back iron. The spread of the envelope seems excessive in the rotor segments, but it should be noted that the large envelope is mainly because of a small amount of dominant local maxima and minima. This is highlighted by the light yellow envelope which shows that the majority of the flux is in quite close vicinity to the averaged flux density. Especially the (light yellow) flux envelope in the middle of a tooth is in very good agreement with the averaged and analytical flux densities. For the yoke there is still a greater deviation even for the light yellow envelope, because of the radial dependency of the yoke flux density. Fig. 8.3e also demonstrates the time-dependent eddy currents calculated directly from FEA and from the averaged fields using (8.3). It can be seen that for all three methods the time-dependence and the magnitude of the iron losses can be estimated with decent agreement. However, a slight difference in the third and fifth harmonics in the no-load flux density yields an overestimation of the analytical stator losses (Fig. 8.3e) compared to the FEA case by 10%.
In Fig. 8.4, the same comparison is performed for HESM no-load operation i.e. with additional harmonic currents I_{dh} and I_{fh}. The excitation system parameters are $f_{\text{exc}} = 200\,\text{Hz}$ and $D = 11.5\%$. Figs. 8.4a-d confirm that the analytical core flux model agrees well with the averaged FE fluxes. However, Figs. 8.4e and f reveal that the eddy losses caused by excitation system harmonics are underestimated compared to the losses obtained via FEA. A possible explanation is the overall larger spread of the flux density envelope when the

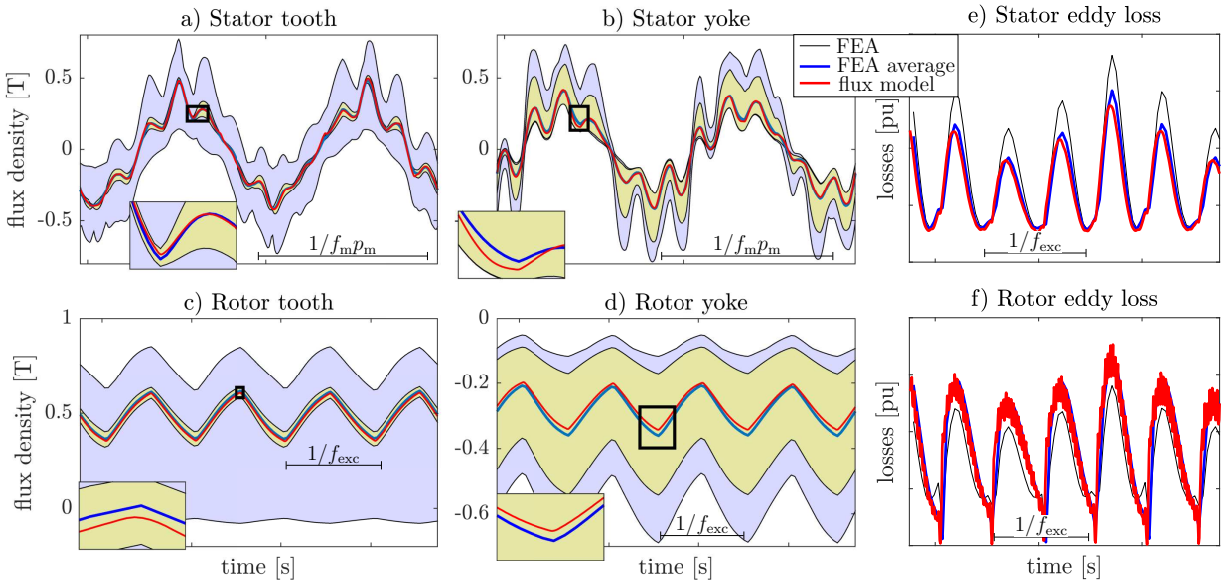

Figure 8.4: Comparison of the flux densities and eddy losses for harmonic excitation at a speed of $n = 500\,\mathrm{rpm}$ and a supplied field current of $I_\mathrm{fm} = 4\,\mathrm{A}$.

machine is harmonic-excited. While the results have only been shown for a single no-load operating point, a similar accuracy could be observed for different speeds and excitation system parameters. Overall, it can be concluded that despite its limitations, the analytical model is a computationally quick method to estimate the core flux.

8.2 Evolution of the Iron Losses

The analytical model is used in this section to investigate the frequency spectrum of the core flux as a function of speed. To this end, the flux density waveforms in each segment are calculated for HESM no-load operation until a maximum speed of 6000 rpm. The spectrogram of the flux densities in stator and rotor is given in Fig. 8.5 for an excitation frequency of $f_\mathrm{exc} = 200\,\mathrm{Hz}$ (configuration 1 in Tab. 8.2). As the magnitude of each spectral component is similar (but not identical) in all tooth segments of the stator and rotor, the average spectral magnitude is plotted. In order to highlight the excitation harmonics, the spectrogram of HESM operation in Fig. 8.5a is contrasted with WRSM operation in Fig. 8.5b.

It can be seen that the iron flux is heavily polluted in case of HESM operation. All spectral lines present in WRSM operation also occur unaltered in the HESM. As expected, in the stator the dominant spectral line $p_\mathrm{m} f_\mathrm{m}$ for both HESM and WRSM operation is the p_m pole-pair fundamental flux ($\nu_\mathrm{m} = 1$). Odd multiples $|\nu_\mathrm{m}| = 3, 5, \ldots$ of this flux also occur with lesser intensity. Analogously, in the rotor the dominant spectral line for both HESM and WRSM operation is the DC excitation field. For HESM operation the second largest spectral

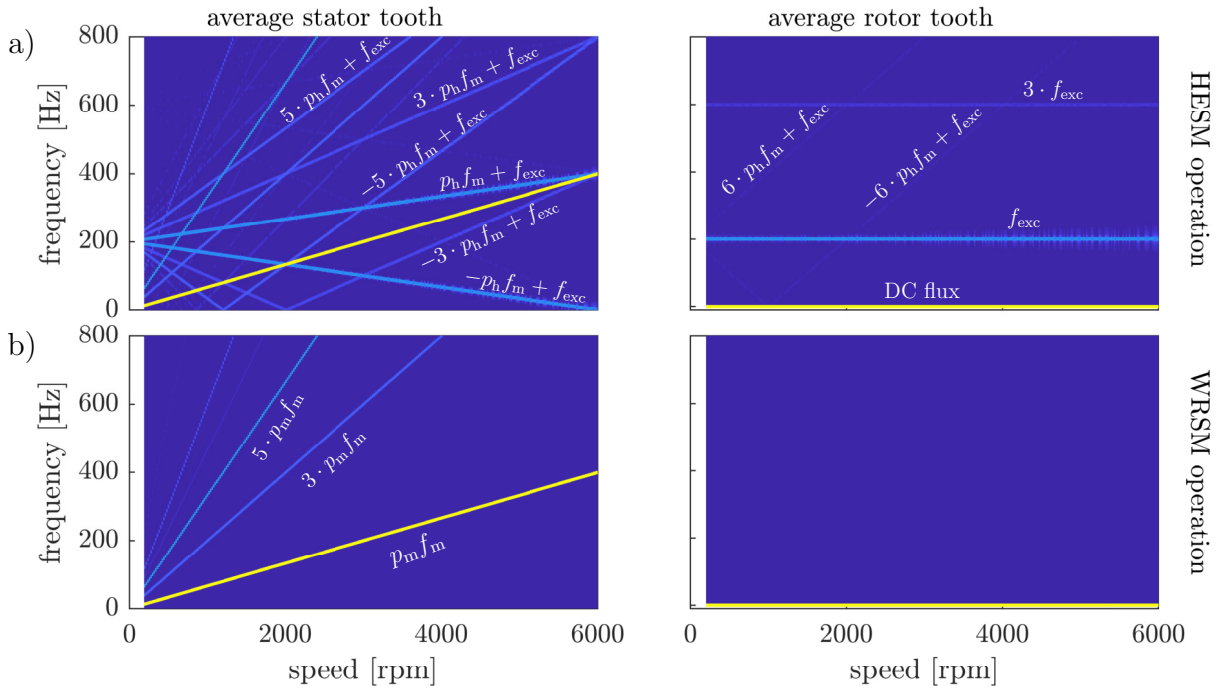

Figure 8.5: Spectrogram of simulated flux density in stator teeth (left), stator yoke (middle) and rotor teeth (right).

lines in the stator originate from the fundamental ($\nu_{h\pm} = \pm 1$) of the forward and backward rotating p_h pole-pair field. Furthermore, the spectral lines related to higher order harmonics $|\nu_{h\pm}| = 3, 5, 7, \ldots$ are significant. Analogously, in the rotor the excitation frequency f_{exc} is the second largest spectral component apart from the DC flux. The stator harmonics $\nu_{h\mp} = \pm 5$ also induce corresponding fluxes which can be seen faintly in the HESM spectrum. Overall, the frequencies in the spectrogram correspond to Tab. 8.1.

Table 8.1: Visible core flux frequencies with ordinal numbers for the forward rotating field $\nu_{h+} = 1, -5, 7, \ldots$ and backward rotating field $\nu_{h-} = -1, 5, -7, \ldots$. For the rotor, fields related to ordinal numbers $\mu = \pm 1, \pm 3, \pm 5, \ldots$ occur. Rectifier harmonics are considered by $h = 1, 3, 5, \ldots$.

		From Stator	From Rotor
To Stator	p_m	$\nu_m p_m \omega_m$	$\mu p_m \omega_m$
	p_h	$\nu_+ p_h \omega_m + h\omega_{exc}$ $\nu_{h-} p_h \omega_m + h\omega_{exc}$	$\mu p_h \omega_m + h\omega_{exc}$
To Rotor	p_m	$(1 - \nu_m) p_m \omega_m$	—
	p_h	$(1 - \nu_{h+}) p_h \omega_m + h\omega_{exc}$ $(-1 - \nu_{h-}) p_h \omega_m + h\omega_{exc}$	$h\omega_{exc}$

An important observation in the HESM spectrogram is that at specific rotor speeds and ordinal numbers, the spectral lines of the p_h and p_m pole-pair machine intersect in stator or rotor. For example, the fundamental of the p_m pole-pair machine $\nu_\mathrm{m} = 1$ intersects with the backward rotating field of the p_h pole-pair machine ($\nu_{\mathrm{h}-} = -1$) at

$$\nu_\mathrm{m} p_\mathrm{m} \omega_\mathrm{m} = -\nu_\mathrm{h} p_\mathrm{h} \omega_\mathrm{m} + h\omega_\mathrm{exc} \qquad \rightarrow \qquad f_\mathrm{m} = \frac{f_\mathrm{exc}}{p_\mathrm{m} + p_\mathrm{h}}$$

which is at 2000 rpm for an excitation frequency $f_\mathrm{exc} = 200\,\mathrm{Hz}$. At these speeds (or these spectral frequencies), the core fluxes of the p_h and p_m pole-pair machines have the same frequency and thus the magnitude is the sum of both components and can take on a maximum or minimum depending on the phase. As the iron losses are proportional to the magnitude to the power of $1.5 - 2$ according to (8.3), the calculated iron losses at these intersecting frequencies are outliers.

In the following sections a qualitative investigation of each of the iron loss components eddy current, hysteresis and excess loss is performed based on the simulated core flux densities. This is performed for the three excitation system configurations in Tab. 8.2 which all supply the same field current $I_\mathrm{fm} = 5\,\mathrm{A}$ at no-load.

Table 8.2: Excitation system operating points under investigation

Configuration	excitation system		supplied field current	p_h pole-pair machine	
	f_exc [Hz]	D [%]	I_fm [A]	$\hat{I}_\mathrm{dh}$ [A]	$\hat{I}_\mathrm{fh}$ [A]
1	200	11.5 %	5 A	3.8 A	1.25 A
2	100	13 %	5 A	5 A	1.5 A
3	50	16 %	5 A	7 A	1.8 A

The duty cycles D are chosen so that the best efficiency at the chosen excitation f_exc is achieved (see Fig. 7.10). Only the iron loss contribution of the p_h pole-pair machine $P_\mathrm{fe,h}$ is important for the analysis of the excitation system losses. In order to obtain this value, first, the calculated p_m pole-pair machine iron losses $P_\mathrm{fe,m}$ are subtracted from the HESM iron losses. This yields only the iron losses $P_\mathrm{fe,h}$ attributable to the excitation system.

8.2.1 Eddy Current Losses

As seen in (8.3), eddy losses can be calculated in frequency domain as the product of flux density and frequency squared. A graphical representation of the loss evolution can therefore be obtained by multiplying each spectral magnitude B_k with its spectral frequency f_k and squaring. This is shown exemplarily for the excitation frequency $f_\mathrm{exc} = 200\,\mathrm{Hz}$ in Fig. 8.6. Spectral components related to the p_m pole-pair machine are removed to isolate the effect of

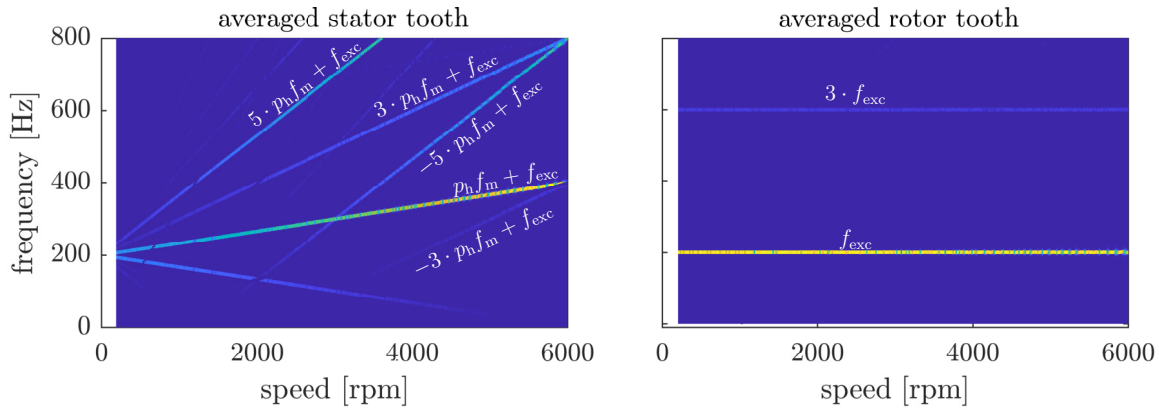

Figure 8.6: Spectrogramm of spectral flux density times frequency squared which is representative of the eddy current losses.

the excitation system. Generally speaking, the increasing intensity of the spectral lines in the stator as a function of speed reveals that eddy current losses increase nonlinearly with rotor speed. It can be seen that the contribution of the forward rotating frequency ν_{h+} dominates the eddy losses produced in the stator. Furthermore, the harmonics of the forward rotating field $\nu_{h+} = -5$ as well as the $\nu_f = 3$rd harmonic of the rotor field make up a significant part of the eddy current losses. On the contrary, the fundamental of the backward rotating field $\nu_{h-} = -1$ contributes insignificantly in a large part of the speed-range. However, the fifth harmonic $\nu_{h-} = 5$ of the backward rotating field does generate significant eddy losses.
In the rotor, Fig. 8.6 shows that the eddy current losses are largely speed-independent and only increase slightly due to the $|\nu_{h\pm}| = 5, 7$th spatial harmonics induced from the stator. An important observation is that a noticeable portion of the rotor losses is due to the speed-independent rectifier harmonics ($h = 3$).

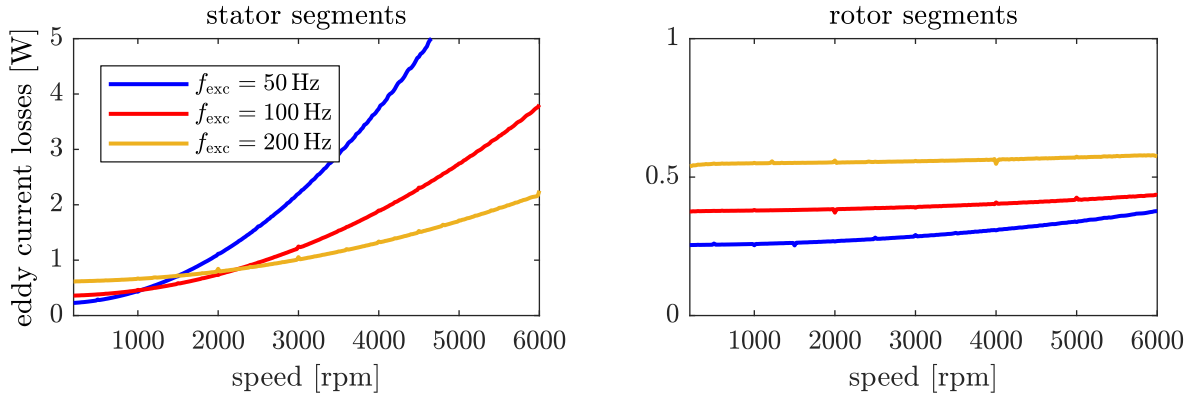

Figure 8.7: Eddy current losses as function of speed for varying excitation frequencies for eddy loss coefficient $K_c = 1$.

If the flux density waveforms of each segment for each of the three excitation frequencies are inserted into (8.3), once for HESM and once for WRSM operation, and then subtracted, the eddy loss evolution $P_{\mathrm{fe,h}}$ is obtained as depicted in Fig. 8.7. A distinction between the losses generated in stator and rotor is made. It can be seen that at very small speeds, the eddy current losses in the stator are proportional to the excitation frequency f_{exc} with the lowest losses produced by $f_{\mathrm{exc}} = 50\,\mathrm{Hz}$. This is because according to (8.3) the eddy current losses are proportional to the frequency squared.

For rising speeds, the eddy current losses increase nonlinearly. The slope of the speed dependence is greater for lower excitation frequencies f_{exc}. As the main contributor to the eddy losses is the forward rotating field f_+, this can be illustrated with a simple example: At $f_{\mathrm{exc}} = 50\,\mathrm{Hz}$ when the speed rises from standstill 0 rpm to 3000 rpm, the forward rotating field of frequency f_+ rises from 50 Hz to 150 Hz by a factor of three. However, for a large excitation frequency $f_{\mathrm{exc}} = 200\,\mathrm{Hz}$, f_+ increases from 200 Hz to 300 Hz by only a factor of 1.5. Thus, while the overall frequencies for $f_{\mathrm{exc}} = 50\,\mathrm{Hz}$ are significantly lower than for $f_{\mathrm{exc}} = 200\,\mathrm{Hz}$, the speed-dependent increase is larger.
In the rotor, the eddy losses are largely constant and proportional to the excitation frequency f_{exc} — as predicted — with only a slight speed-dependent increase due to the 5, 7th winding harmonic from the stator.

8.2.2 Excess Losses

For non-sinusoidal waveforms, excess losses cannot be investigated in frequency domain. Instead, they must be evaluated using the time-dependent flux densities in time domain according to (8.3). In Fig. 8.8, the trends for the speed-dependent excess losses of $P_{\mathrm{fe,h}}$ in stator and rotor are predicted. The trends are generally similar to the eddy loss component. The only difference is that the stator losses decrease first and and afterwards increase nonlinearly. The decreasing region is larger for increasing excitation frequencies.

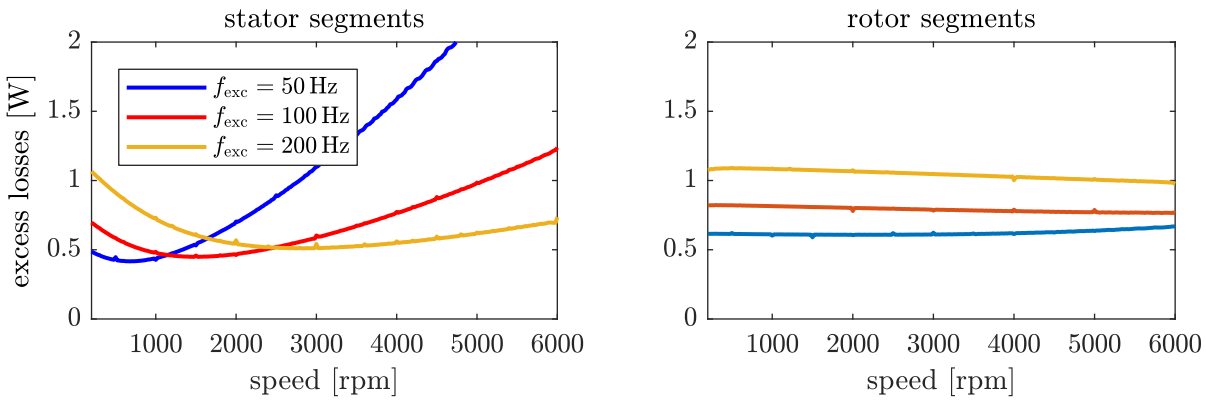

Figure 8.8: Excess losses as function of speed for varying excitation frequencies for excess loss coefficient $K_{\mathrm{e}} = 10$.

8.2.3 Classic Hysteresis Losses

Classic hysteresis losses are the most difficult loss component to evaluate. They do not only depend on the magnitude and frequency of the core flux, but on the area of the hysteresis loop that is produced by the time-dependent flux density. In order to calculate the hysteresis loop thoroughly, hysteresis models such as the Preisach model [53], the Jiles-Atherton Model [54] or phenomenological Play Models [55] have to be used, but even for those models a correct rendition of minor loops is a challenging task that requires model modifications [56] or heuristic parameters [57] so that extensive verification and tuning of the models with experimental data is necessary. The implementation, parametrization and validation of a hysteresis model that accurately predicts major and minor loops under harmonic excitation is not feasible in the scope of this work. This is why the approach from [58] has been implemented which extends the Bertotti approach (8.12) to incorporate major and minor loops in arbitrary flux-density waveforms. In this case, the BH loop is not calculated with a hysteresis model, but the major and minor loops are identified from the field reversals of the time-dependent flux density waveforms. Thus, each identified loop k is fully defined by its DC bias $B_{\mathrm{dc,k}}$ and its amplitude $\hat{B}_{\mathrm{k}}$. The coefficient K_{h} represents the shape – and thus the area — of the actual hysteresis loop that the amplitude B_{k} would produce in the BH coordinate system. As the shape of BH loops depends on the DC bias of that loop, K_{h} is heuristically adjusted as a function of the DC bias B_{dc}

$$p_{\mathrm{hys}} = \sum_{\mathrm{k}} K_{\mathrm{h}}(1 + k_{\mathrm{dc}} \cdot B_{\mathrm{dc,k}}^2)\hat{B}_{\mathrm{m,k}}^2 f \tag{8.12}$$

where $f = 1/T_{\mathrm{sym}}$ denotes the frequency at which the waveform repeats. The recursive algorithm for the identification of the major and minor loops from the flux densities is as follows:

1. Start with minimum value of the flux density waveform and **ascend** through the data until a field reversal $B_{\mathrm{i+1}} < B_{\mathrm{i}}$ (= minor loop) occurs **or** until the maximum value is reached
2. If the maximum value is reached then **descend** through the data until a field reversal $B_{\mathrm{i+1}} > B_{\mathrm{i}}$ (= minor loop) is found **or** until the minimum value is reached (= major loop closed).
3. As all minor loops can include subloops, the algorithm is called recursively for each minor loop.
4. Save the flux density amplitude and DC bias of all detected loops and repeat until every data point has been traversed.

An example for the algorithm is applied in Fig. 8.9 to the flux density in a single stator tooth of the HESM. It can be seen that the major hysteresis loop does not necessarily close after

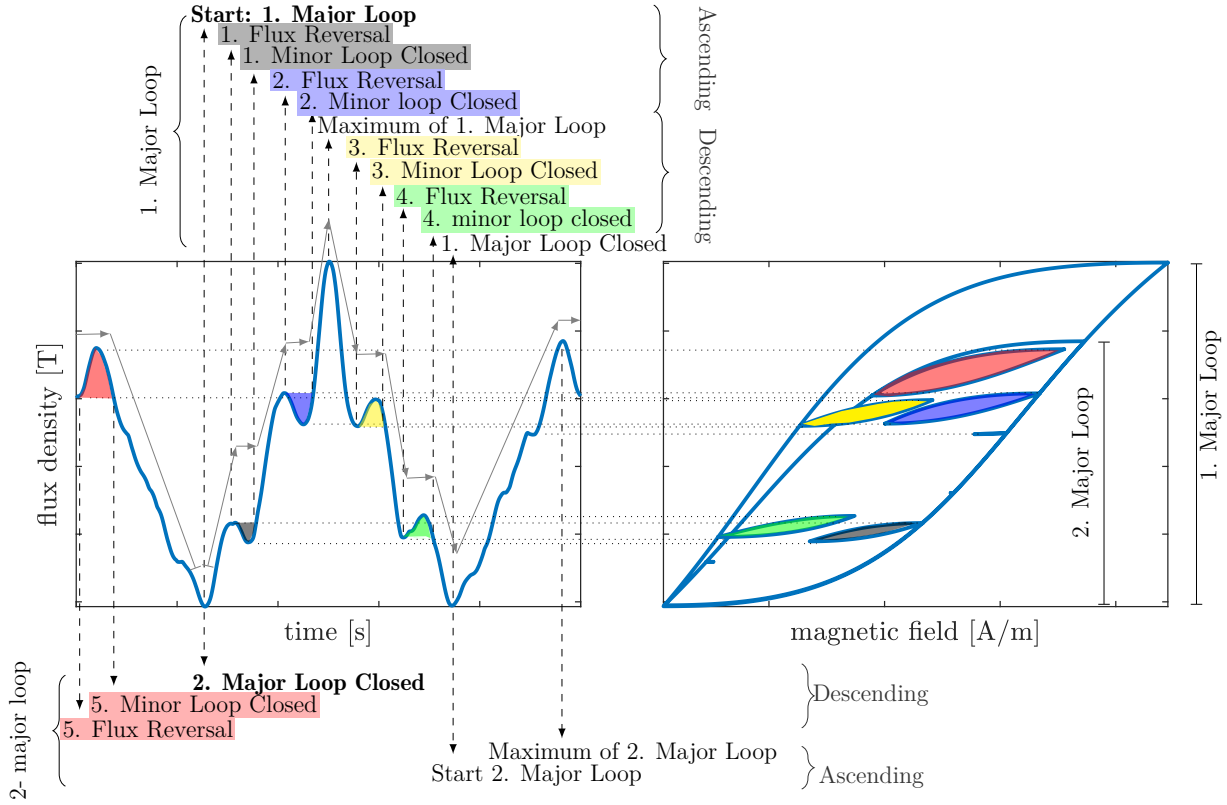

Figure 8.9: Major and minor hysteresis loop identification algorithm applied to exemplary data.

one fundamental p_m pole-pair period, but after two periods in the given case. Minor loops in the ascending and descending branches are identified by field reversals and major loops by the maximum and minimum value remaining in the (untraversed) data. Thus, for each identified loop the flux density amplitude $\hat{B}_{\mathrm{m,k}}$ and DC-bias $B_{\mathrm{dc,k}}$ can be determined. On the right, the actual hysteresis loop of the waveform is shown which highlights the emergence of DC-biased major and minor loops. The hysteresis loop has been calculated exemplarily by a Preisach model implemented in PLECS [59]. It only provides a qualitative rendition of what the actual hysteresis loops might look like.

Applying this algorithm to each segment gives insight into the speed-dependence and origin of the hysteresis losses. In Fig. 8.10, the evolution of minor and major loops in the stator core is shown for no-load operation. The area of each subloop is defined according to the iron loss formula (8.12) from the DC-bias and amplitude of the identified major loops as

$$A = K_\mathrm{h}(1 + k_\mathrm{dc}\hat{B}^2)V$$

where V takes into account the volume of each respective segment. In Fig. 8.10a, the minor loop area in percent denotes the cumulative area of all minor loops in all stator segments divided by the total hysteresis loop area (major **and** minor loops) for HESM excitation.

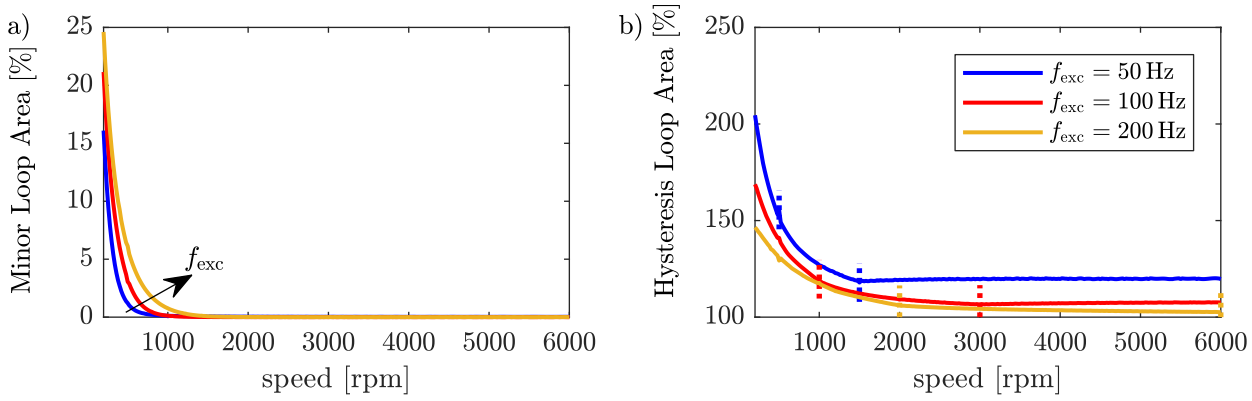

Figure 8.10: Evolution of minor and major loops as a function of rotor speed for different excitation frequencies.

This value is a direct measure for the percentage of iron losses that are attributable to minor loops. It can be seen that iron losses due to minor loops make up around 20 % of the total excitation system iron losses for small speeds, but quickly decrease and almost vanish above 1500 rpm. There is a slight dependence of the minor loop losses on the excitation frequency. For large f_{exc} the impact of minor loops is slightly more pronounced, but in all cases minor loops make up an insignificant part of the iron losses after 1500 rpm.

This is investigated in Fig. 8.10b by first calculating the cumulative major loop area in all stator segments for HESM operation **and** WRSM operation and then dividing both areas from another. The hysteresis loop area in percent indicates how much the (major) hysteresis loop area is enlarged as a function speed and excitation frequency. It can be observed that for small excitation frequencies f_{exc} the hysteresis losses are significantly larger than for higher f_{exc}. This is because more harmonic current $\hat{I}_{\mathrm{dh}}$ and thus higher flux densities are required to supply the field current I_{fm} (see e.g. Fig. 7.10). For all excitation frequencies the hysteresis losses are significantly larger at smaller speeds and decrease for rising speeds. On close inspection, the curves exhibit two transitional speeds where the slope of the curves change. These transitions occur at the intersections of the fundamental p_{m} pole-pair field with the fundamental of the backward and forward rotating field of the p_{h} pole-pair machine. They are highlighted with the dotted lines and depend on the excitation frequency f_{exc}. In the first interval $[0, f_{\mathrm{exc}}/(p_{\mathrm{m}} + p_{\mathrm{h}})]$ the major loop area decreases with the steepest slope. In the second interval $[f_{\mathrm{exc}}/(p_{\mathrm{m}} + p_{\mathrm{h}}), f_{\mathrm{exc}}/(p_{\mathrm{m}} - p_{\mathrm{h}})]$ the area decreases further, but at a reduced rate. After a speed of $f_{\mathrm{exc}}/(p_{\mathrm{m}} - p_{\mathrm{h}})$ the hysteresis loop area stays constant. An explanation for this is that at small speeds the frequency of the forward and backward rotating fields f_+, f_- are much larger than the p_{m} pole-pair machine field of fundamental frequency $p_{\mathrm{m}} f_{\mathrm{m}}$. Thus, each maximum of the p_{m} pole-pair flux density falls on top of a maximum of the oscillating p_{h} pole-pair field. For rising speeds, the number of enlarged minor loops decreases as the difference between p_{h} and p_{m} pole-pair frequencies decreases.

In the third interval the number of enlarged major loops has converged to a constant 50 % so that half of the major loops are larger and the other half smaller than the WRSM loop.

This can be confirmed exemplarily by taking a look at the time-dependent stator and rotor flux densities in a single stator and rotor tooth/yoke for selected speeds as shown in Fig. 8.11 for an excitation frequency of $f_{\mathrm{exc}} = 200\,\mathrm{Hz}$. For illustration purposes only those speeds are portrayed where the symmetry period is two fundamental p_{m} pole-pair periods. In order to highlight the deviation of the (blue) HESM flux densities from the (red) WRSM flux densities both are displayed in the same graph. In the first column of Fig. 8.11 the enlargement of the major loop is shown based on the stator tooth waveforms. It can be seen that at a small speed of 300 rpm both major loops are enlarged compared to the WRSM. If the speed rises, the size of the first major loops decreases which coincides with the major loop trends in Fig. 8.10b. It can also be observed that the major loops are not fully centered, but have a slight DC bias.
The second column of Fig. 8.11 uses the stator yoke flux densities to emphasize that within the major loops multiple additional minor loops occur due to flux reversals. They are denoted as blue areas and have been identified according to the algorithm in Fig. 8.9. It can be seen that the number and area of these minor loops is maximum for small speeds and decreases with rising machine speed. This also coincides with the results of the minor loop evolution shown Fig. 8.10a. The flux density of a single rotor tooth is shown in the third column of Fig. 8.11. As the rotor flux consists of a constant DC component superimposed by an AC component of constant frequency $f_{\mathrm{exc}} = 200\,\mathrm{Hz}$, the shape of the rotor flux density is speed-independent which coincides with the spectrogram in Fig. 8.5. Hence, the area enclosed by the hysteresis loops in the rotor iron stays roughly constant.

In Fig. 8.12 the evolution of the hysteresis loss is quantified. In the stator, the three regions predicted in the evolution of the major loops can be observed divided by the dotted lines. In the first region hysteresis losses decrease slightly and stay roughly constant in the second region. As the hysteresis losses depend on the area of the hysteresis loop multiplied by the frequency according to (8.12), the decrease of the major loop area is mostly compensated by the increase of the frequency. However, in the third region where the area is constant, the hysteresis losses increase linearly. For the rotor, there is almost no speed-dependence, but it can be seen that — unlike for the eddy current losses — at lower excitation frequencies f_{exc}, the hysteresis losses are higher. This is because the hysteresis losses depend on the flux density magnitude **squared**, but only linearly on the frequency. As the magnitude of the flux density is disproportionally larger when the HESM is operated at a lower excitation frequency f_{exc}, the hysteresis losses are also larger.

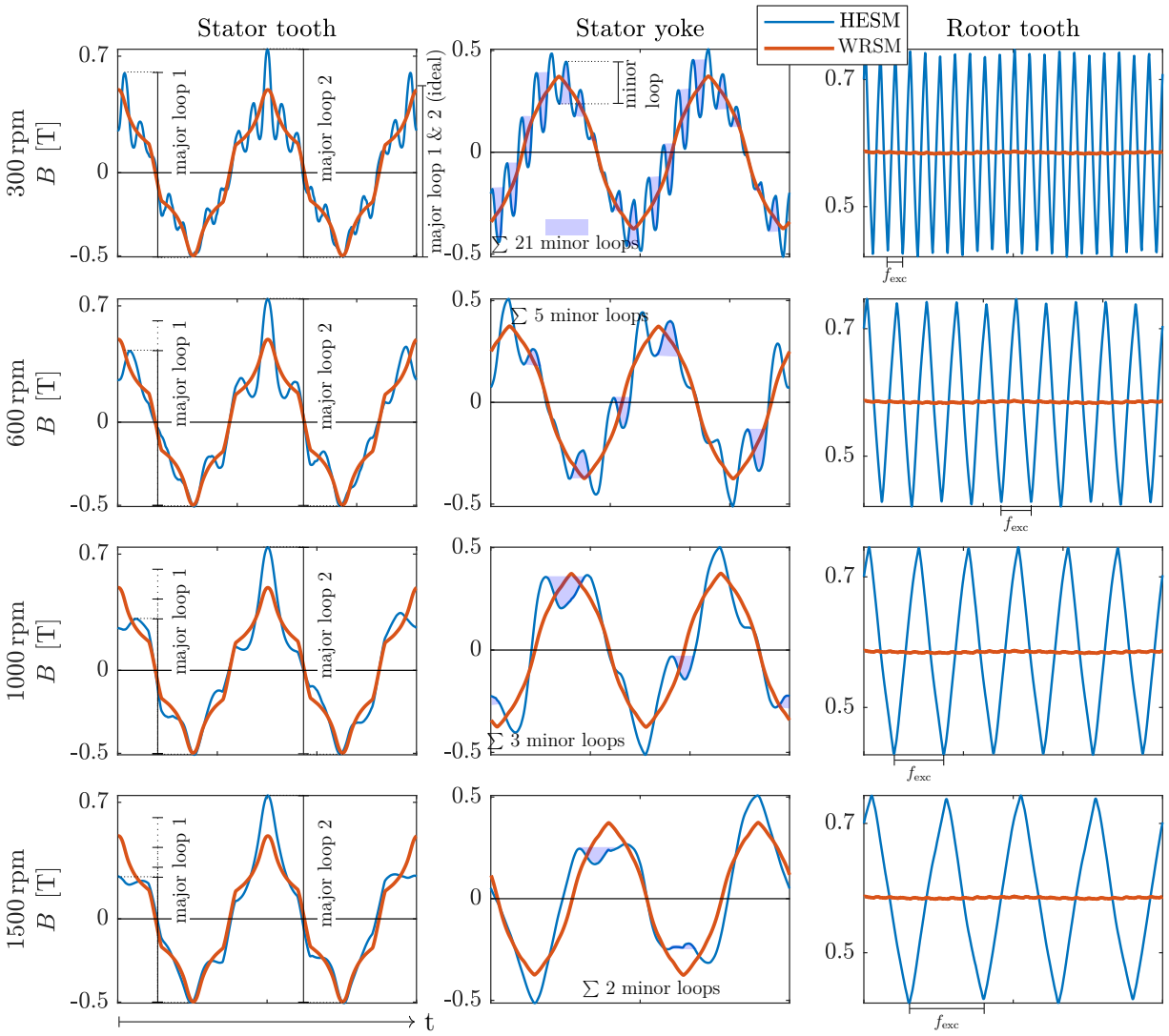

Figure 8.11: Time-dependent flux densities in one stator tooth segment, stator yoke segment and rotor tooth segment for $f_{\mathrm{exc}} = 200\,\mathrm{Hz}$.

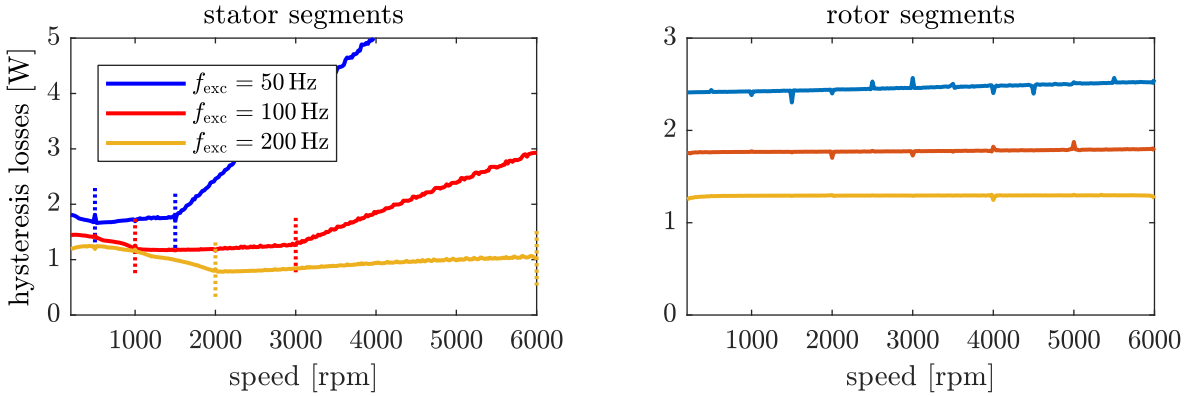

Figure 8.12: Hysteresis losses as function of speed for varying excitation frequencies for hysteresis loss coefficient $K_{\mathrm{h}} = 350$.

8.3 Experimental Verification

Before a comparison of the predicted iron loss models with experiments is attempted, the following remarks should be made: In addition to the simplifications of the iron loss model in Section 8.1.2 and the measurement inaccuracies discussed in Section 7.1.1, some effects occur in the experiment that are completely neglected in the simulation and further increase the difficulty of an experimental verification of the iron loss trends. **Firstly**, in the actual machine unpredictable eddy current losses occur in near metallic objects (frame, end-shield, conductors, etc) due to stray fields which are measured on top of the iron losses. **Secondly,** in the simulation the core flux is calculated without the effect of spatial harmonics ($v = 5, -7, ...$) on the motor currents. **Thirdly**, in the experiment the currents are superimposed by PWM switching harmonics imposed by the two three-phase drive inverters connected to the stator windings **and** by the buck converter in the rotor winding of the HESM. In Section 7.3.1, these have already been observed to produce significant iron losses and are not included in the calculated iron losses in Sections 8.2.1, 8.2.2 and 8.2.3 so far. PWM-induced iron losses make up a significant portion of the total iron losses in an electrical machine and vary with switching frequency, DC link voltage and modulation index [60].

8.3.1 Inclusion of PWM Current Ripple

This is why a verification of the iron loss model can only be performed by including the PWM current ripple into the core flux calculation. So far, the iron losses predicted in this chapter have been calculated from smoothed currents which only account for the fundamental fields as well as higher order winding, slotting and rectifier harmonics. In the following sections it will be seen that these iron losses do not fully explain the loss component $P_{\mathrm{fe,h}}$ measured in the test bench. The reason for the omission of the PWM current ripple so far is threefold: Firstly, far more sophisticated iron loss models in conjunction with FEA are usually used in the literature to accurately include PWM effects such as hysteresis models with variable parameter sets [61], [62]. Nevertheless, some success is attained using the simple Bertotti approach presented in this chapter. Secondly, the determination of the PWM ripple is very time-consuming because it depends on the motor speed (and DC link voltage) via the SPWM modulation strategy. This requires recalculating the dynamic model for each operating point. Thirdly, a separate look at the iron losses produced by the 'smooth' currents allows isolating the effect of the PWM ripple.
In order to include the PWM ripple into the core flux model in a computationally efficient manner, the approach in [61] is used on the linear HESM voltage model. The general idea is to analytically calculate the PWM ripple for each variation in motor speed and then superimpose it onto the smooth (PWM-current-free) currents used previously. The following approach is taken:

1. Use the smooth steady-state dq current vector $\mathbf{I_{dq}}$ to first calculate the smooth terminal voltages in dq coordinates $\mathbf{U_{dq}}$ and then apply the inverse transformations to obtain the smooth phase voltages $\mathbf{U_{ph}}$

$$\mathbf{U_{ph}} = \mathbf{T_{ppU}^{-1}} \mathbf{T_{dqf}^{-1}} \left(\mathbf{R_{dq}} \mathbf{I_{dq}} + \mathbf{L_{dq}} \frac{\mathrm{d}}{\mathrm{d}t} \mathbf{I_{dq}} + \omega_{\mathrm{m}} \mathbf{J_2} \mathbf{L_{dq}} \mathbf{I_{dq}} \right). \tag{8.13}$$

2. Use $\mathbf{U_{ph}}$ to create the pulse-width modulated phase voltages $\mathbf{U_{ph,PWM}}$ by applying the SPWM strategy
3. Transform the isolated PWM voltages $\Delta\mathbf{U_{ph,PWM}}$ back into dq coordinates: $\mathbf{U_{dq,PWM}} = \mathbf{T_{dqf}} \mathbf{T_{ppU}} \mathbf{U_{ph,PWM}}$.
4. The subtraction $\mathbf{U_{dq,PWM}} - \mathbf{U_{dq}}$ isolates only the dq voltage waveform which is responsible for the PWM current ripple. Neglecting the resistances, use the voltage equations to calculate the PWM current ripple in dq coordinates

$$\Delta\mathbf{I_{dq,PWM}} = \mathbf{L_{dq}^{-1}} \left(\mathbf{U_{dq,PWM}} - \mathbf{U_{dq}} \right). \tag{8.14}$$

   As the rotational speed is lower than the switching frequency the induced voltage of the PWM current ripple due to rotation can be neglected.
5. Transform the current ripple $\Delta\mathbf{I_{dq,PWM}}$ back into phase coordinates and add on top of the smooth currents $\mathbf{I_{ph}}$

$$\Delta\mathbf{I_{ph,PWM}} = \mathbf{T_{ppI}^{-1}} \mathbf{T_{dqf}^{-1}} \Delta\mathbf{I_{dq,PWM}} \qquad \mathbf{I_{ph,PWM}} = \mathbf{I_{ph}} + \Delta\mathbf{I_{ph,PWM}} \tag{8.15}$$

The core flux is then calculated using the PWM currents $\mathbf{I_{ph,PWM}}$. As the smooth drive currents in dq coordinates are independent of speed and DC link voltage at a given operating point, the core flux can be calculated for arbitrary DC link voltages and motor speeds. A much finer discretization has to be adopted in order to consider the effects of the PWM ripple which increases the computational time significantly. Therefore, a discontinuous discretization which samples the voltages only at the PWM voltage steps has been utilized instead of continuous discretization. Apart from that, the iron loss components are calculated just as before.

8.3.2 Model Parametrization

In order to parametrize the iron loss model, the conventional WRSM-no-load losses are calculated once for the p_{m} pole-pair machine and once for the p_{h} pole-pair machine by parametrizing the core flux model only with a DC current I_{fm} (I_{fh}).Thus, the calculated no-load eddy, excess and hysteresis losses are obtained as functions of the loss coefficients K_{h}, K_{c} and K_{e}. The calculated iron losses have then been fitted to experimental iron losses

curves recorded during the p_m and p_h pole-pair no-load experiment (see Section 7.2.2). An important remark is that both no-load curves for the p_m and p_h pole-pair machine are used for fitting the coefficients K_h, K_c and K_e because the iron loss model needs to properly reproduce the iron losses in both machines simultaneously. As the linear iron loss model does not include saturation effects, only small field currents until $I_\mathrm{fm} = 8\,\mathrm{A}$ ($I_\mathrm{fh} = 6\,\mathrm{A}$) have been used to fit the p_m (p_h) pole-pair no-load losses to experimental data. In Fig. 8.13 the measured and fitted iron losses are shown. It can be seen that a single set of iron loss coefficients can replicate the measured no-load iron losses of both p_m and p_h pole-pair machine adequately. The result of the fit are the iron loss coefficients $K_\mathrm{h} = 350$, $K_\mathrm{c} = 1$ and $K_\mathrm{e} = 10$, which were used in advance for the iron loss calculation Figs. 8.7, 8.8 and 8.12.

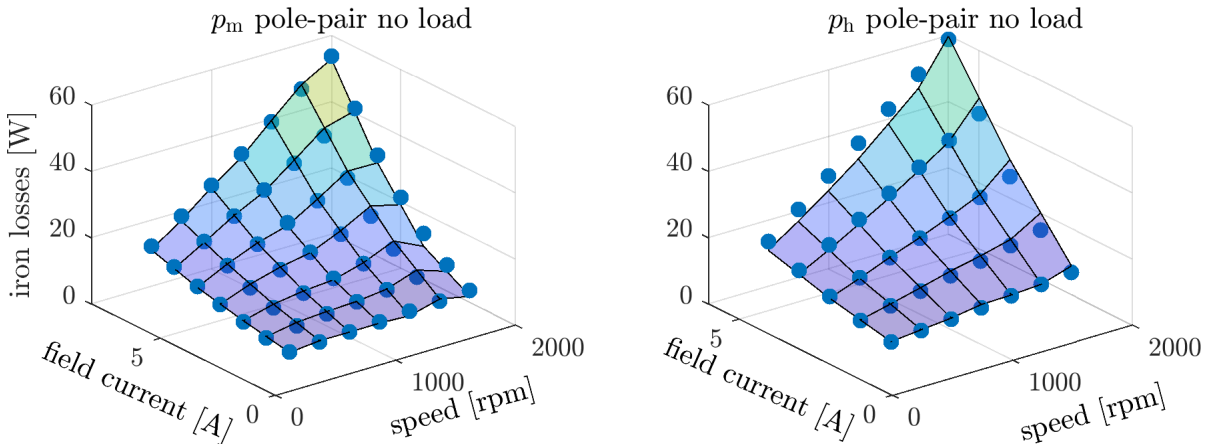

Figure 8.13: Surface fit of the simulated no-load losses with experimental data.

8.3.3 Comparison between Measurement and Calculation

In this section, the core flux densities are calculated with the PWM ripple included and the resultant iron losses are compared to the measured iron losses obtained from an equivalent experiment. The current ripple is determined for a DC link voltage of 250 V and switching frequency of 8 kHz for the stator inverter and 2 kHz for the rotor converter. The measured excitation system iron losses $P_\mathrm{fe,h}$ are determined using (7.16) and (7.18) by first isolating the p_h pole-pair losses and afterwards subtracting the copper and power electronic losses. Just as in Section 7.3.1, the reference no-load losses $P_\mathrm{fe,m}$ are determined once with the stator windings connected to the two B6 inverters and once with the stator windings in open circuit.

In Fig. 8.14 the comparison with the stator windings in open circuit is shown. In order to highlight the effect of the PWM ripple, the blue area denotes the iron losses $P_\mathrm{fe,h}$ calculated with **smooth** currents and the red area the additional PWM-induced iron losses when the PWM ripple is considered in the core flux calculation. It can be seen that the neglect of the PWM ripple in the iron loss calculation yields large deviations with the measurements.

However, with the addition of the PWM ripple into the iron loss model, a good match between the calculated and measured losses is obtained. Both the magnitude and the speed-dependent increase of the losses can be predicted by the core flux model for all excitation frequencies, which is surprising in light of the measurement limitations, the coarsely discretized core flux model and the simplified iron loss model which is fully parametrized by only three coefficients K_h, K_c and K_e.

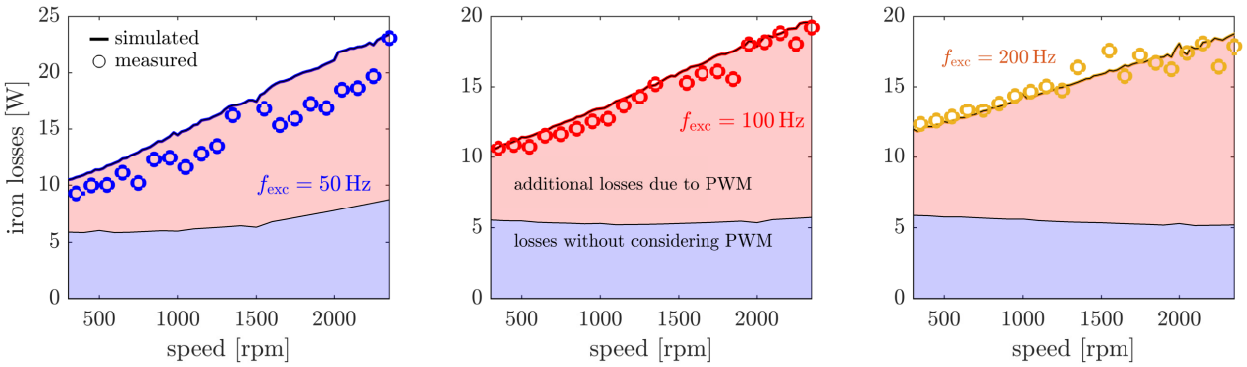

Figure 8.14: Comparison between measured and simulated iron losses $P_\mathrm{fe,h}$ ($P_\mathrm{fe,m}$ obtained with stator windings in open circuit).

Fig. 8.14 serves in demonstrating the significant increase of the iron losses when a PWM current ripple is present and verifies the capability of the iron loss model to predict iron losses even for PWM excitation. However, the experiment is not a good choice to isolate the excitation system iron losses $P_\mathrm{fe,h}$ because it compares the HESM-no-load experiment (where a PWM ripple is present) with the WRSM-no-load experiment with open stator windings (where no PWM ripple present).

A closer estimation of the iron loss increase $P_\mathrm{fe,h}$ can be obtained when the no-load reference losses $P_\mathrm{fe,m}$ are also determined with the stator inverter connected to the machine i.e. PWM-induced iron losses are also present. The corresponding comparison between measurement and calculation is depicted in Fig. 8.15. It can be observed that the accuracy between measurement and calculation is lower than in Fig. 8.14 especially after a speed of about 1700 rpm where noise in the measurement data and significant deviations in the loss trend appear. The reason for this is twofold: Firstly, the losses are overall smaller in Fig. 8.15 compared to Fig. 8.14 especially with increasing speed. This smaller magnitude of the losses makes the measurement much more prone to measurement noise and errors. Secondly, there appears to be a deviation between the numerically estimated and measured reference no-load losses $P_\mathrm{fe,m}$. This discrepancy likely stems from an inaccurate prediction of the PWM current ripple which could be a side effect of the HESM control system: As the p_h pole-pair HESM controller is active during the WRSM-no-load experiment, it reacts to noise, current offsets and slight asymmetries of the phase currents and sets irregular voltage commands U_dh and U_qh, which affect the modulation index and thus the PWM-induced iron losses. Despite

some deviations between measurement and calculation there is a satisfactory agreement in light of the model simplifications, measurement inaccuracies and unknowns. The red areas highlighted in Fig. 8.15 indicate that overall the iron losses due to the PWM ripple increase. However, the additional iron losses due to the PWM ripple do not increase significantly with speed and for $f_{\mathrm{exc}} = 200\,\mathrm{Hz}$ they even decrease with speed. For speeds greater than 1500 rpm the PWM-induced iron losses make up less than 20 % of $P_{\mathrm{fe,h}}$.

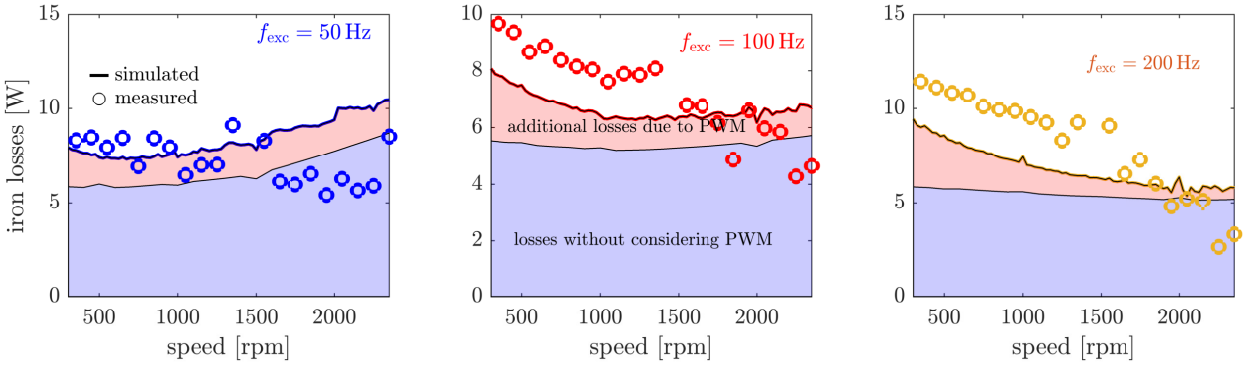

Figure 8.15: Comparison between measured and simulated iron losses $P_{\mathrm{fe,h}}$ ($P_{\mathrm{fe,m}}$ obtained with stator windings connected to the inverter).

In conclusion, the explanation and estimation of the excitation system iron losses with a computational quick and simple iron loss model has been achieved in this chapter. While the results have only been investigated for no-load operation, the approach is analogous for operation under load. The experimental analysis of the iron losses under load has been omitted here, because the mechanical power dominates the stator and shaft power so that the iron losses constitute only a vanishingly small portion of the power flow.

Chapter 9

Torque-Speed Region of the HESM

In the previous numerical and experimental analyses, the focus was mainly on isolating the effect of the p_h pole-pair machine excitation system and its losses, instead of analysing the HESM as a single machine. Furthermore, in a variable-speed drive system, a machine is not operated in a single operating point, but within a torque-speed region which encompasses all feasible operating points. The operating points in the torque-speed region are determined by an optimization which minimizes the total losses (MTPL = *maximum torque per loss*) or the stator current (MTPA = *Maximum-torque-per-ampere*) under the following constraints:

- Mechanical considerations which limit the maximum speed.
- Overcurrent protection of the power electronics which limits the maximum currents.
- Maximum output power of the drive inverter.
- The temperature which limits the maximum continuous and short-term currents and leads to a distinction between the *continuous* and *overload* torque-speed region.
- The maximum DC link voltage which determines the constant torque region (armature setting region) and the field-weakening region.

The most critical constraint is the maximum DC link voltage which directly limits the maximum voltage that can be applied to the machine windings. This constraint splits the torque-speed region into two parts: The **armature-setting region** describes the operating points until the maximum possible terminal voltage is reached. In this region, the torque is either limited by the maximum stator and rotor currents $I_\mathrm{S,max}$, $I_\mathrm{fm,max}$ or by a fixed maximum torque value $M_\mathrm{el,max}$. As the motor speed rises, at a certain corner speed the constant torque cannot be maintained with the same currents without exceeding the maximum possible terminal voltage. In this case the machine has to transition into the **field-weakening region** where the induced voltage is weakened by adjusting the drive currents. In the field-weakening region, the drive currents are optimized (within their constraints) to realize the maximum possible torque per speed.

In a WRSM there are three degrees of freedom, the stator d-axis current I_{dm}, q-axis current I_{qm} and the field current I_{fm}. The capability of adjusting the field current depending on the speed and load presents considerable efficiency advantages in the field-weakening and partial load region compared to a permanent excitation field as shown in [45], [63]. The optimal choice for the three degrees of freedom at a given torque and speed is non-trivial. In fact, both the d-axis current I_{dm} **and** the field current I_{fm} are used for field-weakening.
While this is also valid in the HESM, there is a critical difference compared to conventional WRSMs: In a WRSM, the supply of the field current I_{fm} does not occupy any DC link voltage. However, in the HESM the additional p_{h} pole-pair currents required for the injection of I_{fm} very much take up DC link voltage that cannot be used for the p_{m} pole-pair machine any more. This additional voltage demand affects the torque-speed region in a HESM negatively. In the previous chapters, the voltage demand of the excitation system has only been analyzed without going into detail: The steady-state equations of the HESM in Section 5.2.3 predicted a factor k_{Uh} that quantifies the voltage demand of the p_{h} pole-pair machine. This factor could be experimentally verified in Section 7.3.1 and partly motivated that the rated torque in Section 7.3.3 was shown only for a low speed of 500 rpm. In this section, the voltage demand and its impact on the torque-speed region of the HESM is revisited in detail.

9.1 Maximum Torque per Speed Curve

The maximum torque-speed curve describes the boundaries of the torque-speed region. By comparing the maximum torque per speed of the HESM and WRSM, the impact of the excitation system on the speed range can be quantified. The following simplifications are made in order to investigate the HESM speed region:

- The machine is not investigated in the deep **saturation** region so that
  - the p_{m} pole-pair machine and p_{h} pole-pair machine are perfectly decoupled. This is valid if the machine is not deeply saturated as shown in Section 6.2.
  - saturation in the p_{h} pole-pair machine is neglected which is valid as shown in Section 6.4.1.
  - saliency is neglected ($L_{\mathrm{qm}} = L_{\mathrm{dm}}$) so that an analytical solution is tenable
- The DC link **voltage demand** of the p_{h} pole-pair machine is considered by the constant factor k_{Uh} valid in the speed interval $f_{\mathrm{m}} = [0, \frac{f_{\mathrm{exc}}}{p_{\mathrm{m}} - p_{\mathrm{h}}}]$ as has been shown in Section 5.2.3. The parameter k_{Uh} fully replicates the influence of the p_{h} pole-pair machine on the operational limits of the drive system.
- A **current constraint** for the stator current $I_{\mathrm{S,max}}$ and rotor current $I_{\mathrm{fm,max}}$ is considered only for the p_{m} pole-pair machine. This is because the excitation system currents I_{dh}

and I_{fh} depend on the field current I_{fm}. The maximum field current $I_{\mathrm{fm,max}}$ therefore uniquely determines the current limits of the p_{h} pole-pair machine. Thus, the **current demand** of the p_{h} pole-pair machine is only implicitly taken into account

With these simplifications, the entire HESM can be modelled using only the Park equations of the p_{m} pole-pair machine extended by the factor k_{Uh}. It can be determined experimentally as a constant value or as a speed-dependent value. However, here a single constant $k_{\mathrm{Uh}} = 15\,\frac{\mathrm{V}}{\mathrm{A}}$ is used as extracted from Fig. 7.11.

The determination of the maximum torque-per-speed curve can be defined as an optimization problem that consists of finding the maximum torque at a given speed that satisfies the voltage and current constraints

$$\max M_{\mathrm{el}} \text{ for } \begin{cases} U_{\mathrm{dc}} = \frac{\hat{U}_{\mathrm{m}}}{k_{\mathrm{mod}}} + k_{\mathrm{Uh}} I_{\mathrm{fm}} < U_{\mathrm{dc,max}} & \text{DC link Voltage Constraint} \\ I_{\mathrm{fm}} < I_{\mathrm{fm,max}} & \text{Rotor Current Constraint} \\ \hat{I}_{\mathrm{m}} < I_{\mathrm{S,max}} & \text{Stator Current Constraint} \end{cases} . \tag{9.1}$$

In (9.1) the term highlighted in red considers the additional DC link voltage demand due to the p_{h} pole-pair machine currents. This additional voltage demand is the reason for the reduced speed range of the HESM compared to a conventional WRSM. Otherwise, the equations that govern the optimization (9.1) are the conventional torque equation (9.2) and voltage equation (9.3) which is extended by the voltage demand of the excitation system $\hat{U}_{\mathrm{h}}$

$$M_{\mathrm{el}} = \frac{3}{2} p_{\mathrm{m}} L_{\mathrm{dfm}} I_{\mathrm{fm}} I_{\mathrm{qm}} + \frac{3}{2} p_{\mathrm{m}} \left(L_{\mathrm{dm}} - L_{\mathrm{qm}} \right) I_{\mathrm{dm}} I_{\mathrm{qm}} \tag{9.2}$$

$$\hat{U}_{\mathrm{m}} = p_{\mathrm{m}} \omega_{\mathrm{m}} \sqrt{(\underbrace{L_{\mathrm{dfm}} I_{\mathrm{fm}} + L_{\mathrm{dm}} I_{\mathrm{dm}}}_{=\Psi_{\mathrm{dm}}})^2 + (\underbrace{L_{\mathrm{qm}} I_{\mathrm{qm}}}_{=\Psi_{\mathrm{qm}}})^2} \tag{9.3}$$

$$U_{\mathrm{dc}} = \frac{\hat{U}_{\mathrm{m}}}{k_{\mathrm{mod}}} + k_{\mathrm{Uh}} I_{\mathrm{fm}} \quad . \tag{9.4}$$

In a conventional WRSM ($k_{\mathrm{Uh}} = 0$) the DC link voltage demand U_{dc} depends only on the p_{m} pole-pair terminal voltage $\hat{U}_{\mathrm{m}}$ which can be lowered by either decreasing the d-axis flux Ψ_{dm} or the q-axis flux Ψ_{qm}. As Ψ_{qm} is proportional to the torque-producing current I_{qm}, the main method of reducing the voltage is by lowering the d-axis flux Ψ_{dm} (= field weakening). Contrary to the field current I_{fm}, the d-axis current I_{dm} is independent of the torque (if saliency is neglected) and therefore the primary means of reducing the flux Ψ_{dm}. Thus, field-weakening in conventional WRSM consists in primarily applying a negative I_{dm} and only lowering the current components I_{qm} and I_{fm} responsible for torque-production if absolutely necessary [63].
In the HESM, the same principle applies. However, the cost of supplying a field current I_{fm} is far higher than in WRSMs, because I_{fm} not only affects the p_{m} pole-pair voltage $\hat{U}_{\mathrm{m}}$, but

also the p_h pole-pair voltage $\hat{U}_\mathrm{h}$. As the current I_dm only affects the voltage demand $\hat{U}_\mathrm{m}$, its field-weakening capability is limited and most field-weakening must be achieved by adjusting I_fm which negatively affects the torque. This is shown by performing the optimization (9.1) in MATLAB using the *fmincon* function. The calculated torque-speed curve for a DC link voltage of $U_\mathrm{dc} = 250\,\mathrm{V}$ is shown exemplarily in Fig. 9.1. The following regions can be distinguished:

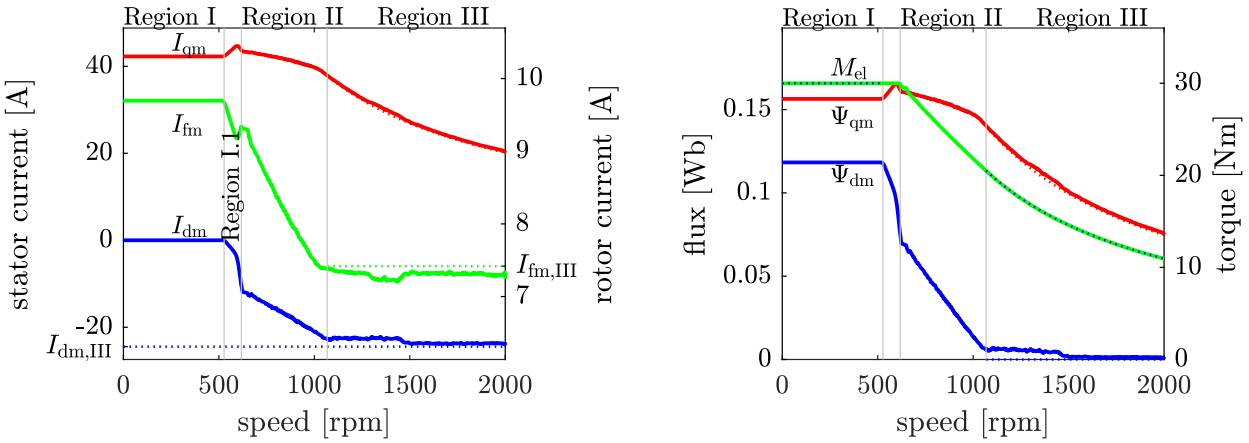

Figure 9.1: Maximum torque-speed curves of the HESM for a DC link voltage of $U_\mathrm{dc} = 250\,\mathrm{V}$ with predicted corner speeds without saliency.

Region I: Armature Setting Range

In the armature setting range the maximum torque M_el^* stays constant and the machine operates below the maximum terminal voltage. The operating currents $I_\mathrm{dm,I}, I_\mathrm{qm,I}$ and $I_\mathrm{fm,I}$ are constant if the MTPA strategy is used. As the induced voltage of the machine rises with speed, at a certain speed $\omega_\mathrm{m,I}$, the voltage demand of the machine reaches the limits imposed by the maximum DC link voltage. This speed can be obtained by inserting the known drive currents $I_\mathrm{dm,I}, I_\mathrm{qm,I}, I_\mathrm{fm,I}$ into (9.4) and rearranging

$$\omega_\mathrm{m,I} = \frac{1}{p_\mathrm{m}} \frac{k_\mathrm{mod} U_\mathrm{dc,max} - k_\mathrm{mod} k_\mathrm{Uh} I_\mathrm{fm,I}}{\sqrt{\left(L_\mathrm{dfm} I_\mathrm{fm,I} + L_\mathrm{dm} I_\mathrm{dm,I}\right)^2 + \left(L_\mathrm{qm} I_\mathrm{qm,I}\right)^2}} \quad . \tag{9.5}$$

After this speed, field weakening must be used which keeps the voltage demand just at the limits of the DC link voltage $U_\mathrm{dc} = U_\mathrm{dc,max}$. The red term in (9.5) indicates that field-weakening must be initiated sooner in HESMs compared to WRSMs.

Region I.1: Field-Weakening at Constant Torque
Beyond the armature setting region the maximum torque M_{el}^{*} can only be maintained if the maximum stator current $\sqrt{I_{\mathrm{dm,I}}^2 + I_{\mathrm{qm,I}}^2} < I_{\mathrm{S,max}}$ isn't reached yet. If the HESM already operates at its maximum currents, region I.1 does not occur. In Fig. 9.1 a constant torque line below the maximum torque is chosen for the armature setting region so that the maximum currents are not reached yet. In region I.1 the HESM uses field-weakening via a negative d-axis current I_{dm} **and** by lowering the field current I_{fm} to lower the voltage demand. In order to maintain the torque due to the lower field current, the q-axis current I_{qm} has to be increased. The steep decline of the field current I_{fm} demonstrates that the voltage can not be compensated by a negative I_{dm} alone and is mostly attributable to high excitation system voltage demand (k_{Uh}). This is in contrast to a WRSM where the field current I_{fm} stays constant in the maximum torque line and mostly I_{dm} is used for field-weakening if the condition $L_{\mathrm{dfm}} I_{\mathrm{fm,I}} < L_{\mathrm{dm}} I_{\mathrm{S,max}}$ is fulfilled (which is the case here) [45], [63]. Region I.1 lasts until the maximum stator current $I_{\mathrm{S,max}}$ is reached.

Region II: Field-Weakening with Decreasing Torque and Flux
The torque cannot stay constant when the HESM operates at its maximum stator current $I_{\mathrm{S,max}}$ because the voltage can only be reduced by freeing field-weakening current I_{dm} (which reduces $I_{\mathrm{qm}} = \sqrt{I_{\mathrm{S,max}}^2 - I_{\mathrm{dm}}^2}$) or by further reducing the field current I_{fm}. As both current components I_{qm} and I_{fm} reduce the torque, the torque inevitably decreases in Region II. Thus, the field-weakening strategy consists in reducing I_{qm} and I_{fm} so that the torque is least affected. In Fig. 9.1, it can be seen that both I_{dm} and I_{fm} are used for field-weakening with the largest contribution to field-weakening from lowering I_{fm}. Again, this is unlike a conventional WRSM and emphasizes that most of the voltage demand is due to the excitation system. The current I_{qm} only decreases slightly to make room for I_{dm}. It can be observed that the field-weakening currents — and thus the d-axis flux Ψ_{dm} — decrease linearly. The end of region II is reached once the d-axis flux Ψ_{dm} has reached zero. In Fig. 9.1 a small non-zero Ψ_{dm} remains in region III due to local minima in the optimization.

Region III: Field-Weakening with Decreasing Torque and $\Psi_{\mathrm{dm}} = 0$
Once $\Psi_{\mathrm{dm}} = 0$ is reached, it stays at zero. In this case (9.4) simplifies to

$$U_{\mathrm{dc}} = \frac{1}{k_{\mathrm{mod}}} \omega_{\mathrm{m}} p_{\mathrm{m}} L_{\mathrm{qm}} I_{\mathrm{qm}} + k_{\mathrm{Uh}} I_{\mathrm{fm}} \qquad \Rightarrow \qquad I_{\mathrm{qm}} = \frac{k_{\mathrm{mod}} U_{\mathrm{dc}} - k_{\mathrm{mod}} k_{\mathrm{Uh}} I_{\mathrm{fm}}}{\omega_{\mathrm{m}} p_{\mathrm{m}} L_{\mathrm{qm}}}. \tag{9.6}$$

The torque (9.2) can then be expressed only in terms of I_{fm} by inserting (9.6) into (9.2). This equation expresses the torque as a function of field current I_{fm} at the maximum DC

link voltage $U_{\mathrm{dc,max}}$ for a given speed ω_{m}

$$M_{\mathrm{el}}(I_{\mathrm{fm}}) = \frac{3}{2}\frac{L_{\mathrm{dfm}}}{L_{\mathrm{qm}}} k_{\mathrm{mod}} I_{\mathrm{fm}} \frac{U_{\mathrm{dc,max}} - k_{\mathrm{Uh}} I_{\mathrm{fm}}}{\omega_{\mathrm{m}}}. \tag{9.7}$$

In order to obtain the maximum torque at a given speed ω_{m}, the extremum is found

$$\frac{\partial M_{\mathrm{el}}}{\partial I_{\mathrm{fm}}} = \frac{3}{2}\frac{L_{\mathrm{dfm}}}{L_{\mathrm{qm}}}\frac{k_{\mathrm{mod}}}{\omega_{\mathrm{m}}}\left(U_{\mathrm{dc,max}} - 2k_{\mathrm{Uh}} I_{\mathrm{fm}}\right) \stackrel{!}{=} 0 \qquad \Rightarrow \qquad I_{\mathrm{fm,III}} = \frac{U_{\mathrm{dc}}}{2k_{\mathrm{Uh}}}. \tag{9.8}$$

The value $I_{\mathrm{fm,III}}$ denotes that the field current stays constant in region III. With the condition of zero d-axis flux Ψ_{dm}, the corresponding stator current I_{dm} in region III is defined as

$$\Psi_{\mathrm{dm}} = L_{\mathrm{dfm}} I_{\mathrm{fm}} + L_{\mathrm{dm}} I_{\mathrm{dm}} \stackrel{!}{=} 0 \qquad \Rightarrow \qquad I_{\mathrm{dm,III}} = -\frac{L_{\mathrm{dfm}}}{L_{\mathrm{dm}}} I_{\mathrm{fm,III}} \tag{9.9}$$

This shows that the field-weakening current $I_{\mathrm{dm,III}}$ only depends on $I_{\mathrm{fm,III}}$ and is also constant. Thus, the voltage U_{dc} can now only be reduced further by lowering the q-axis flux Ψ_{qm}. Thus, in region III, the voltage demand can only be lowered by decreasing I_{qm} so that the stator current falls below the maximum current $I_{\mathrm{S,max}}$. Inserting $I_{\mathrm{fm,III}}$ into (9.4) the speed-dependent current I_{qm} follows

$$I_{\mathrm{qm}} = \frac{1}{2}\frac{k_{\mathrm{mod}} U_{\mathrm{dc}}}{p_{\mathrm{m}} L_{\mathrm{qm}}}\frac{1}{\omega_{\mathrm{m}}}. \tag{9.10}$$

The torque in region III is therefore also defined as

$$M_{\mathrm{el}} = \frac{3}{4}\frac{L_{\mathrm{dfm}}}{L_{\mathrm{qm}}}\frac{1}{k_{\mathrm{Uh}}}\left(k_{\mathrm{mod}} U_{\mathrm{dc,max}}\right)^2 \frac{1}{\omega_{\mathrm{m}}}. \tag{9.11}$$

This result coincides very well with the results shown by the numerical optimization in Fig. 9.1. An important conclusion of this analysis is that the field current I_{fm} and the field-weakening current I_{dm} are held constant in the deep field-weakening region III at values that depend **only** on the DC link voltage U_{dc}

$$I_{\mathrm{fm,III}} = \frac{U_{\mathrm{dc}} k_{\mathrm{mod}}}{k_{\mathrm{Uh}}} \qquad\qquad I_{\mathrm{dm,III}} = -\frac{L_{\mathrm{dfm}}}{L_{\mathrm{dm}}}\frac{U_{\mathrm{dc}}}{2k_{\mathrm{Uh}}}. \tag{9.12}$$

This means that the higher the DC link voltage $U_{\mathrm{dc,max}}$ and the lower k_{Uh}, the more field weakening via I_{dm} can be used. This is demonstrated in Fig. 9.2 for different DC link voltages U_{dc}: For a low DC link voltage of $U_{\mathrm{dc}} = 200\,\mathrm{V}$ the excitation system voltage demand dominates the available DC link voltage. In this case the constant torque region I is almost non-existent and only very low field currents I_{fm} are possible in region III. There is no such limitation in conventional WRSMs, where the field current in the deep field-weakening

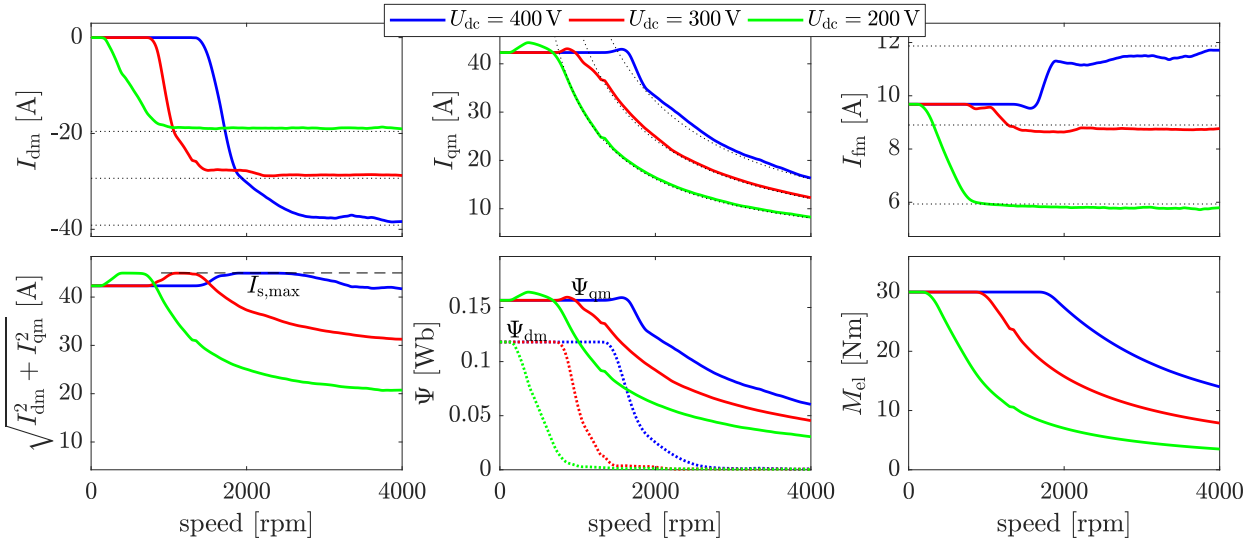

Figure 9.2: Maximum torque-speed curve for different DC link voltages U_{dc}. Dotted lines denote the analytically predicted currents in the field-weakening region III.

region mostly depends on whether sufficient I_{dm} is available to reduce the d-axis flux Ψ_{dm}. However, for larger DC link voltages the field-weakening behavior approaches conventional WRSM operation. More precisely, if $I_{fm,III}$ in (9.12) exceeds the maximum field current $I_{fm,max}$, the field-weakening behavior is identical to a conventional WRSM, i.e. only I_{dm} is used for field-weakening and the field I_{fm} stays at its maximum.

As the maximum DC link voltage is usually fixed in a drive system, the excitation system parameter k_{Uh} is the main parameter which determines the reduction of the speed region of HESMs compared to WRSMs. For $k_{Uh} = 0$ the HESM is identical to a conventional WRSM. The influence of the k_{Uh} value is demonstrated in Fig. 9.3 for three exemplary values of k_{Uh}. The reduction of k_{Uh} is purely exemplary and does not imply that such a reduction can (or cannot) be realized. It can be seen that the HESM speed region is significantly reduced because of the large k_{Uh}. The derating of the HESM speed range compared to the WRSM speed range can be approximated by the division of the corner speeds $\omega_{m,I}$ of the HESM from the respective corner speed of the WRSM ($k_{Uh} = 0$)

$$\text{Derating} = \frac{U_{dc,max} - k_{Uh} I_{fm,I}}{U_{dc,max}} \quad [\%]. \tag{9.13}$$

Hence, it must be stressed that the significant reduction of the speed range is the most profound disadvantage of the proposed excitation system.

While the analysis in this section neglects rotor saliency, the results apply to salient-pole machines analogously. When taking into account saliency $L_{qm} < L_{dm}$ the negative reluctance torque in the field-weakening region rewards field-weakening with I_{fm} even more than field-weakening with I_{dm}. This is why I_{fm} is reduced even further in the field-weakening region.

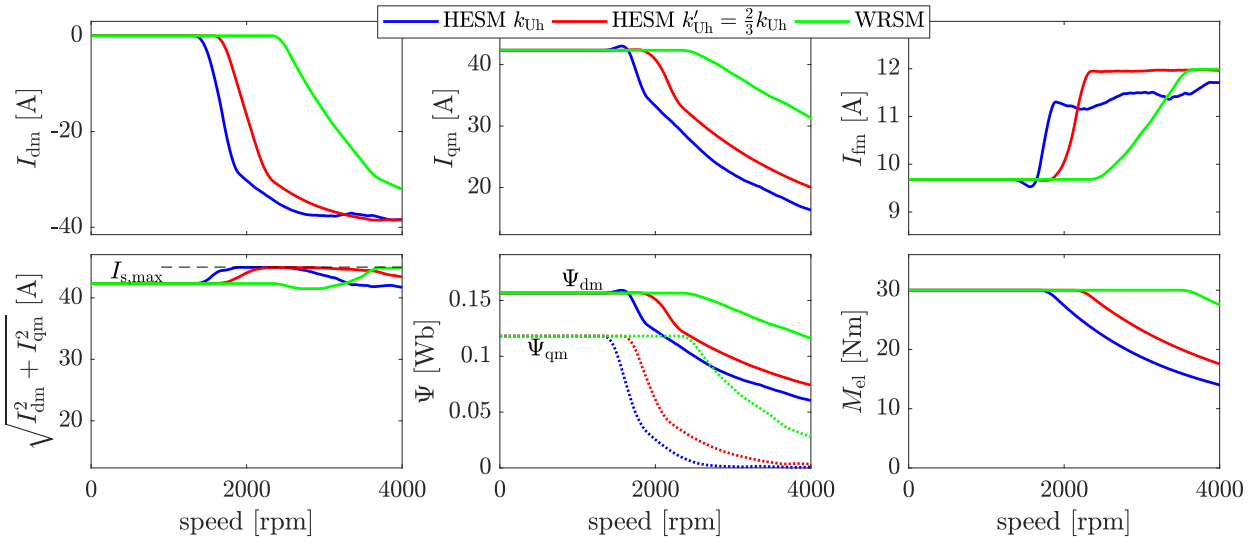

Figure 9.3: Maximum torque-speed curves of the HESM for DC link voltages $U_{\mathrm{dc}} = 400\,\mathrm{V}$ for different k_{Uh}.

However, the maximum torque per speed is similar because the saliency-induced torque reduction in the field-weakening region is compensated at least partially by the lower voltage demand due to the lower q-axis flux $\Psi_{\mathrm{qm}} \sim L_{\mathrm{qm}}$.

9.2 Torque-Speed Map

While the previous section has focused on the boundaries of the torque-speed map, this section will address the performance in the entire operation region. The same simplifications as in Section 9.1 are made, but now saturation-dependent inductances obtained from the verified FEA model are used to calculate the voltage demand and torque (see Section 6.2). Furthermore, saliency is now considered. The optimization problem consists in minimizing the losses at a given speed n and load torque M_{el}^*

$$\min P_{\mathrm{v,tot}} \text{ for } \begin{cases} M_{\mathrm{el}} = M_{\mathrm{el}}^* & \text{Torque Constraint} \\ U_{\mathrm{dc}} = \frac{\hat{U}_{\mathrm{m}}}{k_{\mathrm{mod}}} + k_{\mathrm{Uh}} I_{\mathrm{fm}} < U_{\mathrm{dc,max}} & \text{DC link Voltage Constraint} \\ I_{\mathrm{fm}} < I_{\mathrm{fm,max}} & \text{Rotor Current Constraint} \\ \hat{I}_{\mathrm{m}} < I_{\mathrm{S,max}} & \text{Stator Current Constraint} \end{cases} \tag{9.14}$$

The total dissipated power $P_{\mathrm{v,tot}}$ in the machine consists of the p_{m} pole-pair machine and p_{h} pole-pair machine losses and is calculated as in (9.15). The stator copper losses of the p_{m} pole-pair machine are calculated using Joule's law from the dq currents. The iron losses $P_{\mathrm{fe,m}}$ are a function of the magnetizing currents and speed and are calculated from look-up tables obtained from FEA. The term $P_{\mathrm{v,mech}}$ denotes the frictional loss at the bearings and

slip rings as well as the windage losses due to air friction.

$$P_{\mathrm{v,tot}} = \frac{3}{2} R_{\mathrm{sm}} \hat{I}_{\mathrm{m}}^2 + P_{\mathrm{fe,m}}(I_{\mathrm{dm,mag}}, I_{\mathrm{qm,mag}}, f_{\mathrm{m}}) + P_{\mathrm{exc}} \frac{1}{\eta_{\mathrm{exc}}}(f_{\mathrm{m}}) + P_{\mathrm{v,mech}} \tag{9.15}$$

For the p_{h} pole-pair machine, it was shown in the previous chapters that the excitation system losses are difficult to predict mainly because of the iron losses $P_{\mathrm{fe,h}}$. A numerical solution of the harmonic machine iron losses $P_{\mathrm{fe,h}}$ for each variation of speed and load under consideration of the PWM ripple is not feasible from the perspective of calculation time. However, it could be seen in Chapter 8 that the overall excitation system efficiency η_{exc} is around $75 - 80\%$ in no-load operation and speed-dependent. While no generalization of the no-load excitation system efficiency η_{exc} to arbitrary load operating points is possible, a constant averaged worst-case excitation system efficiency $\eta_{\mathrm{exc}} = 75\,\%$ is used in (9.15).
The solution to the optimization (9.14) for a DC link voltage of $U_{\mathrm{dc}} = 400\,\mathrm{V}$ yields the contour maps for the drive currents and for the drive system efficiency η_{gen} in Fig. 9.4. Generally, the HESM has all the characteristics of a conventional WRSM. It can be seen that due to saliency the HESM benefits from a slight d-axis current I_{dm} in the armature setting region. The advantage of the variable excitation field compared to PMSMs can be observed by the reduction of the field current I_{fm} in the partial load region. In the (yellow) field-weakening region, it is apparent that the HESM uses both the d-axis current I_{dm} and the field current I_{fm} for field-weakening. The HESM can achieve high efficiencies close to $90\,\%$, although they are limited by the premature ending of the torque-speed region. The substantial speed range reduction compared to a WRSM is highlighted by the gray area which indicates the additional speed range of a WRSM (calculated using $k_{\mathrm{Uh}} = 0$).
In Fig. 9.5 the difference between the HESM drive system efficiency to that of the WRSM is shown. The WRSM efficiency has been obtained by setting the excitation system efficiency η_{exc} to $100\,\%$ indicating ideal excitation through slip-rings and brushes. It can be seen that the difference in efficiency is relatively small despite the lower excitation frequency η_{exc} which is an expected result as the excitation power is only a small portion of the mechanical (output) power. The loss of efficiency is at maximum $4\,\%$ in the deep field-weakening region and below $1\,\%$ in a large part of the torque-speed region. On the one hand, these additional losses are caused by the excitation system losses. On the other hand, they are caused by slightly different drive currents in the armature setting region because the HESM behaves like a WRSM with a higher field resistance $R_{\mathrm{fm}}/\eta_{\mathrm{exc}}$. Hence, the optimization of the losses penalizes larger field currents in the HESM more severely than in the WRSM. This yields lower field currents I_{fm} in favor of more stator current $I_{\mathrm{dm}}, I_{\mathrm{qm}}$. Furthermore, a significant drop of the HESM efficiency is observed due to the early onset of the field-weakening region. Here, the suboptimal drive currents of the HESM cause additional losses compared to the WRSM which still operates in the armature setting region with optimal drive currents to reach a given torque.

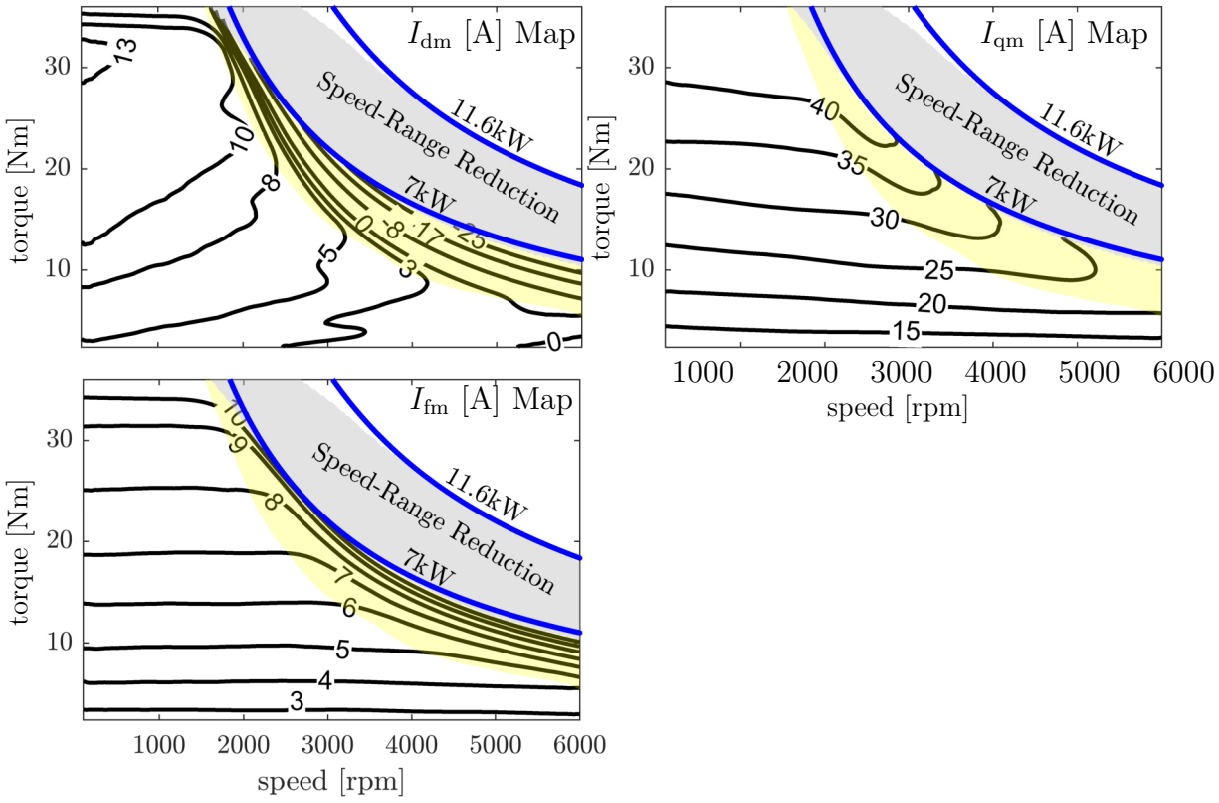

Figure 9.4: Simulated Contour map for the drive currents I_{dm}, I_{qm}, I_{fm} and the drive efficiency η_{gen} in the entire torque-speed region for HESM operation and $U_{dc,max} = 400\,V$. The yellow area denotes the field-weakening area where the drive system operates at the maximum DC link voltage $U_{dc,max}$. The gray area denotes the reduction of the torque-speed-region.

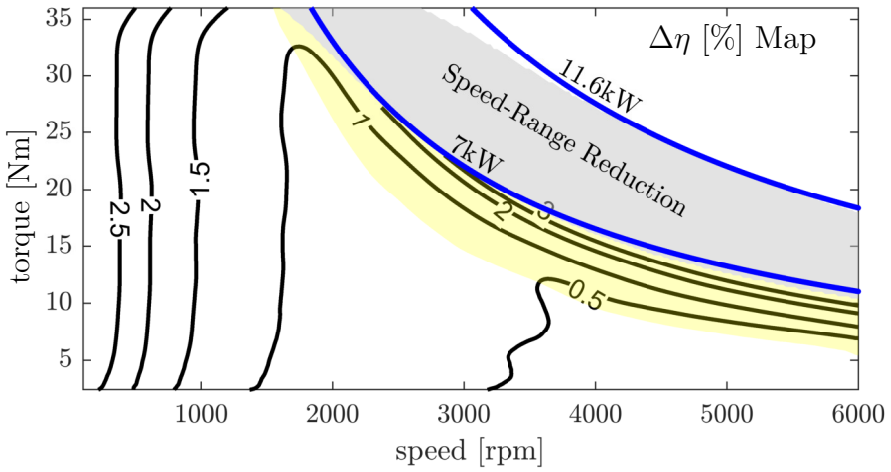

Figure 9.5: Difference in drive system efficiency for HESM and WRSM operation in the entire torque-speed region. The yellow and gray area definitions are identical with Fig. 9.4.

It can be concluded that while the excitation concept generates noticeable iron losses, copper losses and power electronic losses — which require further optimization — they reduce the efficiency by at most a few percent. The more critical limitation of the excitation system is the reduction of the speed range summarized in the parameter k_{Uh}.

9.2.1 Measurement of the Torque-Speed Region

In this section the analytically and numerically predicted torque-speed curves are confirmed experimentally. Due to the limitations in the test bench, all experiments are performed only until $n = 2000\,\mathrm{rpm}$. A reduced DC link voltage of $U_{\mathrm{dc}} = 200\,\mathrm{V}$ is used to showcase the field-weakening region. First, the (theoretical) optimal control currents I^*_{dm}, I^*_{qm} and I^*_{fm} for $U_{\mathrm{dc}} = 200\,\mathrm{V}$ are determined numerically from the optimization (9.14) where I^*_{dh} follows from $I^*_{\mathrm{fm}}/k_{\mathrm{Idh}}$ with $k_{\mathrm{Idh}} = 1.3$ according to Fig. 7.11. The resulting drive currents — shown in Fig. 9.6c – are then set as references in the test bench. It can be seen in the chosen torque-speed region for $U_{\mathrm{dc}} = 200\,\mathrm{V}$ that field-weakening is predominantly achieved using I_{fm} due to the high excitation system voltage demand. The maximum torque-per speed curve and the torque lines between 5 Nm and 25 Nm for speeds from 500 rpm to 2000 rpm are set as operating points in generator mode. The calculated drive system efficiency η is then determined from the measured electrical output power P_{out} and the shaft input power P_{in}

$$\eta_{\mathrm{gen}} = \frac{P_{\mathrm{out}}}{P_{\mathrm{in}}}. \tag{9.16}$$

Furthermore, the required DC link voltage demand is calculated from the internal controller voltages $\hat{U}_{\mathrm{h}} = \sqrt{U^2_{\mathrm{dh}} + U^2_{\mathrm{qh}}}$ and $\hat{U}_{\mathrm{m}} = \sqrt{U^2_{\mathrm{dm}} + U^2_{\mathrm{qm}}}$ of the p_{h} and p_{m} pole-pair machine which are recorded during each experiment. In Fig. 9.6a, the measured drive efficiency and the recorded voltage demand are shown. It can be confirmed that the drive currents determined from the optimization correspond to the desired torque with satisfactory agreement, even though the torque line 25 Nm is not reached exactly, because k_{Idh} drops slightly. Analogously, the maximum torque per speed line at larger speeds is slightly higher than predicted. This can be explained by a slight disagreement between the desired field current I^*_{fm} and the actual (measured) field current induced as a consequence of the open-loop control of $\hat{I}^*_{\mathrm{dh}} = I^*_{\mathrm{fm}}/k_{\mathrm{Idh}}$. This problem can be solved by a simple I_{fm}-observer which adjusts $\hat{I}_{\mathrm{dh}}$ so that the desired I_{fm} is reached. The predicted drive efficiency corresponds to the measured efficiency with decent agreement. The required DC bus voltage is a constant 185 V at the maximum torque per speed line and hence below the $U_{\mathrm{dc}} = 200\,\mathrm{V}$ value used in the optimization. This is because the k_{Uh} value 15 V/A used in the operating point optimization in the previous calculations has been intentionally chosen a bit larger than required to account for irregular voltage harmonics and spikes.

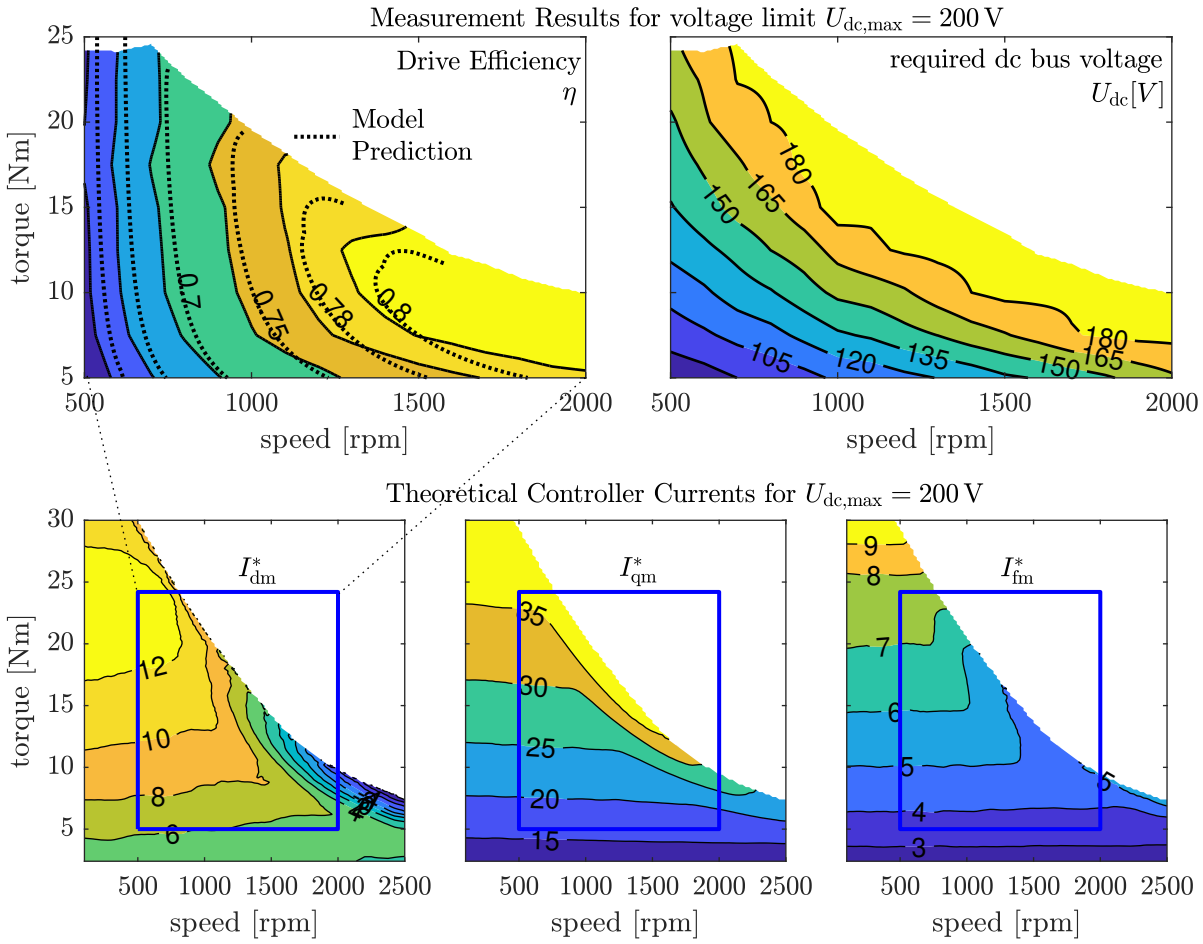

Figure 9.6: Experimental results for the drive efficiency η and required DC link voltage U_{dc} for predicted torque-speed region.

To conclude, the experiments confirm the validity of the torque-speed-region prediction. The computationally fast modelling approach which represents the p_h pole-pair machine by constant parameters k_{Uh} and η_{exc} seems to be a feasible simplification for the prediction of the torque-speed map, even though some inaccuracies in the supplied field current I_{fm} are observed. While more extensive measurements for higher DC bus voltages and load torques in the overload region are pending, they have been omitted due to test bench limitations.

9.3 Improvement of the Torque-Speed Region

In the preceding sections, it has been shown analytically and confirmed experimentally that the reduction of the torque-speed region is the biggest drawback in the HESM concept. Therefore, in this section some ideas concerning its improvement are given. Generally, the high voltage demand of the excitation system can be reduced by the following levers.

- A **geometry optimization** of the HESM with the goal of reducing the leakage inductances and increasing the mutual inductance L_{dfh} leads to a better power transfer capability.
- From a control perspective, **better tracking** of the sinusoidal reference current allows reducing the current demand $\hat{I}_{\mathrm{dh}}$ (see Section 6.3) and thus the voltage demand.
- An **improved rotor circuitry**, e.g. the utilization of an active rectifier on the rotor can not only eliminate rectifier harmonics, but also allows I_{fh} to be adjusted independently from I_{dh} as a degree of freedom.
- From an **operational** standpoint, the dependence of k_{Uh} on the excitation frequency (see Fig. 7.11) allows reducing the voltage demand by reducing the excitation frequency in the field-weakening region.

However, all these approaches only reduce k_{Uh} slightly. The origin of the excessive voltage demand lies in the large frequencies due to the forward rotating fields of fundamental frequency f_+. The simultaneous use of both a forward and backward rotating field f_+ and f_- for harmonic excitation were motivated by two factors: On the one hand, a rotating single-phase field winding fed by an AC current inevitably induces voltages of both frequency components back into the stator anyway (see Section 3.2.3). On the other hand, the usage of both frequency components creates a pulsating rotating field which only excites the dh-axis which couples with the field winding (and not the qh-axis) and thus reduces the stator copper losses by half (see Section 3.2.2).
Both aspects are related to the single-phase p_{h} pole-pair rotor winding and can be addressed by utilizing a multi-phase rotor winding for pole pair p_{h}. In this case a rotating field of a single frequency f_+ **or** f_- can be used. As the high frequencies of the forward rotating field f_+ are responsible for both the high voltage demand **and** a large portion of the iron losses (see e.g. Fig. 8.6) it is apparent that the utilization of **only** the backward rotating field f_- can tackle the two major limitations of the proposed HESM. Thus, an extension to the proposed HESM consists in integrating a multi-phase winding into the rotor — for which one possibility is briefly presented here:
In the current HESM concept only each second salient pole is wound and only a field pointing in the direction of the dh-axis can be produced if the p_{h} pole-pair paths of the field winding are excited. However, if the *unwound* salient-poles are used to accommodate **a second identical field winding** shifted simply by one salient pole, a field in qh-direction can also be produced. The corresponding winding scheme is depicted in Fig. 9.7a. It can be seen that the rotor copper of the existing HESM is simply split up into two field windings — each consisting of four coils just as before (compare Fig. 4.2). The Fd coil groups F1d, F2d, F3d, F4d also occur in the existing HESM concept while the additional (blue) Fq coil groups F1q, F2q, F3q, F4q denote the extended concept. The coil groups are arranged into the bridge configurations in Fig. 9.7b. In Fig. 9.7c the capability of this coil arrangement

to excite both the dh- and qh-axis is shown by feeding the currents I_{fdh} and I_{fqh} into the respective p_{h} pole-pair terminals. On the contrary, feeding the currents I_{fm1} and I_{fm2} into the p_{m} pole-pair terminals of the Fd and Fq windings both excites the dm-axis. Thus, a two-phase rotor winding with respect to the p_{h} pole-pair paths is created which behaves as a single-phase winding with respect to the p_{m} pole-pair machine. The windings Fd and Fq can then both be connected to an independent rotor circuit according to Fig. 5.2. This means that an additional set of power electronics must be placed on the rotor, but it is only rated for half the current.

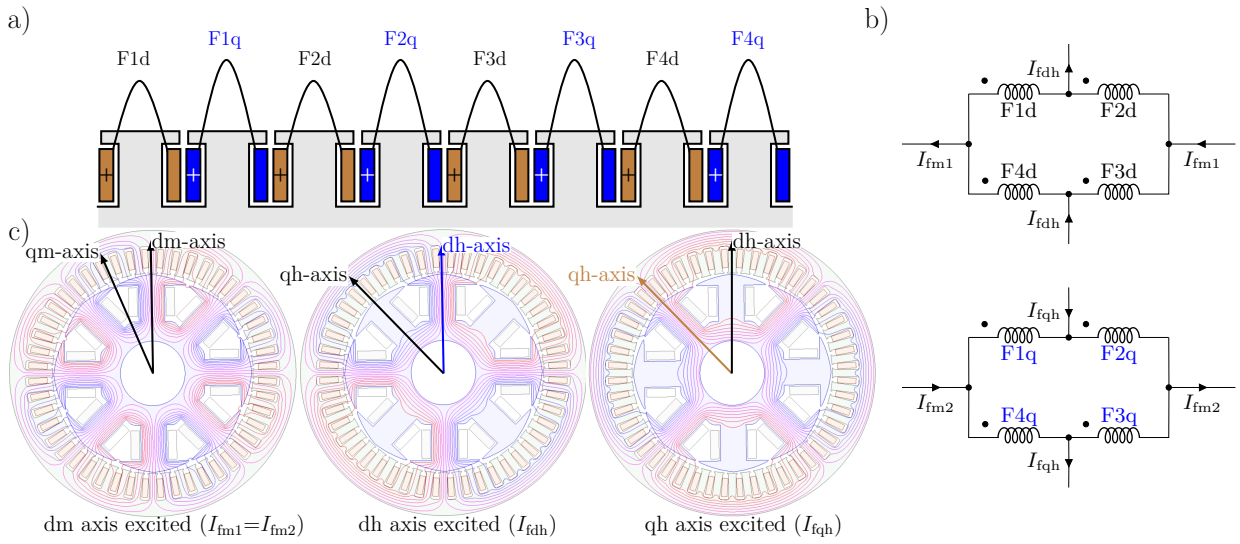

Figure 9.7: Extension of the HESM concept.

The realization of a two-phase winding allows the elimination of the voltage demand in the high-speed region by cleverly adjusting the frequency of the backward rotating field f_- as a function of speed. Fig. 9.8 shows the operating behavior of this extended HESM concept. It should be noted that these curves are not based on quantitative simulation or experimental results, but are only meant to explain the concept:

1. **Low-speed region:** In the low speed region the voltage demand is irrelevant because the maximum terminal voltage is not reached yet. Therefore, the HESM can be excited with a high and constant excitation frequency, e.g. $f_{\mathrm{exc}} = 200\,\mathrm{Hz}$ which is optimized for maximum efficiency. As only the backward rotating field occurs, the harmonic stator frequency $f_- = f_{\mathrm{exc}} - p_{\mathrm{h}} f_{\mathrm{m}}$ decreases with increasing speed. Thus, the excitation system voltage demand decreases simultaneously. This decreasing voltage demand indicates that the speed-range derating will be lower.
2. **Transitional region:** While the voltage demand for the high excitation frequency $f_{\mathrm{exc}} =$ 200 Hz decreases, it is still significant and does not reach zero until a very high speed of 6000 rpm where the backward rotating field f_- reaches 0 Hz. This is

why at some point the maximum terminal voltage is reached. Now the excitation frequency f_{exc} must be lowered to further reduce the voltage demand at the cost of lower excitation system efficiency. The increasing speed and the decreasing excitation frequency lead to a drastic reduction of voltage demand that reaches almost zero when $f_{-} = 0\,\mathrm{Hz}$, eg. at $f_{\mathrm{exc}} = 115\,\mathrm{Hz}$ and $f_{\mathrm{m}} = 3450\,\mathrm{rpm}$.

3. **Zero voltage region:** In this region the harmonic stator frequency remains at $f_{-} = 0\,\mathrm{Hz}$ which means that only a DC current is supplied that causes only a small ohmic voltage drop. In this case, the excitation frequency satisfies the condition $f_{\mathrm{exc}} = p_{\mathrm{h}} f_{\mathrm{m}}$ and increases with the motor speed. This indicates that the efficiency increases again. In conclusion, in the high-speed region the excitation system operates with high efficiency and with negligible additional voltage demand.

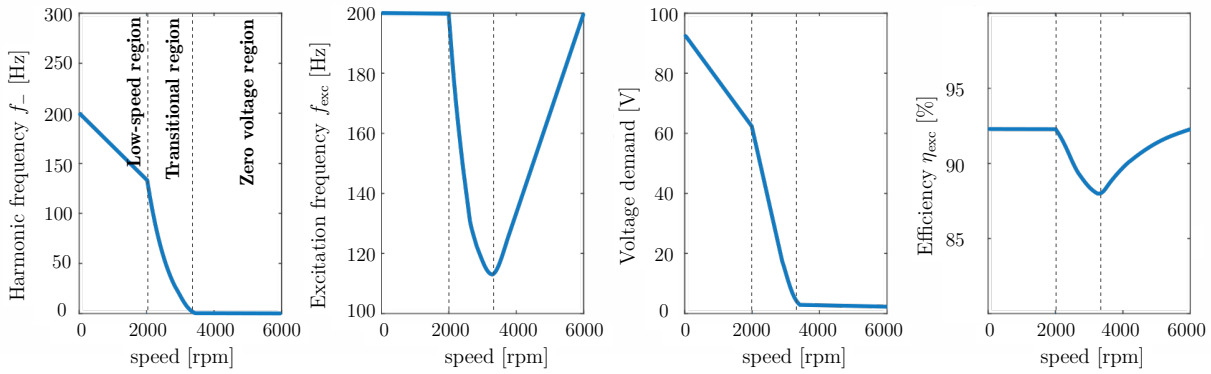

Figure 9.8: Conceptual operational curves of extended HESM.

A proof of concept is shown in Fig. 9.9 by comparing the existing HESM with the extended HESM concept proposed here. The results have been obtained from transient coupled-circuit FEA analysis. In order to demonstrate the elimination of the voltage demand, the condition $f_{\mathrm{exc}} \stackrel{!}{=} p_{\mathrm{h}} f_{\mathrm{m}}$ must be fulfilled, so that a speed of 6000 rpm is required for excitation frequency $f_{\mathrm{exc}} = 200\,\mathrm{Hz}$. The operating point is no load at a supplied field current of 7.2 A. The duty cycle is $D = 10\,\%$ for the existing HESM concept and $D = 12\,\%$ for the extended HESM. In the existing HESM concept only the dh-axis is excited with I_{dh} which induces an AC current I_{fh} into the p_{h} pole-pair field winding. After the rectifier circuitry this yields the p_{m} pole-pair field current I_{fm}. In contrast, the extended HESM concept uses **both** stator components I_{dh} **and** I_{qh} to induce the currents I_{fdh} **and** I_{fqh} into the dh- and qh- axis of the p_{h} pole-pair rotor field winding. The stator (rotor) currents I_{dh} and I_{qh} (I_{fdh} and I_{fqh}) are phase-shifted by 90% and thus produce a rotating stator (rotor) field. After the rectifier circuitry both currents are rectified into the two rotor DC field currents I_{fm1} and I_{fm2} which each provide half of the the p_{m} pole-pair field excitation. The copper losses in both concepts are similar as indicated by the current amplitudes which are smaller by a factor $\sqrt{2}$.

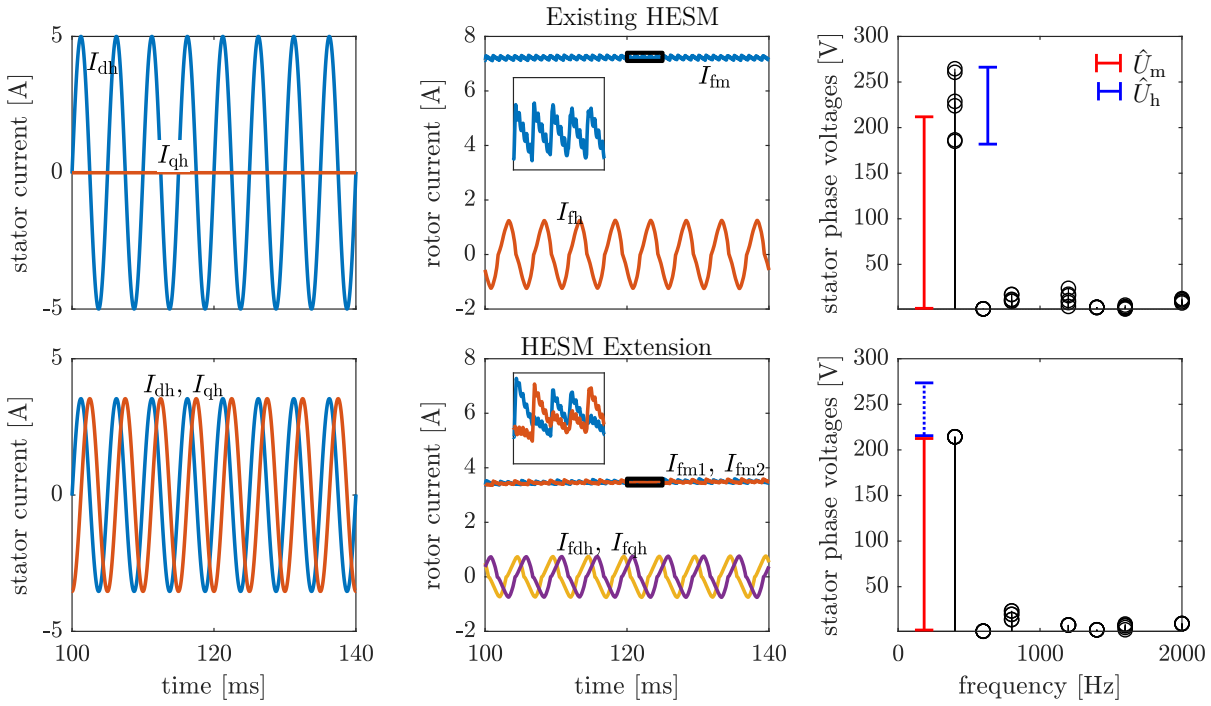

Figure 9.9: Comparison between existing and extended HESM concepts.

The most important distinction between the existing and extended concepts is in the Fourier spectrum of the six phase voltages at fundamental frequency: In the existing HESM concept the frequency of the backward rotating field $f_- = f_{exc} - p_h f_m$ is zero, but the frequency of the forward rotating field $f_+ = f_{exc} + p_h f_m$ is large[2] and requires a significant voltage $\hat{U}_h$ which is superimposed on the phase voltages and increases the DC link voltage demand. On the contrary, the extended HESM has no additional induced voltages due to the excitation system apart from parasitical induced voltages at higher order slotting and winding harmonics. Here, the induced voltage at 400 Hz is purely the p_m pole-pair voltage $\hat{U}_m$ induced by the rotor current $I_{fm} = I_{fm1} + I_{fm2}$. It should be noted that the comparatively high $\hat{U}_m$ compared to $\hat{U}_h$ in Fig. 9.9 is only due to the high speed to fulfill the zero voltage demand condition $f_{exc} \stackrel{!}{=} p_h f_m$ at $f_{exc} = 200\,Hz$.
While the results in this section are only a first glance at a possible improvement to the existing HESM concept, they do suggest that the most critical drawbacks can be improved. Further analysis is left for future work.

[2]In the special case of 6000 rpm and $f_{exc} = 200$ Hz the forward rotating frequency $\omega_+ = p_h\omega_m + \omega_{exc}$ of the p_h pole-pair machine is equal to electrical frequency $p_m\omega_m$ of the p_m pole-pair machine. For most other speeds it takes on distinct frequencies.

Chapter 10

Conclusion and Outlook

The wound-rotor synchronous machine (WRSM) is a promising alternative to permanent-magnet synchronous machines for variable-speed applications offering ecological and operational benefits. One of the main reasons against their more widespread use are the slip rings and brushes needed to supply the rotating field winding. In order to feed the field winding brushlessly, research in academia and industry is mostly focusing on external inductive or capacitive power transfer devices which use wide-bandgap semiconductors to reach high operating frequencies and thus small exciter dimensions.
In this dissertation a different approach was taken. Instead of developing an external power transfer device, the general idea is integrating an exciter machine into a conventional WRSM which jointly uses the existing iron stack and windings. The three main requirements for such a harmonic-excited synchronous machine (HESM) concept are **firstly** that an arbitrary field current can be supplied independently of the speed (i.e. it is viable for variable-speed applications). **Secondly**, no significant torque ripple should be produced by the excitation system. Therefore, only those topologies are examined which can attribute torque production and harmonic excitation to distinct pole pairs p_m and p_h which do not generate common space harmonics. This endeavor is constrained by the **third** requirement that no significant degradation of the torque capability or machine size is allowed to integrate the exciter machine. This requirement motivates the elimination of any kind of auxiliary winding in either stator or rotor.

In order to achieve this, the available methods to produce two different pole pairs from a single winding have been reviewed, i.e. pole-amplitude modulation (PAM) and pole-phase modulation (PPM). Based on these concepts a general design approach starting from the coil groups of the conventional WRSM windings has been derived. For the stator, the coil groups have been arranged as in a Dahlander winding and then fed from independent inverter legs. The rotor coils have been arranged in a bridge configuration and connected to a rectifier circuit. These modifications enable the simultaneous creation of the two pole-pair

numbers $p_\mathrm{m} = 4$ and $p_\mathrm{h} = 2$. A novelty of this work is that this has been realized without any auxiliary windings. A unique feature of this concept is that the realized p_h pole-pair machine shares the entire copper diameter with the p_m pole-pair machine rated for much higher operating currents and thus produces low copper losses. However, a problematic property of the concept is that a buck converter is needed on the rotor to adjust the load impedance between the p_h and p_m terminals of the rotor winding.

A physical machine model of the HESM concept has been derived. It has been seen that three coordinate systems can be distinguished: *Phase coordinates* describe the HESM by its actual six physical stator coils and four physical rotor coils which are cumbersome for control or modelling purposes. These can be transformed into a virtual *pole-pair coordinate* system which isolates the information about the pole pairs p_m and p_h. This representation mimics a machine with two independent winding sets which can then each be transformed into their respective, independent *dq coordinate* systems. A simplified steady-state model for the HESM has been presented which can be used to predict the excitation system performance. A field-oriented control system for the HESM is proposed which consists of two field-oriented controllers — one for the p_h and one for the p_m machine. The challenge of the p_h pole-pair controller consists in tracking a sinusoidal reference current which is needed to inductively excite the field winding. A solution with sinusoidal controllers has been proposed.

A prototype for the machine concept has been designed and later constructed using linear scaling laws and Finite-Element-Analysis (FEA). The machine prototype is equipped with slip rings and brushes for prototyping purposes. The FE model of the prototype has then been used to investigate the effect of cross-saturation as a consequence of the combined flux paths of the p_h **and** p_m pole-pair machine fields in the iron laminations. It was seen that the saturation state of the HESM is determined by magnetizing currents from both pole pairs. The excitation system currents create an oscillating saturation wave that also degrades the torque-production, albeit only to a small extent in the low saturation region. However, it shows that not only the ability of the excitation system to provide the field-current, but also the torque capability of the HESM degrades in the deep-saturation region.

In order to investigate the p_h pole-pair machine controller the complete drive system consisting of the full-order machine model, the field-oriented control system and power electronics have been implemented in the circuit simulator PLECS. It has been seen that odd harmonics of the excitation system frequency f_exc imposed by the rotor diode full-bridge rectifier propagate through the control system. The sinusoidal controllers used in the field-oriented controller cannot attenuate and even amplify the rectifier harmonics for careless designs, which leads to a degradation of the power transfer capability. Despite these harmonics, the HESM drive system has successfully been validated via simulations. The improvement of the controllers presents an area of optimization for future work.

To verify the designed machine prototype, an automated test bench for the HESM prototype has been built from scratch. To this end, two three-phase stator inverters and the rotor circuitry have been designed. This test bench has then been used to identify the p_m and p_h pole-pair machine parameters of the HESM. Afterwards, the HESM has successfully been put into operation and the degrees of freedom of the excitation system have been investigated experimentally. An excitation system efficiency between $\eta_\mathrm{exc} \approx 75 - 80\,\%$ could be identified with an increasing trend for rising speeds. However, the measurement of η_exc has only been performed for no-load operation and limited speeds due to test bench limitations. Therefore, in the future more accurate and numerous measurements are required to quantify the excitation system efficiency.
The rated torque (field current) has successfully been achieved for HESM operation. However, three important effects were observed:

- The efficiency of the excitation system is lower than can be explained purely with copper losses and features a significant speed-dependence. This can be attributed to iron losses.
- The DC link voltage demand required to inject the p_h pole-pair machine currents is large. Thus, less voltage for the p_m pole-pair machine remains.
- In addition to the rectifier harmonics, the higher order winding factors of the p_h pole-pair machine result in a rich harmonic spectrum in the machine currents.

In order to explain the high iron losses, an analysis of the HESM core flux has been performed. As the core flux is composed of both the p_m and p_h pole-pair frequencies, the symmetry period is significantly larger than in a conventional WRSM. Thus, a simplified core flux density model has been implemented and verified with FEA. Based on this model, the speed-dependence of the hysteresis, eddy current and excess loss components have been analyzed. It has been identified that the PWM current ripple plays a major role in the generation of the iron losses. An inclusion of the PWM ripple into the iron loss model has been accomplished, which gives a surprisingly decent agreement of the model with measurements. Due to the limited precision of the torque readings, a more accurate measurement of the iron losses produced is left for future work.

In order to quantify the voltage demand, the torque-speed region of the HESM has been investigated numerically and experimentally and compared to the torque-speed region of a conventional WRSM. A very simple HESM model which captures the effects of the excitation system voltage demand and efficiency has been introduced which enables an analytical investigation of the maximum torque-speed curve. It has been shown that the HESM suffers from a significant degradation of the speed range.
The operating points in the entire torque-speed region of the HESM have been calculated via optimization revealing that the efficiency of the entire HESM drive system is only decreased by less than one percent in a large region of the available speed region.

As the reduction of the torque-speed region is the most critical issue for the HESM concept, an extension to the investigated HESM concept has been discussed which can reduce the voltage demand of the p_h pole-pair machine to the ohmic voltage drop. The general idea is to split and duplicate the existing field winding so that a two-phase rotor winding of pole pair p_h is realized. This allows eliminating the dominant forward rotating frequency which is responsible for the large voltage demand. More detailed analysis and experimental verification have not been possible in the scope of this work.

While a host of topics have been addressed in this work, it should be mentioned that the HESM has mostly been investigated electromagnetically even though thermal, structural and acoustic questions arise: A detailed analysis of the thermal derating of the HESM due to the additional losses is necessary. Furthermore, at the present prototyping stage the rotor circuitry is still located outside of the machine and connected to the field winding via slip rings and brushes. In future work, they have to be placed on the rotor which exposes the power electronics to the hot rotor environment and necessitates a thermal analysis. The placement of the rotor circuitry also presents structural challenges which have been omitted in this work. During operation, higher acoustic noise compared to conventional WRSM operation have been heard which warrants an inspection of the radial forces and vibrations. Moreover, high induced voltages into the field coils during dynamic events or faults must not damage the rotor DC link or the power-electronics. Therefore, the question of safety during transients arises when operating the HESM as a variable-speed drive.

Lastly, based on the analysis conducted in this work, a realistic assessment of the proposed concept, its limitations and improvements are briefly discussed here: The focus is not on inherent limitations of harmonic excitation (like larger rotor time constant, earlier saturation and difficult monitoring of the rotor values) but on the operational drawbacks specific to the HESM in this work.
First of all, the obvious should be stated: The HESM concept in the proposed configuration and control scheme **is not competitive** with external brushless exciters neither from the perspective of efficiency nor from an operational standpoint. The most critical limitation of the HESM is the excessive DC link voltage demand required to inductively supply the field current. The second major limitation of the HESM is the low excitation system efficiency of around $75 - 80\,\%$ caused mainly by the additional iron losses of the p_h pole-pair machine. The proposed extension with a two-phase rotor winding may tackle both issue although the analysis is still in its infancy and is left for future research. However, it should be conceded that the considerable increase of complexity and cost of the additional power electronics in conjunction with safety, acoustic, thermal and mechanical challenges presently calls into question the economic viability of such a machine.

Glossary

Abbreviations

back EMF	**E**lectro-**M**otive **F**orce (induced voltage)
DPNV	**D**ual **P**urpose **N**o **V**oltage
EMI	**E**lectro**m**agnetic **I**nterference
FE	**F**inite-**E**lement
FEA	**F**inite-**E**lement **A**nalysis
FMM	**F**lux **M**odulation **M**achine
FOC	**F**ield-**O**riented **C**ontrol
FSM	**F**lux **S**witching **M**achine
HESM	**H**armonic-**E**xcited **S**ynchronous **M**achine
LUT	**L**ook-**U**p **T**able
MMF	**M**agneto-**M**otive **F**orce Θ
MTPA	**M**aximum **T**orque **P**er **A**mpere
PAM	**P**ole **A**mplitude **M**odulation
PMSM	**P**ermanent-**M**agnet **S**ynchronous **M**achine
PPM	**P**ole **P**hase **M**odulation
PWM	**P**ulse **W**idth **M**odulation
VBR	**V**oltage-**B**ehind-**R**eactance
WRSM	**W**ound-**R**otor **S**ynchronous **M**achine

Most important parameters

	HESM		WRSM
	torque-production	brushless excitation	generic machine
d-axis current	I_{dm}	I_{dh}	I_{d}
q-axis current	I_{qm}	I_{qh}	I_{q}
field current	I_{fm}	I_{fh}	I_{f}
fundamental stator winding factor	k_{wsm}	k_{wsh}	${}^{1}k_{\mathrm{ws}}$

fundamental rotor winding factor	k_{wfm}	k_{wfh}	${}^1k_{\mathrm{wf}}$
mutual inductance between d-axis and field winding	L_{dfm}	L_{dfh}	L_{df}
d-axis self inductance	L_{dm}	L_{dh}	L_{d}
q-axis self inductance	L_{qm}	L_{qh}	L_{q}
field winding self inductance	L_{fm}	L_{fh}	L_{f}
d-axis magnetizing inductance	$L_{\mathrm{hd,m}}$	$L_{\mathrm{hd,h}}$	—
number of series turns of stator winding	N_{sm}	N_{sh}	N_{s}
number of series turns of field winding	N_{fm}	N_{fh}	N_{f}
pole-pair number	p_{m}	p_{h}	p
isolated iron losses	$P_{\mathrm{fe,m}}$	$P_{\mathrm{fe,h}}$	—
stator resistance	R_{sm}	R_{sh}	R_{s}
field resistance	R_{fm}	R_{fh}	—
d-axis terminal voltage	U_{dm}	U_{dh}	U_{d}
q-axis terminal voltage	U_{qm}	U_{qh}	U_{q}
field winding terminal voltage	U_{fm}	U_{fh}	—
induced voltage into field winding	—	$U_{\mathrm{fh,ind}}$	—
referral field to d-axis current	u_{m}	u_{h}	—-
ordinal numbers of stator winding	v_{m}	$v_{\mathrm{h}+}$ and $v_{\mathrm{h}-}$	v
ordinal number of field winding	μ_{m}	μ_{h}	μ
radial electrical frequency	$p_{\mathrm{m}}\omega_{\mathrm{m}}$	ω_+ and ω_-	$p\omega$
stator current phase shift	—	—	θ_{s}
d-axis flux	Ψ_{dm}	—	Ψ_{d}
q-axis flux	Ψ_{qm}	—	Ψ_{d}

Superscripts and Subscripts

c	stator coil
cf	rotor coil
d	d-axis
dq	dq coordinates
f	rotor/ field winding
h	p_{h} pole-pair machine
k	looping index
m	p_{m} pole-pair machine
mag	magnetizing current
ph	phase coordinates
pp	pole-pair coordinates
q	q-axis
r	looping index of rotor coils
s	stator
σ	leakage
δ	airgap
$'$	referred to stator (Chapter 5 onward)
*	desired (control) value

Symbols

a	ordinal number for integration
A	surface current
A_{cu}	copper area
AT	ampere turns
b_{tooth}	tooth width of stator or rotor
B	flux density
d	inner stator (bore) diameter ($d = 2r$)
$\mathbf{dL}$	differential inductance matrix
dL	differential inductance
f_{exc}	excitation frequency
h_{yoke}	yoke height of stator or rotor
h_δ	mechanical airgap length
I	current
j	complex number $\sqrt{-1}$
k_{c}	double-sided carter factor
k_{cs}	stator-side carter factor
${}^{v}k_{\mathrm{ws}}$	stator winding factor
${}^{\mu}k_{\mathrm{wf}}$	rotor winding factor
k_{Uh}	DC link voltage to supply 1 ampere of field current I_{fm}
k_{Idh}	stator current to supply 1 ampere of field current I_{fm}
l_{Fe}	stack length
$\mathbf{L}$	absolute inductance matrix
m	number of phases
M_{el}	electromagnetic torque
n_{s}, n_{f}	ordinal number of permeance waves
n	phase shift parameter (Chapter 4)
N	number of series turns
p	pole-pair number
p_{hys}	hysteresis losses $[\frac{\mathrm{W}}{\mathrm{kg}}]$
p_{eddy}	eddy losses $[\frac{\mathrm{W}}{\mathrm{kg}}]$
p_{exc}	excess losses $[\frac{\mathrm{W}}{\mathrm{kg}}]$
r	radius to middle of airgap
R_{eq}	equivalent input resistance of rectifier circuit
$\mathbf{R}$	resistance matrix
D	duty cycle of buck converter
$\mathbf{T}$	transformation matrix
U	voltage
U_{dc}	DC link voltage
W	winding function
Z	number of slots
Ψ	flux
Λ	permeance wave
Θ	MMF
φ	position along airgap circumference (stator coordinates)
φ_{f}	position along airgap circumference (rotor coordinates)
ω_{m}	radial shaft speed
β	rotor displacement
θ_{I}	phase shift of rotor current
ω_{exc}	$2\pi f_{\mathrm{exc}}$
η	drive system efficiency
η_{exc}	excitation system efficiency

Bibliography

[1] *China's Rare Earth Metals Monopoly Could Be Coming to an End*, https://www.newsweek.com/china-monopoly-rare-earths-critical-minerals-market-green-clean-energy-1756042, Accessed: 2022-12-23.

[2] *How Rare-Earth Mining Has Devastated China's Environment*, https://earth.org/rare-earth-mining-has-devastated-chinas-environment, Accessed: 2022-12-23.

[3] G. Friedrich, "Experimental Comparison between Wound Rotor and Permanent Magnet Synchronous Machine for Integrated Starter Generator Applications," in *2010 IEEE Energy Conversion Congress and Exposition*, 2010, pp. 1731–1736. DOI: 10.1109/ecce.2010.5618122.

[4] I. K. Geoff Klempner, *Operation and Maintenance of Large Turbo-Generators*. John Wiley and Sons, Ltd, 2004, ISBN: 9780471683384. DOI: https://doi.org/10.1002/0471683388.

[5] G. Müller – B. Ponick, *Grundlagen Elektrischer Maschinen*. Weinheim: Wiley, 2014, ISBN: 9783527412051. DOI: 10.1002/9783527676095.

[6] S. Schmülling, "Die Asynchrone Erregermaschine als Erregereinrichtung für Generatoren Kleiner und Mittlerer Leistung," Ph.D. dissertation, TU Dortmund University, 2015.

[7] D. Li – R. Qu – J. Li, "Topologies and Analysis of Flux-Modulation Machines," in *2015 IEEE Energy Conversion Congress and Exposition (ECCE)*, 2015, pp. 2153–2160. DOI: 10.1109/ECCE.2015.7309964.

[8] Y. Tang – J. J. H. Paulides – T. E. Motoasca – E. A. Lomonova, "Flux-Switching Machine with DC Excitation," *IEEE Transactions on Magnetics*, vol. 48, no. 11, pp. 3583–3586, Nov. 2012. DOI: 10.1109/tmag.2012.2199100.

[9] T. D. Strous – H. Polinder – J. A. Ferreira, "Brushless Doubly-fed Induction Machines for Wind Turbines: Developments and Research Challenges," *IET Electric Power Applications*, vol. 11, no. 6, pp. 991–1000, 2017. DOI: https://doi.org/10.1049/iet-epa.2016.0118.

[10] P. Löhdefink – A. Dietz – A. Möckel, "Direct Drive Concept for Heavy-Duty Traction Applications with the Brushless Doubly-fed Induction Machine," in *2018 Thirteenth International Conference on Ecological Vehicles and Renewable Energies (EVER)*, Apr. 2018, pp. 1–6. DOI: 10.1109/ever.2018.8362360.

[11] R. E. Betz – M. G. Jovanović, "The Brushless Doubly Fed Reluctance Machine and the Synchronous Reluctance Machine - A Comparison," in *IEEE Industry Applications Conference. 34th IAS Annual Meeting*, vol. 2, 1999, pp. 854–861. DOI: 10.1109/IAS.1999.801609.

[12] R. Manko – S. Čorović – D. Miljavec, "Analysis and Design of Rotary Transformer for Wireless Power Transmission," in *2020 IEEE Problems of Automated Electrodrive. Theory and Practice (PAEP)*, 2020, pp. 1–6. DOI: 10.1109/paep49887.2020.9240870.

[13] S. Hagen – J. Dai – I. P. Brown – D. C. Ludois, "Low-Cost, Printed Circuit Board Construction, Capacitively Coupled Excitation System for Wound Field Synchronous Machines," in *2019 IEEE Energy Conversion Congress and Exposition (ECCE)*, 2019, pp. 5358–5364. DOI: 10.1109/ECCE.2019.8913084.

[14] R. Perrin – G. Bueno-Mariani, "Control and Integration of a Multiphase Brushless Wounded Synchronous Motor Drive," in *2022 24th European Conference on Power Electronics and Applications (EPE'22 ECCE Europe)*, 2022, pp. 1–10.

[15] K. Inoue – H. Yamashita – E. Nakamae – T. Fujikawa, "A Brushless Self-Exciting Three-Phase Synchronous Generator utilizing the 5th-Space Harmonic Component of Magneto Motive Force through Armature Currents," *IEEE Transactions on Energy Conversion*, vol. 7, no. 3, pp. 517–524, 1992. DOI: 10.1109/60.148574.

[16] M. Ayub – G. Jawad – B.-i. Kwon, "Consequent-Pole Hybrid Excitation Brushless Wound Field Synchronous Machine with Fractional Slot Concentrated Winding," *IEEE Transactions on Magnetics*, vol. 55, no. 7, pp. 1–5, 2019. DOI: 10.1109/TMAG.2018.2890509.

[17] Y. T. Rao – S. Basak – C. Chakraborty – S. S. Gupta, "Brushless Induction Synchronous Generator," in *2016 IEEE 25th International Symposium on Industrial Electronics (ISIE)*, Jun. 2016, pp. 147–152. DOI: 10.1109/isie.2016.7744881.

[18] J. Oyama – T. Higuchi – T. Abe – E. Yamada – K. Shibahara, "Principle and Characteristics of a New Type AC Servo Motor 'VARIFIELD'," in *1993 Fifth European Conference on Power Electronics and Applications*, 1993, 123–128 vol.6.

[19] S. Nonaka – T. Kawaguchi, "Excitation Scheme of Brushless Self-Excited-Type Three-Phase Synchronous Machine," *IEEE Transactions on Industry Applications*, vol. 28, no. 6, pp. 1322–1329, Nov. 1992. DOI: 10.1109/28.175284.

[20] M. Ayub – S. S. H. Bukhari – G. Jawad – B.-i. Kwon, "Brushless Wound Field Synchronous Machine with Third-Harmonic Field Excitation using a Single Inverter," *Electrical Engineering*, vol. 101, no. 1, pp. 165–173, 2019. DOI: 10.1007/s00202-019-00763-3.

[21] Q. Ali – T. A. Lipo – B. Kwon, "Design and Analysis of a Novel Brushless Wound Rotor Synchronous Machine," *IEEE Transactions on Magnetics*, vol. 51, no. 11, pp. 1–4, Nov. 2015, ISSN: 1941-0069. DOI: 10.1109/tmag.2015.2440433.

[22] G. Dajaku – D. Gerling, "Self-Excited Synchronous Machine with High Torque Capability at Zero Speed," in *2018 International Symposium on Power Electronics, Electrical Drives, Automation and Motion (SPEEDAM)*, 2018, pp. 1165–1171. DOI: 10.1109/SPEEDAM.2018.8445318.

[23] F. Yao – D. Sun – L. Sun – T. A. Lipo, "Dual Third-Harmonic-Current Excitation Principle of a Brushless Synchronous Machine Based on Double Three-Phase Armature Windings," in *2019 International Conference on Electrical Machines and Systems (ICEMS)*, 2019, pp. 1–4. DOI: 10.1109/icems.2019.8922370.

[24] R. Lyra – T. Lipo, "Torque Density Improvement in a Six-Phase Induction Motor with Third Harmonic Current Injection," *IEEE Transactions on Industry Applications*, vol. 38, no. 5, pp. 1351–1360, 2002. DOI: 10.1109/TIA.2002.802938.

[25] K. Oberretl, "General Field-Harmonic Theory for Three-Phase, Single-Phase and Linear Motors with Squirrel Cage Rotor, taking Multiple Armature Reaction and Slot Openings into Account - Part I: Theory and Method of Calculation," *Archiv für Elektrotechnik*, vol. 76, pp. 194–194, Mar. 1993. DOI: 10.1007/bf01597589.

[26] E. Bolte, *Elektrische Maschinen und Antriebe, Grundlagen · Magnetfelder · Erwärmung · Funktionsprinzipien · Betriebsarten · Einsatz · Entwurf · Wirtschaftlichkeit*, 2nd ed. Berlin, Heidelberg: Springer Vieweg, 2018. DOI: 10.1007/978-3-662-54688-8.

[27] A. Binder, *Elektrische Maschinen und Antriebe, Grundlagen, Betriebsverhalten*, 2nd ed. Berlin, Heidelberg: Springer Vieweg, 2017. DOI: 10.1007/978-3-662-53241-6.

[28] O. Misir – F. Dobbert – B. Ponick, "Analytical Method for the Air Gap Permeance Calculation of Salient Pole Synchronous Machines," in *E & I Elektrotechnik und Informationstechnik 133*, 2016, pp. 103–111. DOI: https://doi.org/10.1007/s00502-016-0395-9.

[29] G. Kovacs, "Pole-Changing Windings for Close Ratio and 1:N Ratio Using the 3//Y / 3//Y Method," *Advances in Science, Technology and Engineering Systems Journal*, vol. 3, pp. 241–253, Aug. 2018. DOI: 10.25046/aj030424.

[30] L. Melcescu – M. Cistelecan – O. Craiu – H. Cosan, "A New 4/6 Pole-Changing Double Layer Winding for Three Phase Electrical Machines," in *2010 International Conference on Electrical Machines (ICEM)*, Oct. 2010, pp. 1–6. DOI: 10.1109/ICELMACH.2010.5608041.

[31] R. Raj – P. Subramaniyane – L. Peretti, "Design of a Variable Phase-Pole Induction Machine for Electric Vehicle Applications," in *2022 International Conference on Electrical Machines (ICEM)*, 2022, pp. 976–982. DOI: 10.1109/ICEM51905.2022.9910688.

[32] H. Liu – J. Wang – Z. Zhang, "Performance Analysis of Variable Speed Multiphase Induction Motor with Pole Phase Modulation," *Archives of Electrical Engineering*, vol. 65, Sep. 2016. DOI: 10.1515/aee-2016-0031.

[33] E. L. Severson – R. Nilssen – T. Undeland – N. Mohan, "Design of Dual Purpose No-Voltage Combined Windings for Bearingless Motors," *IEEE Transactions on Industry Applications*, vol. 53, no. 5, pp. 4368–4379, 2017. DOI: 10.1109/TIA.2017.2706653.

[34] A. Broadway – G. Thomas, "Single-Unit P.A.M. Induction Frequency Convertors," *Proceedings of the Institution of Electrical Engineers*, vol. 114, pp. 958–964, 7 Jul. 1967.

[35] J. Pötter – M. Pfost – G. Schullerus, "Topology Analysis of Harmonic-Excited Wound-Rotor Synchronous Machines," in *2021 IEEE International Electric Machines Drives Conference (IEMDC)*, 2021, pp. 1–7. DOI: 10.1109/iemdc47953.2021.9449529.

[36] J. Specovius, *Grundkurs Leistungselektronik, Bauelemente, Schaltungen und Systeme*, 10th ed. Wiesbaden: Springer Vieweg, 2020. DOI: 10.1007/978-3-658-30399-0.

[37] R. H. Park, "Two-Reaction Theory of Synchronous Machines Generalized Method of Analysis - Part I," *Transactions of the American Institute of Electrical Engineers*, vol. 48, no. 3, pp. 716–727, 1929. DOI: 10.1109/T-AIEE.1929.5055275.

[38] S. L. Kellner, "Parameteridentifikation bei Permanenterregten Synchronmaschinen," doctoralthesis, Friedrich-Alexander-Universität Erlangen-Nürnberg (FAU), 2012.

[39] M. Chapariha – F. Therrien – J. Jatskevich – H. W. Dommel, "Explicit Formulations for Constant-Parameter Voltage-Behind-Reactance Interfacing of Synchronous Machine Models," *IEEE Transactions on Energy Conversion*, vol. 28, no. 4, pp. 1053–1063, 2013. DOI: 10.1109/TEC.2013.2284774.

[40] P. Krause – O. Wasynczuk – S. Sudhoff – S. Pekarek, *Analysis of electric machinery and drive systems*. Piscataway, NJ: IEEE Press, 2013. DOI: 10.1002/9781118524336.

[41] D. Schröder – J. Böcker, *Elektrische Antriebe – Regelung von Antriebssystemen*, 5th ed. Berlin, Heidelberg: Springer Vieweg, 2021. DOI: 10.1007/978-3-662-62700-6.

[42] S. Fukuda – R. Imamura, "Application of a Sinusoidal Internal Model to Current Control of Three-Phase Utility-Interface Converters," *IEEE Transactions on Industrial Electronics*, vol. 52, no. 2, pp. 420–426, 2005. DOI: 10.1109/TIE.2005.843914.

[43] F. Graffeo – S. Vaschetto – M. Cossale – M. Kerschbaumer – E. C. Bortoni – A. Cavagnino, "Cylindrical Wound-Rotor Synchronous Machines for Traction Applications," in *2020 International Conference on Electrical Machines (ICEM)*, vol. 1, 2020, pp. 1736–1742. DOI: 10.1109/ICEM49940.2020.9270992.

[44] S. Stipetic – D. Zarko – M. Popescu, "Scaling Laws for Synchronous Permanent Magnet Machines," in *2015 Tenth International Conference on Ecological Vehicles and Renewable Energies (EVER)*, 2015, pp. 1–7. DOI: 10.1109/EVER.2015.7113006.

[45] R. Grune, "Verlustoptimaler Betrieb einer Elektrisch Erregten Synchronmaschine für den Einsatz in Elektrofahrzeugen," Ph.D. dissertation, TU Berlin, Jan. 2013. DOI: 10.14279/depositonce-3485.

[46] J. Walker – D. Dorrell – C. Cossar, "Flux-Linkage Calculation in Permanent-Magnet Motors Using the Frozen Permeabilities Method," *IEEE Transactions on Magnetics*, vol. 41, no. 10, pp. 3946–3948, 2005. DOI: 10.1109/TMAG.2005.854973.

[47] *ANSYS Electronics Help - Inductance Computation for 2D and 3D Transient Solutions*, Ansys Inc, 2021.

[48] IEC 60034-2-1, *Rotating Electrical Machines - Part 2-1: Standard Methods for Determining Losses and Efficiency from Tests (Excluding Machines for Traction Vehicles)*, 2014.

[49] G. Bertotti, "General Properties of Power Losses in Soft Ferromagnetic Materials," *IEEE Transactions on Magnetics*, vol. 24, no. 1, pp. 621–630, 1988. DOI: 10.1109/20.43994.

[50] D. Lin – P. Zhou – W. N. Fu – Z. Badics – Z. J. Cendes, "A Dynamic Core Loss Model for Soft Ferromagnetic and Power Ferrite Materials in Transient Finite Element Analysis," *IEEE Transactions on Magnetics*, vol. 40, no. 2, pp. 1318–1321, 2004. DOI: 10.1109/tmag.2004.825025.

[51] K. Oberretl, "Iron Losses, Flux Pulsations and Magnetic Slot Wedges in Squirrel-Cage Induction Motors," *Electrical Engineering*, vol. 82, pp. 301–311, May 2012. DOI: 10.1007/s002020000050.

[52] A. Tessarolo, "Accurate Computation of Multiphase Synchronous Machine Inductances Based on Winding Function Theory," *IEEE Transactions on Energy Conversion*, vol. 27, no. 4, pp. 895–904, 2012. DOI: 10.1109/TEC.2012.2219050.

[53] I. D. Mayergoyz, "The Classical Preisach Model of Hysteresis and Reversibility," *Journal of Applied Physics*, vol. 69, no. 8, pp. 4602–4604, 1991. DOI: 10.1063/1.348323.

[54] D. Jiles – D. Atherton, "Theory of Ferromagnetic Hysteresis," *Journal of Magnetism and Magnetic Materials*, vol. 61, no. 1, pp. 48–60, 1986. DOI: 10.1016/0304-8853(86)90066-1.

[55] D. Lin – P. Zhou – A. Bergqvist, "Improved Vector Play Model and Parameter Identification for Magnetic Hysteresis Materials," *IEEE Transactions on Magnetics*, vol. 50, no. 2, pp. 357–360, 2014. DOI: 10.1109/TMAG.2013.2281567.

[56] D. Jiles, "A Self Consistent Generalized Model for the Calculation of Minor Loop Excursions in the Theory of Hysteresis," *IEEE Transactions on Magnetics*, vol. 28, no. 5, pp. 2602–2604, 1992. DOI: 10.1109/20.179570.

[57] A. Benabou – J. Leite – S. Clénet – C. Simão – N. Sadowski, "Minor Loops Modelling with a Modified Jiles–Atherton Model and Comparison with the Preisach Model," *Journal of Magnetism and Magnetic Materials*, vol. 320, no. 20, pp. 1034–1038, 2008, Proceedings of the 18th International Symposium on Soft Magnetic Materials.

[58] K. Venkatachalam – C. R. Sullivan – T. Abdallah – H. Tacca, "Accurate Prediction of Ferrite Core Loss with Nonsinusoidal Waveforms Using only Steinmetz Parameters," in *2002 IEEE Workshop on Computers in Power Electronics, 2002. Proceedings.*, Jun. 2002, pp. 36–41. DOI: 10.1109/cipe.2002.1196712.

[59] *Plecs User Manual - Hysteretic Core based on Preisach model*, Plexim GmbH, 2022.

[60] K. Bradley – W. Cao – J. Clare – P. Wheeler, "Predicting Inverter-Induced Harmonic Loss by Improved Harmonic Injection," *IEEE Transactions on Power Electronics*, vol. 23, no. 5, pp. 2619–2624, 2008. DOI: 10.1109/TPEL.2008.2002329.

[61] L. Chang – T. M. Jahns, "Prediction and Evaluation of PWM-Induced Current Ripple in IPM Machines Incorporating Slotting, Saturation, and Cross-Coupling Effects," in *2017 20th International Conference on Electrical Machines and Systems (ICEMS)*, 2017, pp. 1–6. DOI: 10.1109/ICEMS.2017.8056205.

[62] L. Chang – T. M. Jahns – R. Blissenbach, "Estimation of PWM - Induced Iron Loss in IPM Machines Incorporating the Impact of Flux Ripple Waveshape and Nonlinear Magnetic Characteristics," in *2018 IEEE Energy Conversion Congress and Exposition (ECCE)*, 2018, pp. 4956–4963. DOI: 10.1109/ECCE.2018.8557748.

[63] W. Q. Chu – Z. Q. Zhu – J. Zhang – X. Liu – D. A. Stone – M. P. Foster, "Investigation on Operational Envelops and Efficiency Maps of Electrically Excited Machines for Electrical Vehicle Applications," *IEEE Transactions on Magnetics*, vol. 51, no. 4, pp. 1–10, 2015. DOI: 10.1109/tmag.2014.2359008.